

# **Validation of CFD Codes for Parawing Geometries in Subsonic to Supersonic Flows**

*Juan G. Cruz-Ayoroa*  
Georgia Institute of Technology, Atlanta, GA  
Ames Research Center, Moffett Field, California

*Joseph A. Garcia*  
Systems Analysis Branch  
NASA Ames Research Center

*John E. Melton*  
Systems Analysis Branch  
NASA Ames Research Center



## NASA STI Program ... in Profile

Since its founding, NASA has been dedicated to the advancement of aeronautics and space science. The NASA scientific and technical information (STI) program plays a key part in helping NASA maintain this important role.

The NASA STI program operates under the auspices of the Agency Chief Information Officer. It collects, organizes, provides for archiving, and disseminates NASA's STI. The NASA STI program provides access to the NASA Aeronautics and Space Database and its public interface, the NASA Technical Reports Server, thus providing one of the largest collections of aeronautical and space science STI in the world. Results are published in both non-NASA channels and by NASA in the NASA STI Report Series, which includes the following report types:

- **TECHNICAL PUBLICATION.** Reports of completed research or a major significant phase of research that present the results of NASA Programs and include extensive data or theoretical analysis. Includes compilations of significant scientific and technical data and information deemed to be of continuing reference value. NASA counterpart of peer-reviewed formal professional papers but has less stringent limitations on manuscript length and extent of graphic presentations.
- **TECHNICAL MEMORANDUM.** Scientific and technical findings that are preliminary or of specialized interest, e.g., quick release reports, working papers, and bibliographies that contain minimal annotation. Does not contain extensive analysis.
- **CONTRACTOR REPORT.** Scientific and technical findings by NASA-sponsored contractors and grantees.

- **CONFERENCE PUBLICATION.** Collected papers from scientific and technical conferences, symposia, seminars, or other meetings sponsored or co-sponsored by NASA.

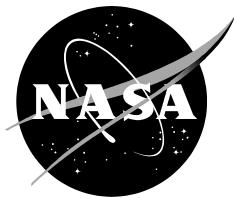
- **SPECIAL PUBLICATION.** Scientific, technical, or historical information from NASA programs, projects, and missions, often concerned with subjects having substantial public interest.

- **TECHNICAL TRANSLATION.** English-language translations of foreign scientific and technical material pertinent to NASA's mission.

Specialized services also include organizing and publishing research results, distributing specialized research announcements and feeds, providing information desk and personal search support, and enabling data exchange services.

For more information about the NASA STI program, see the following:

- Access the NASA STI program home page at <http://www.sti.nasa.gov>
- E-mail your question to [help@sti.nasa.gov](mailto:help@sti.nasa.gov)
- Fax your question to the NASA STI Information Desk at 443-757-5803
- Phone the NASA STI Information Desk at 443-757-5802
- Write to:  
STI Information Desk  
NASA Center for AeroSpace Information  
7115 Standard Drive  
Hanover, MD 21076-1320



# **Validation of CFD Codes for Parawing Geometries in Subsonic to Supersonic Flows**

*Juan G. Cruz-Ayoroa*  
Georgia Institute of Technology, Atlanta, GA  
Ames Research Center, Moffett Field, California

*Joseph A. Garcia*  
Systems Analysis Branch  
NASA Ames Research Center

*John E. Melton*  
Systems Analysis Branch  
NASA Ames Research Center

National Aeronautics and  
Space Administration

*Ames Research Center*  
Moffett Field, CA 94035-1000

---

**May 2013**



## **Acknowledgments**

The work done by the first author was supported by the Universities Space Research Association (USRA) Education Associates Program under NASA's co-operative agreement number NNX09AG76A.

Available from:

NASA Center for AeroSpace Information  
7115 Standard Drive  
Hanover, MD 21076-1320  
443-757-5802

This report is also available in electronic form at

<http://ntrs.nasa.gov/search.jsp>



## Abstract

Computational Fluid Dynamic studies of a rigid parawing at Mach numbers from 0.8 to 4.65 were carried out using three established inviscid, viscous and independent panel method codes. Pressure distributions along four chordwise sections of the wing were compared to experimental wind tunnel data gathered from NASA technical reports. Results show good prediction of the overall trends and magnitudes of the pressure distributions for the inviscid and viscous solvers. Pressure results for the panel method code diverge from test data at large angles of attack due to shock interaction phenomena. Trends in the flow behavior and their effect on the integrated force and moments on this type of wing are examined in detail using the inviscid CFD code results.

## Introduction

The use of parawings for supersonic applications presents both appealing benefits and potential challenges. The particular concave shape of the wing poses distinctive aerodynamic behaviors, especially at supersonic conditions. In order to predict parawing aerodynamic performance at these conditions, it is important to develop an understanding of the ability of modern Computational Fluid Dynamic (CFD) tools to effectively model these behaviors.

This study presents CFD results of a rigid parawing model at low-subsonic to high-supersonic Mach numbers using three established inviscid, viscous and independent panel method codes, and a comparison of the computational results to experimental data obtained from previous wind-tunnel studies [1,2,3]. The simulation codes tested consist of CBAERO, CART3D, and STAR-CCM+. The CBAERO software package is an engineering level tool for predicting the aerodynamic and aero-thermodynamic characteristics of general vehicle configurations. For subsonic Mach numbers, CBAERO uses a fast, unstructured, multi-pole panel algorithm coupled with a streamline tracing formulation to define the viscous surface solution. For supersonic and hypersonic Mach numbers, CBAERO uses various independent panel methods coupled with a streamline tracing formulation, an attachment line detection method, and stagnation-attachment line heating models to define the viscous aero-thermal environment. [4,5]. CART3D is a high-fidelity inviscid analysis package for conceptual preliminary aerodynamic design. The package uses an automatic generation of topologically unstructured, adaptively refined Cartesian meshes and an adjoint solver [5-7]. Viscous results were also obtained using the commercial code STAR-CCM+ [8]. STAR-CCM+ solves the Navier-Stokes equations using a prismatic unstructured mesh near the wall surface, and an unstructured field mesh to discretize between the outermost layer of the prismatic mesh and the outer boundaries. Boundary layers are modeled using wall functions with a variety of conventional turbulence models.

The geometry analyzed consists of a 61.6 degree swept parawing with a cylindrical leading edge and slender keel. The canopy forms half of a right circular cone and is considered to be rigid both in the computational and experimental studies. Pressure distributions along four chordwise sections of the wing were compared to experimental wind tunnel data gathered from NASA technical reports [1-3]. The reports provide wind tunnel data for a 14.6 inch rigid model of the same shape, at Mach numbers from 0.8 to 4.65 and angles of attack of 0 to 90 degrees.

## Description of Geometry

A diagram of the model and the pressure port locations is presented in Figure 1. The experimental model presented in the reports consists of two 1/10 inch thick metal conical

canopy shapes so that the trailing edges forms half circles and the leading edges had 62.5 degree sweep. The canopies were welded to a 14.2 inch center keel and plastic leading edges of 3/8 inch diameter were cast to the canopies to complete the model [1]. An auxiliary strut extended below the reference plane of the models as shown in the left view of Figure 1. Wires were attached from the auxiliary strut to the tip leading edge of the wings in order to reduce the deflection of the wings under aerodynamic loads (see Figure 1b of Ref. 3).

The computational models recreated all the features of the model, including the auxiliary strut, but excluding the wires, as their effect on the surface pressure in the wings was assumed negligible. Although previous studies have suggested that the shape of the flexible canopy can have a significant impact on the aerodynamics of an actual parawing at supersonic and hypersonic conditions [9], a rigid parawing model is appropriate for this investigation, as this study focused solely on the aerodynamic modeling capabilities of various CFD tools. The experimental setup is assumed sufficiently rigid, so any effects of aeroelastic deformations during the testing were ignored. The tunnel walls were not modeled in the computational study. Instead, a wall correction supplied by the experimental data was applied and will be discussed in the Methodology section of this report.

Pressure was measured at specific locations on the surface of the wings of both experimental and computational models. These locations consist of four chordwise sections distributed uniformly along the span, containing 25 measurement locations each, distributed along the top and bottom of the wing as shown in Figure 1.

## Methodology

Tables 1, 2 and 3 present the test matrices for this study. The selection of test Mach number and angles of attack was driven mainly by the available experimental data. A significant level of experimental uncertainty exists on these numbers due to limitations in the information presented in the experimental reports. The Mach number for the subsonic case was calculated by using given approximate values of dynamic pressure and Reynolds number, and assuming a flow temperature of 20° C. A 0.15° angle of attack correction was applied to the subsonic nominal angles of attack based on a reported estimated sting deflection of around 0.1° to 0.2°. The same correction was applied to the transonic cases. The experimental reports also stated that the Mach 1.2 data might have been affected by reflected compressions and expansions from the wind-tunnel walls, and the data was not corrected for these effects. Finally, for the supersonic cases, a flow misalignment angle was provided for each Mach number and was used accordingly. No bounds on measurement errors or wind tunnel condition uncertainties are known.

The CART3D test matrix covers Mach numbers from 0.8 to 4.65 and angles of attack of 0° to 90° in increments of 10°. An additional set of cases with angle of attack increment of 2.5° were carried out for the Mach 3.95 and 4.65 cases between 50° and 70° in order to study in more detail the flow behavior in this regime. These cases were solved using the CART3D adjoint solver with a total drag functional. Ten adaptation cycles were used, except in 80° and 90° angle of attack cases where the number of adaptation cycles was limited to 7 due to convergence issues.

The CBAERO tests focus on reproducing the available high-supersonic experimental data. The tangent-wedge surface pressure approximation option was used for these cases, as it was found to reproduce experimental results better than the Modified Newtonian model.

The STAR-CCM+ study was focused on selected cases in the subsonic, transonic and supersonic regimes. A fully turbulent boundary layer was assumed to exist over the entire model, and the  $k-\omega$  SST turbulence model was used for all cases.

## Presentation of Data

Surface pressure data for experimental and computational results of the Parawing (Rogallo Wing) are presented in Figures 2 to 4. Figure 2 contains the results for the CART3D test cases compared to the experimental results. The center of the diagrams show top (left) and bottom (right) views of the wing, colored by computational pressure coefficient ( $C_p$ ) magnitudes. Chordwise lines specify the location of the four measurement sections, and circles colored by experimental  $C_p$  measurements are located along these lines, corresponding to their location on the actual model. Plots of surface pressure coefficient versus normalized chordwise location for each of the four chordwise sections are located on the four corners of each diagram. The solid black lines represent computational results, while the red circles correspond to experimental measured data, where available.

Figure 3 contains the STAR-CCM+ results compared to CART3D results and to experimental data. The center of the diagrams contains surface  $C_p$  magnitude contours for the bottom of the model with STAR-CCM+ simulations shown on the left and CART3D simulations on the right. The  $C_p$  plots on the corners show STAR-CCM+ results in blue, CART3D results in black, and experimental data in red symbols.

Figure 4 shows all the CBAERO results compared to CART3D results and to experimental data. The center of the diagrams contains surface  $C_p$  contours for the bottom of the model with CBAERO simulations on the left and CART3D simulations on the right. The  $C_p$  plots on the corners show CBAERO results in blue, CART3D results in black, and experimental data in red symbols.

Finally, Figures 5 and 6 show contour plots of pressure coefficient for a mid-keel section of the wing, and force coefficient results, respectively from CART3D simulations.

## Discussion of Results

### Comparison of CART3D Results to Experimental Results

The CART3D results show an overall good prediction of surface pressure magnitudes and trends across the subsonic, transonic and supersonic regimes. The subsonic results (Mach 0.2) show a very good comparison to experimental data, except for a marked over-prediction of pressure coefficients in the top surface of the wing at the angles of attack of 50° and 60°. This is consistent with the possibility of an inaccurate prediction of the flow separation angle due to inviscid assumptions. The transonic results (Mach 0.8 to 1.2) show an excellent correlation of the surface pressure trends, but a consistent over-prediction of surface pressures, particularly for the Mach 1.2 cases. A possible explanation is the influence of reflected shocks from the tunnel walls, mentioned in the experimental reports. The supersonic cases (Mach 2.29 to 4.65) also show excellent predictions of pressure magnitudes and trends.

### Comparison of STAR-CCM+ Results to CART3D and Experimental Results

STAR-CCM+ results proved to be very similar to CART3D results across all Mach number regimes. In the subsonic regime, STAR-CCM+ showed slightly better prediction of the flow separation angle when compared to CART3D. The transonic results show slightly different predictions for the pressures in the top of the wing, but also show a consistent over-prediction of pressures when compared to experimental results. In the supersonic regime, CART3D and STAR-CCM+ showed equal predictive capabilities.

## Comparison of CBAERO Results to CART3D and Experimental Results

The CBAERO results show a good agreement with experimental data and with CART3D results up to an angle of attack of around  $30^\circ$ . At this point, the results start diverging significantly as the angle of attack increases, particularly for the lower surface of the wing. At  $70^\circ$  angle of attack the experimental data shows a fairly uniform pressure distribution under the wing, while CBAERO predicts a distribution that increases in magnitude from leading to trailing edge. As would be expected, these discrepancies can be attributed to the effects of shock interactions on the wing, which are not captured by the panel method.

## Parawing Supersonic Aerodynamic Behavior

The CART3D solutions were used to examine the predicted flow behavior at supersonic conditions in more detail, and to determine how these predictions are supported by experimental data. As shown in Figure 5, the pressure contours on a transverse section of the wing at Mach 4.65 show a shock structure composed of three bow shocks, formed by the leading edges and the keel. As the angle of attack of the vehicle increases, the bow shocks grow larger and stronger and eventually merge together into a single shock covering the parawing.

The effect of these shocks on the surface pressure distribution can be observed in the surface pressure contour plots for the Mach 4.65 case (Figures 2.97 to 2.112). At angles of attack of  $0^\circ$  to  $40^\circ$  the shocks are still weak and the pressure distribution is fairly uniform. Beyond  $50^\circ$  angle of attack, two contour lines of localized high pressure can be observed on each wing, parallel to the leading edge and the keel. As the angle of attack increases, these areas of high pressure move closer to the leading edge and keel. At  $65^\circ$  angle of attack, the lines of high pressure have reached the leading edge and the keel, and the pressure under the wing becomes relatively constant. This point corresponds to the merging of the three shock structures. From  $65.9^\circ$  to  $90.0^\circ$  angle of attack the pressure under the wing stays uniform while increasing in magnitude. The experimental data for these cases clearly shows the same behavior, indicating that this effect is physical.

The lift, drag and moment coefficients computed by CART3D are shown in Figure 6. A change in the trend of these curves can be observed at around  $65^\circ$  angle of attack for the supersonic and hypersonic cases, particularly in the lift and moment plots, which corresponds to the shock structure merge phenomenon. The most notable effect is in the moment coefficient plot, where the curve abruptly changes from negative to positive slope. This could have negative implications in the stability of this wing at these angles of attack and regimes. The lift curve also shows a change in slope from positive to negative at this angle of attack. Comparing the pressure distributions of the panel method and the experimental results at  $70^\circ$ , it can also be concluded that the shock merge effect increases the pressure under the wing significantly, and this could produce an increased drag performance.

For the Mach 3.95 and 4.65 cases, these conclusions can be directly supported by the experimental data, which shows very similar surface pressure distributions which would lead to similar force coefficients. Although there is no experimental data for the Mach 10 hypersonic case, the computational results predict that the same behavior is present, although it is less abrupt and happens at a higher angle of attack.

## Conclusions

Computational Fluid Dynamic results of a rigid parawing at Mach numbers from 0.8 to 4.65 were presented for three established inviscid, viscous and independent panel method codes. Results show good prediction of the overall trends and magnitudes of the pressure

distributions for the inviscid and viscous solvers. No particular advantages were observed for the viscous solver in comparison to the inviscid solver at supersonic conditions. Surface pressure results for the panel code diverge significantly from test data at large angles of attack due to the importance of shock interaction phenomena. Close study of the inviscid solver results showed a shock structure composed of separate bow shocks on the leading edges and the keel, which merge together into a single, large shock as the angle of attack increases. This process, which was clearly observed in both the computational and experimental data, has a significant effect on the surface pressure distributions. Based on the resulting force coefficients from the computational analysis, it is concluded that these effects can have a significant impact on the aerodynamic characteristics of the wing, particularly in a reduction in lift, increase in drag, and a decrease in static stability. Although no experimental data was available for a hypersonic case, a Mach 10 computational solution showed that these effects were still present, but occurred at a higher angle of attack. These results are a function of the concave shape of the wing and the supersonic flow conditions, and perhaps shed some light into the aerodynamics of other concave shapes in similar flows. Finally, these results show that modern CFD methods can be used to simulate these Parawing concepts and in turn help optimize them to achieve desirable aerodynamic performance.

## References

- [1] Fournier, Paul G., and B. Bell. "Low Subsonic Pressure Distributions on Three Rigid Wings Simulating Paragliders with Varied Canopy Curvature and Leading-Edge Sweep", NASA Technical Note (NASA TN D-983). 1961.
- [2] Bell, B. A., and P. G. Fournier. "Transonic Pressure Distributions on Three Rigid Wings Simulating Paragliders with Varied Canopy Curvature and Leading-Edge Sweep." NASA Technical Note (NASA TN D-1009), 1962.
- [3] Fournier, Paul G. "Pressure Distributions on Three Rigid Wings Simulating Parawings with Varied Canopy Curvature and Leading-edge Sweep at Mach Numbers from 2.29 to 4.65", NASA Technical Note (NASA TN D-1618), 1963.
- [4] Kinney, D. J., "Aero-Thermodynamics for Conceptual Design," AIAA-2004-31, 42nd AIAA Aerospace Sciences Meeting and Exhibit, Reno NV, Jan. 2004.
- [5] Kinney, D. J., "Predicted Convective and Radiative Aerothermodynamic Environments for Various Reentry Vehicles Using CBAERO," AIAA-2006-659, 44th AIAA Aerospace Sciences Meeting and Exhibit, Reno NV, Jan. 2006.
- [6] Aftosmis, M. J., Berger, M. J., and Melton, J. E., "Robust and Efficient Cartesian Mesh Generation for Componenet-Based Geometry," AIAA Journal, Vol. 36, No. 6, 1998, pp. 952–960.
- [7] Nemec, M., Aftosmis, M.J., Murman, S.M., and Pulliam T., "Adjoint formulation for an embedded-boundary Cartesian method" AIAA Paper 2005-0877, Jan. 2005.
- [8] STAR-CCM+, CFD Software Package, CD-adapco, Melville, New York.
- [9] Fralich, Robert. Stress and shape analysis of a paraglider wing. Diss. Virginia Polytechnic Institute, 1963.

**Table 1. CART3D Test Matrix**

Experimental Data Reference	Mach Number	Angle of Attack [degrees]								
		10.15	20.15	30.15	40.15	50.15	-	60.15	-	-
NASA TN D-983	0.204	0.15	10.15	20.15	30.15	40.15	-	-	-	70.15
	0.8	0.00	10.15	20.15	30.15	40.15	-	-	-	80.00
	0.94	0.00	10.15	20.15	30.00	40.00	50.00	-	-	90.00
	0.98	0.00	10.15	20.15	30.15	40.15	50.15	-	-	90.15
	1.02	0.00	10.15	20.15	30.00	40.00	50.00	-	-	90.00
	1.2	0.00	10.15	20.15	30.15	40.15	50.15	-	-	90.00
NASA TN D-1009	2.29	0.45	10.45	20.45	30.45	40.45	50.00	-	-	70.15
	2.96	0.25	10.25	20.25	30.25	40.25	50.25	-	-	70.00
	3.95	0.00	10.00	20.00	30.00	40.00	50.50	53.0	55.5	63.0
	4.65	0.90	10.90	20.90	30.90	40.90	50.90	53.4	55.9	60.50
								58.4	60.90	63.4
								65.9	68.4	70.90

\* Cases where experimental data is available are marked in blue

**Table 2. CBAERO Test Matrix**

Experimental Data Reference	Mach Number	Angle of Attack [degrees]								
		0.00	10.00	20.00	30.00	40.00	50.50	60.50	70.50	80.00
NASA TN D-1618	3.95	0.90	10.90	20.90	30.90	40.90	50.90	60.90	70.90	80.00

\* Cases where experimental data is available are marked in blue

**Table 3. STAR-CCM+ Test Matrix**

Experimental Data Reference	Mach Number	Angle of Attack [degrees]								
		20.15	30.15	40.15	50.15	-	-	-	60.15	-
NASA TN D-983	0.204	0.15	-	-	50.15	-	-	-	-	-
NASA TN D-1009	0.98	-	20.15	30.15	40.15	50.15	-	-	-	-
NASA TN D-1618	4.65	0.90	20.90	-	40.90	50.90	53.4	55.9	58.4	60.90
							63.4	65.9	66.9	70.90

\* Cases where experimental data is available are marked in blue

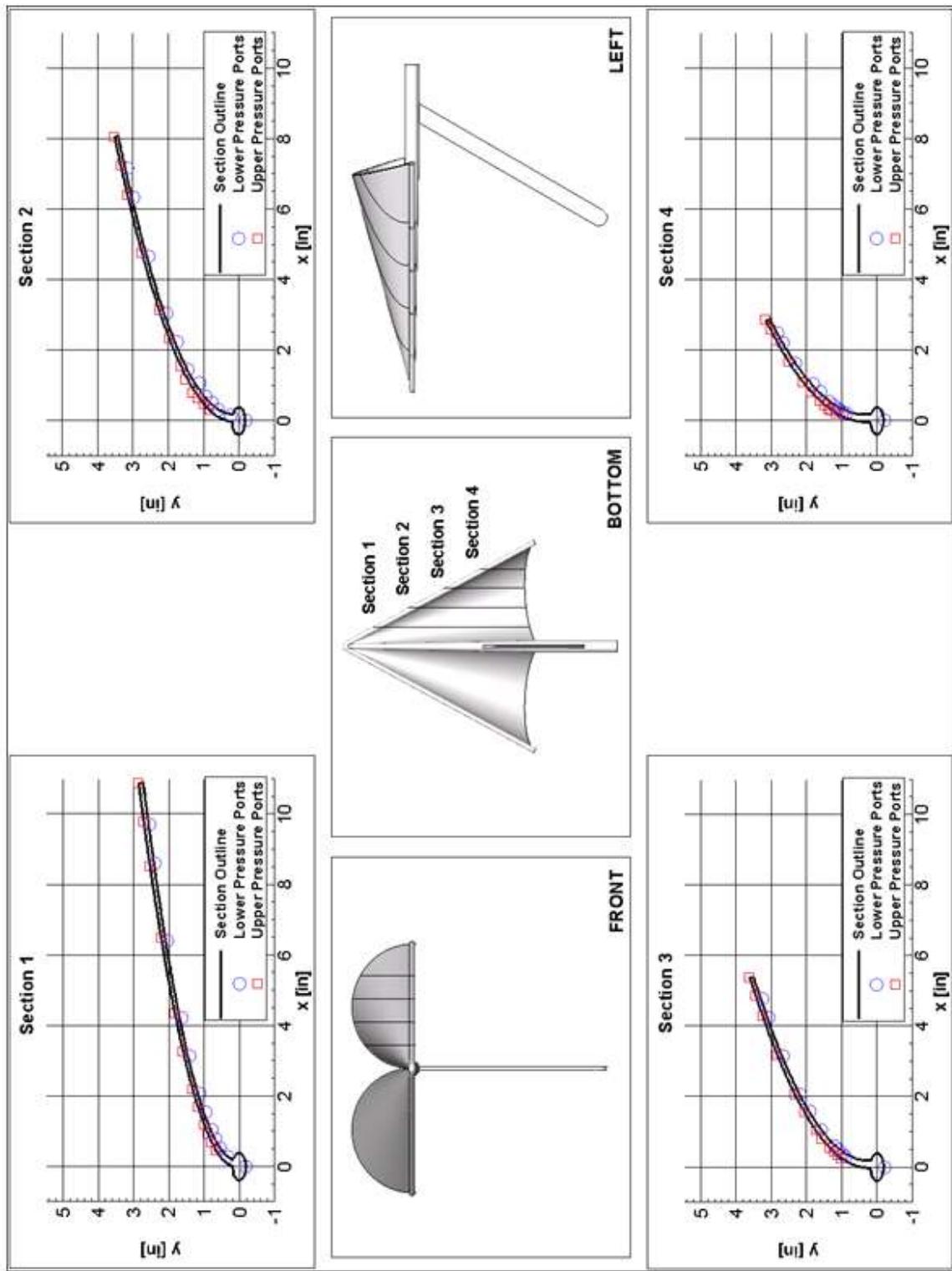


Figure 1. Parawing geometry and pressure port locations

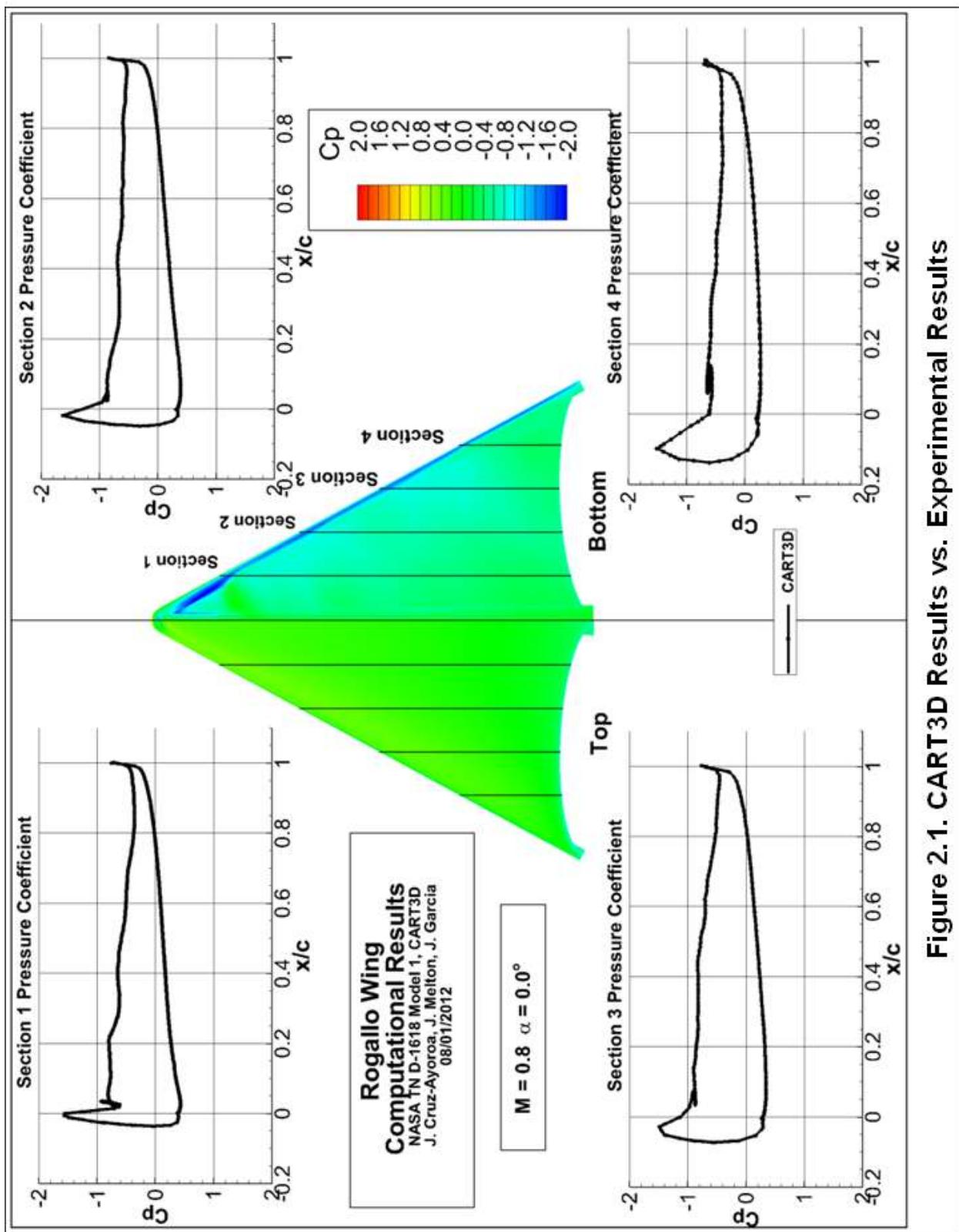


Figure 2.1. CART3D Results vs. Experimental Results

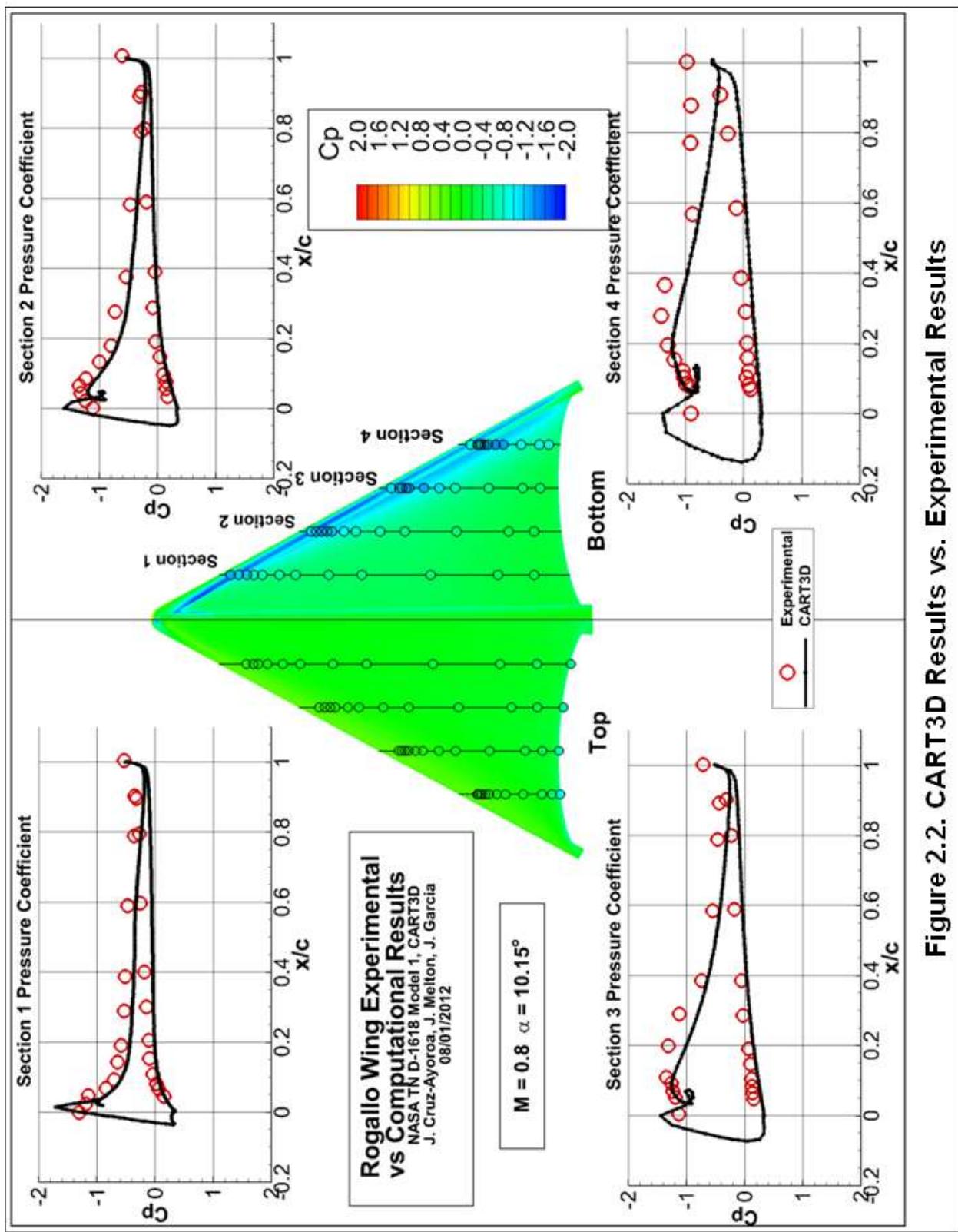


Figure 2.2. CART3D Results vs. Experimental Results

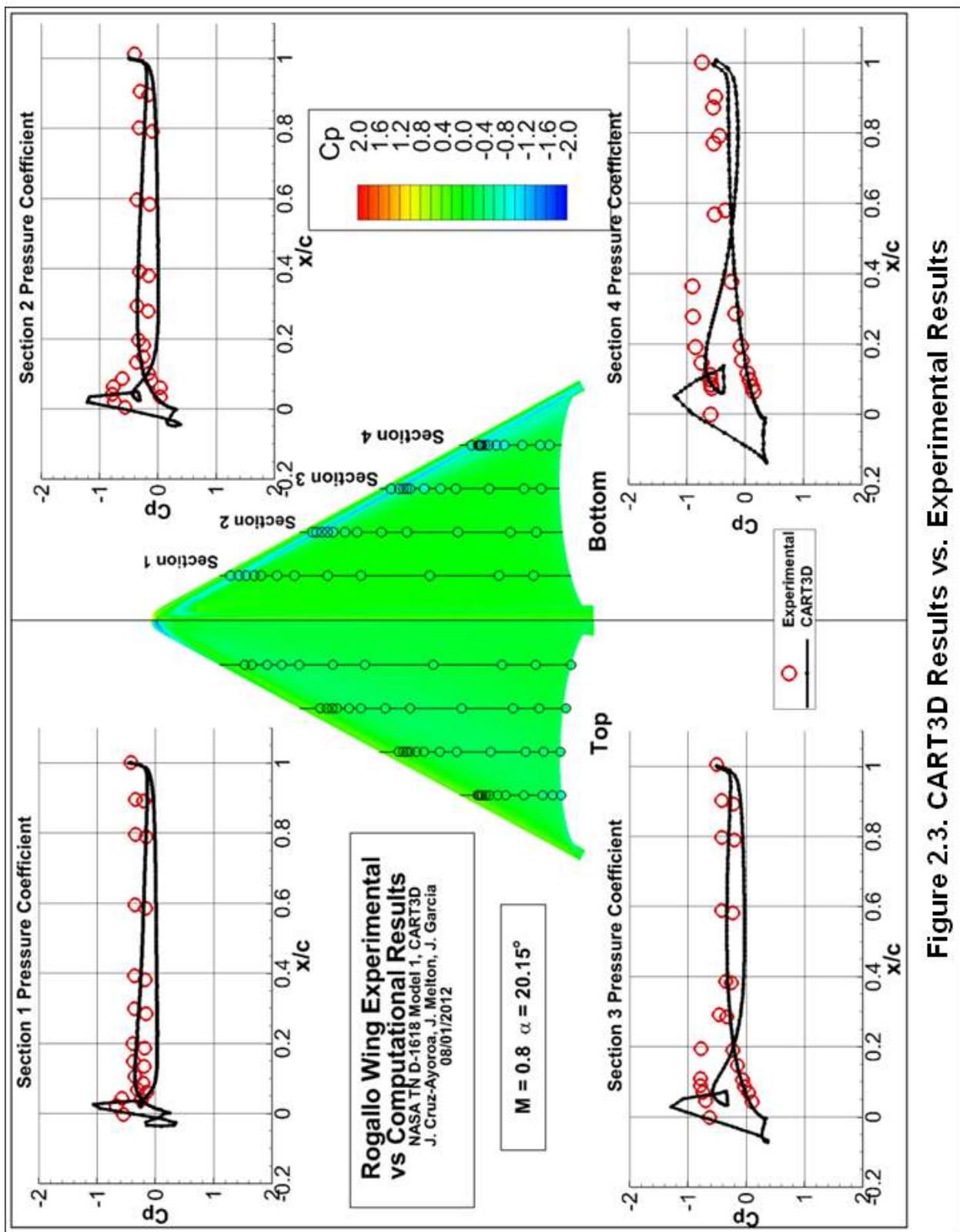


Figure 2.3. CART3D Results vs. Experimental Results

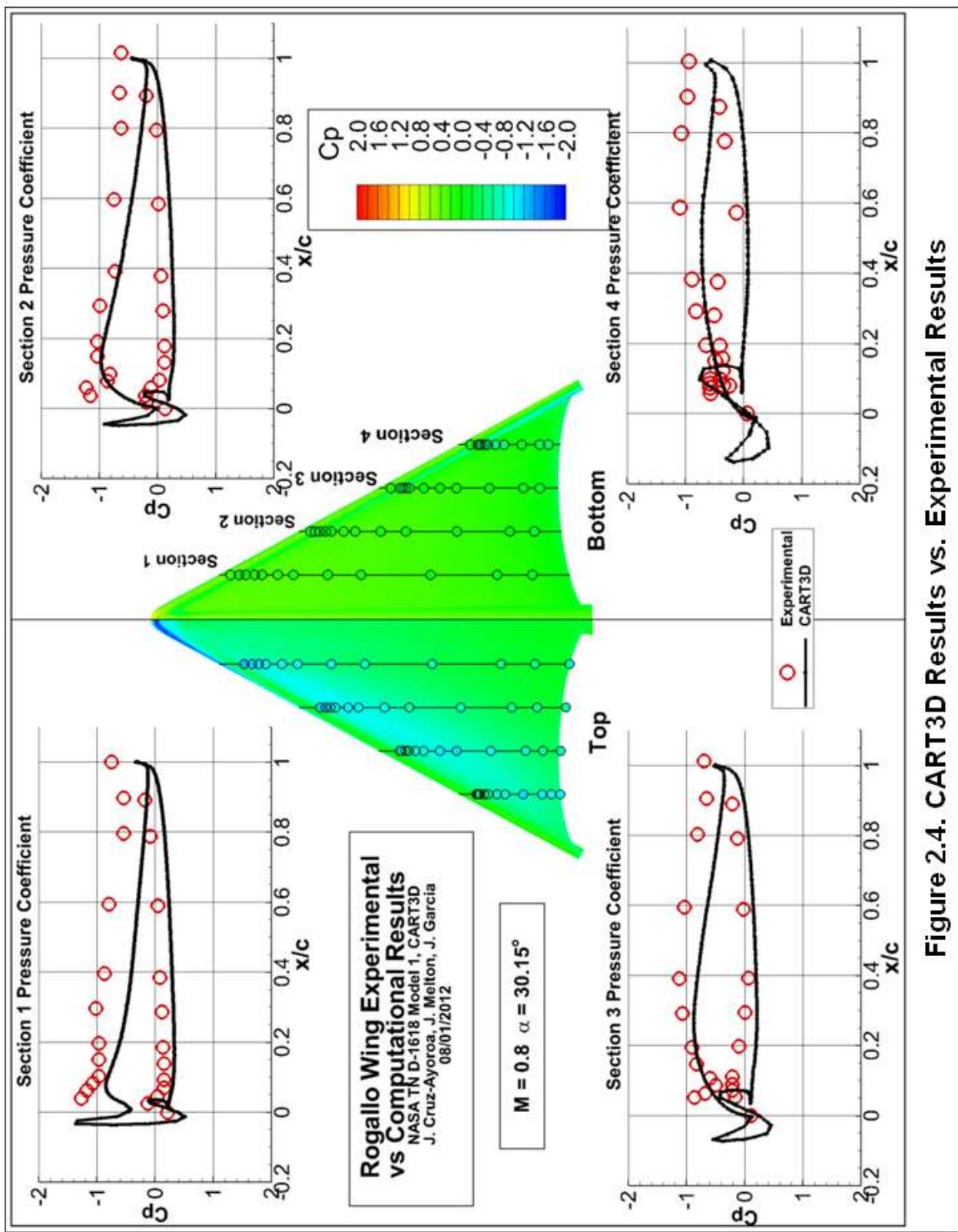


Figure 2.4. CART3D Results vs. Experimental Results

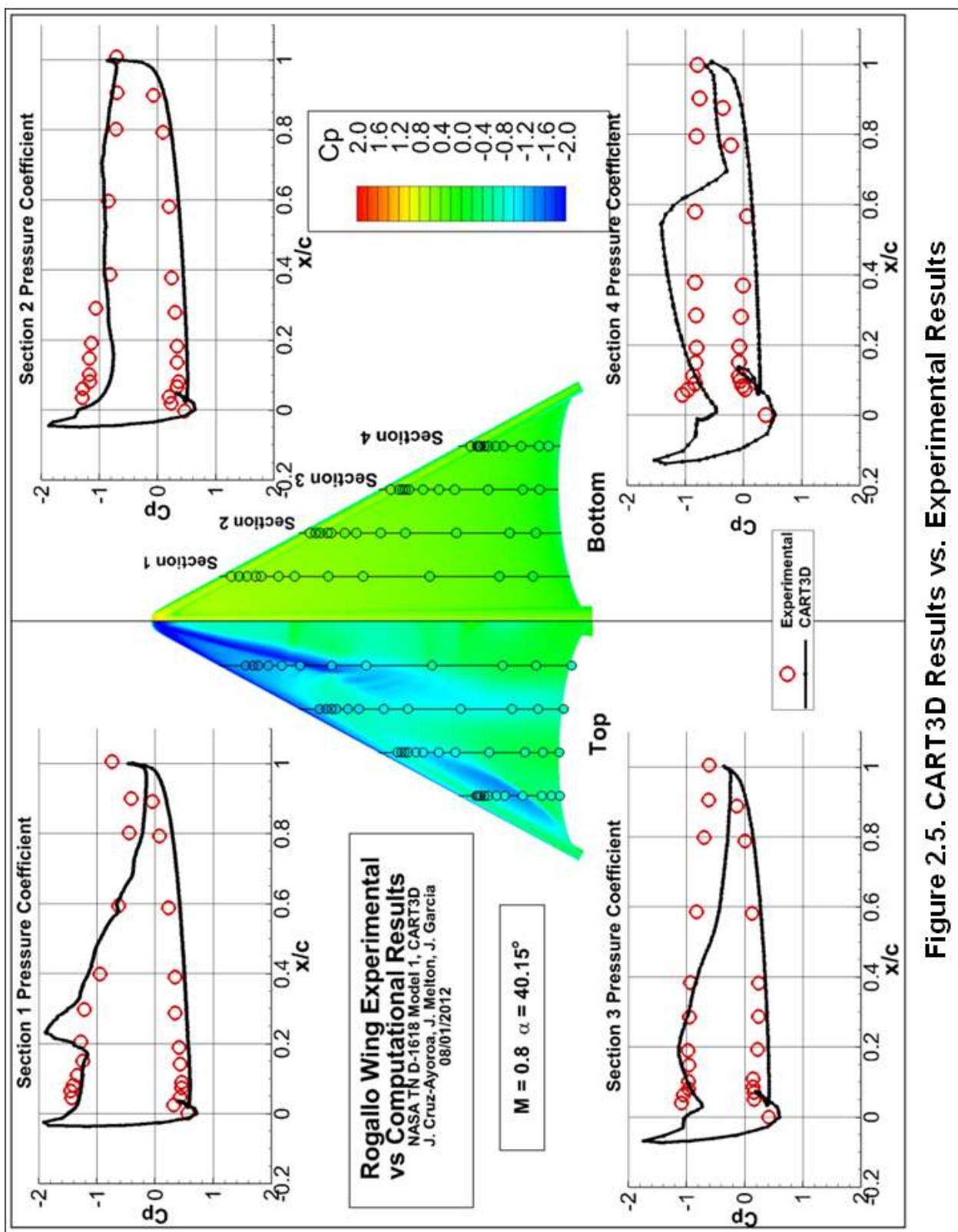


Figure 2.5. CART3D Results vs. Experimental Results

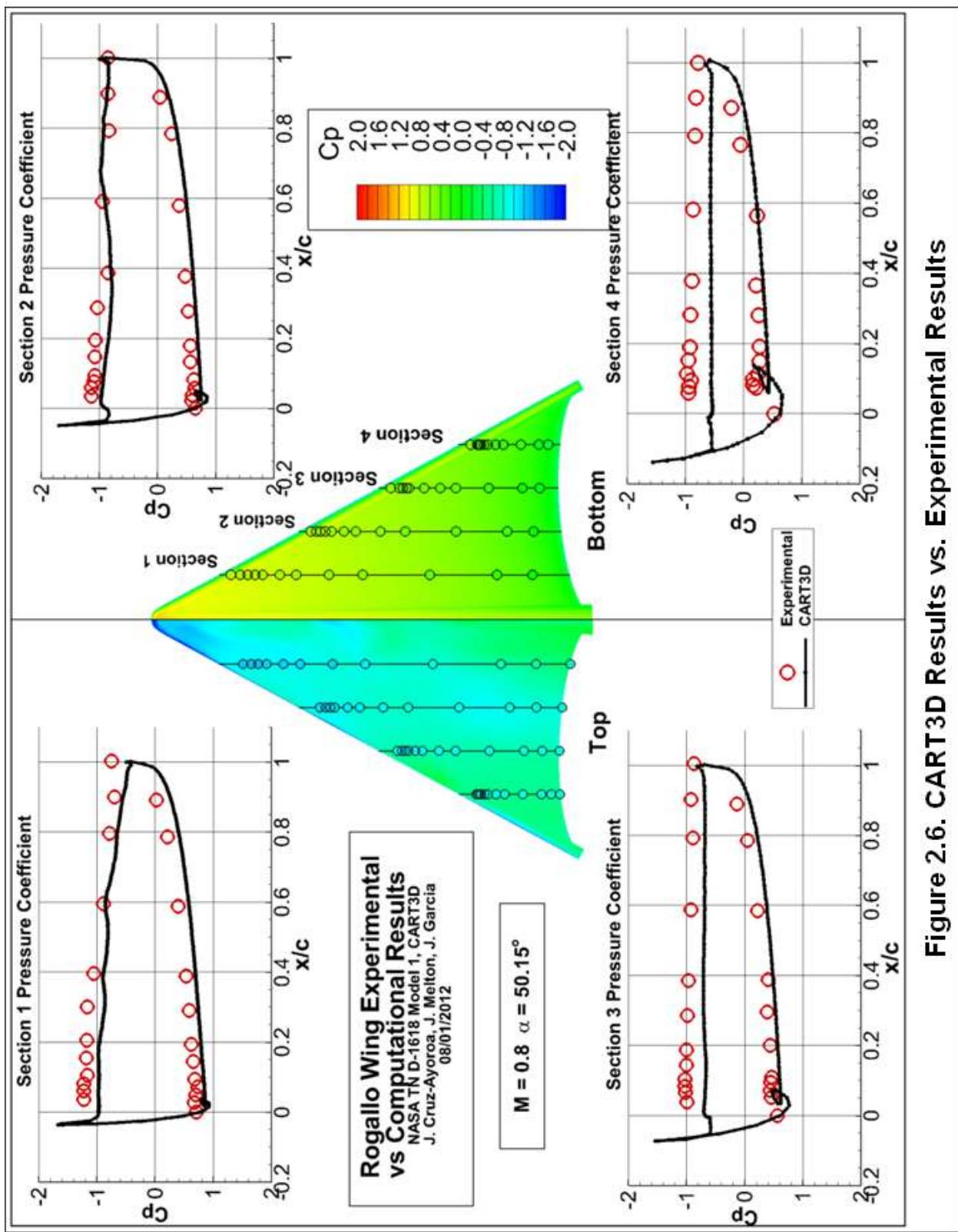


Figure 2.6. CART3D Results vs. Experimental Results

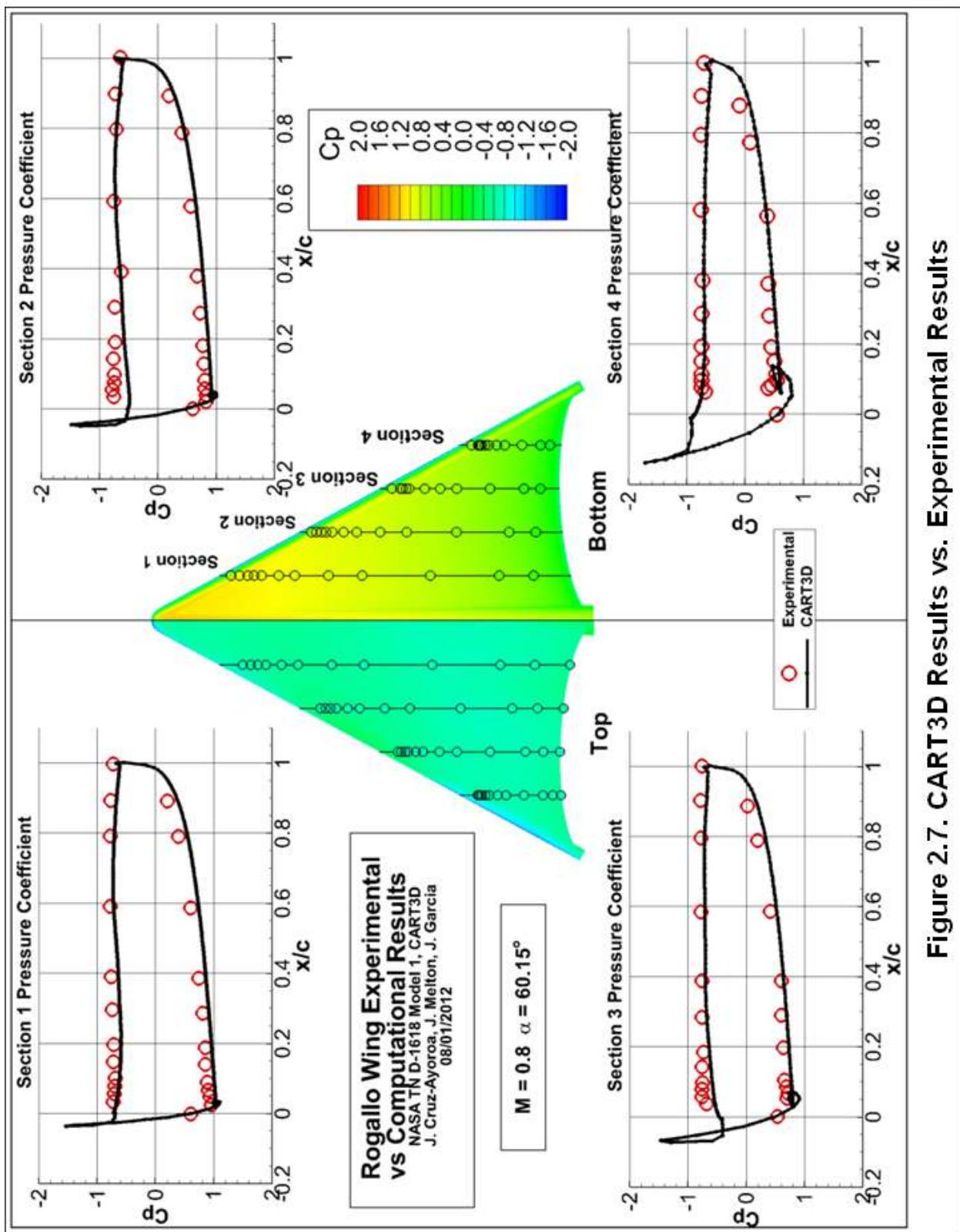


Figure 2.7. CART3D Results vs. Experimental Results

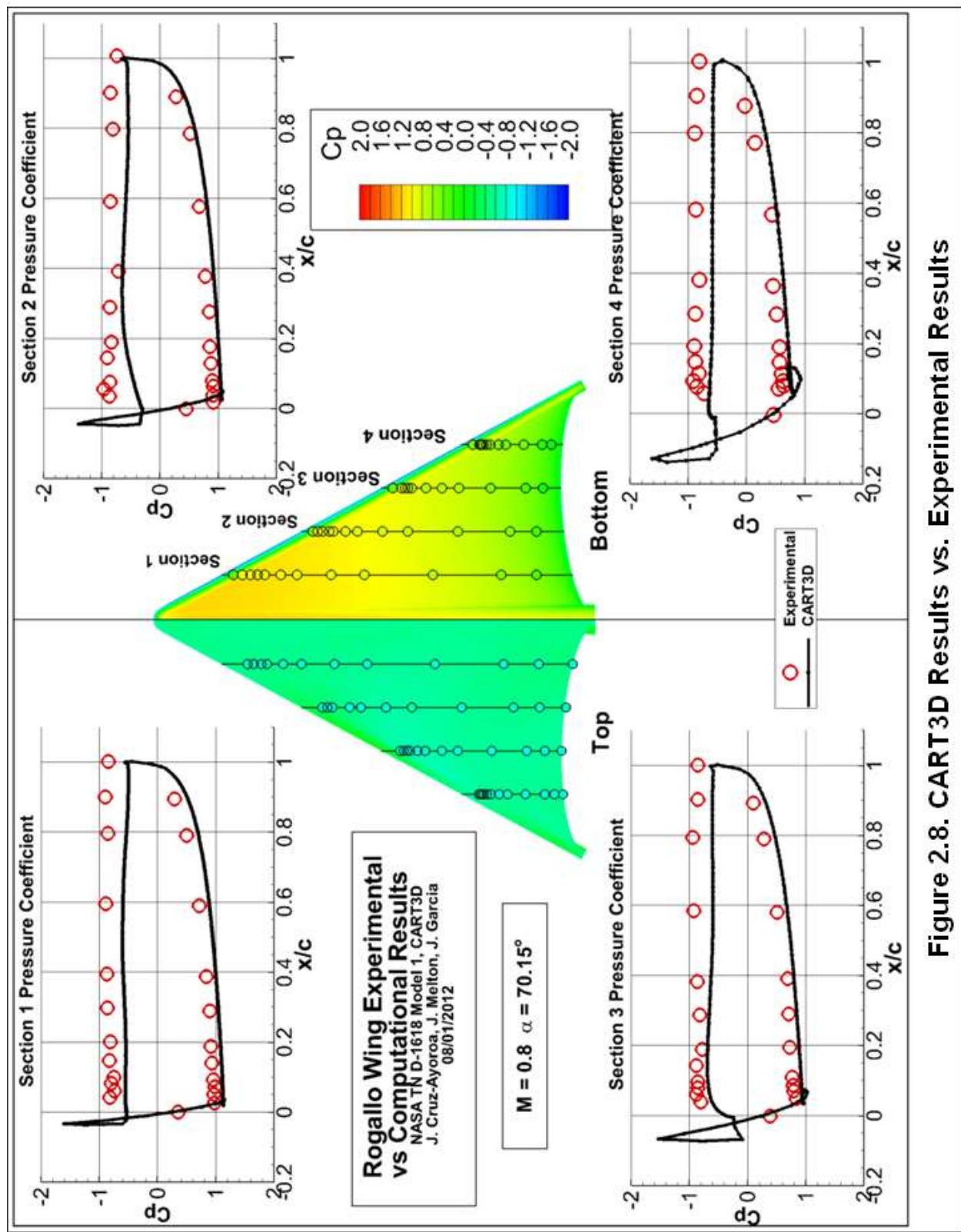


Figure 2.8. CART3D Results vs. Experimental Results

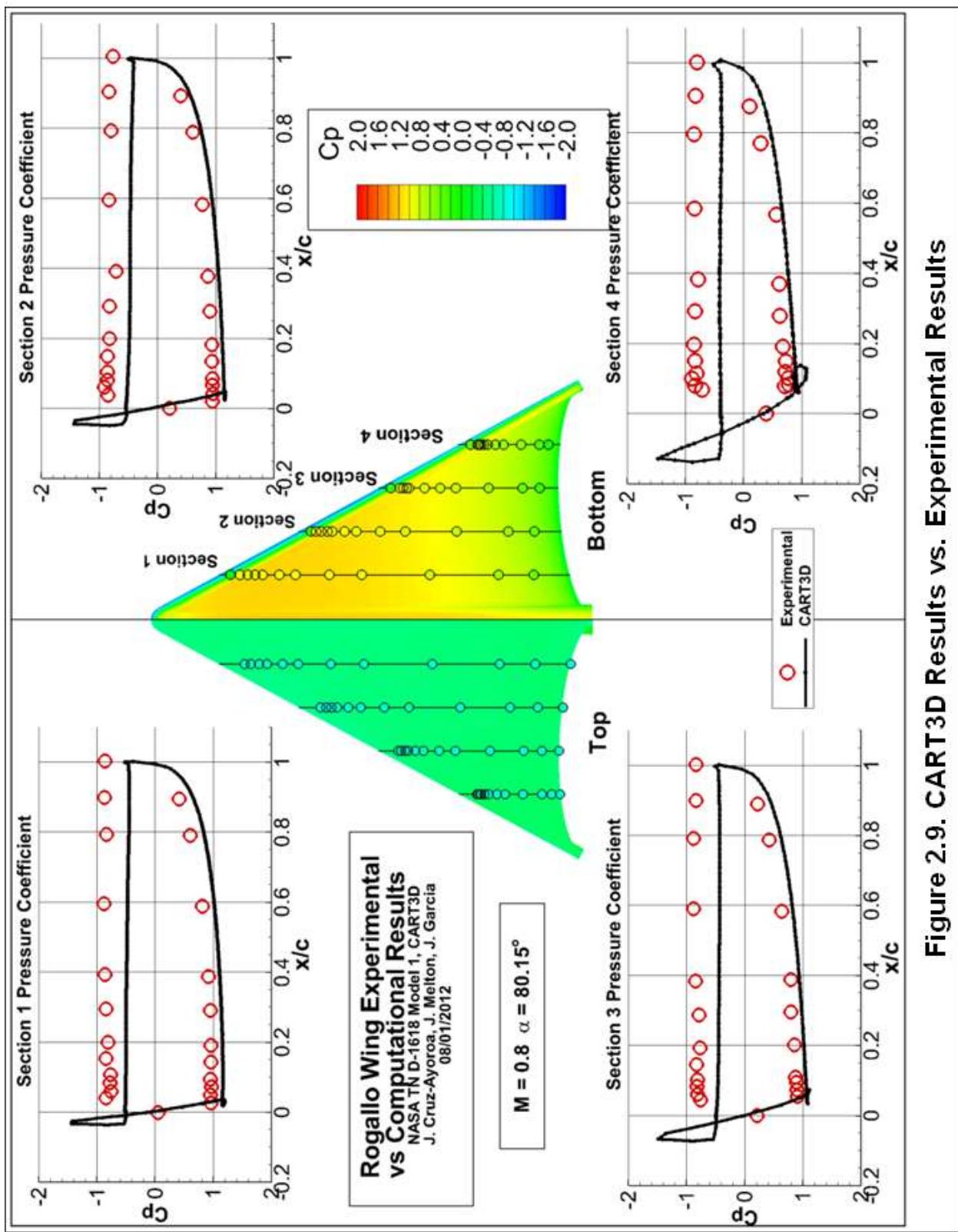


Figure 2.9. CART3D Results vs. Experimental Results

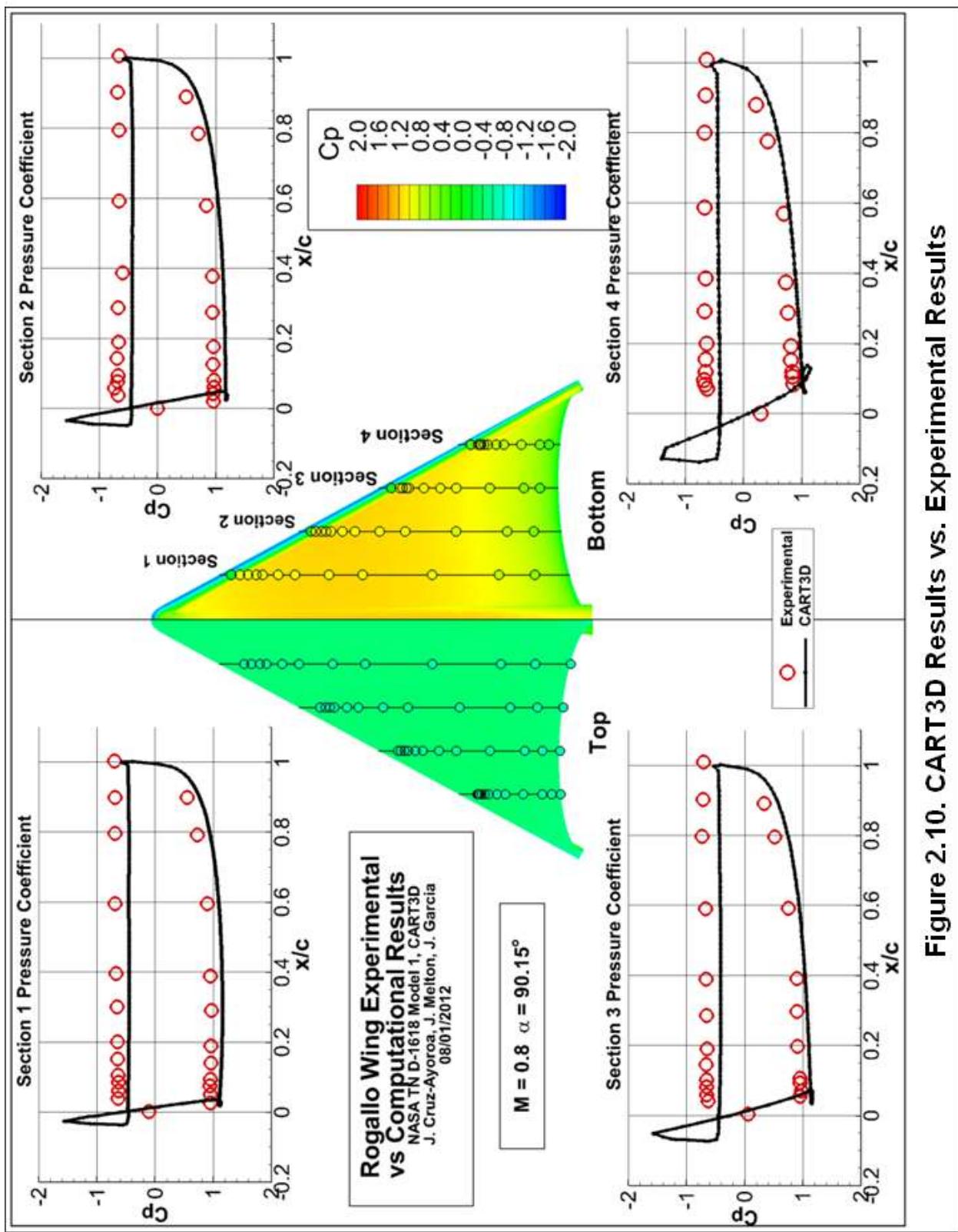


Figure 2.10. CART3D Results vs. Experimental Results

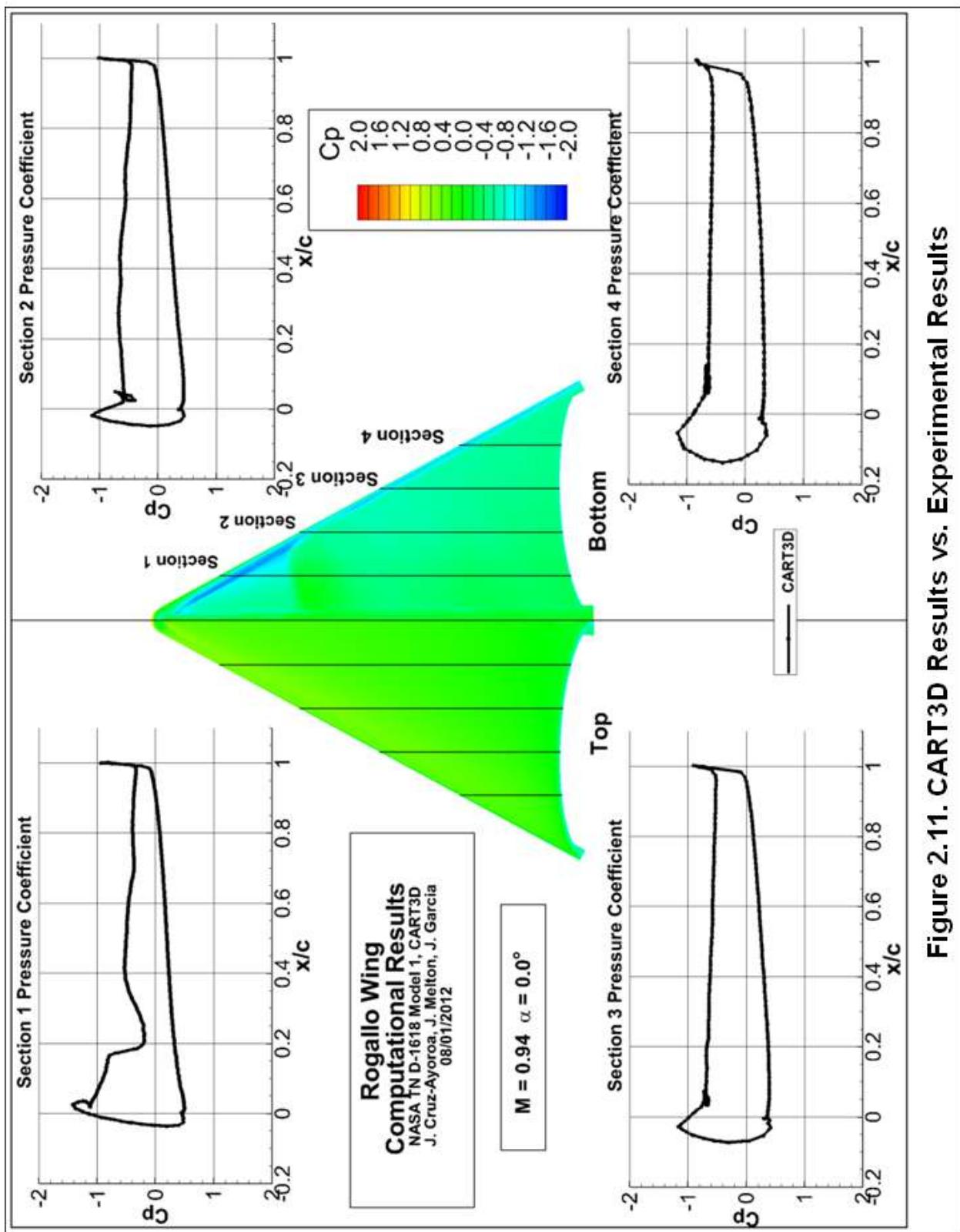


Figure 2.11. CART3D Results vs. Experimental Results

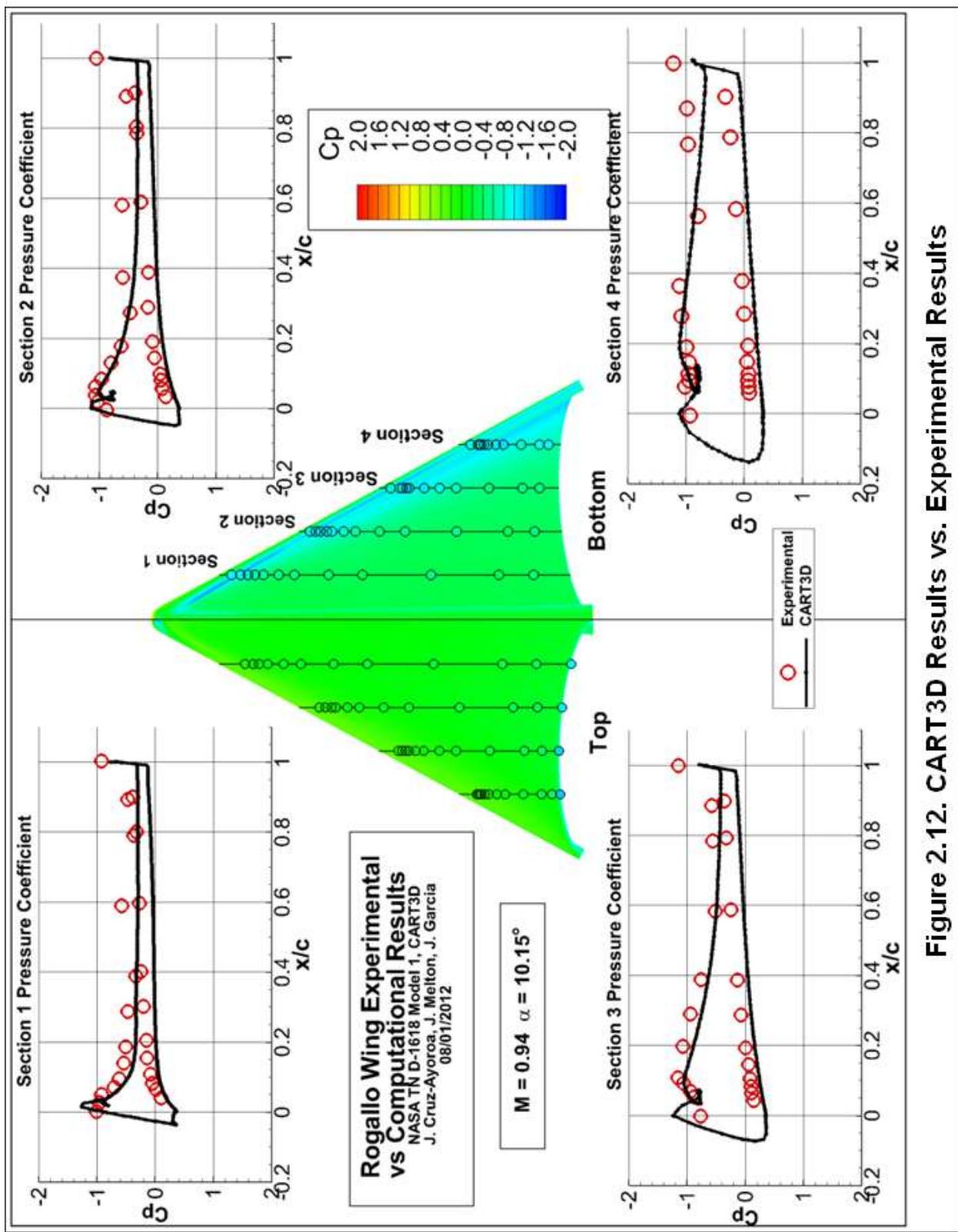


Figure 2.12. CART3D Results vs. Experimental Results

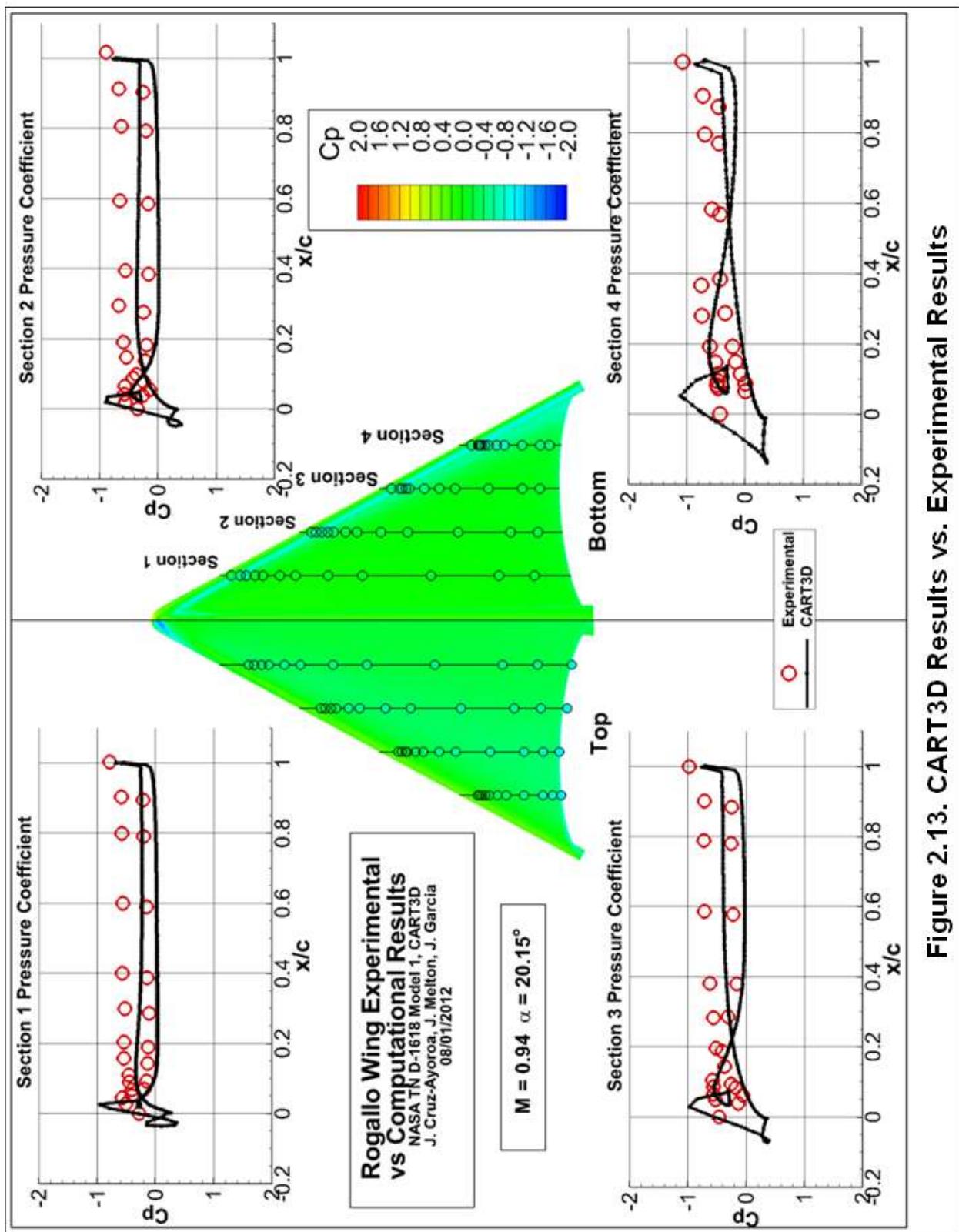


Figure 2.13. CART3D Results vs. Experimental Results

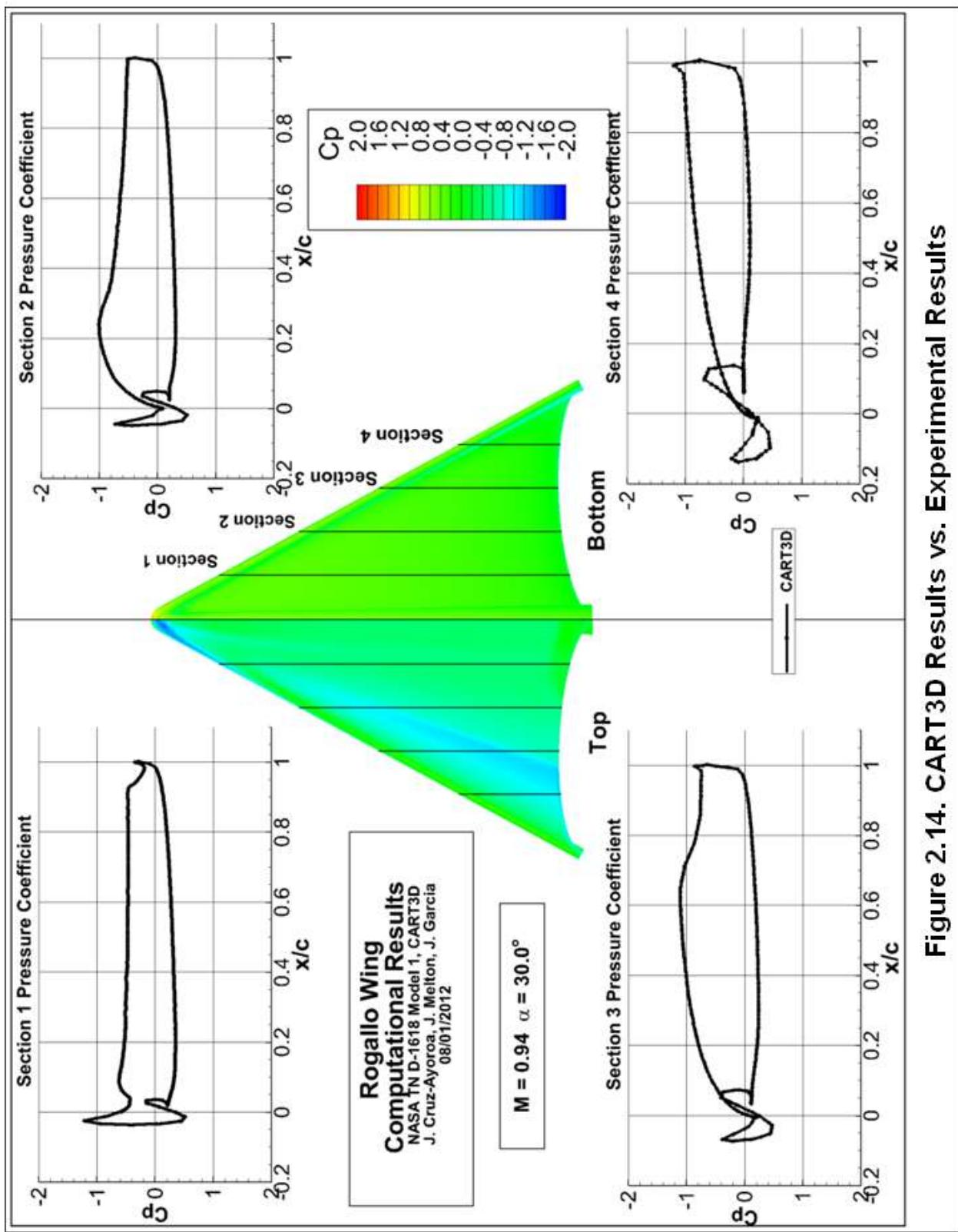


Figure 2.14. CART3D Results vs. Experimental Results

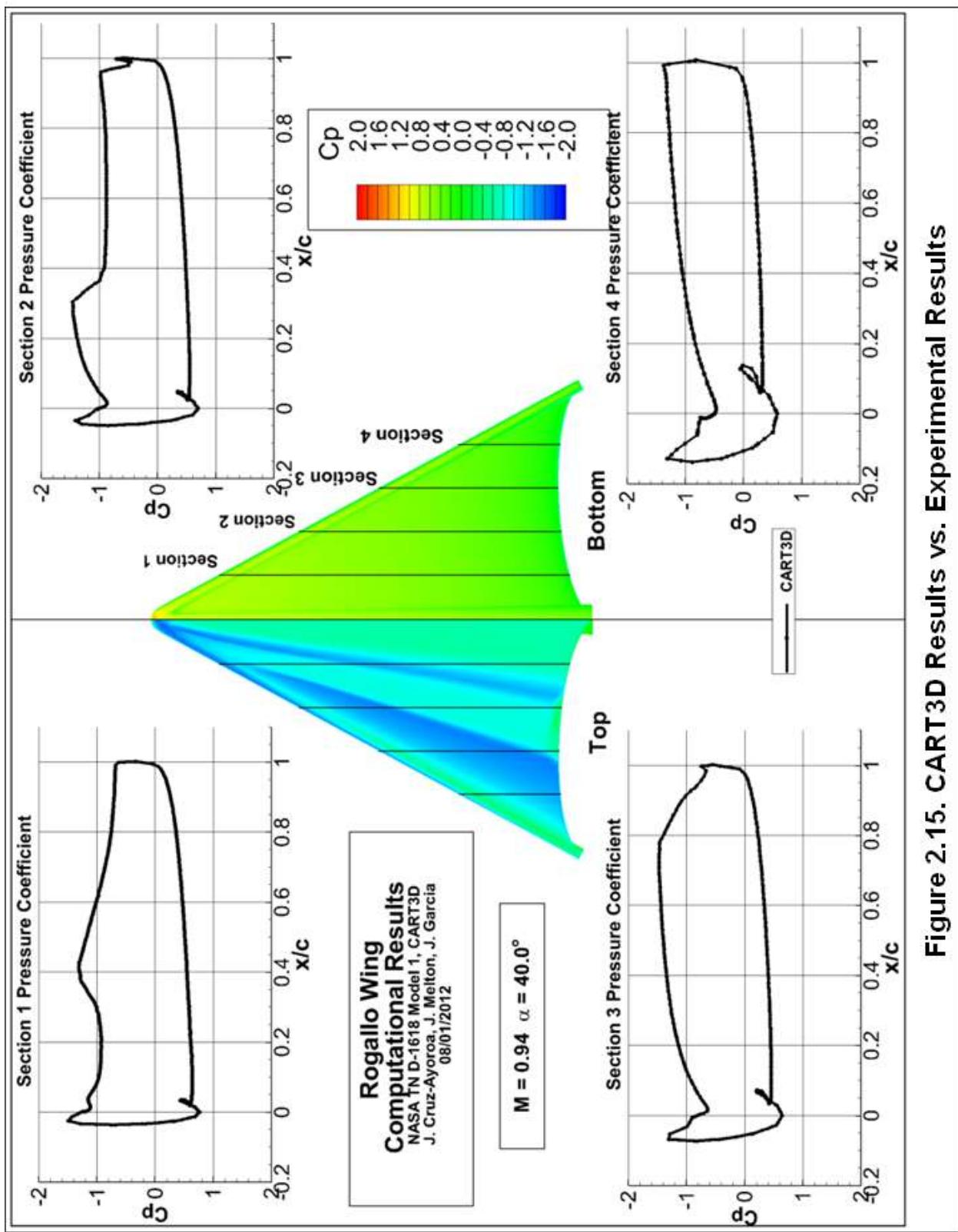


Figure 2.15. CART3D Results vs. Experimental Results

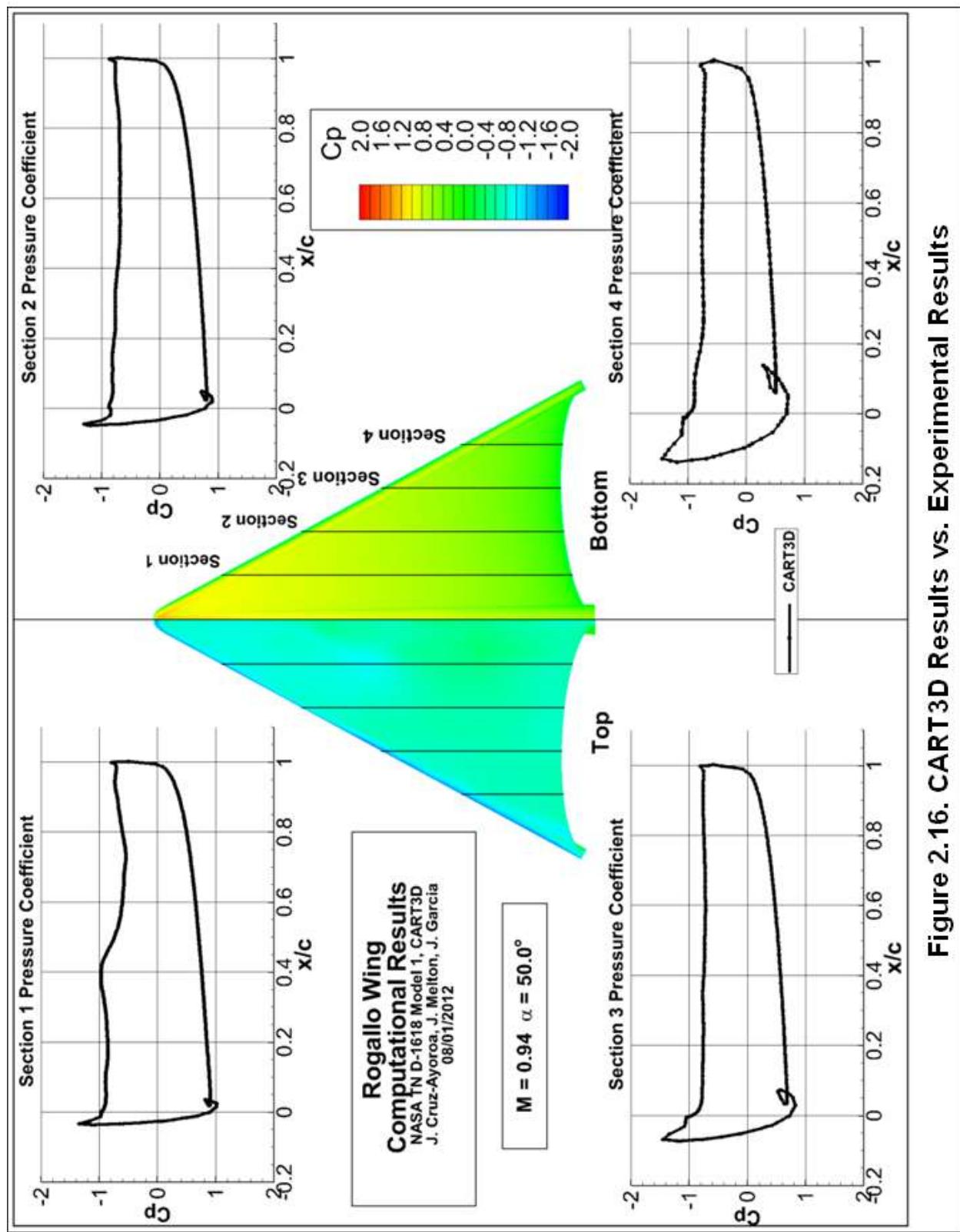


Figure 2.16. CART3D Results vs. Experimental Results

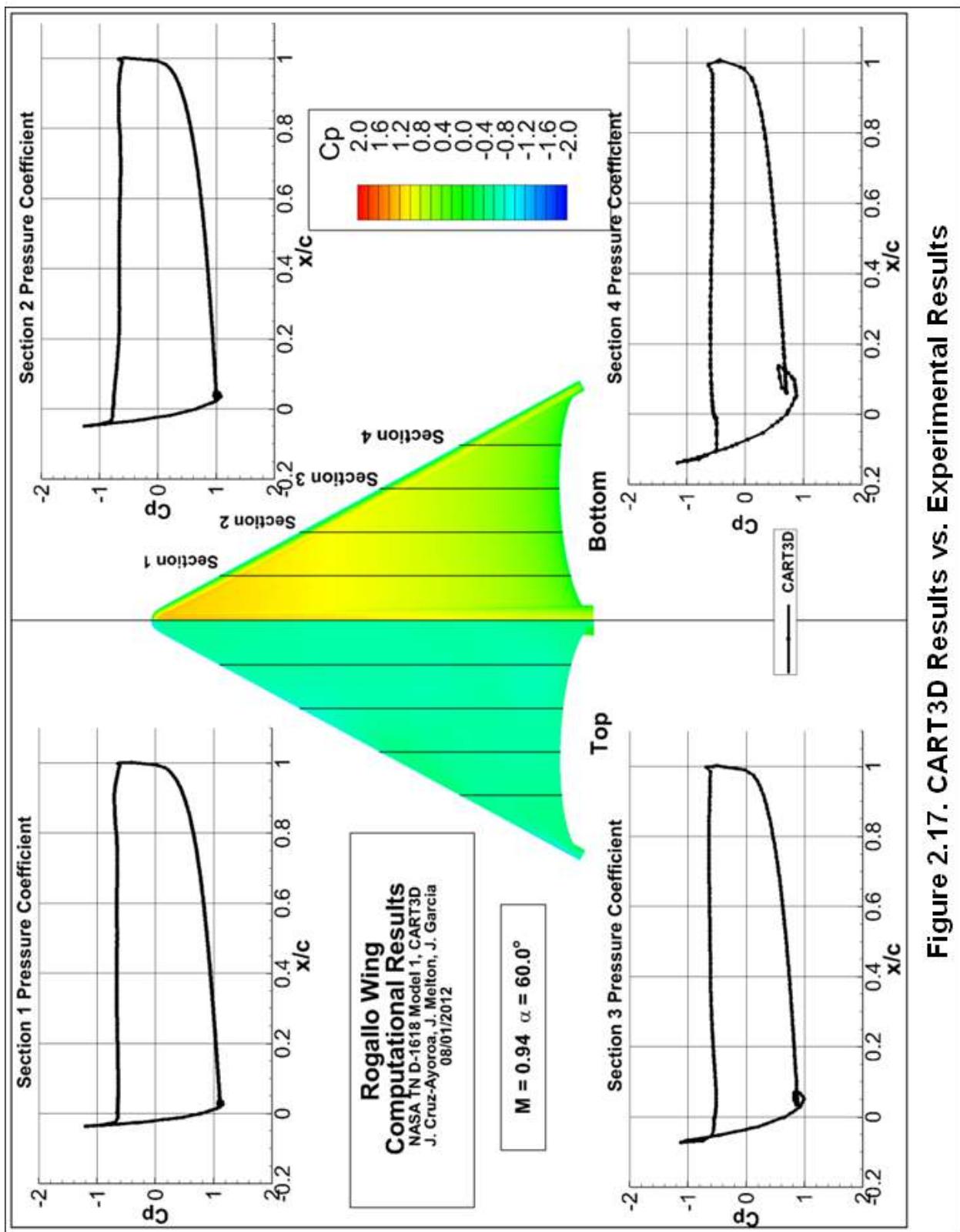


Figure 2.17. CART3D Results vs. Experimental Results

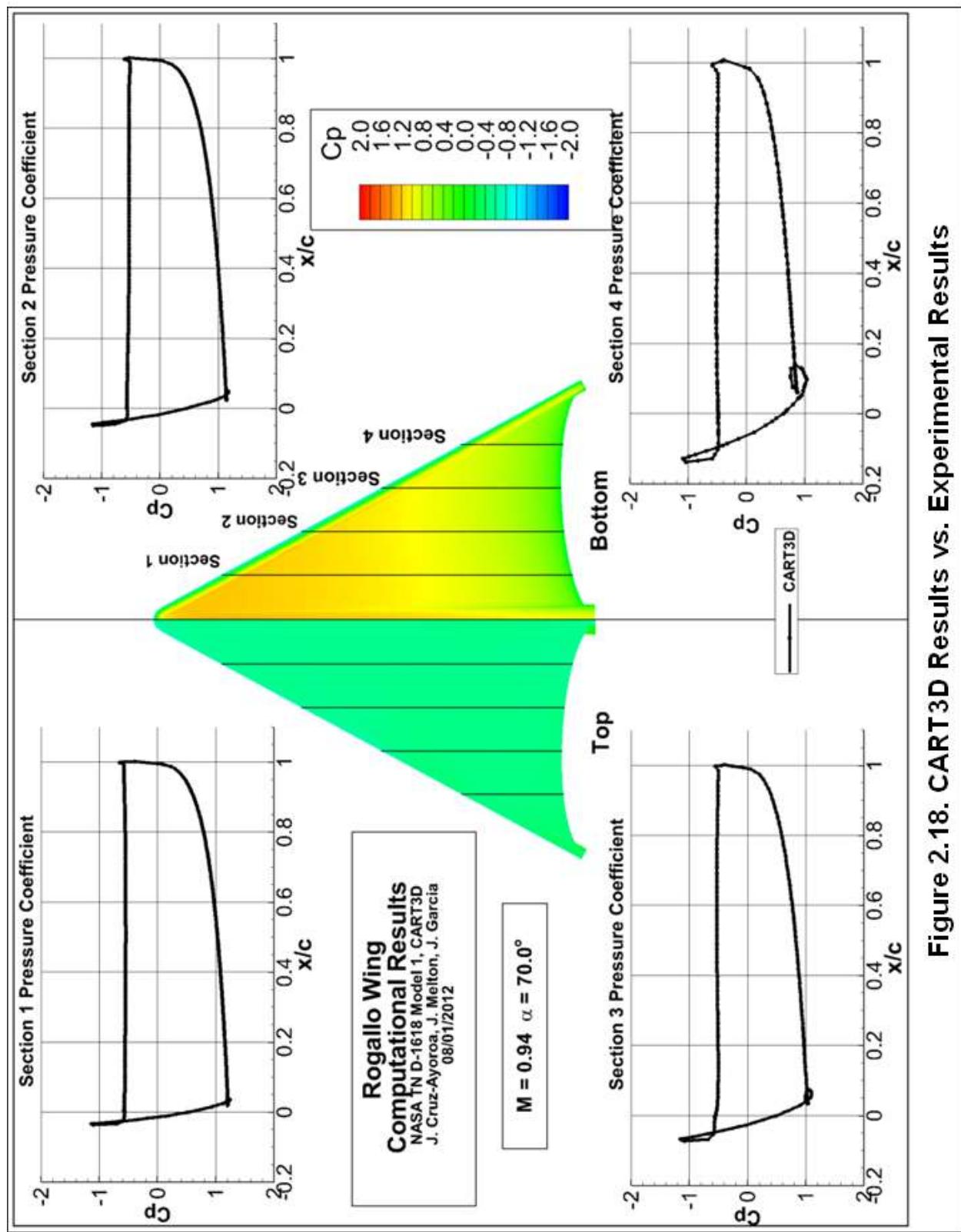


Figure 2.18. CART3D Results vs. Experimental Results

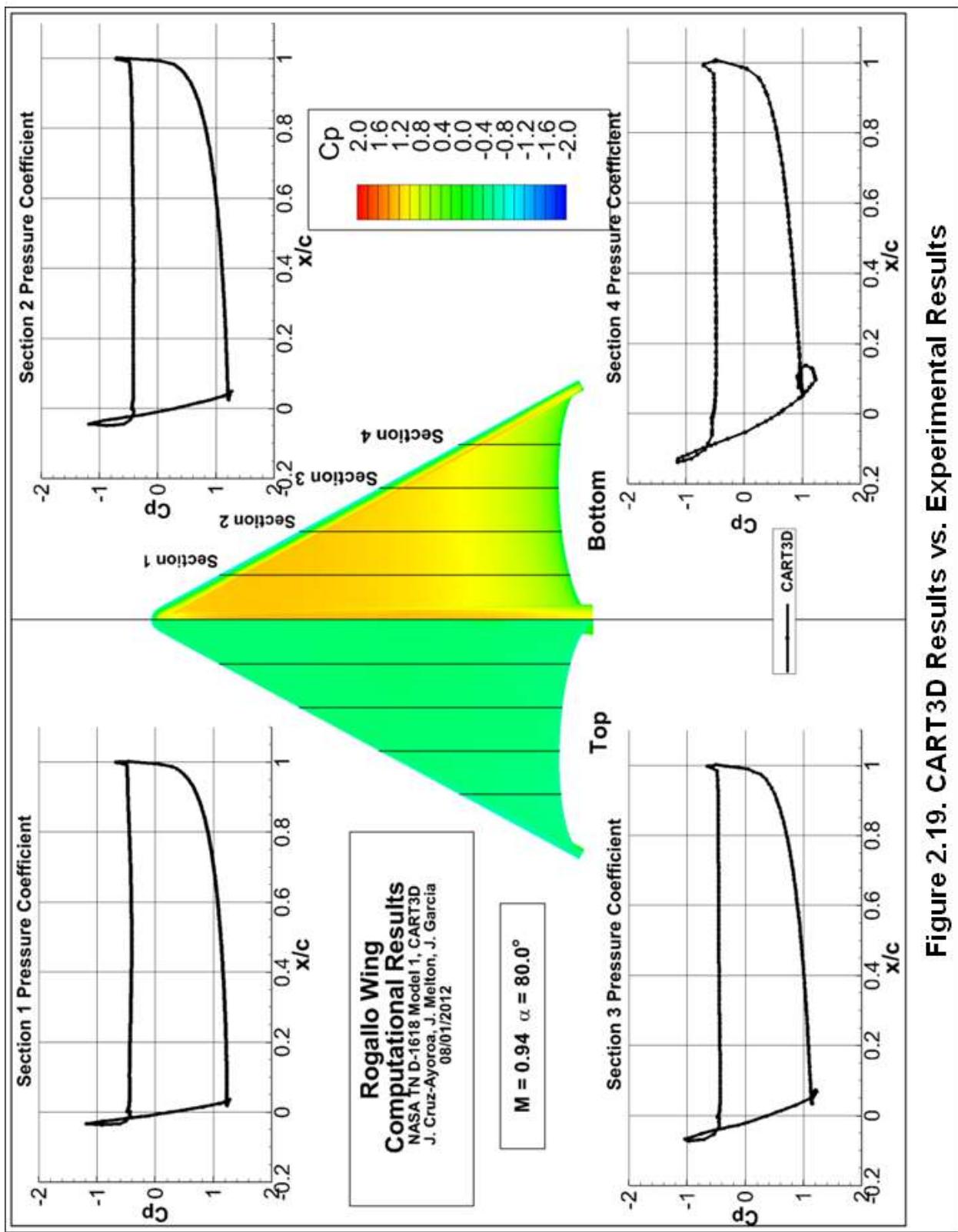


Figure 2.19. CART3D Results vs. Experimental Results

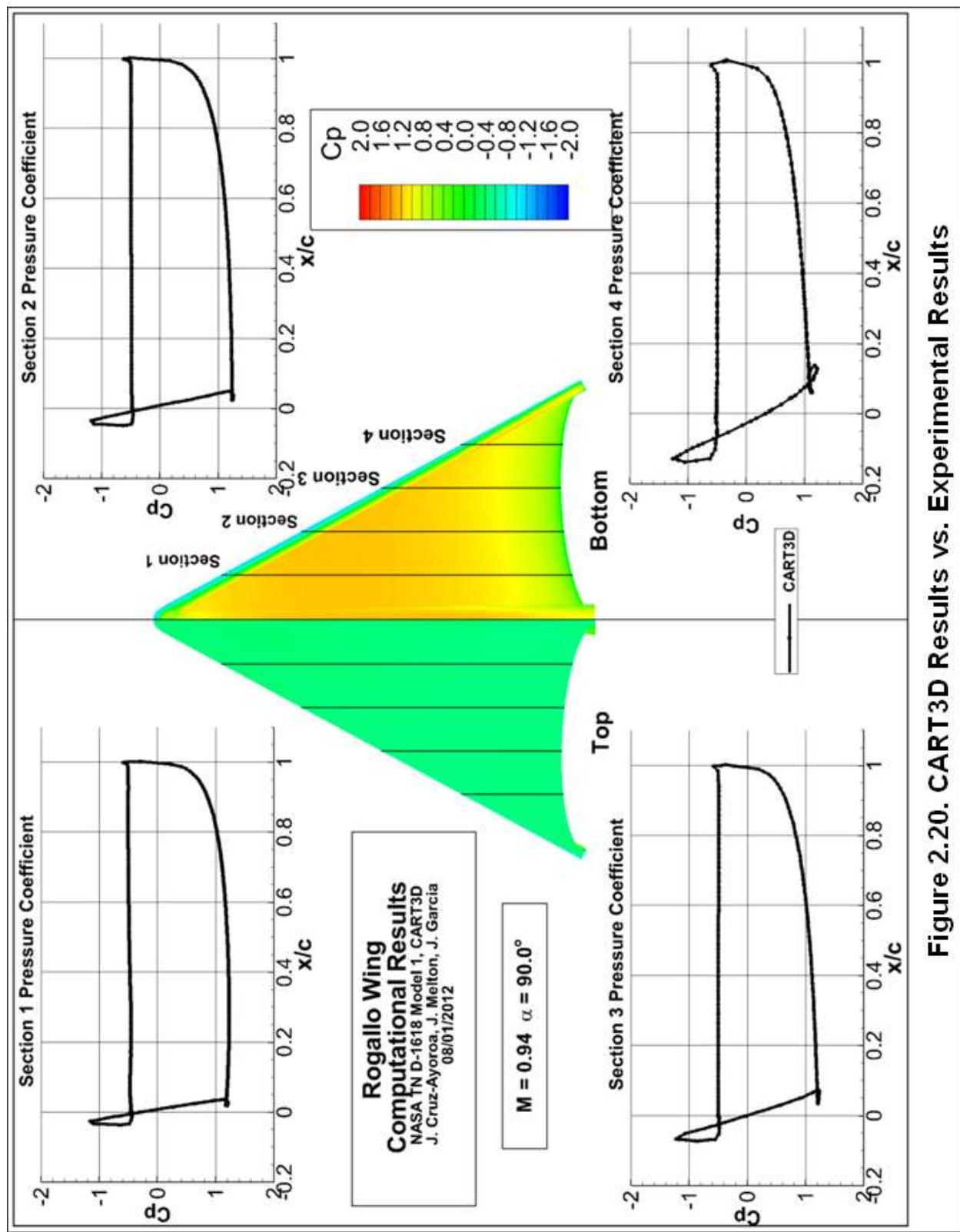


Figure 2.20. CART3D Results vs. Experimental Results

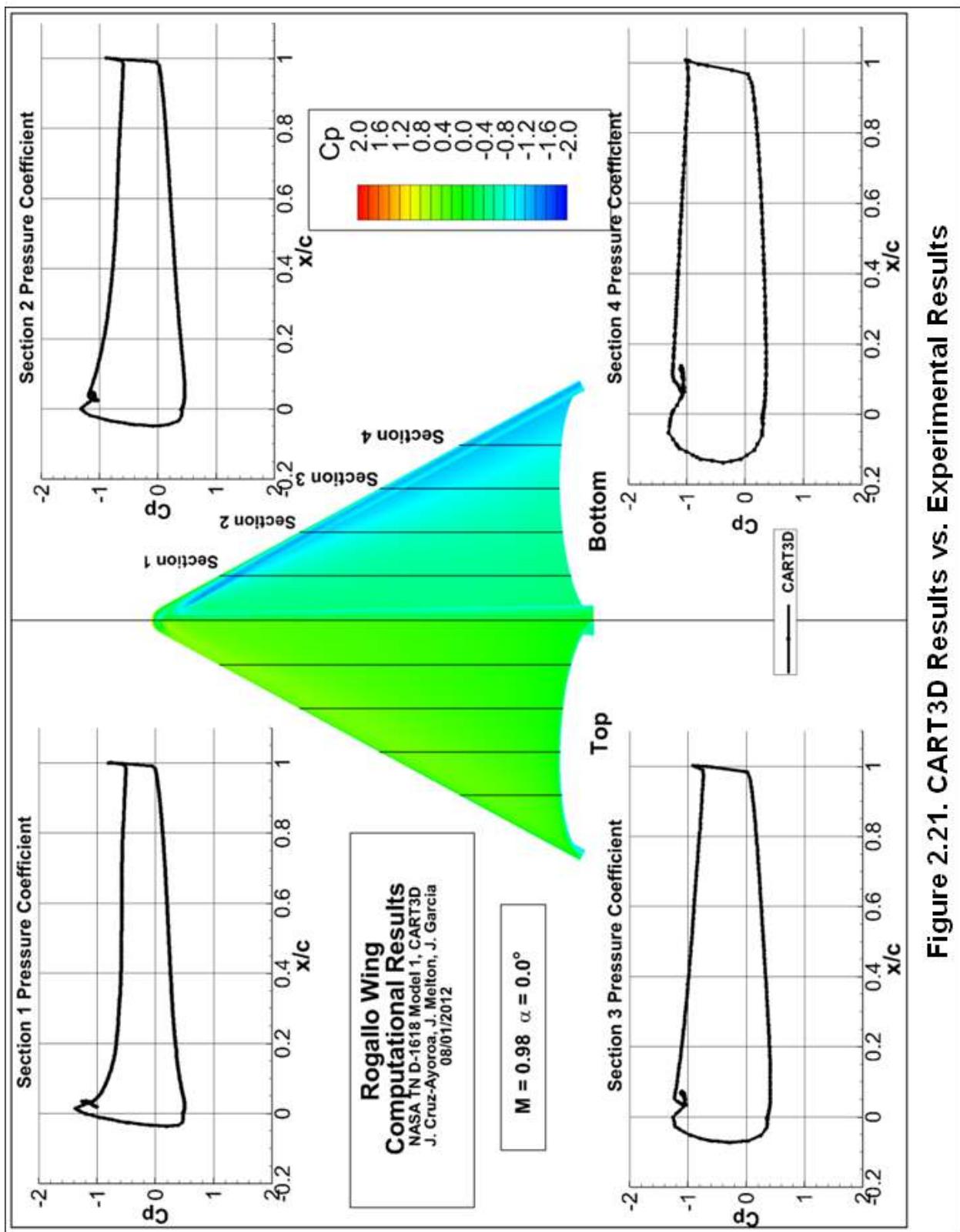


Figure 2.21. CART3D Results vs. Experimental Results

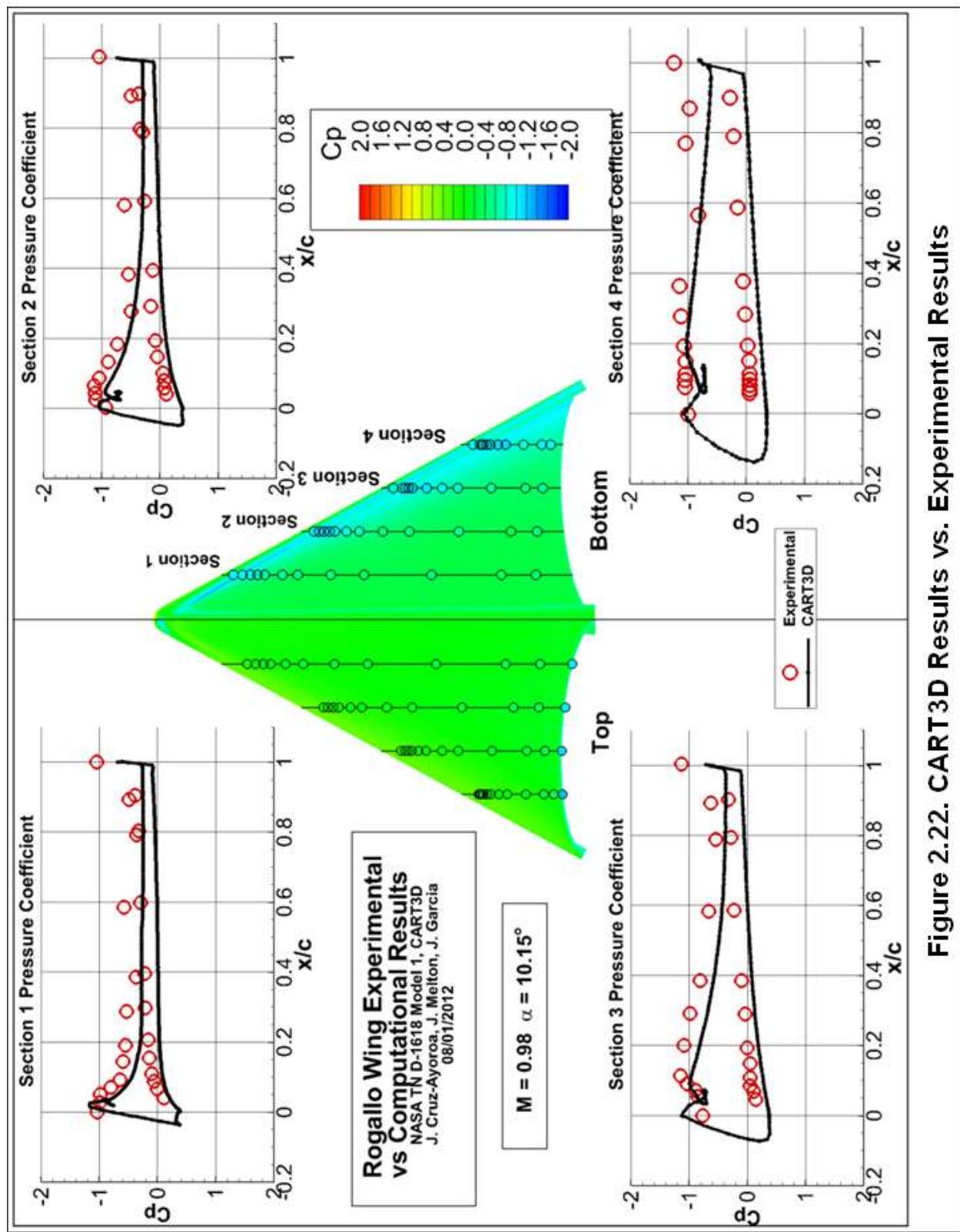


Figure 2.22. CART3D Results vs. Experimental Results

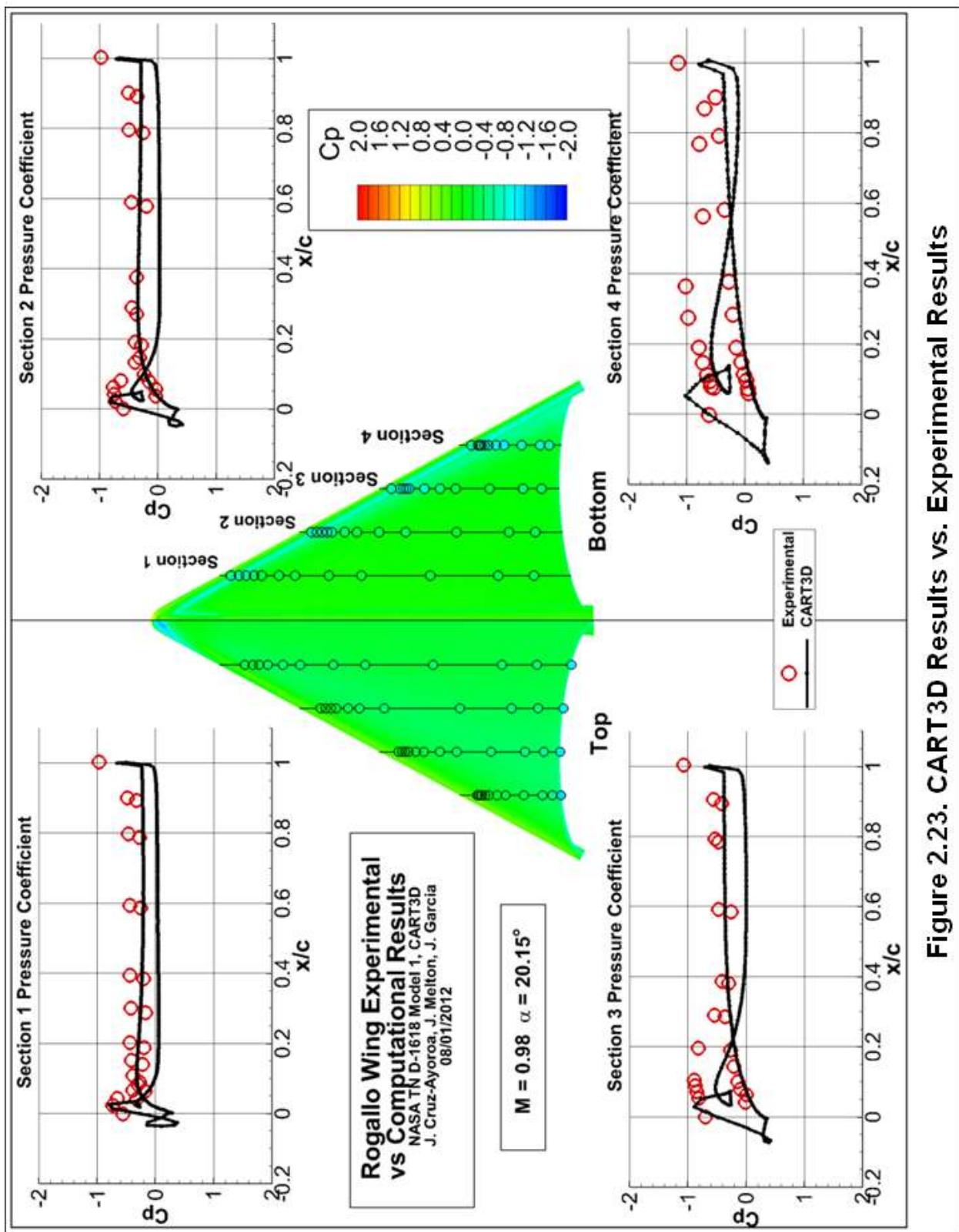


Figure 2.23. CART3D Results vs. Experimental Results

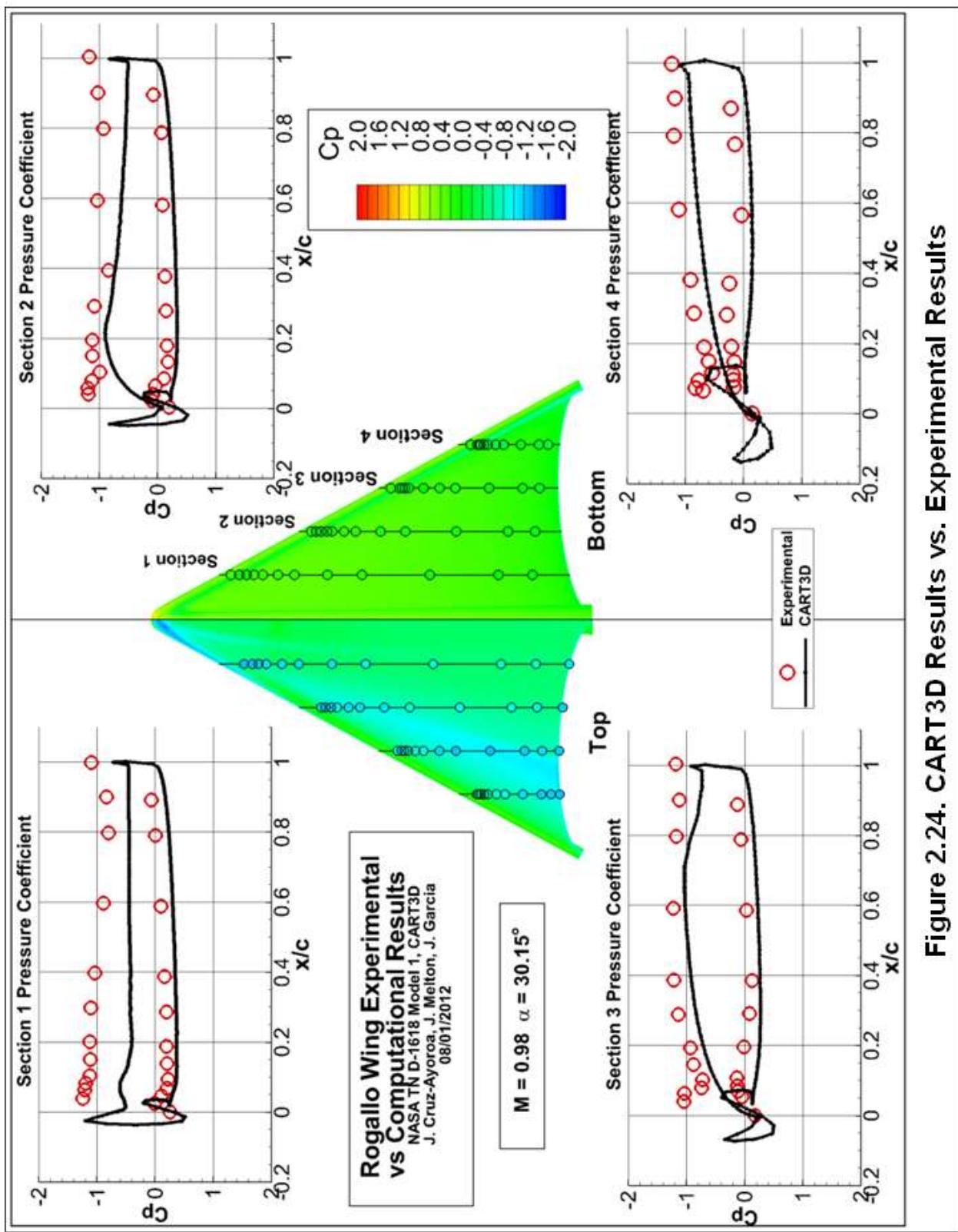


Figure 2.24. CART3D Results vs. Experimental Results

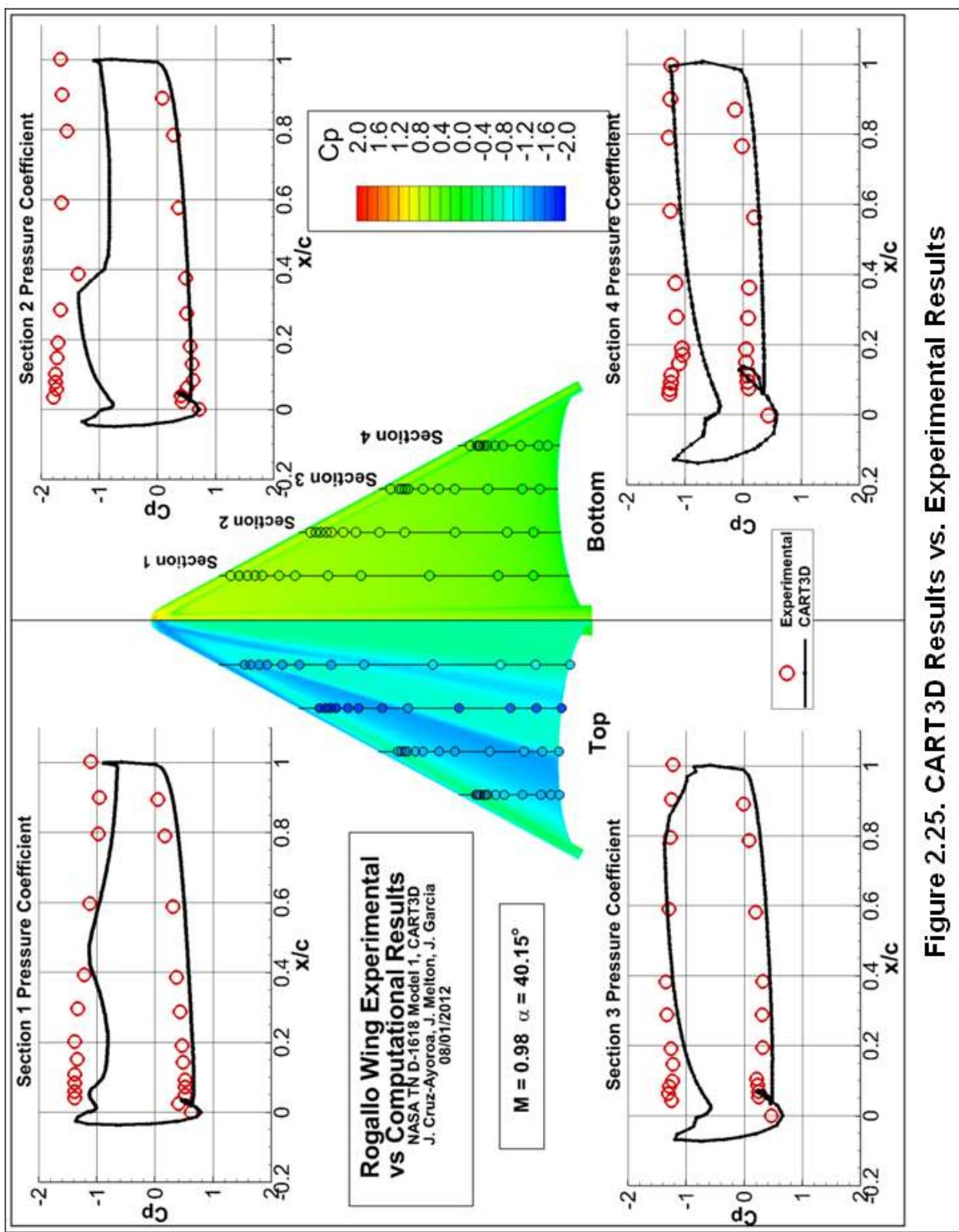


Figure 2.25. CART3D Results vs. Experimental Results

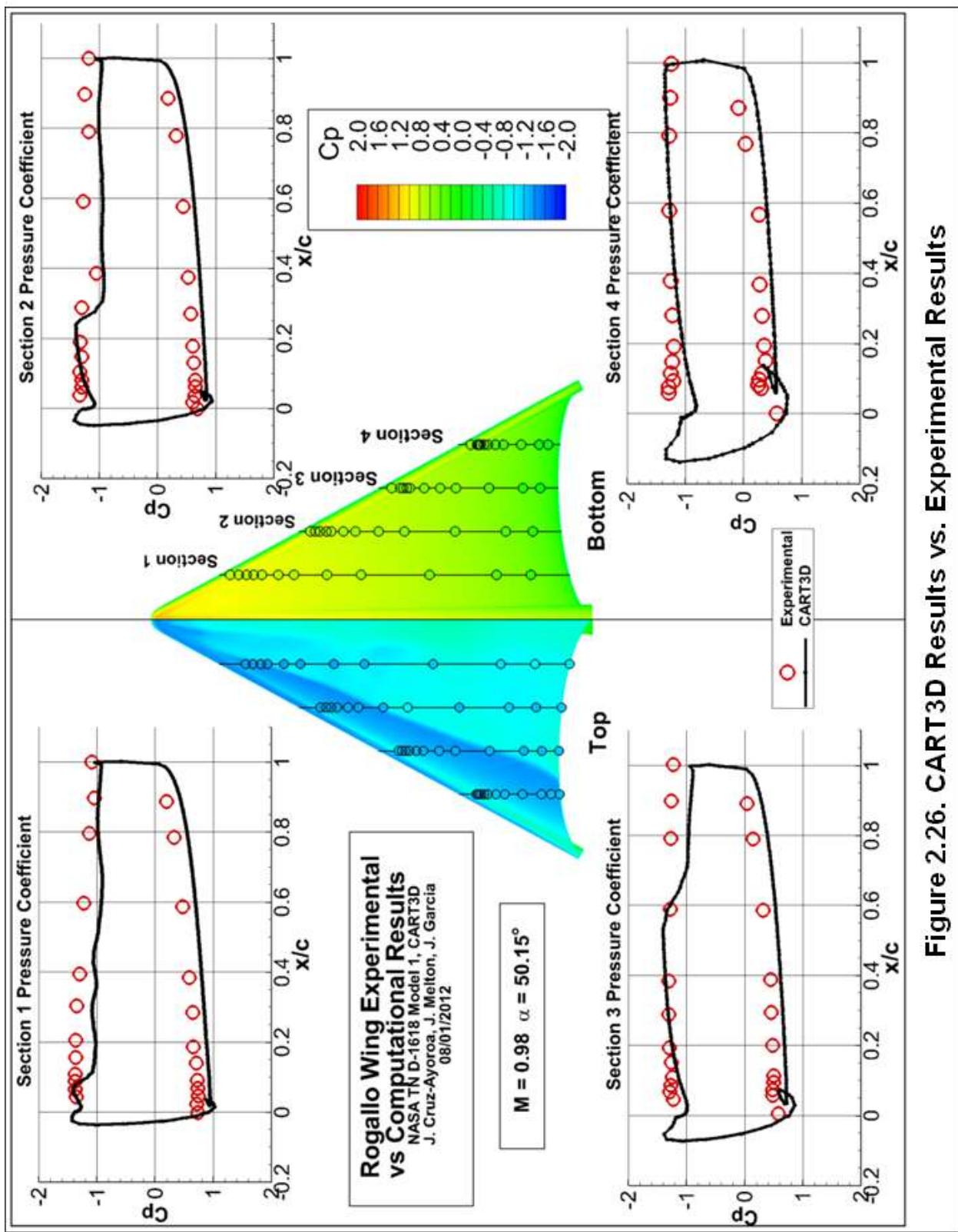


Figure 2.26. CART3D Results vs. Experimental Results

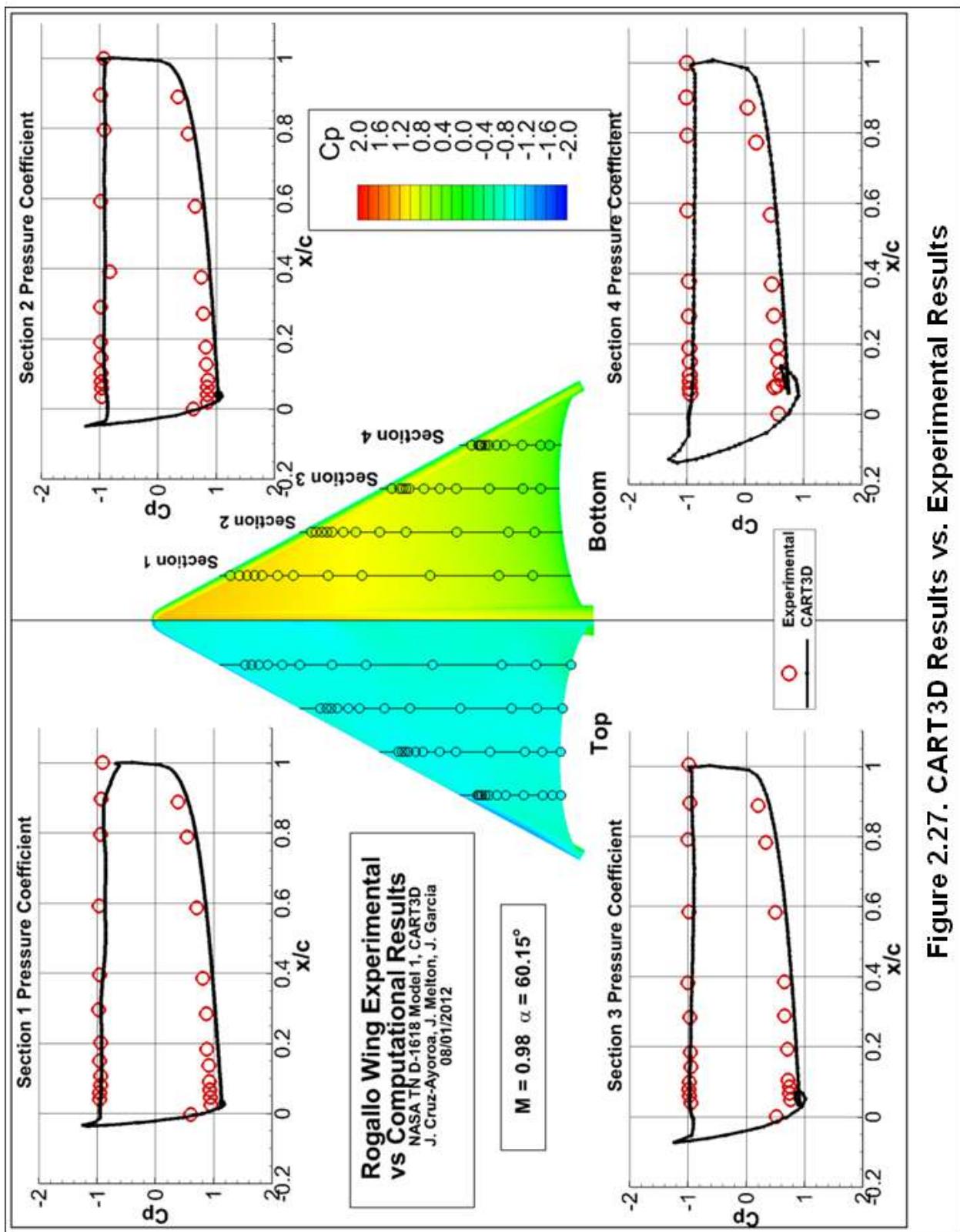


Figure 2.27. CART3D Results vs. Experimental Results

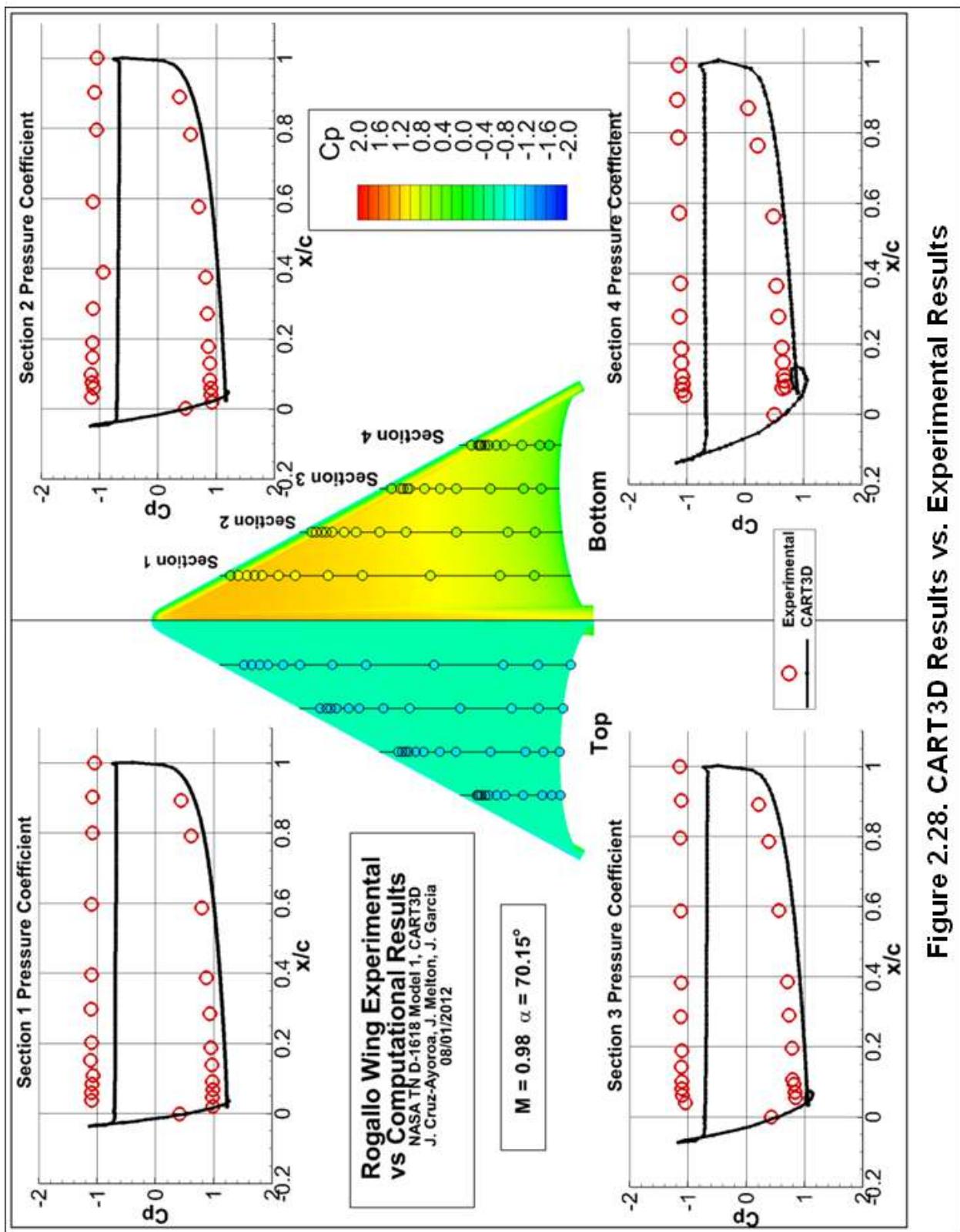


Figure 2.28. CART3D Results vs. Experimental Results

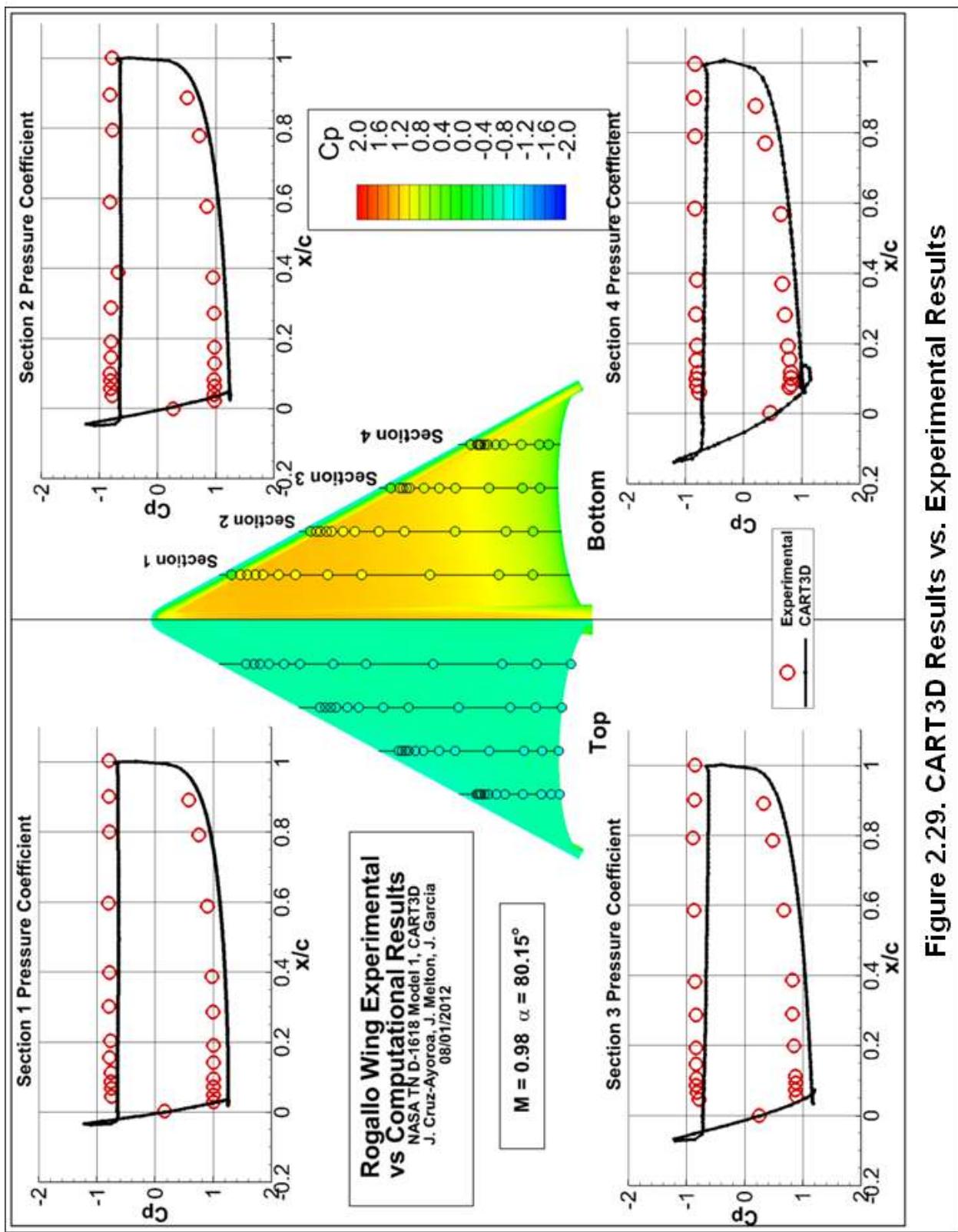


Figure 2.29. CART3D Results vs. Experimental Results

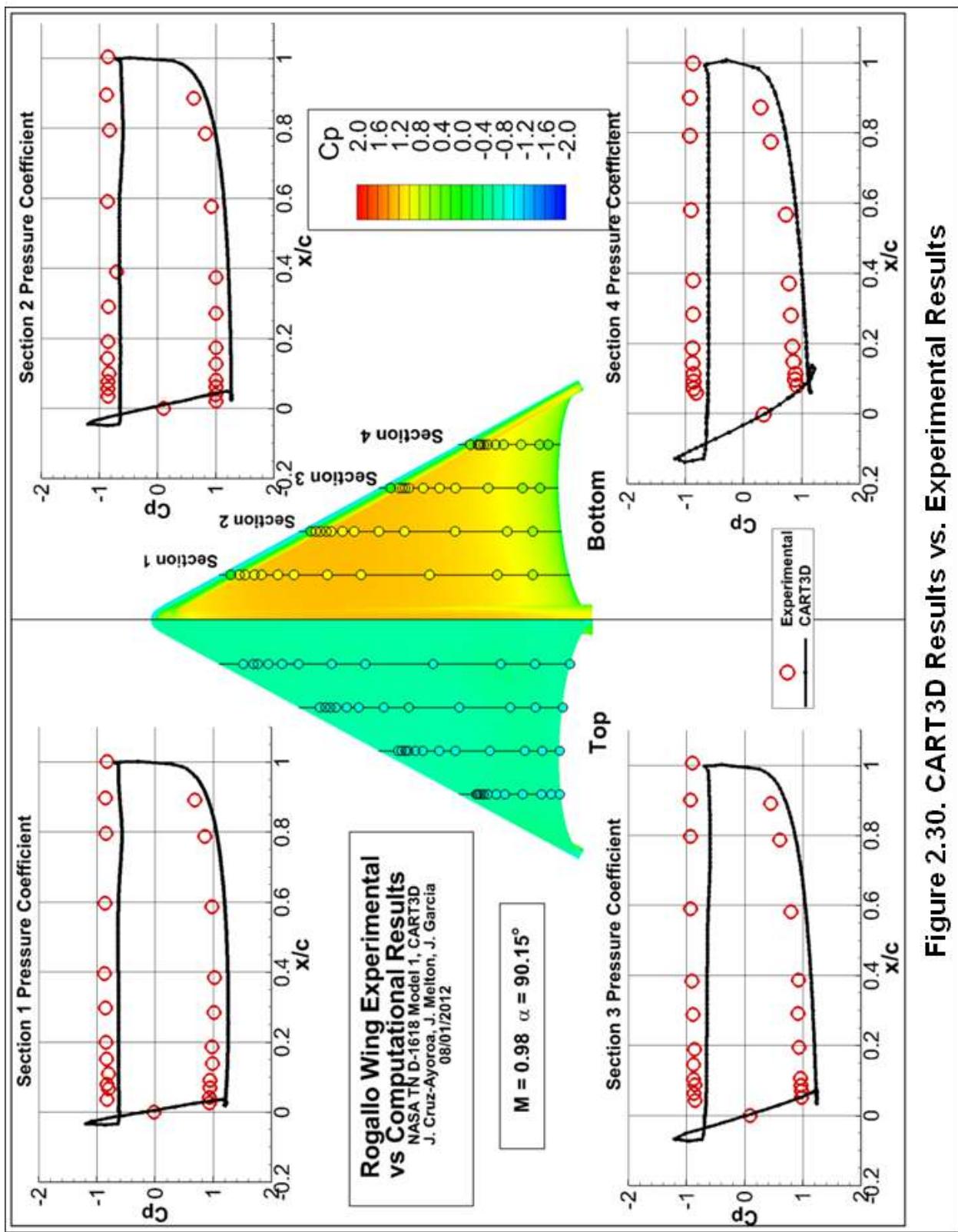


Figure 2.30. CART3D Results vs. Experimental Results

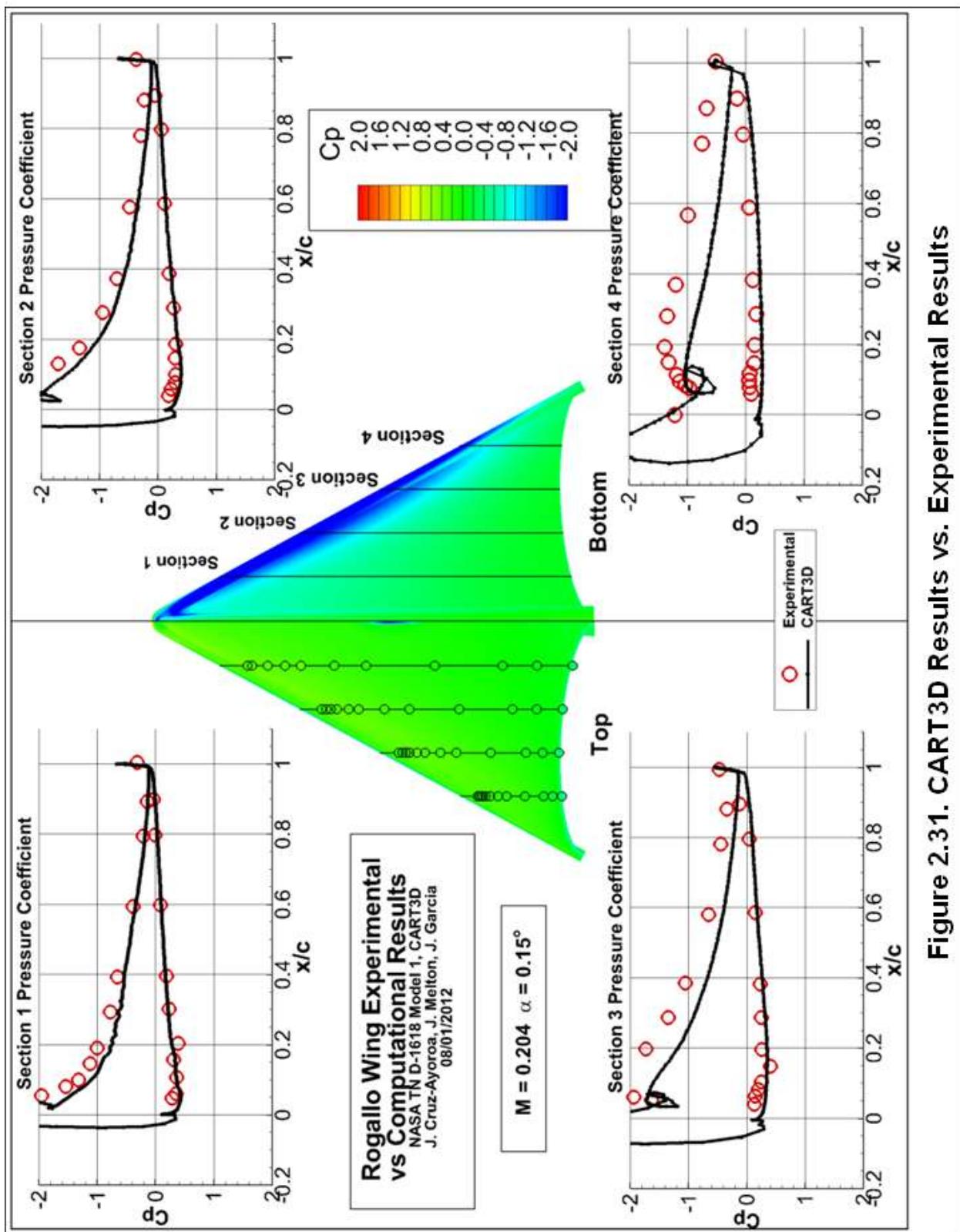


Figure 2.31. CART3D Results vs. Experimental Results

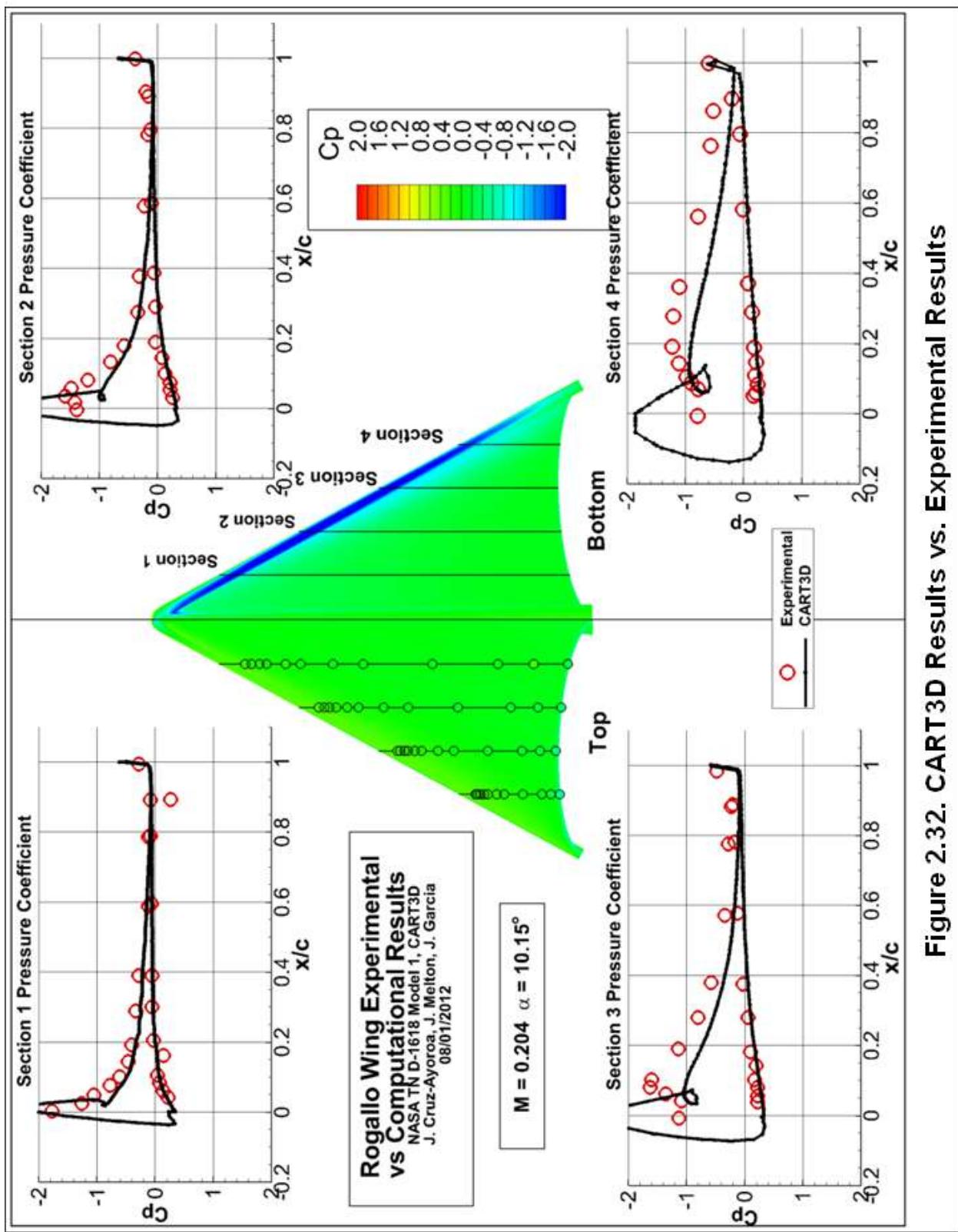


Figure 2.32. CART3D Results vs. Experimental Results

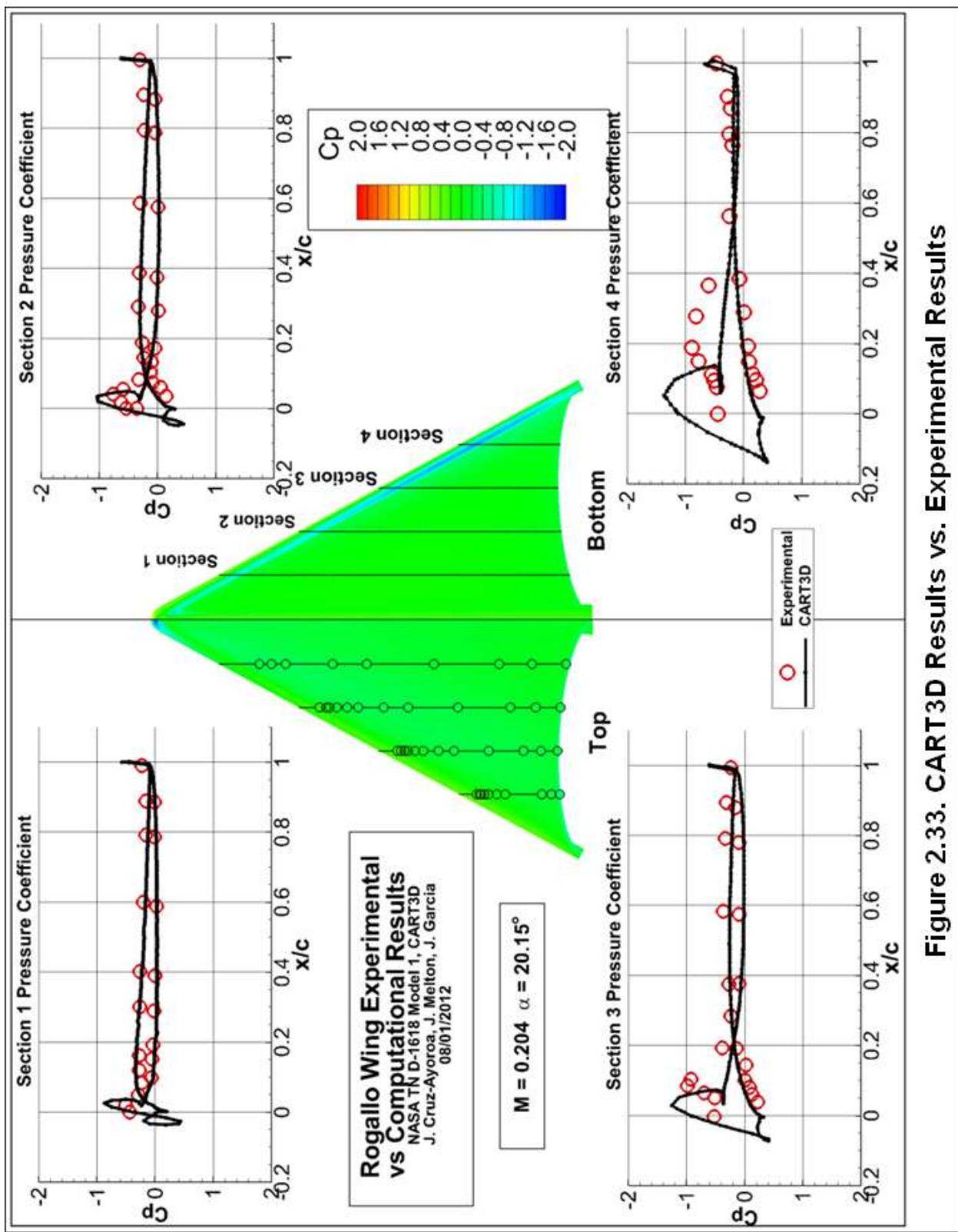


Figure 2.33. CART3D Results vs. Experimental Results

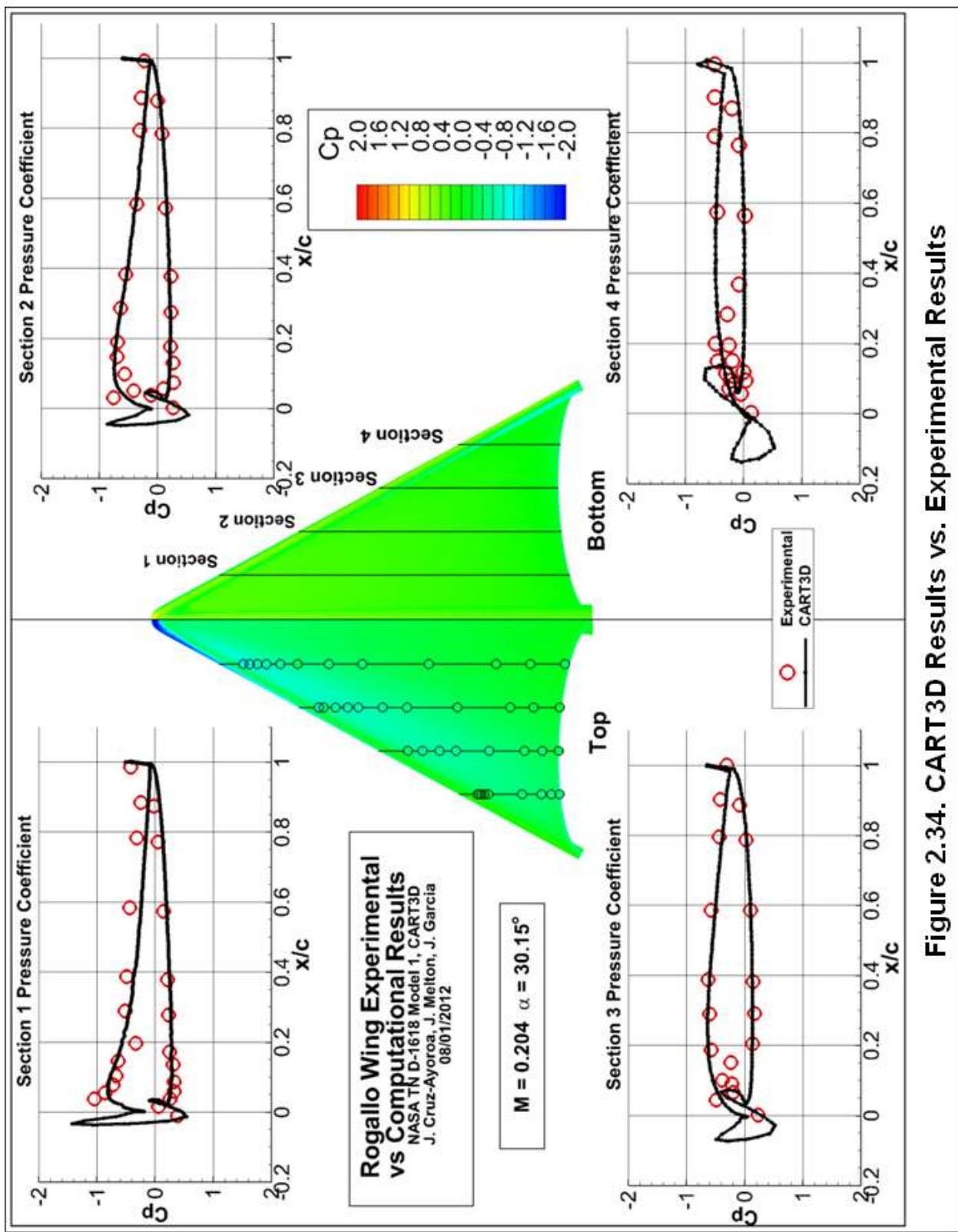


Figure 2.34. CART3D Results vs. Experimental Results

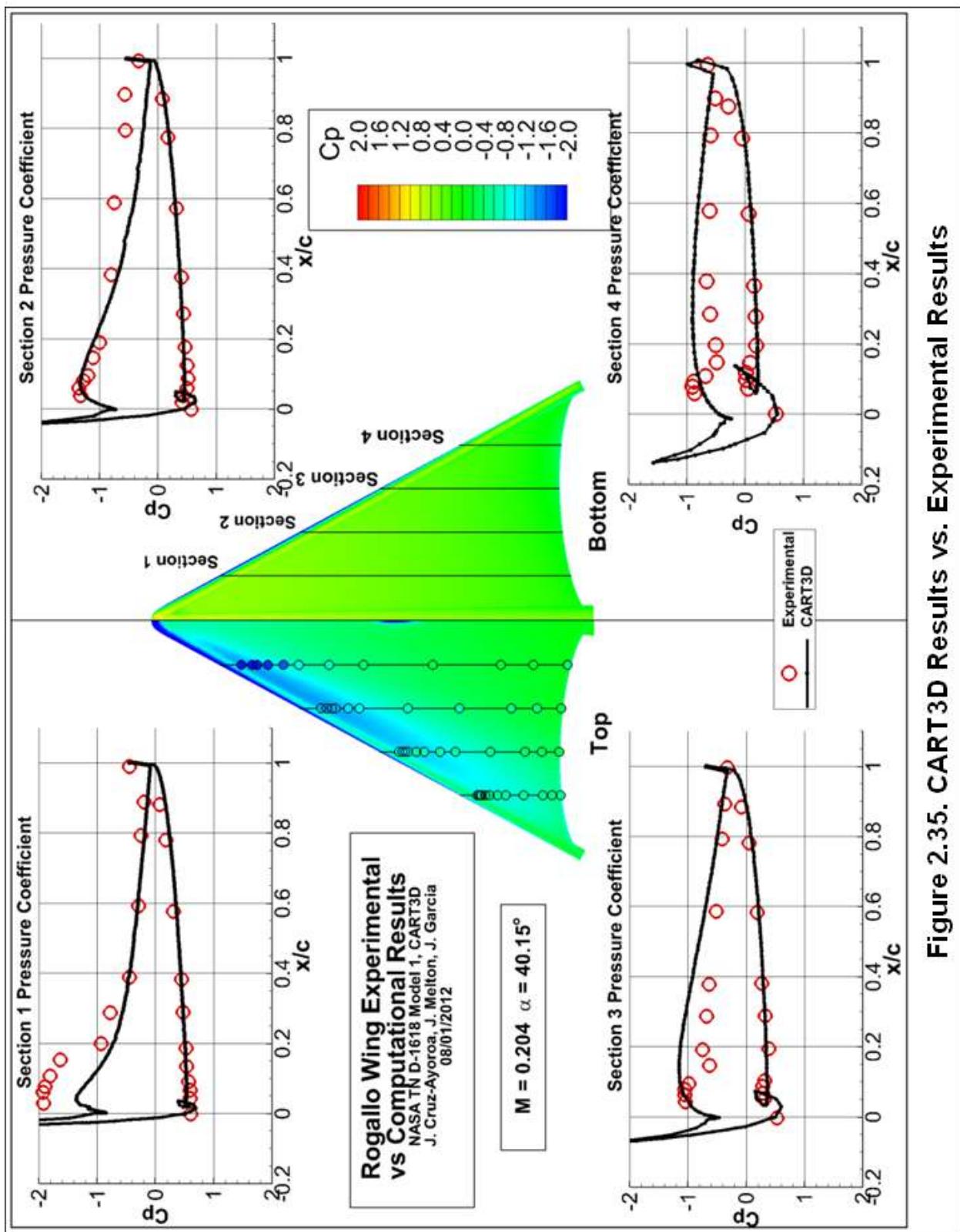


Figure 2.35. CART3D Results vs. Experimental Results

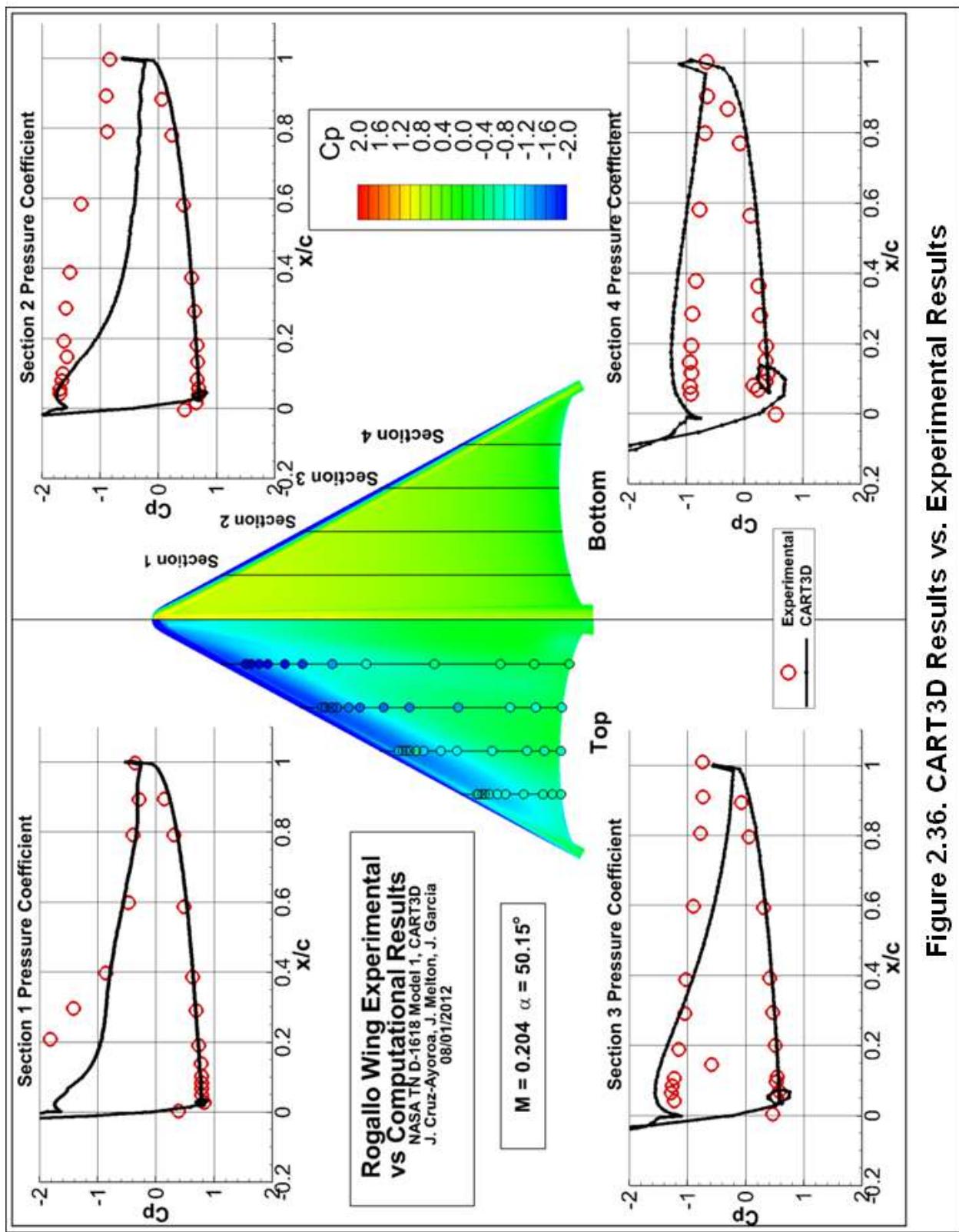


Figure 2.36. CART3D Results vs. Experimental Results

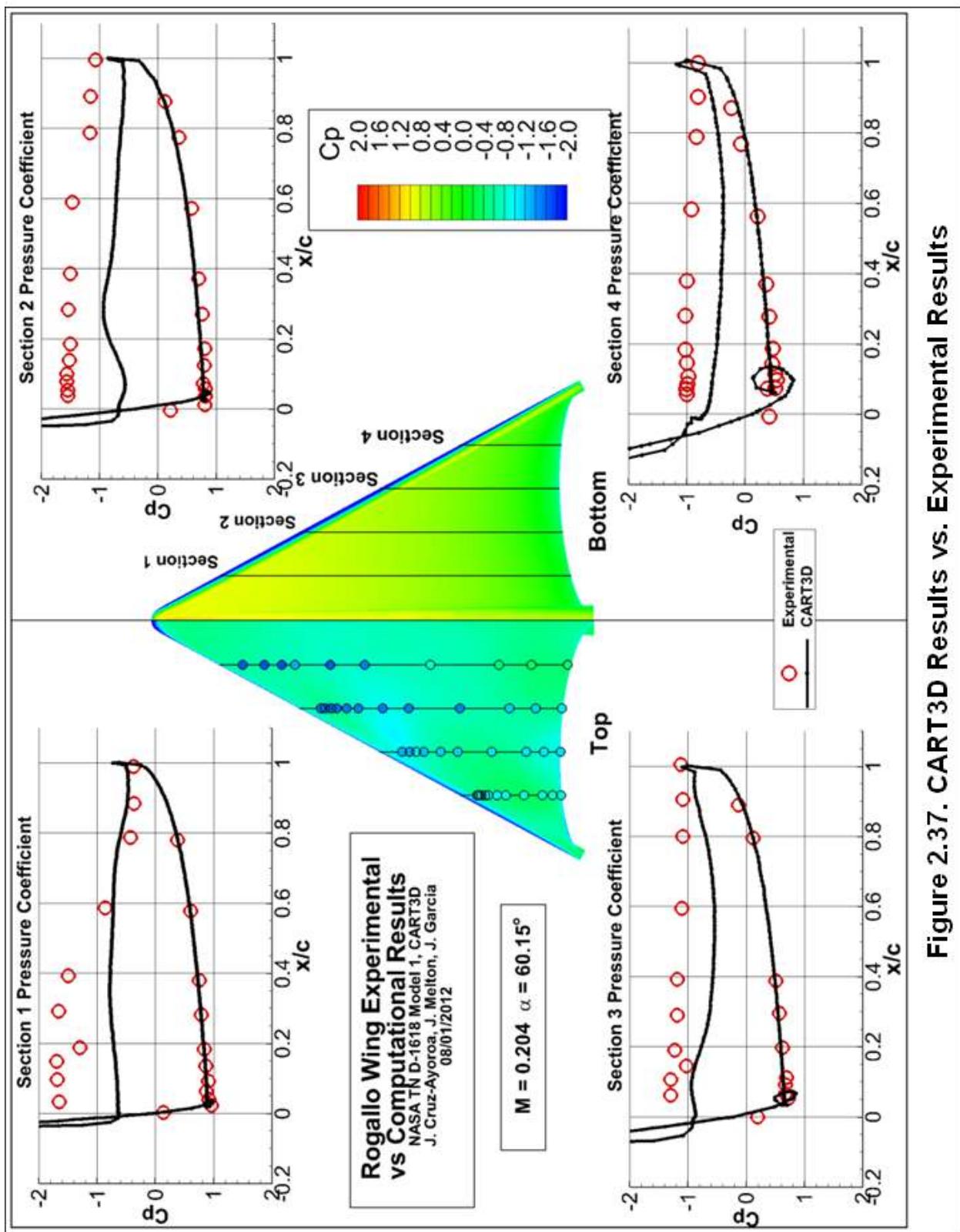


Figure 2.37. CART3D Results vs. Experimental Results

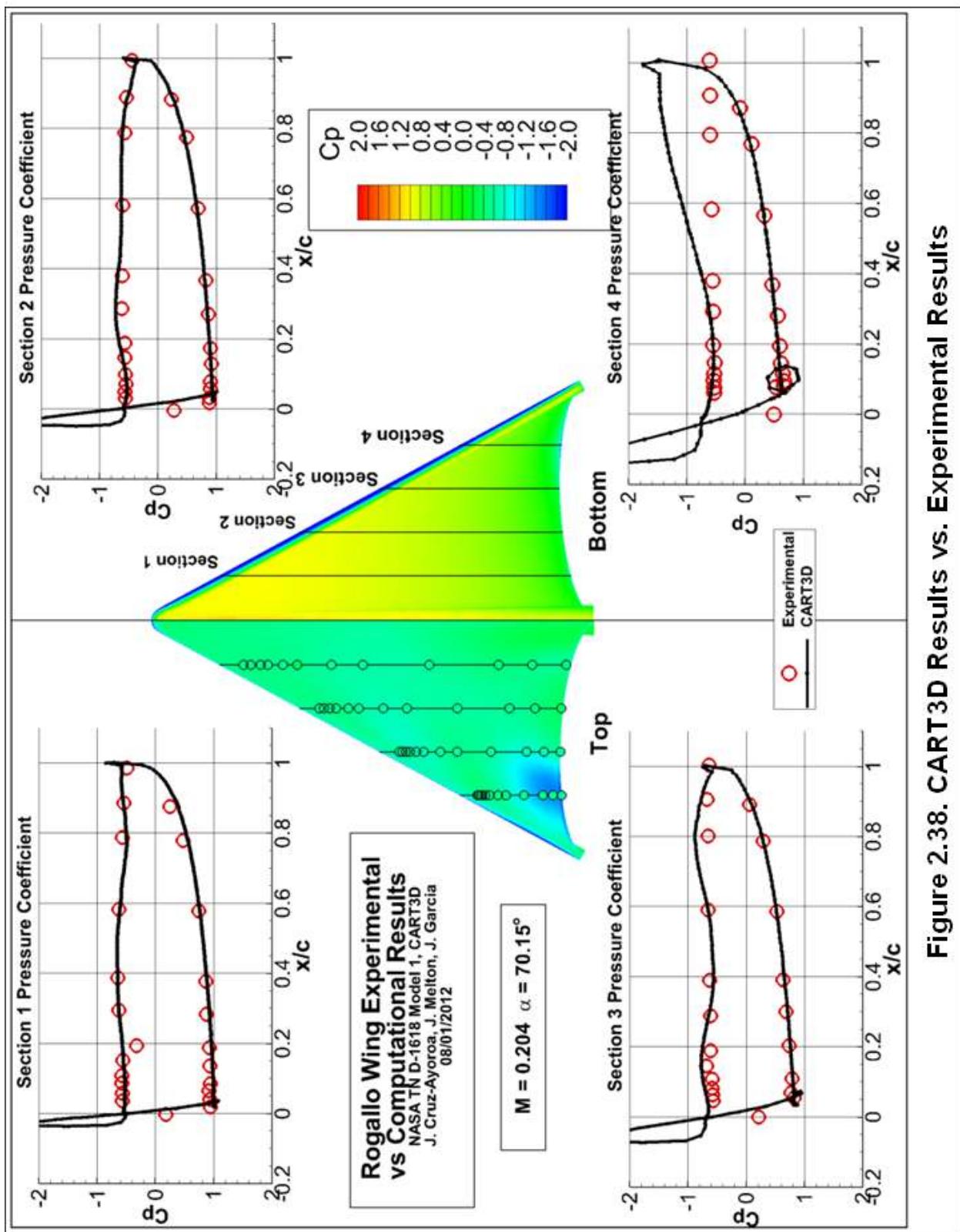


Figure 2.38. CART3D Results vs. Experimental Results

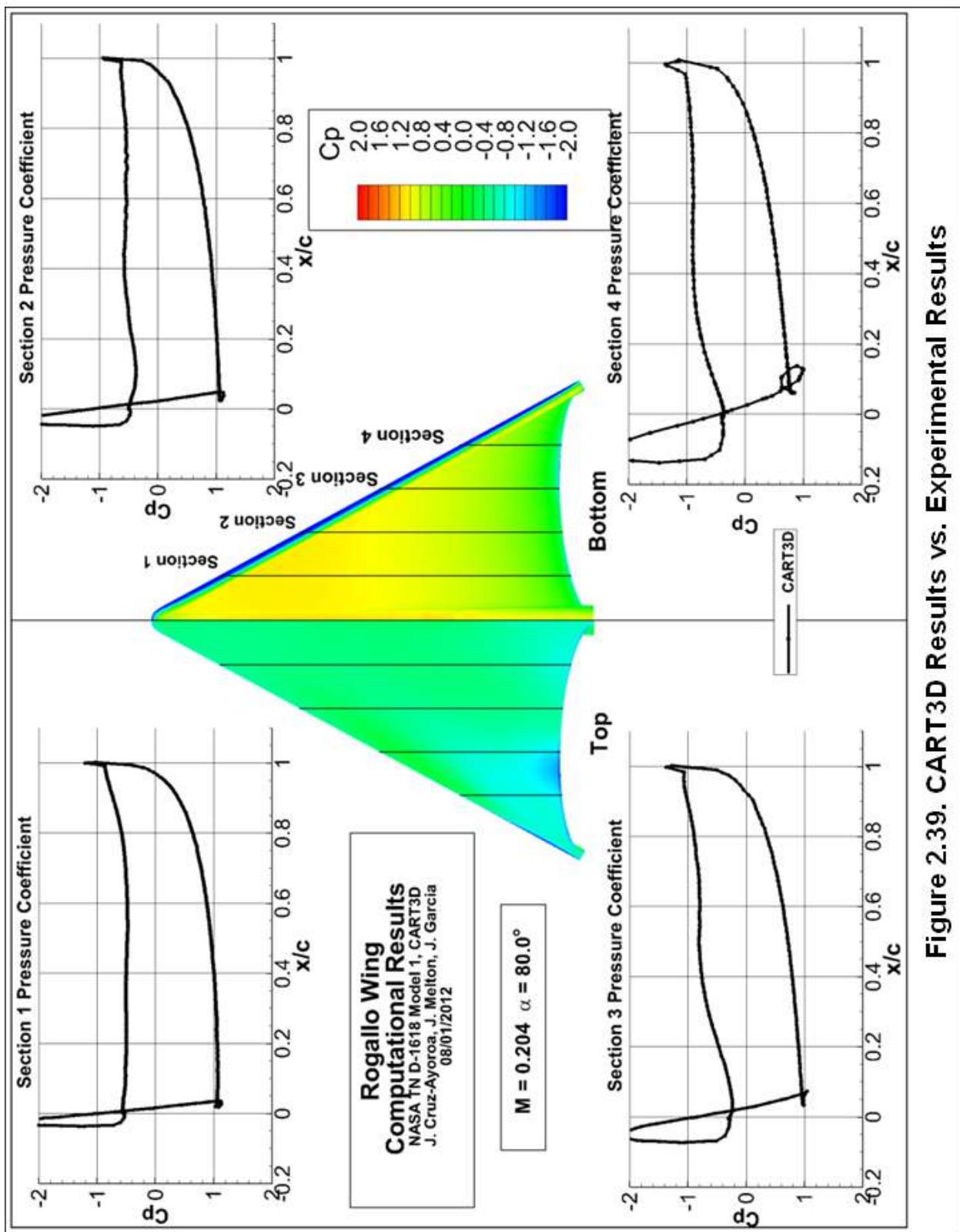


Figure 2.39. CART3D Results vs. Experimental Results

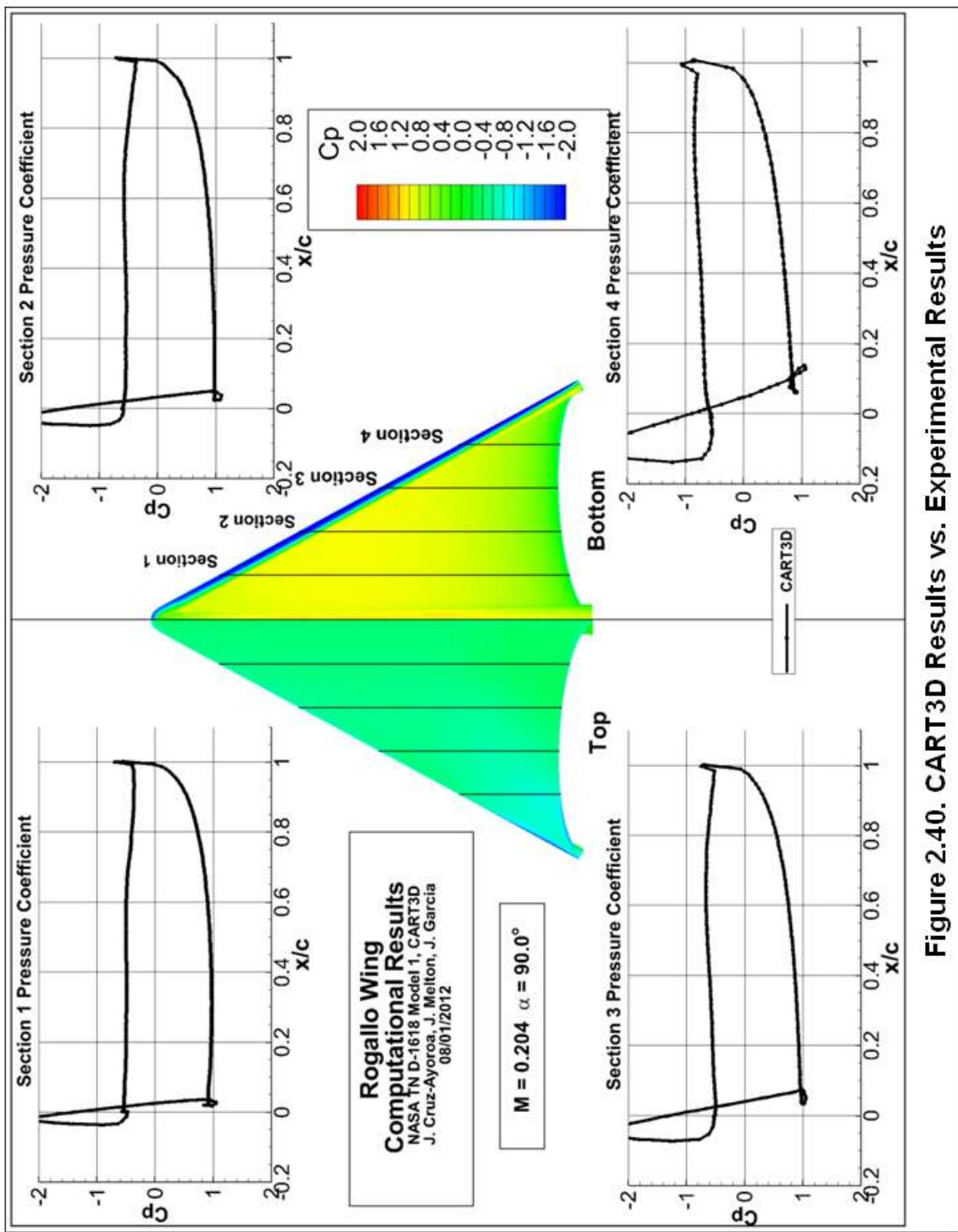


Figure 2.40. CART3D Results vs. Experimental Results

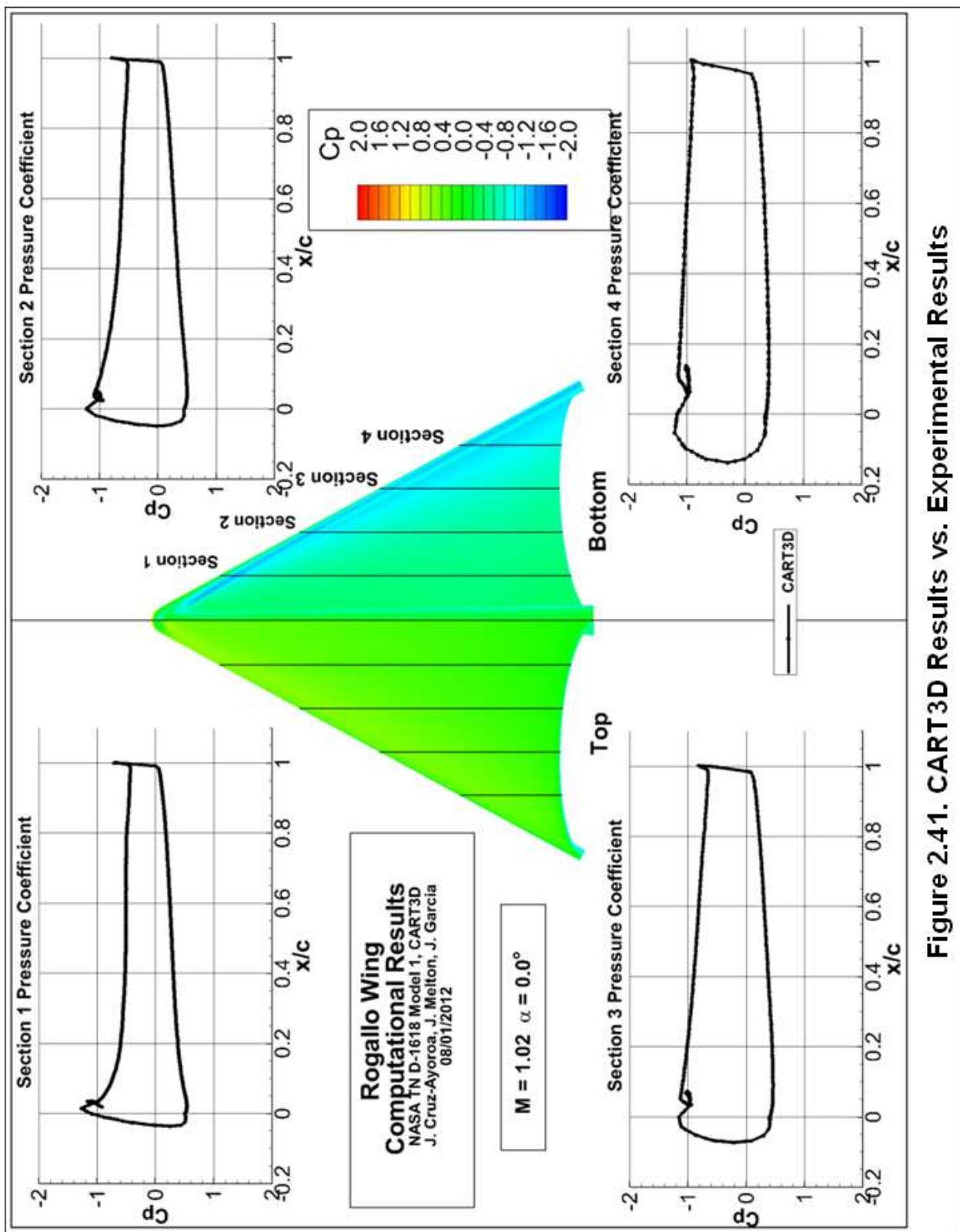


Figure 2.41. CART3D Results vs. Experimental Results

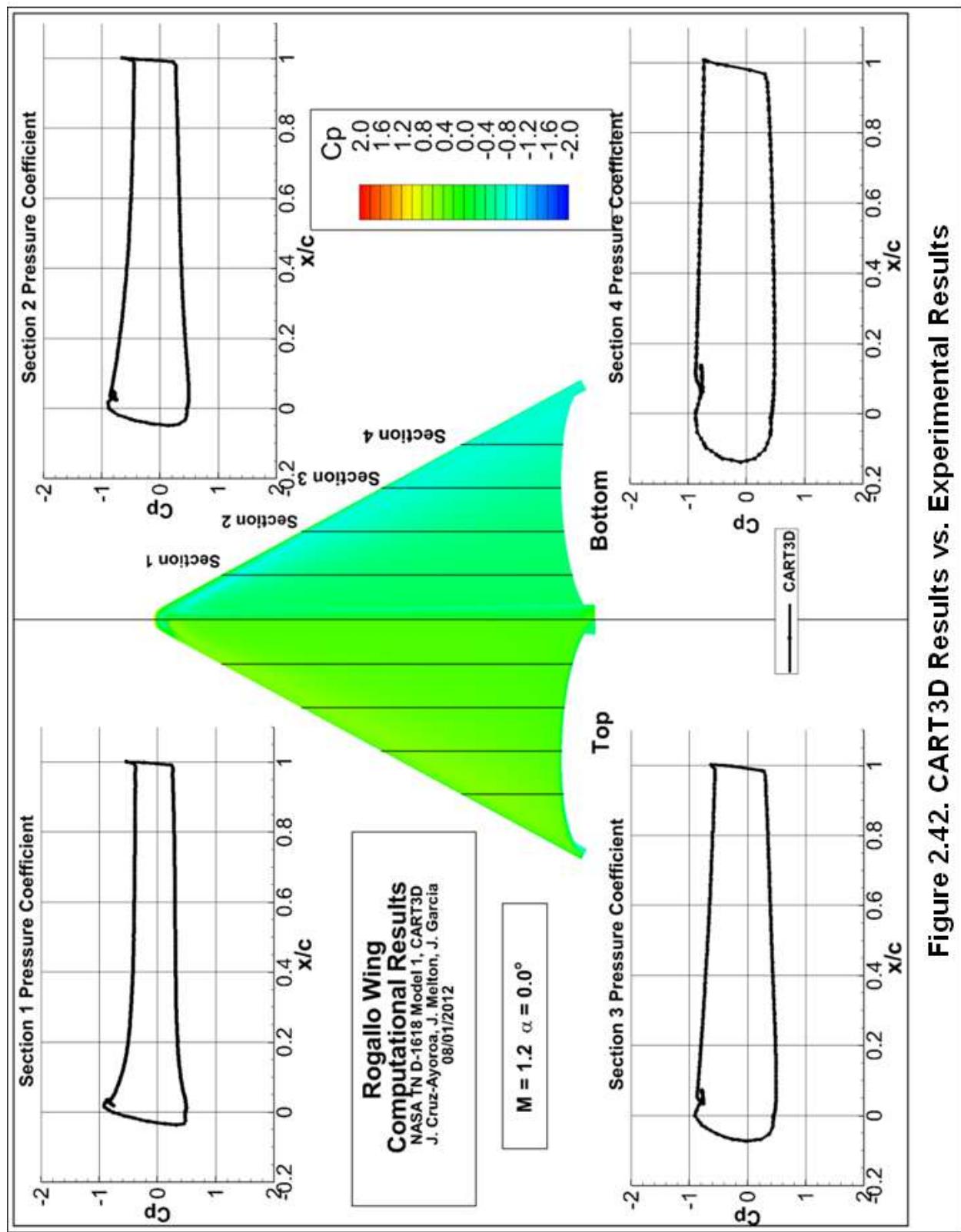


Figure 2.42. CART3D Results vs. Experimental Results

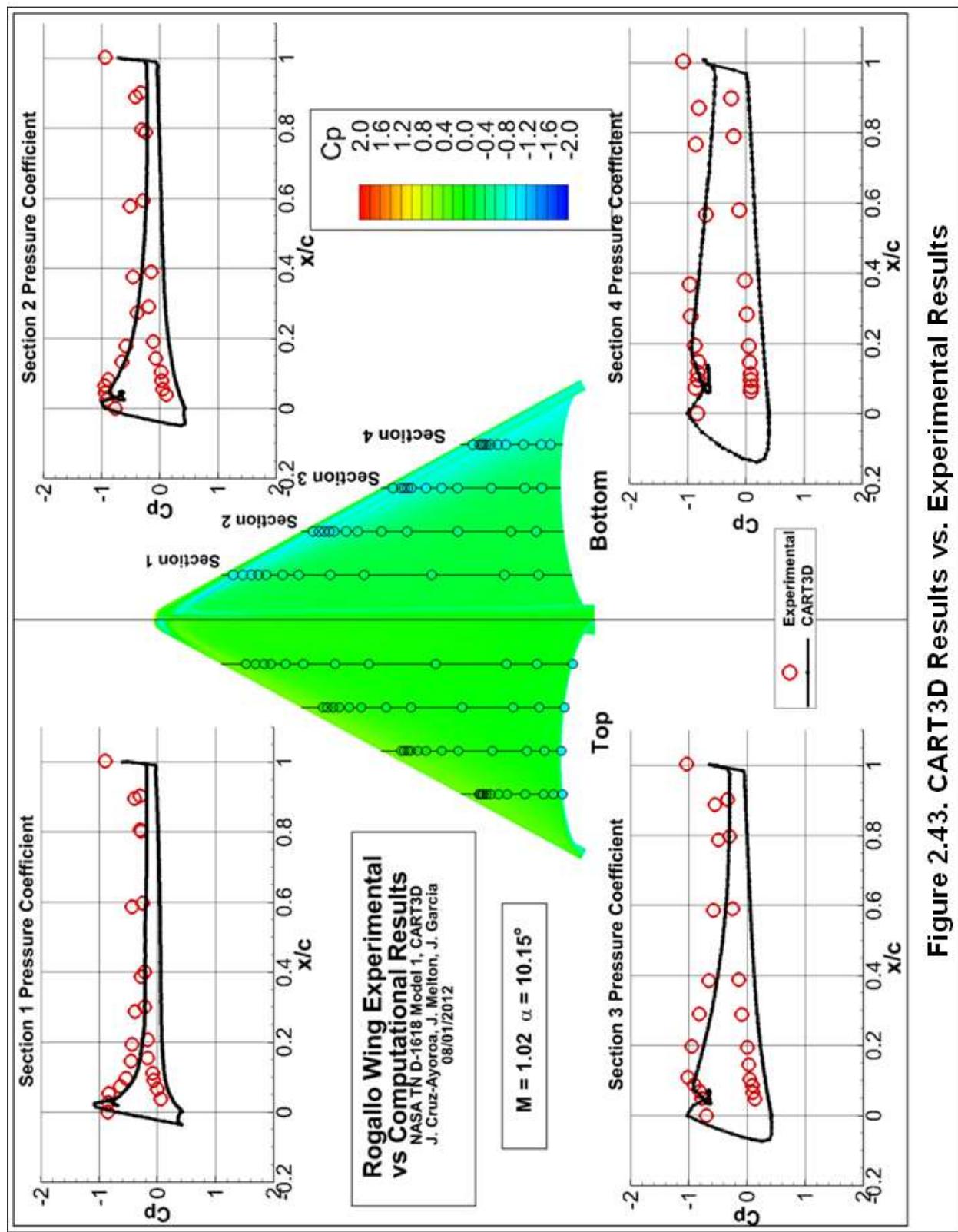


Figure 2.4.3. CART3D Results vs. Experimental Results

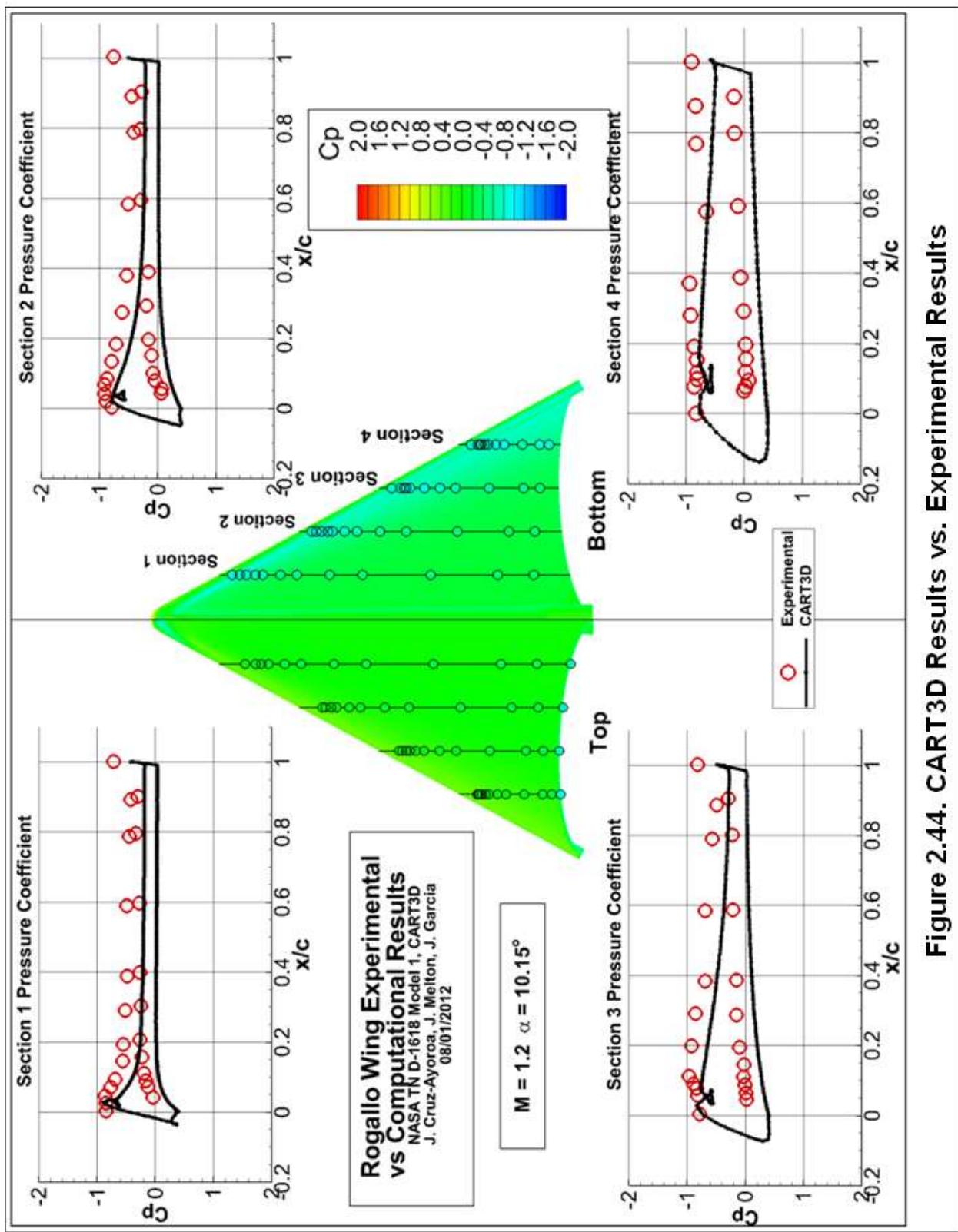


Figure 2.44. CART3D Results vs. Experimental Results

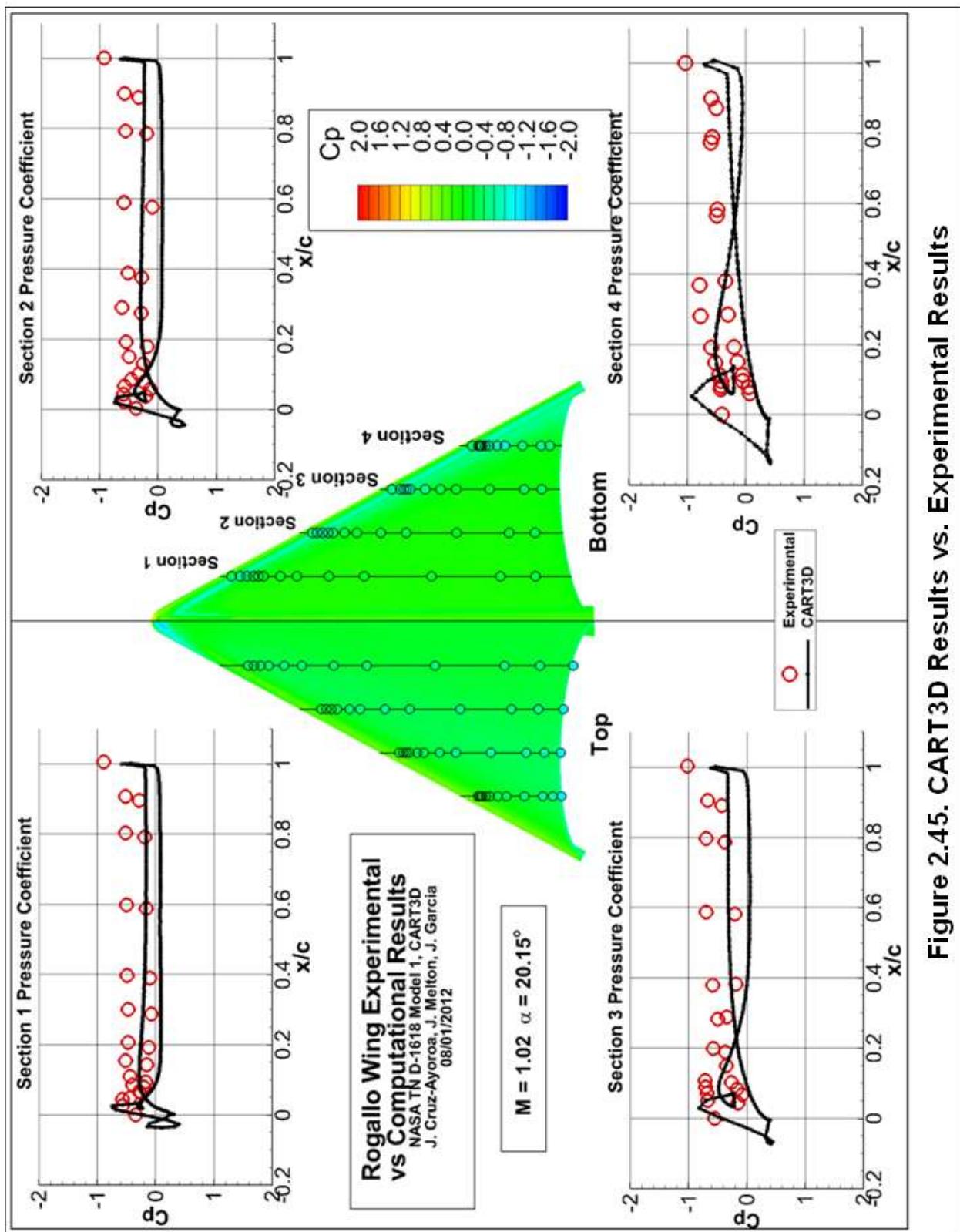


Figure 2.45. CART3D Results vs. Experimental Results

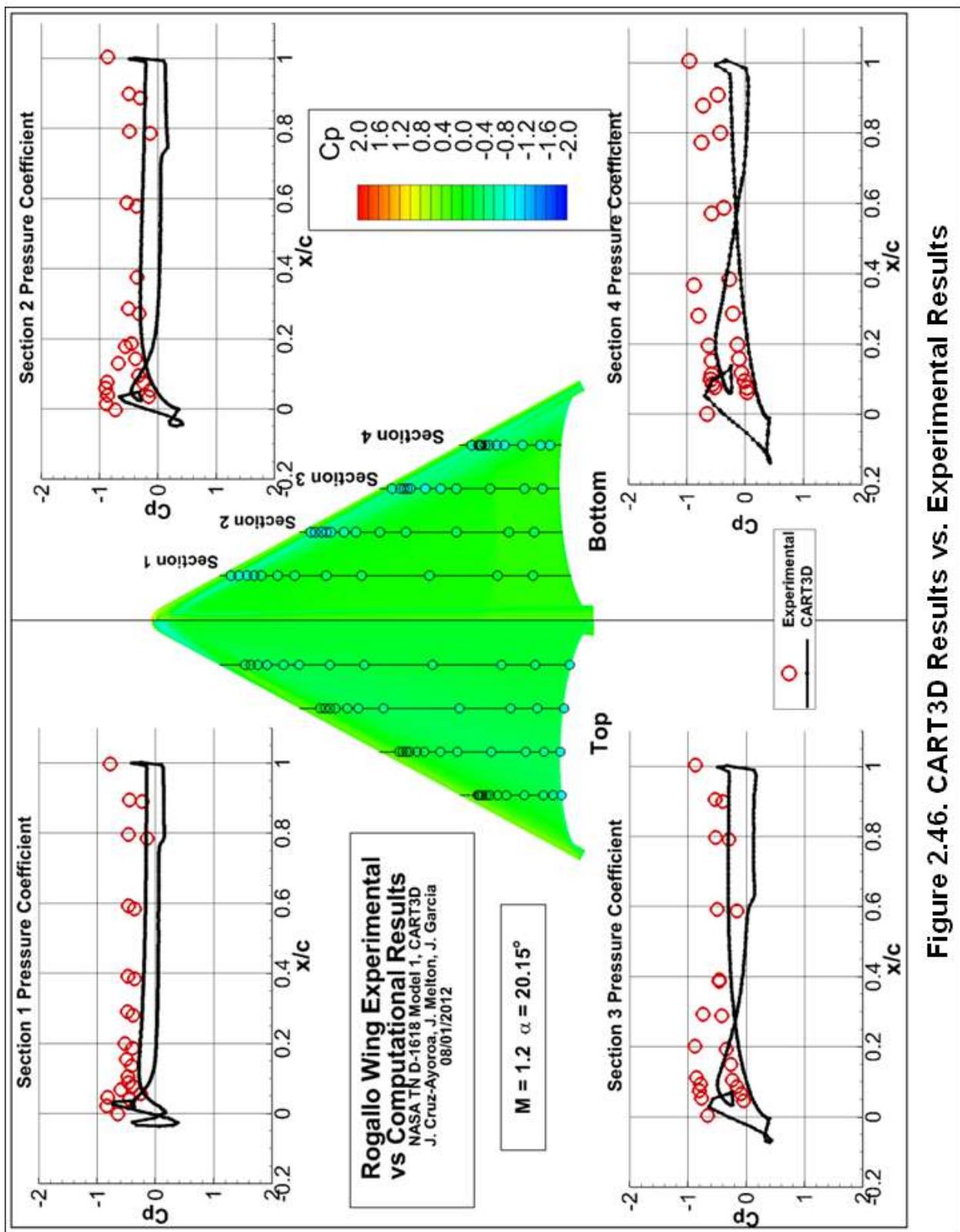


Figure 2.46. CART3D Results vs. Experimental Results

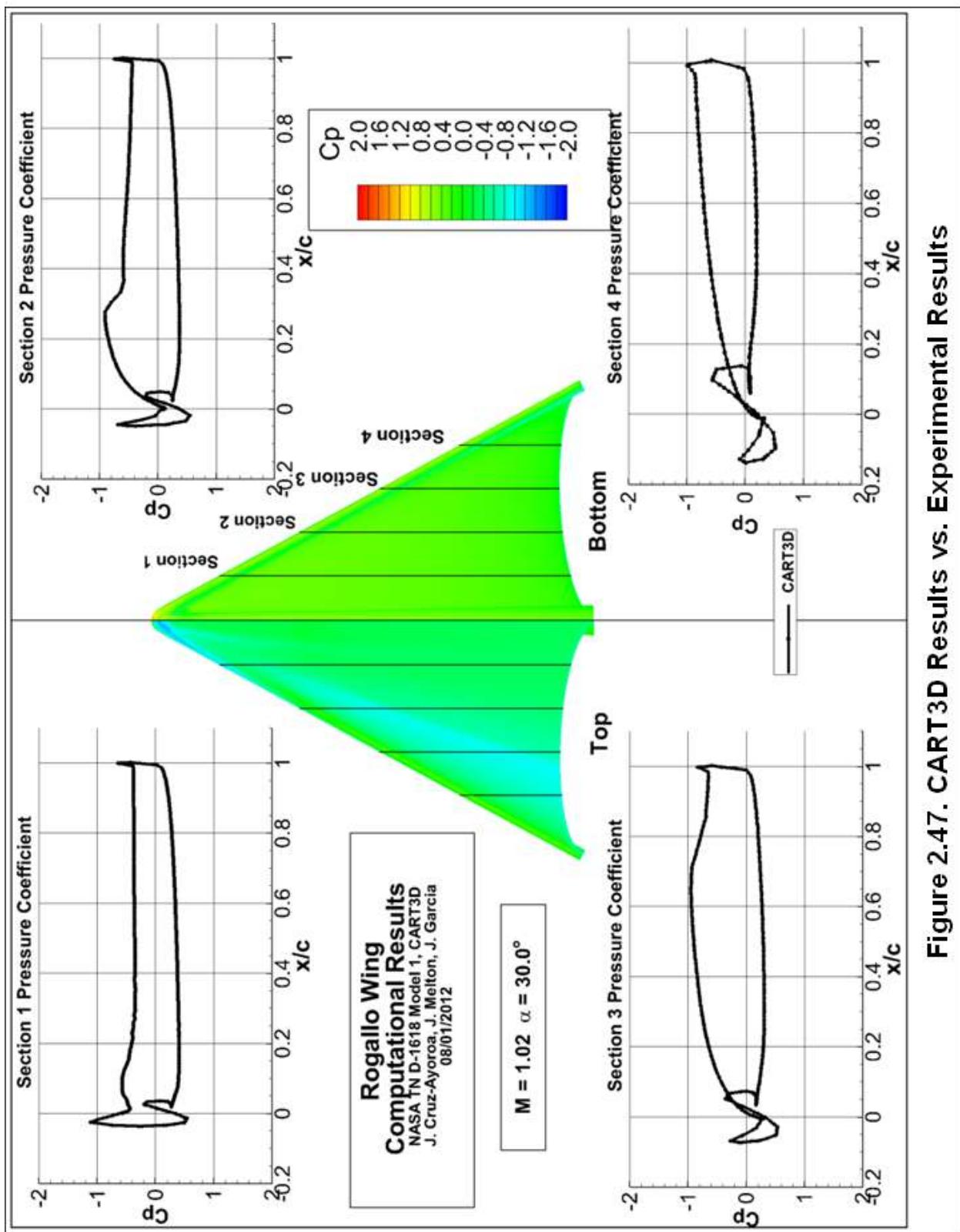


Figure 2.47. CART3D Results vs. Experimental Results

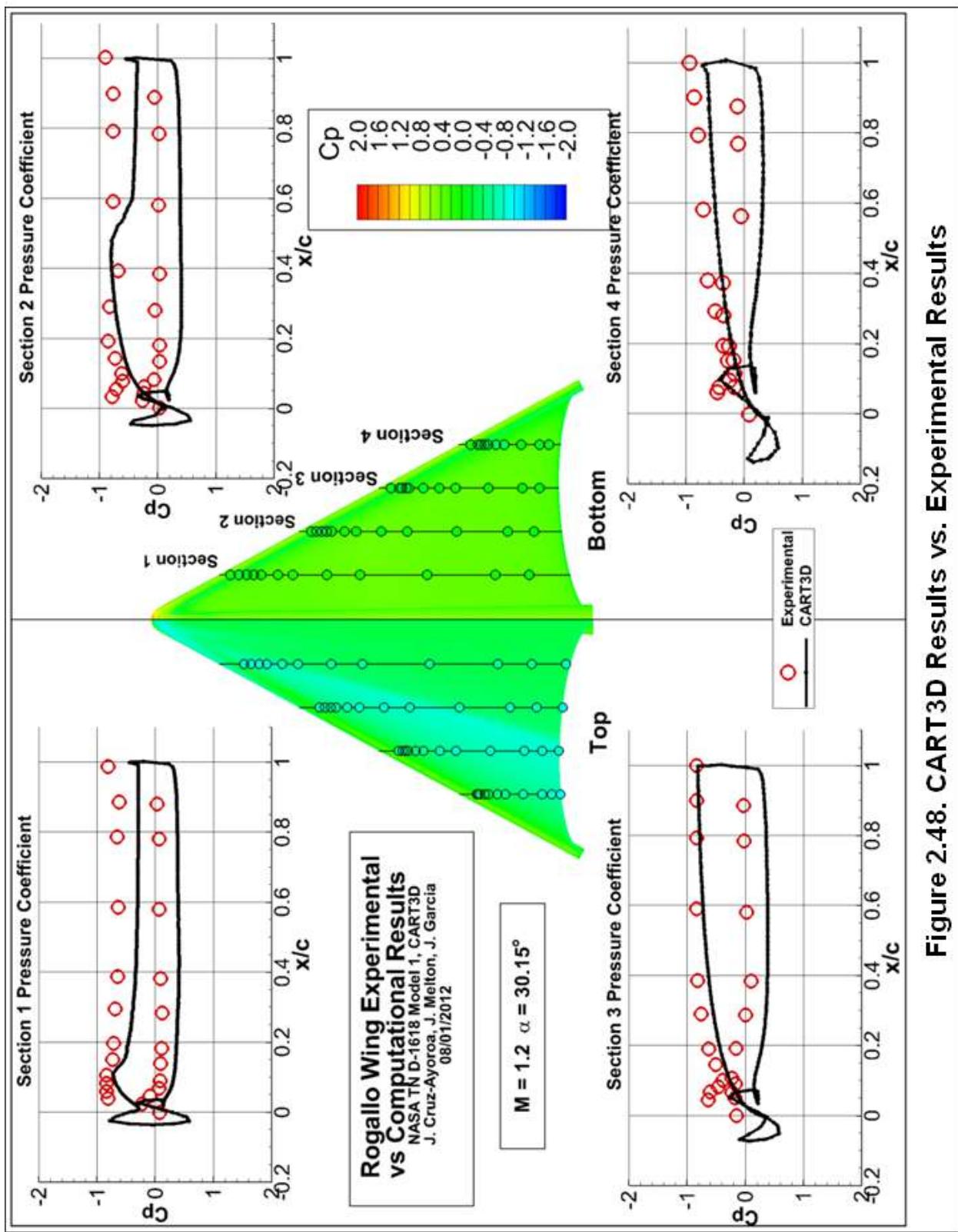


Figure 2.48. CART3D Results vs. Experimental Results

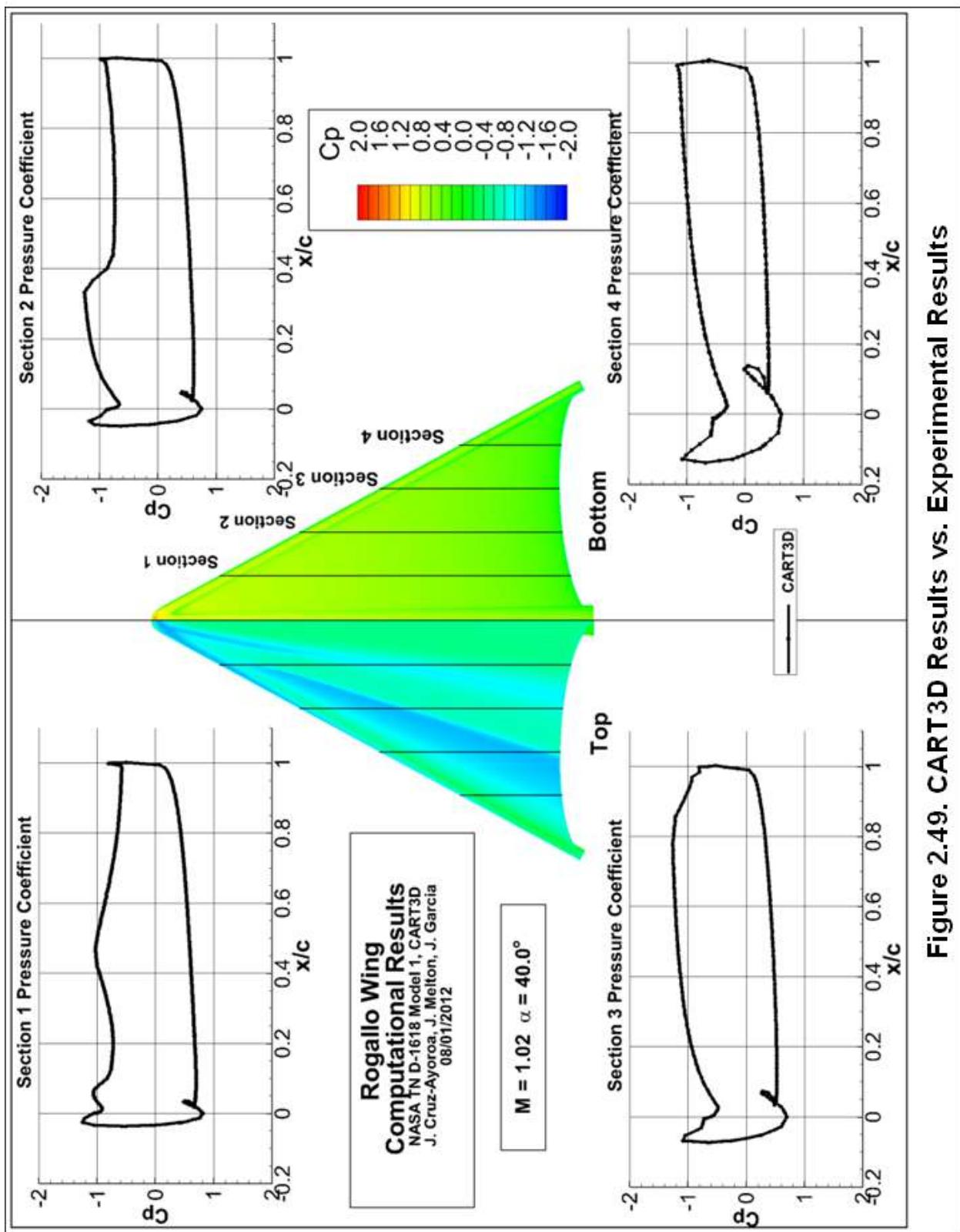


Figure 2.49. CART3D Results vs. Experimental Results

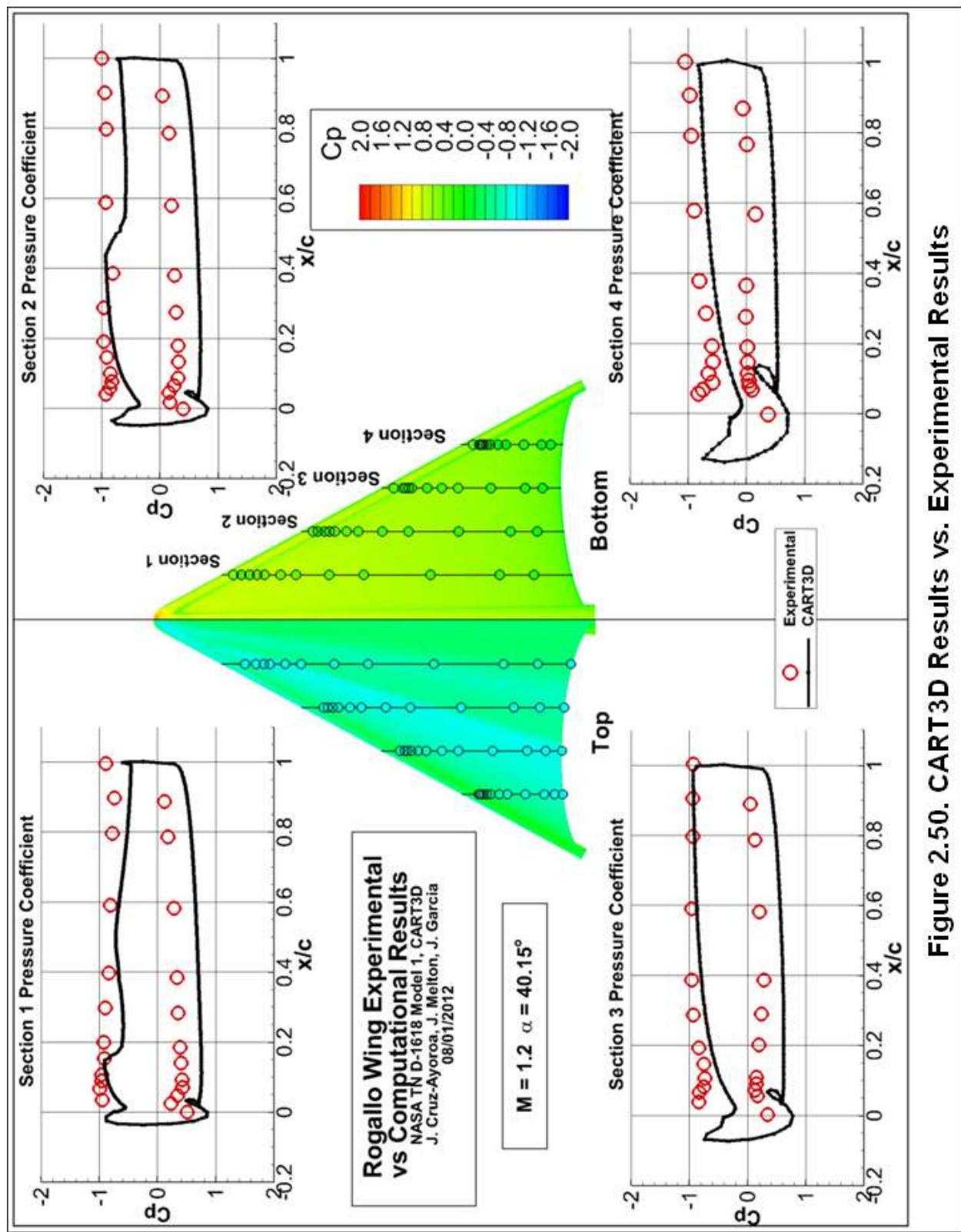


Figure 2.50. CART3D Results vs. Experimental Results

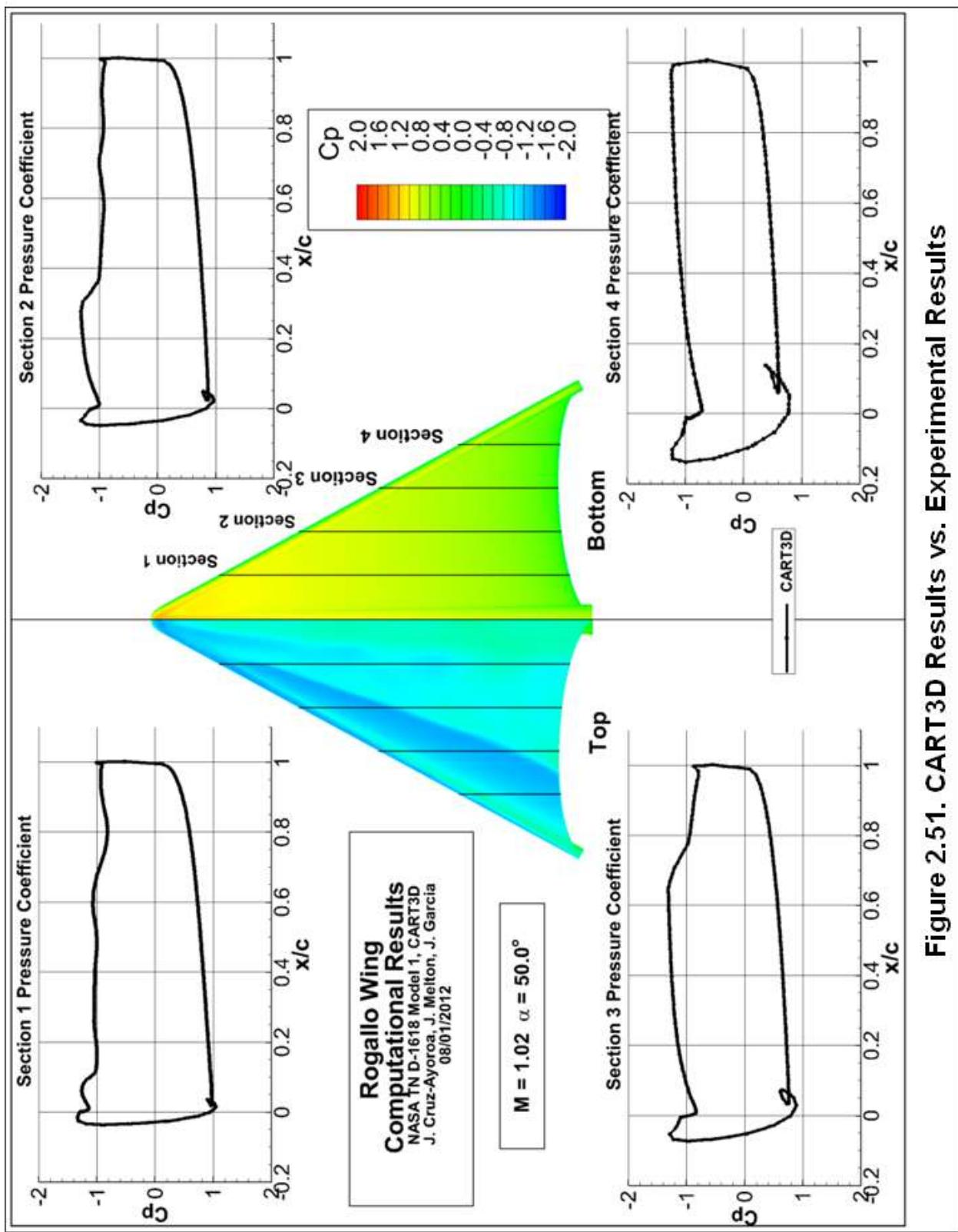


Figure 2.51. CART3D Results vs. Experimental Results

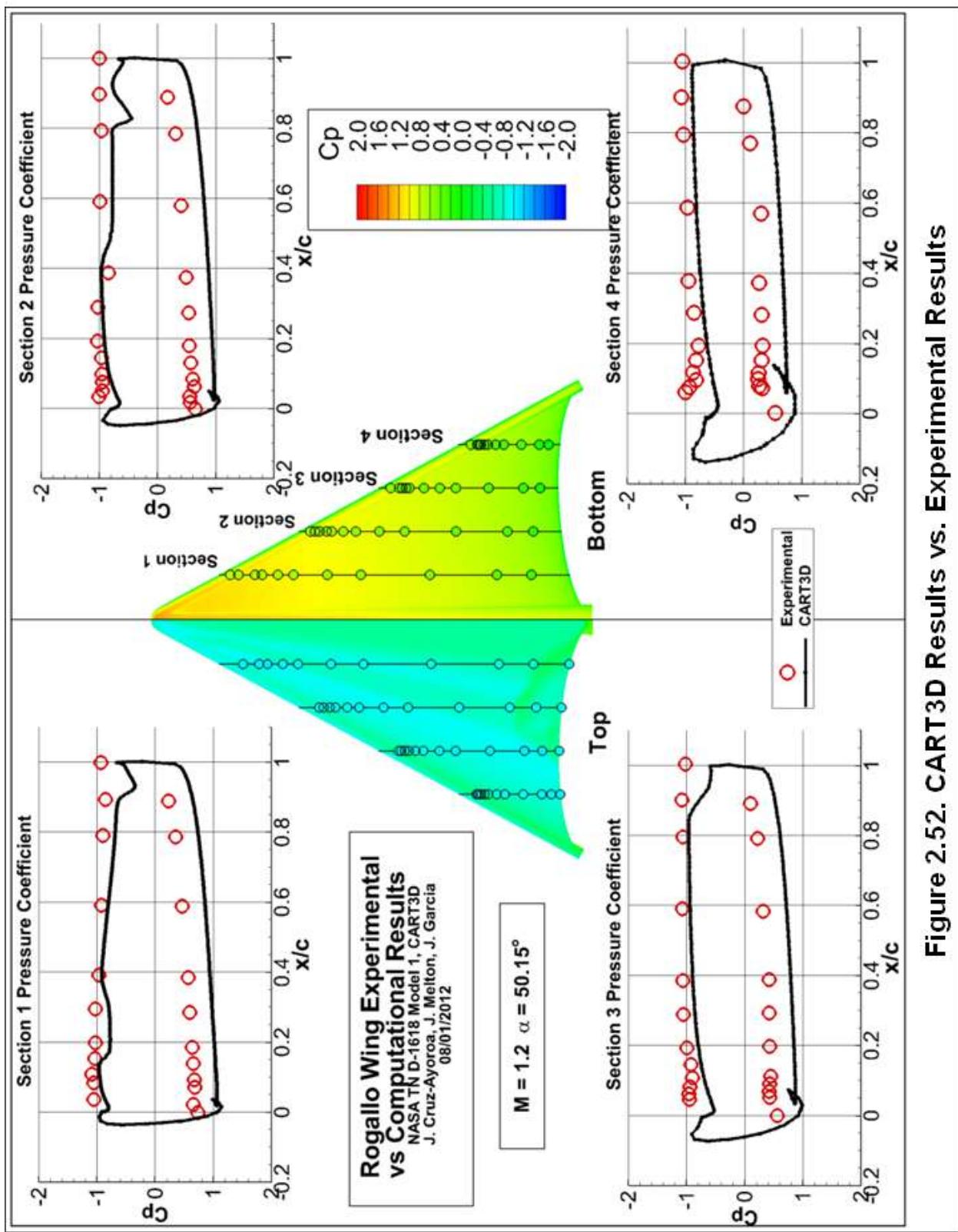


Figure 2.52. CART3D Results vs. Experimental Results

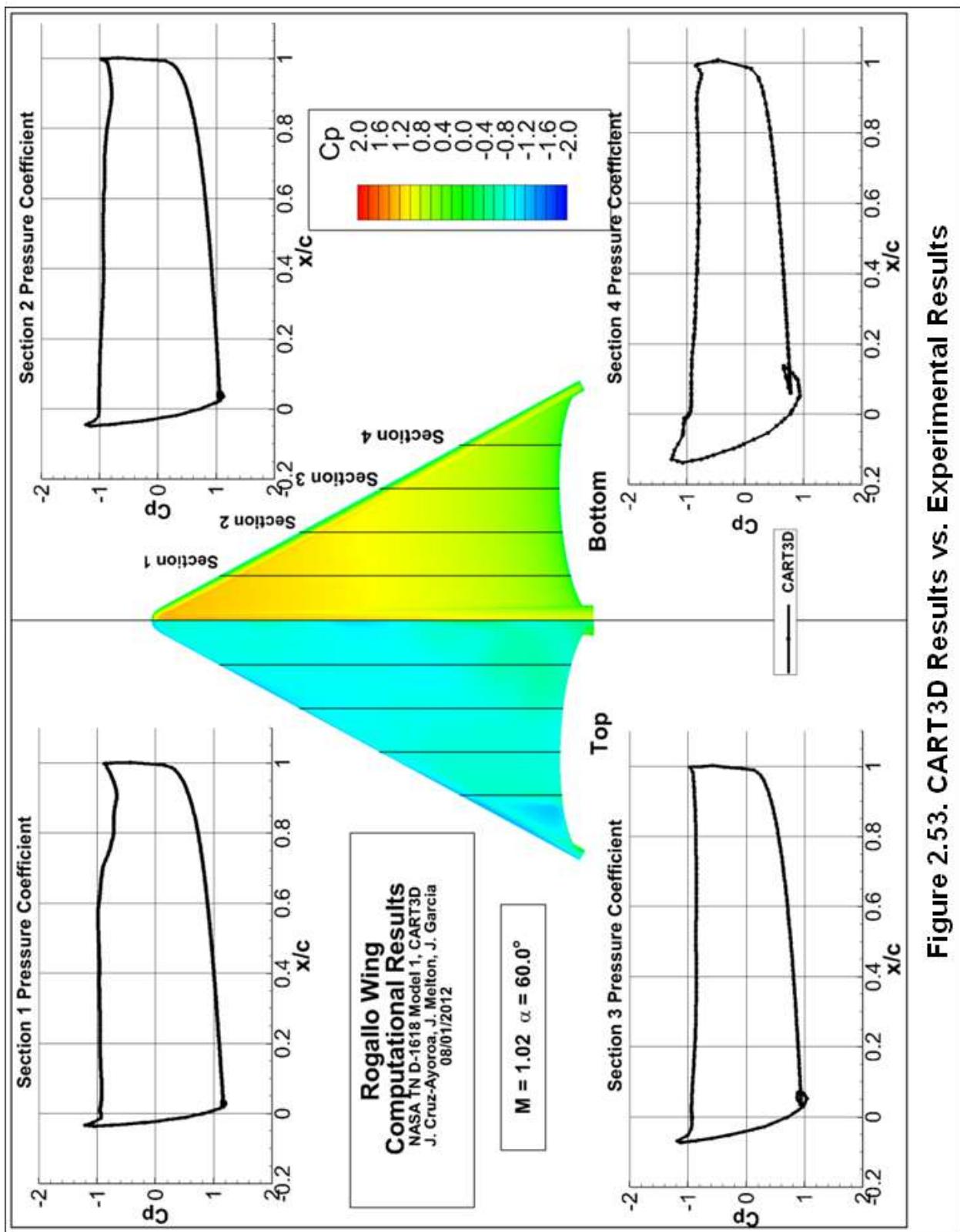


Figure 2.53. CART3D Results vs. Experimental Results

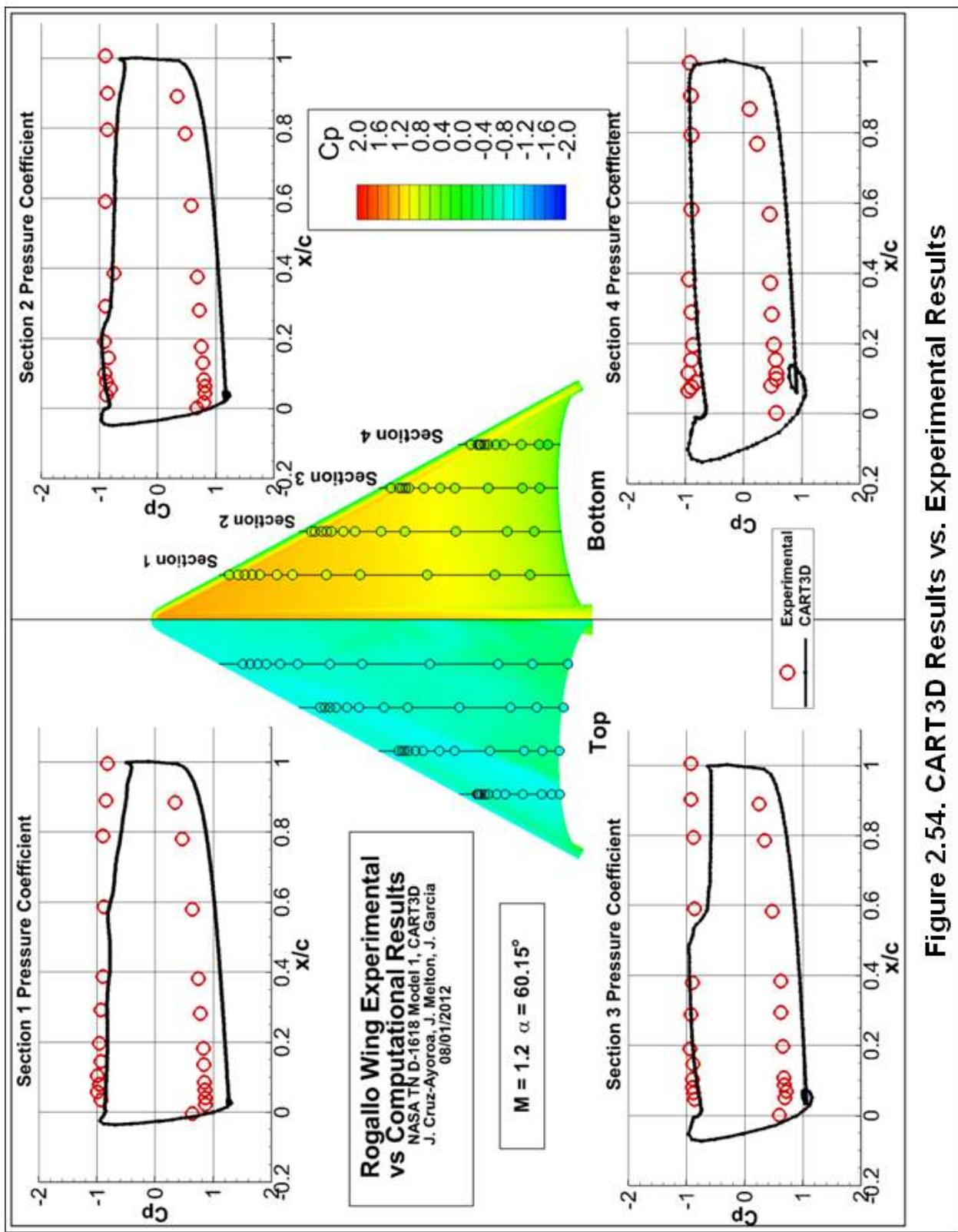


Figure 2.54. CART3D Results vs. Experimental Results

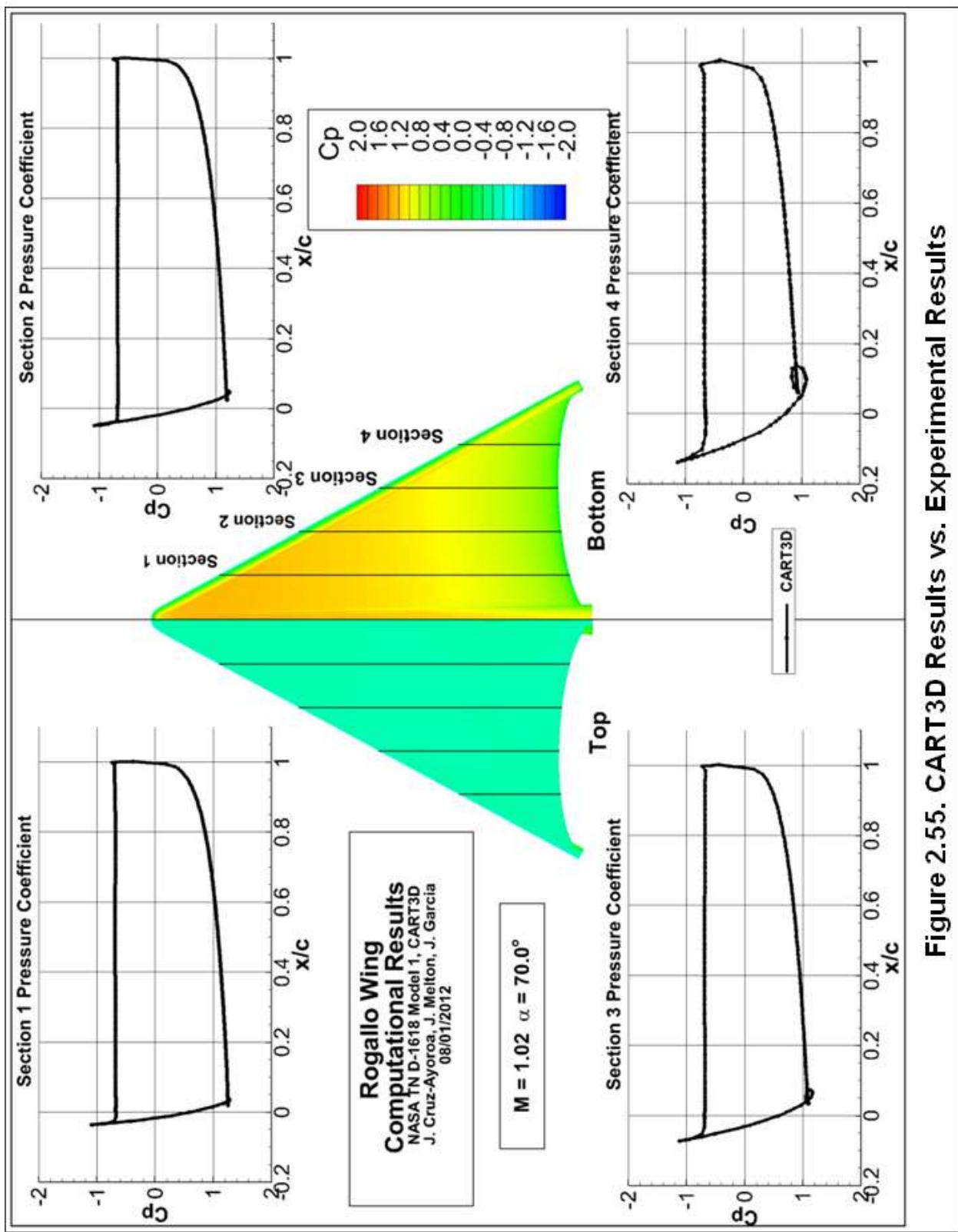


Figure 2.55. CART3D Results vs. Experimental Results

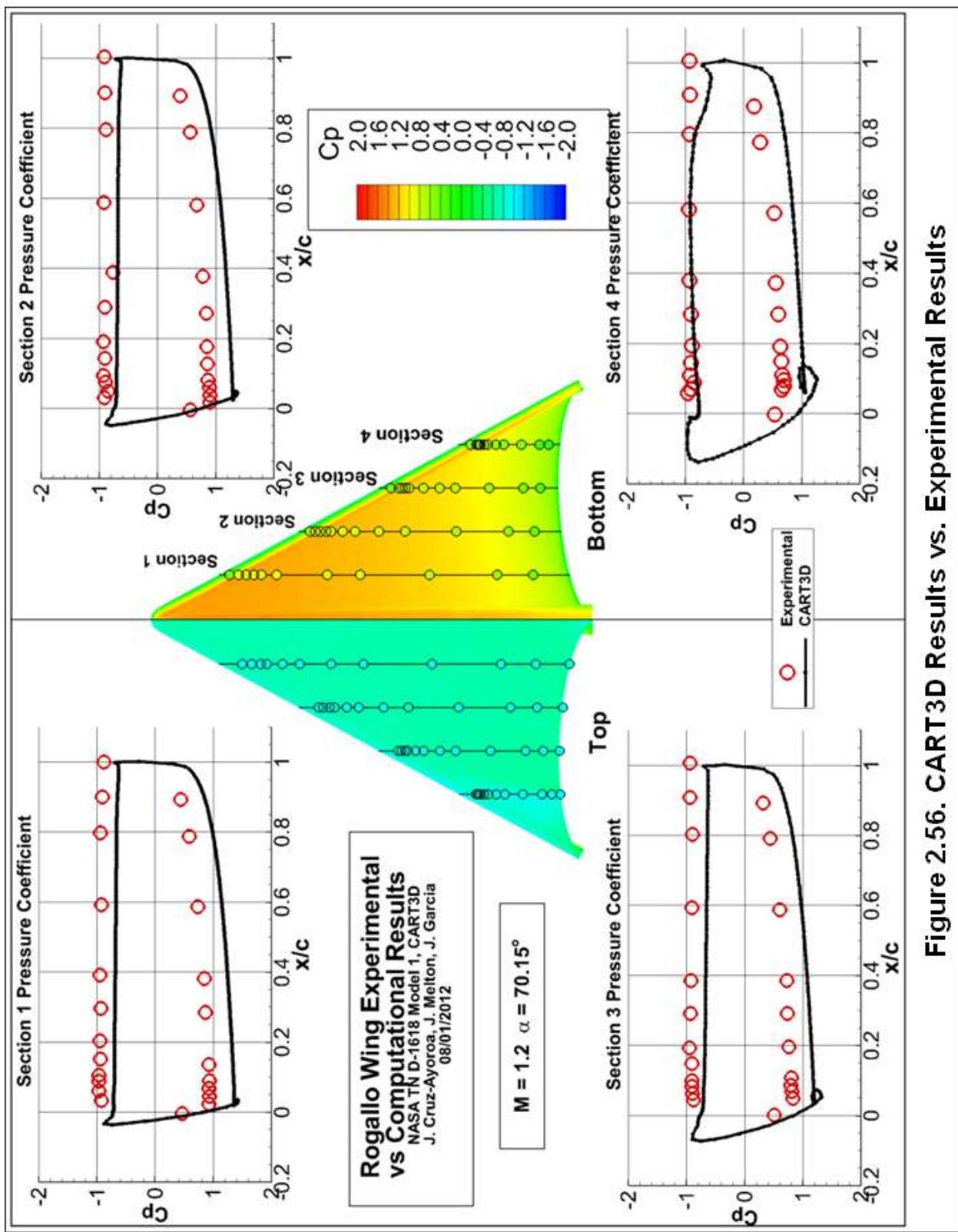


Figure 2.56. CART3D Results vs. Experimental Results

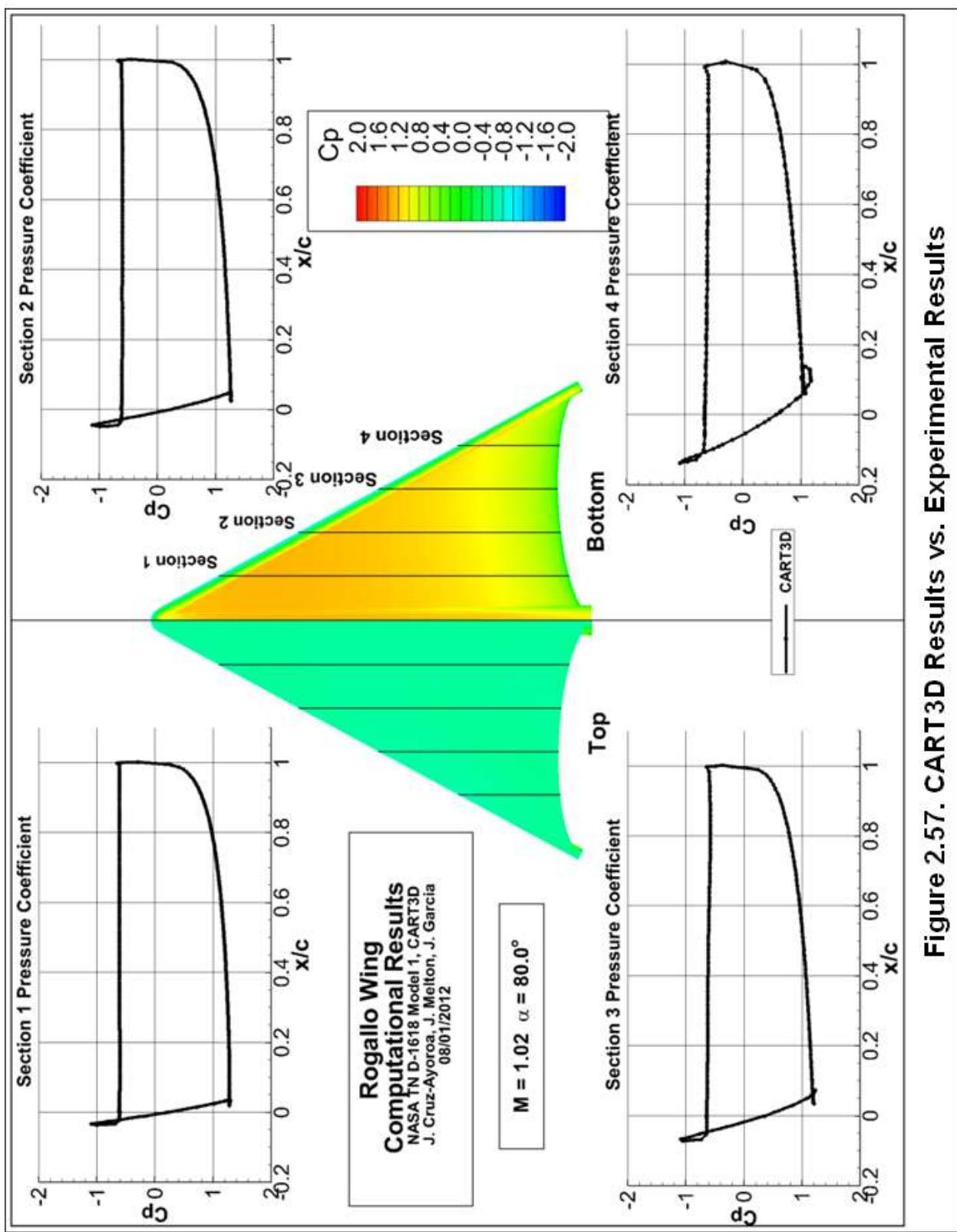


Figure 2.57. CART3D Results vs. Experimental Results

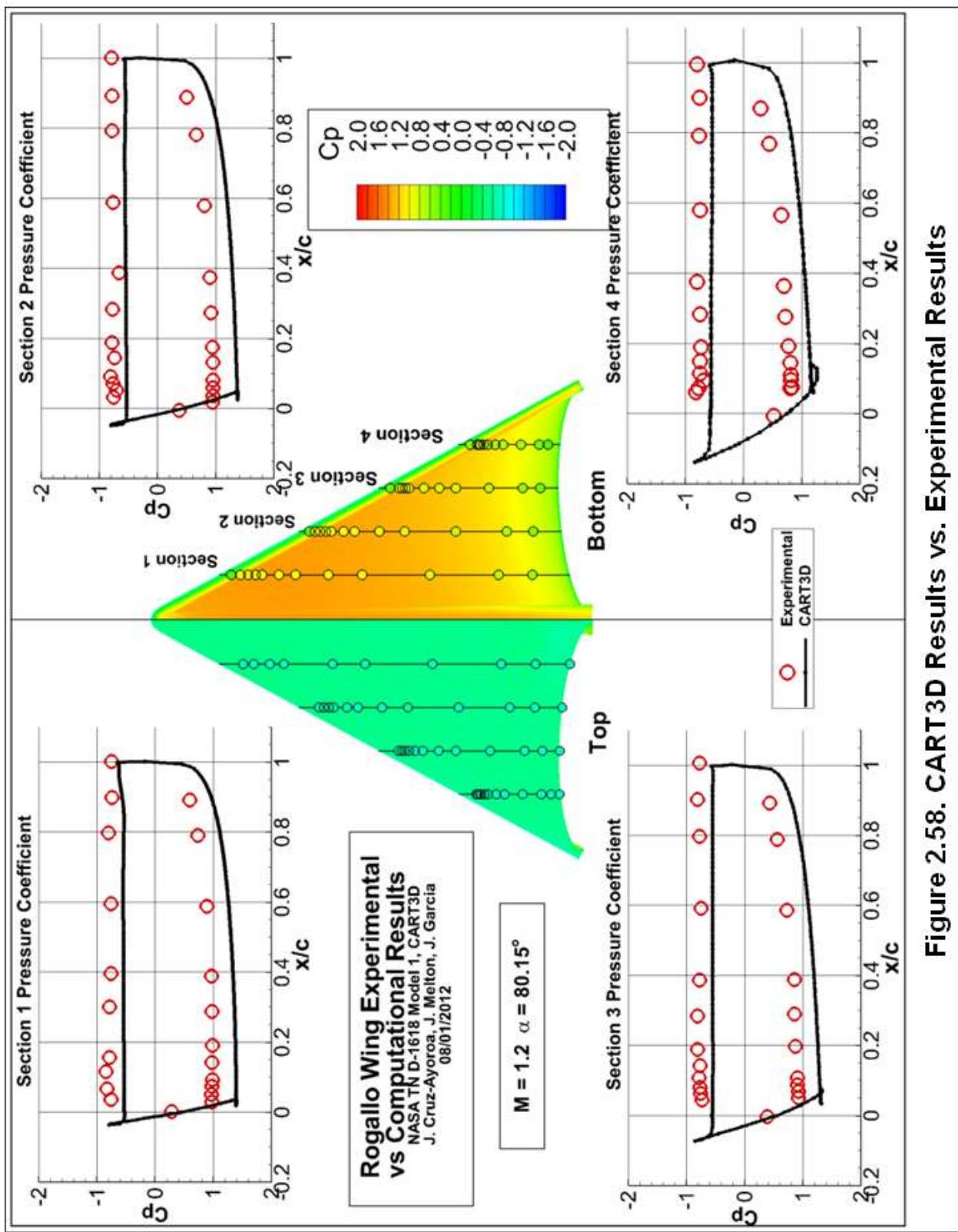


Figure 2.58. CART3D Results vs. Experimental Results

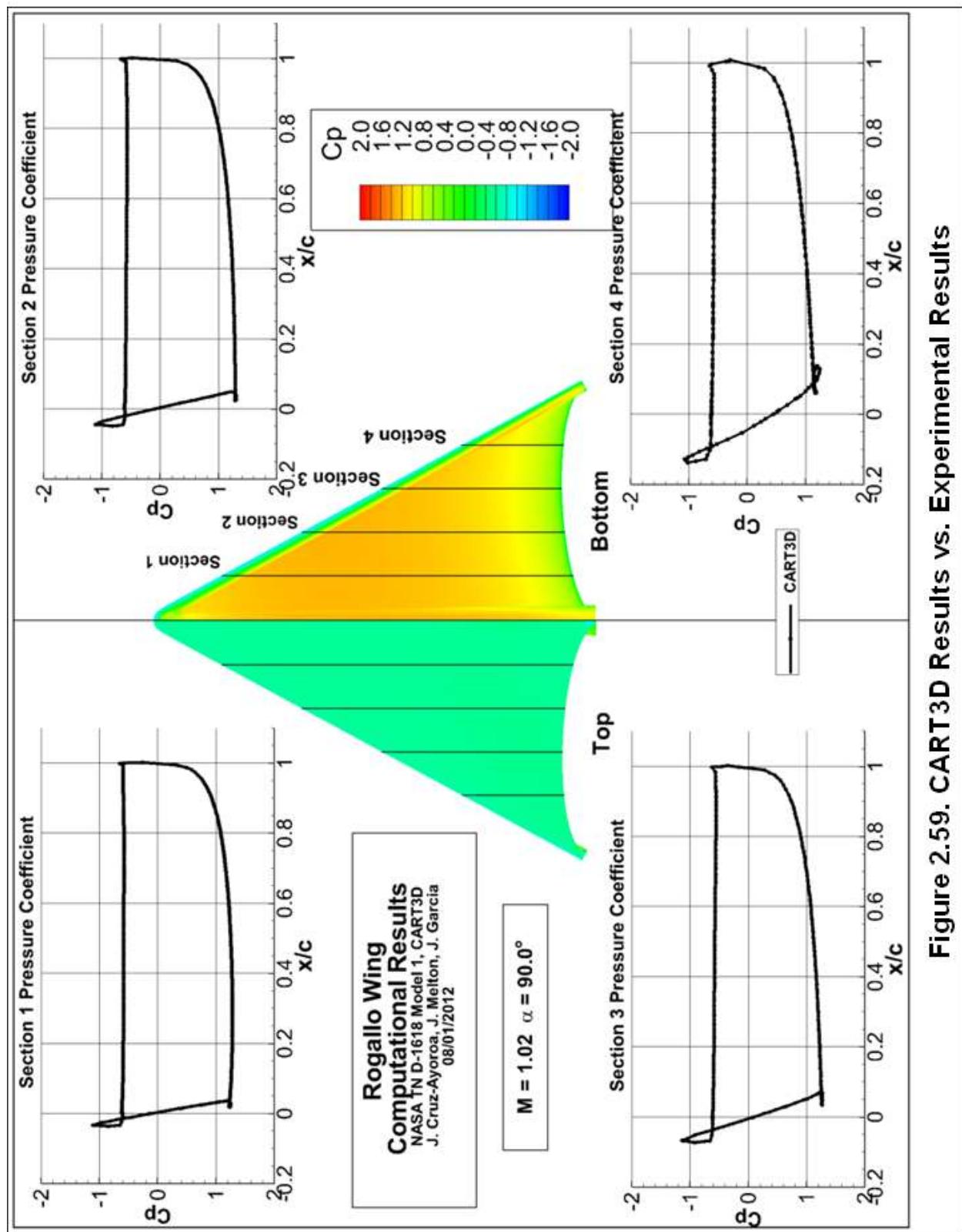


Figure 2.59. CART3D Results vs. Experimental Results

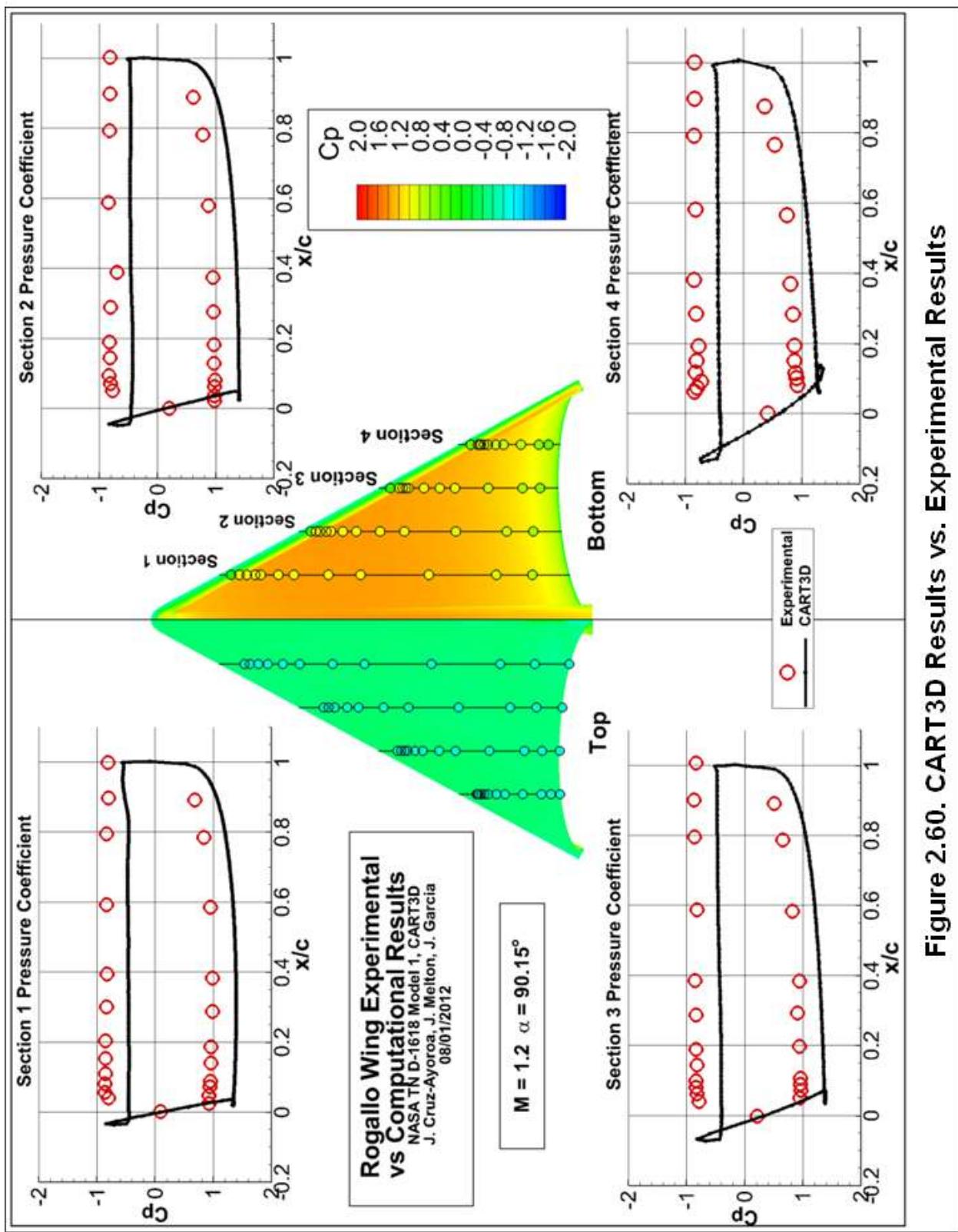


Figure 2.60. CART3D Results vs. Experimental Results

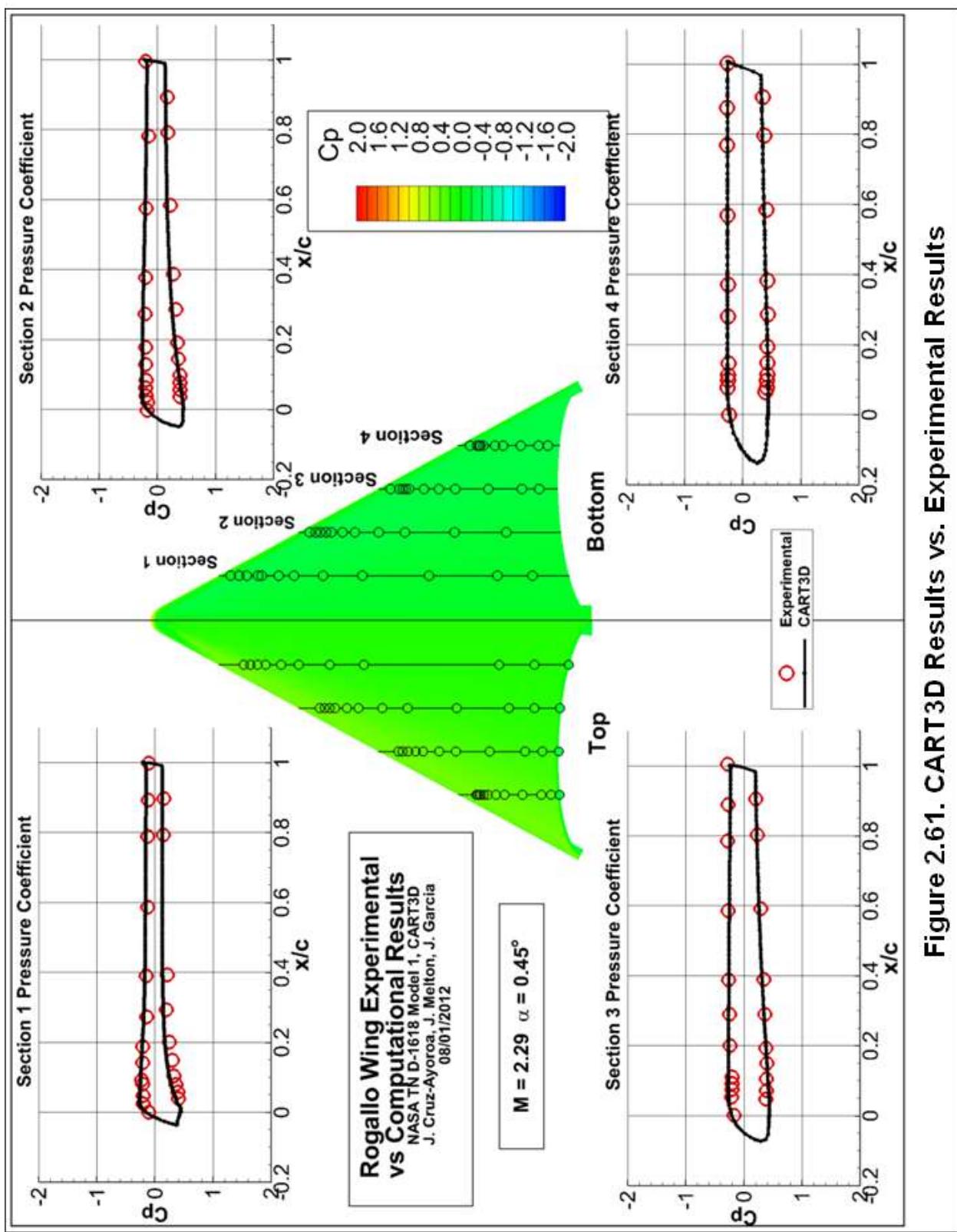


Figure 2.61. CART3D Results vs. Experimental Results

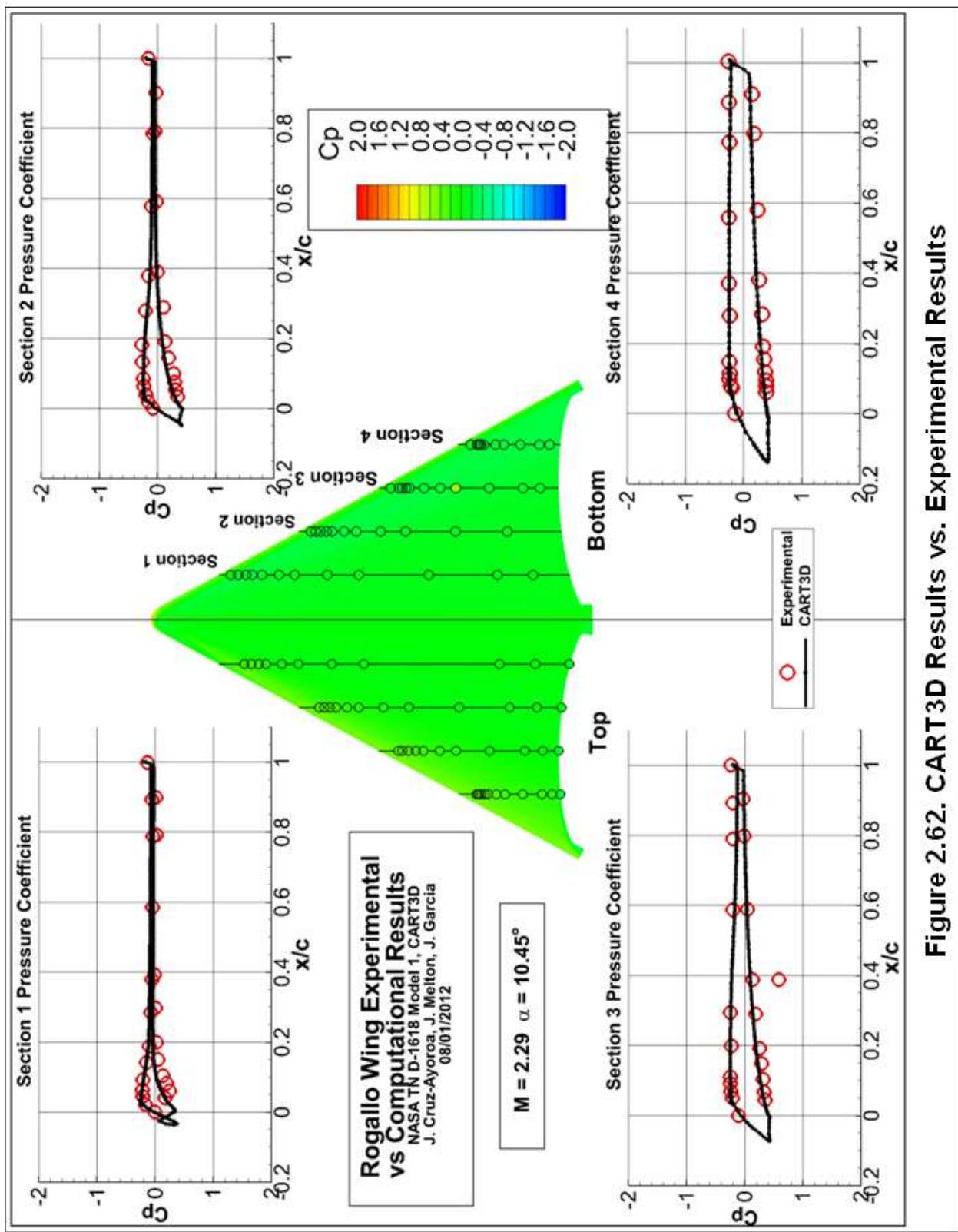


Figure 2.62. CART3D Results vs. Experimental Results

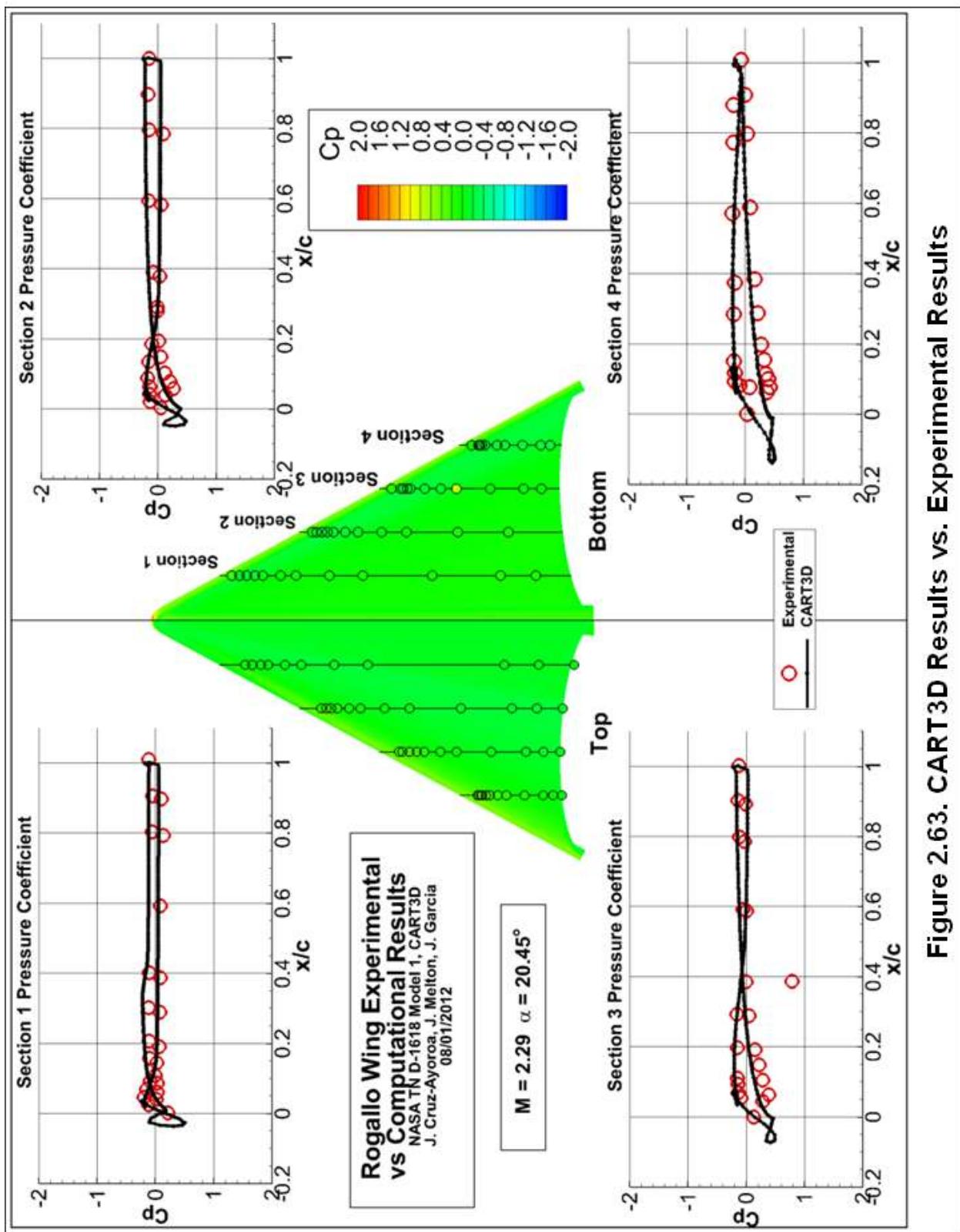


Figure 2.63. CART3D Results vs. Experimental Results

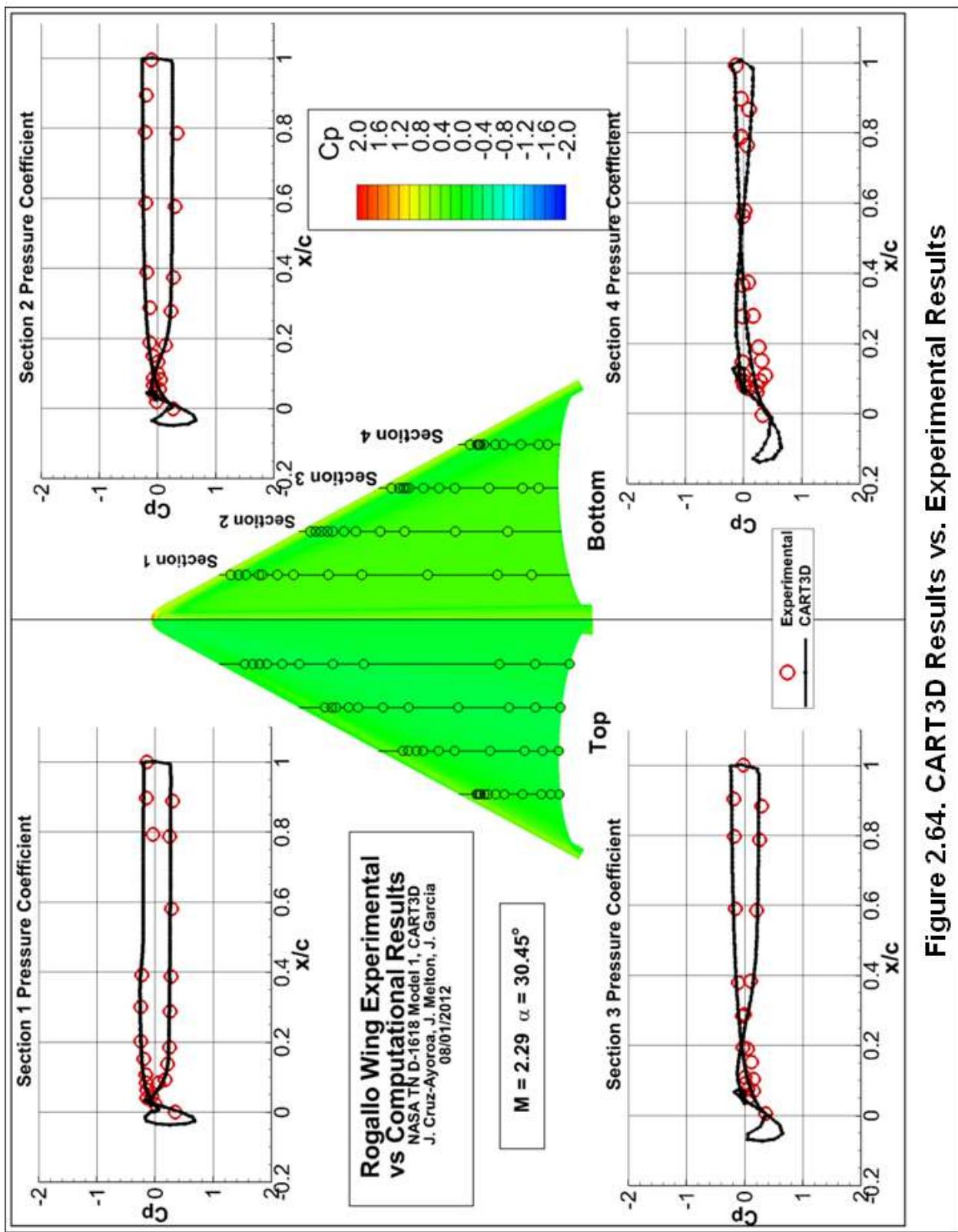


Figure 2.64. CART3D Results vs. Experimental Results

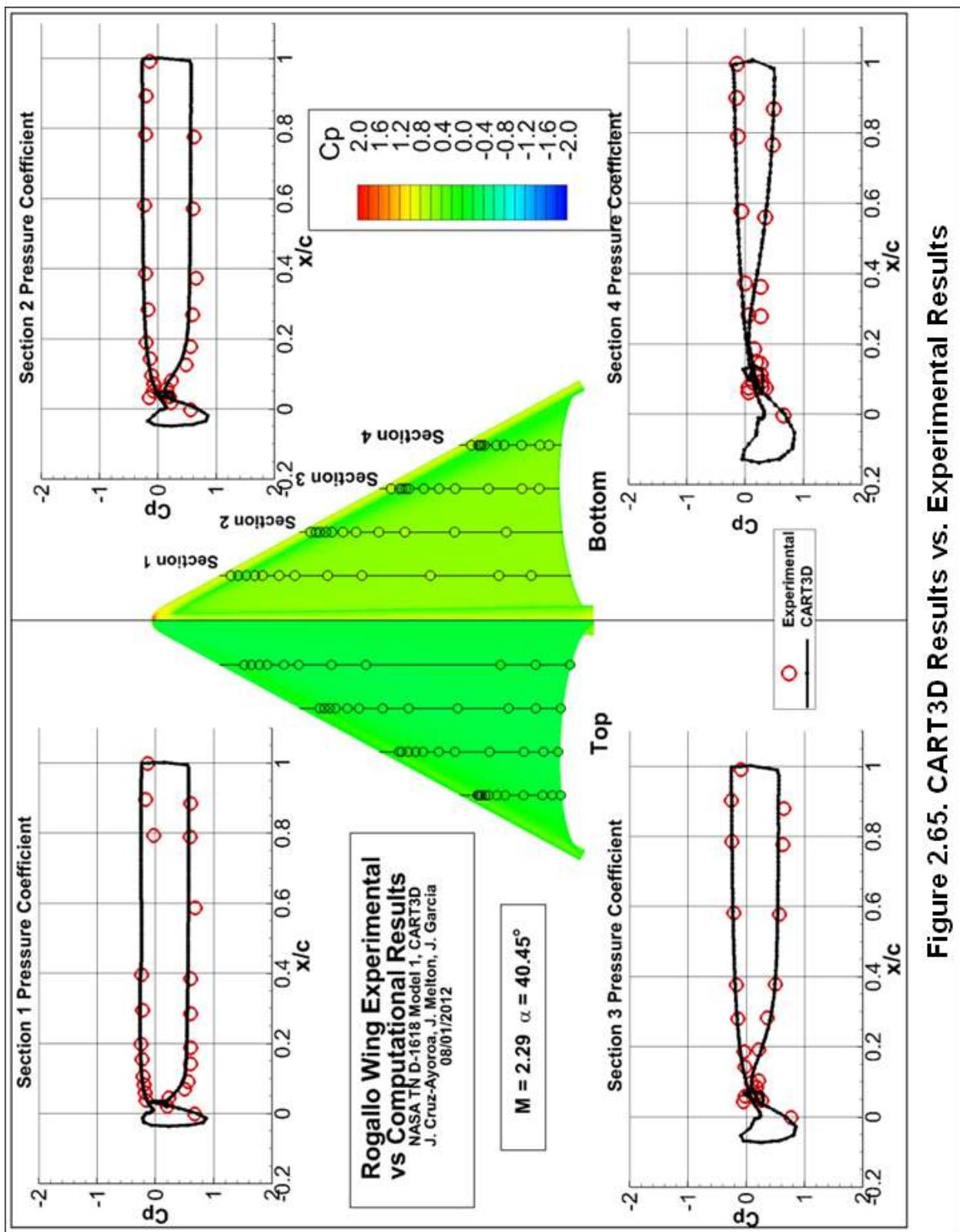


Figure 2.65. CART3D Results vs. Experimental Results

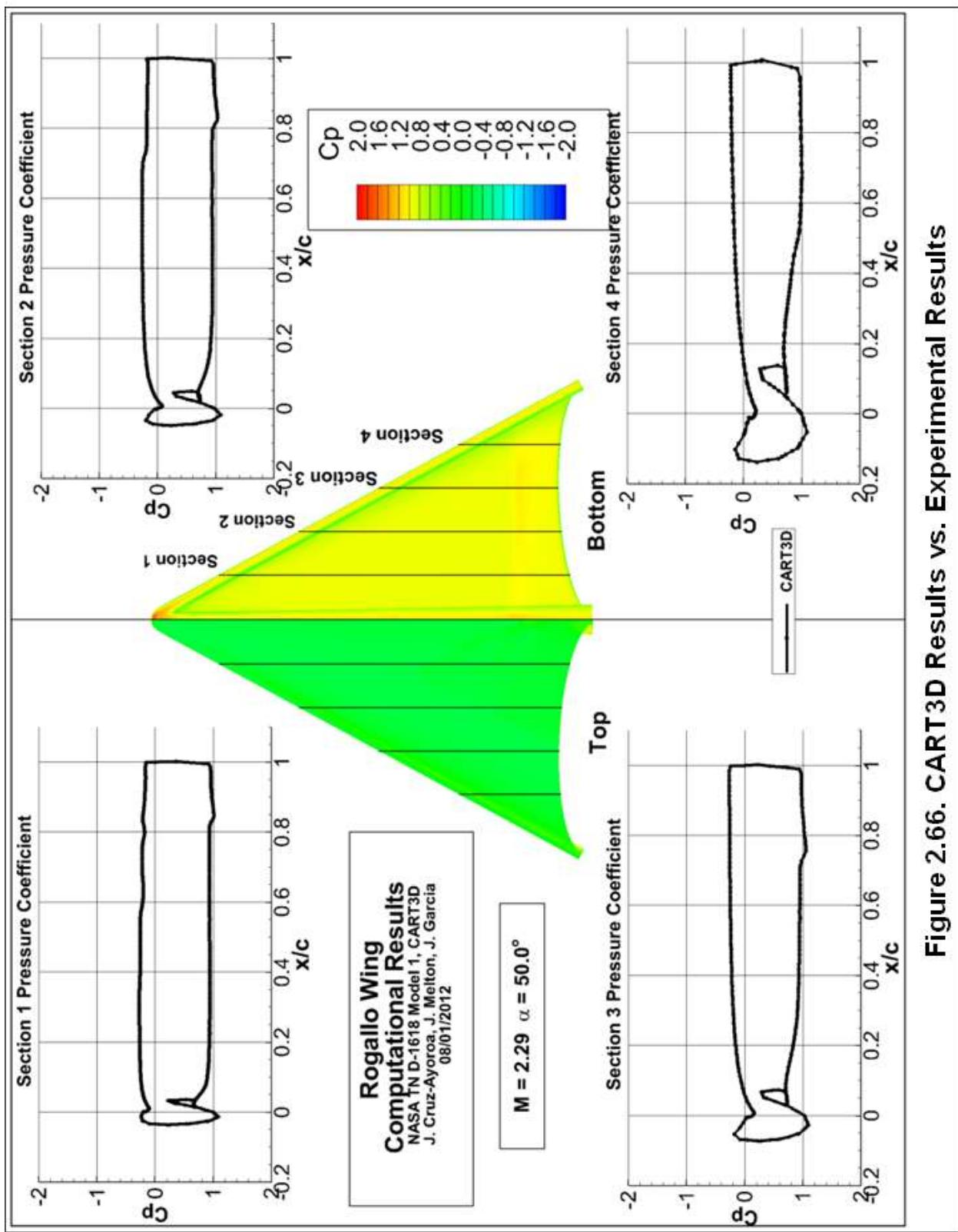


Figure 2.66. CART3D Results vs. Experimental Results

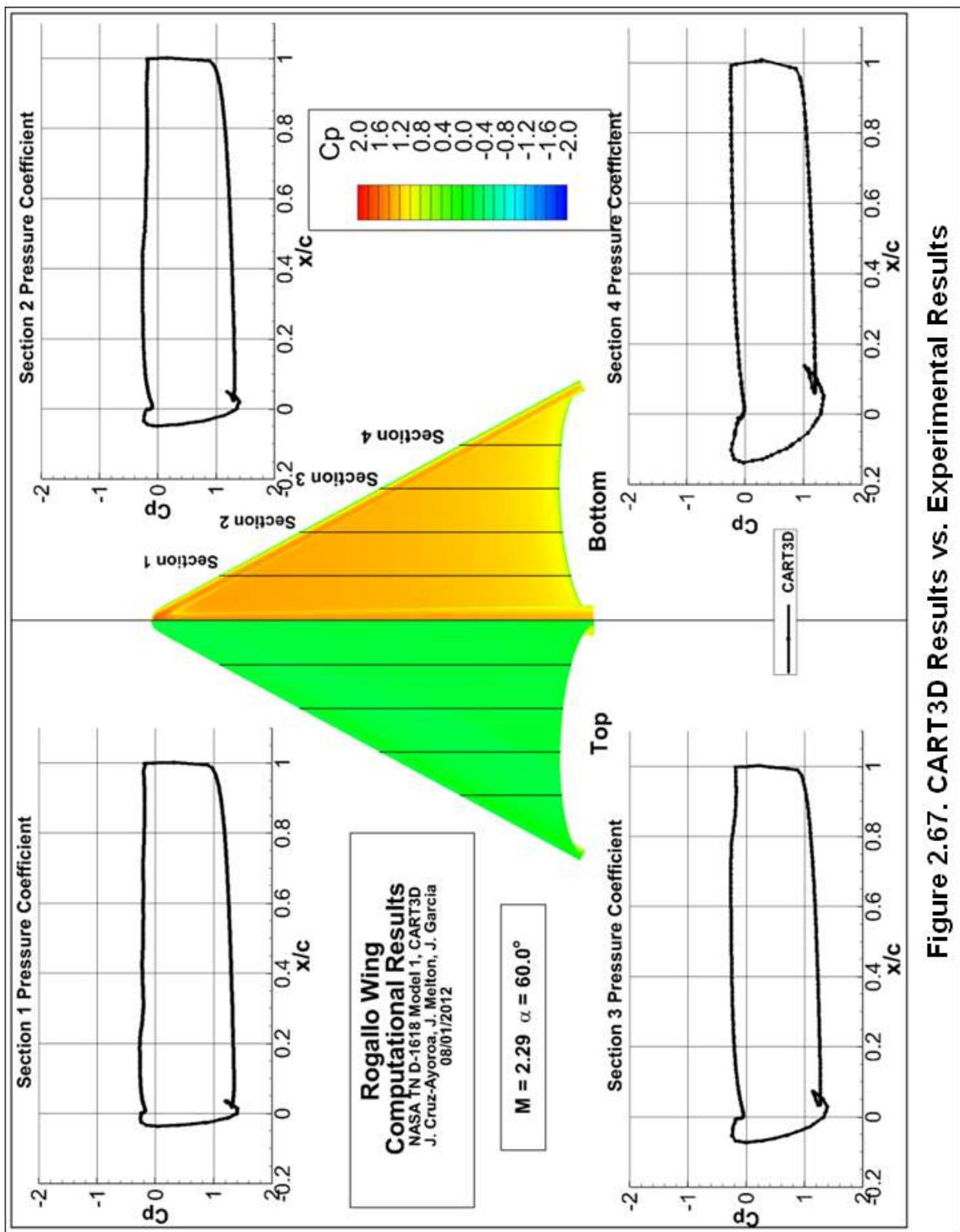


Figure 2.67. CART3D Results vs. Experimental Results

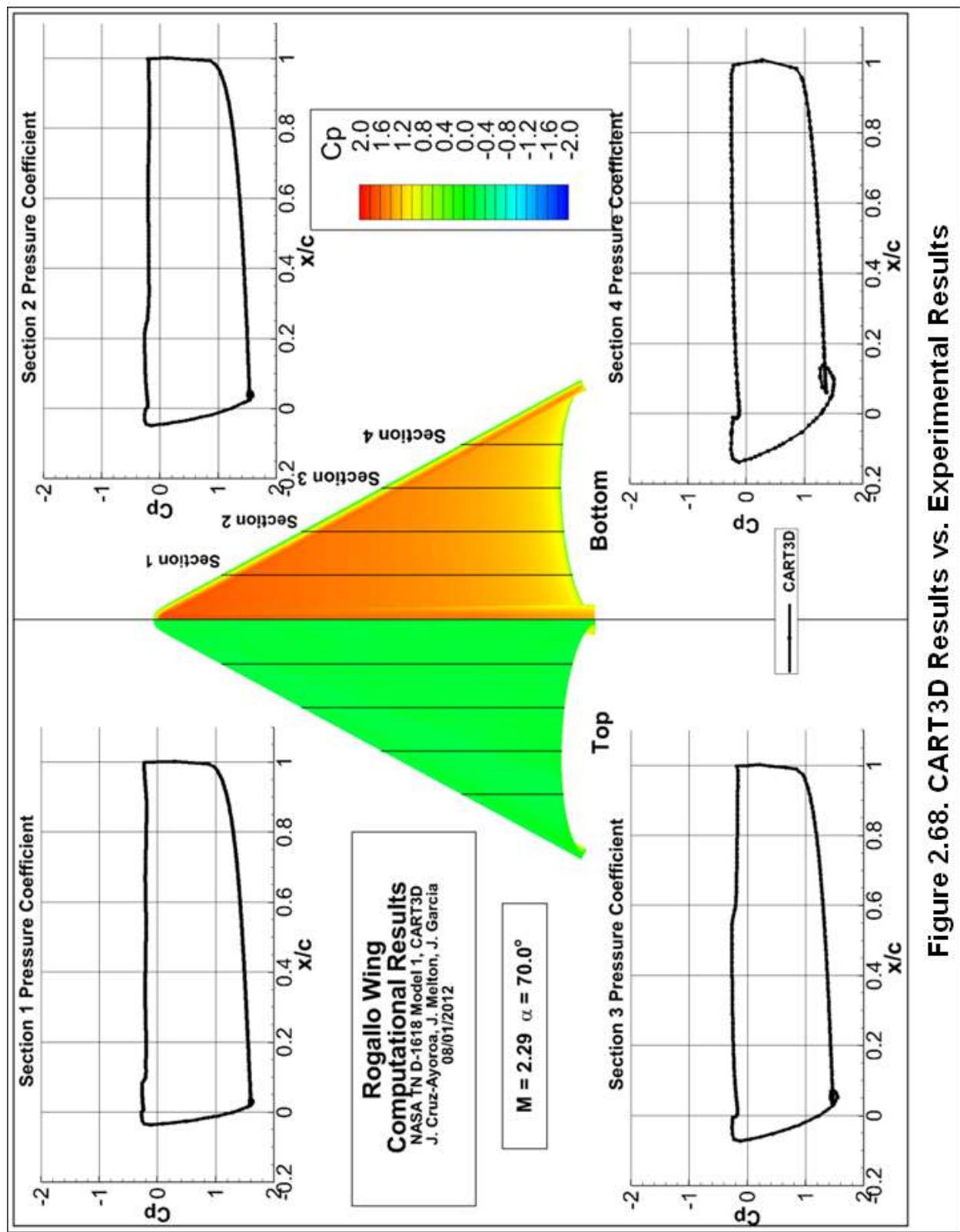


Figure 2.68. CART3D Results vs. Experimental Results

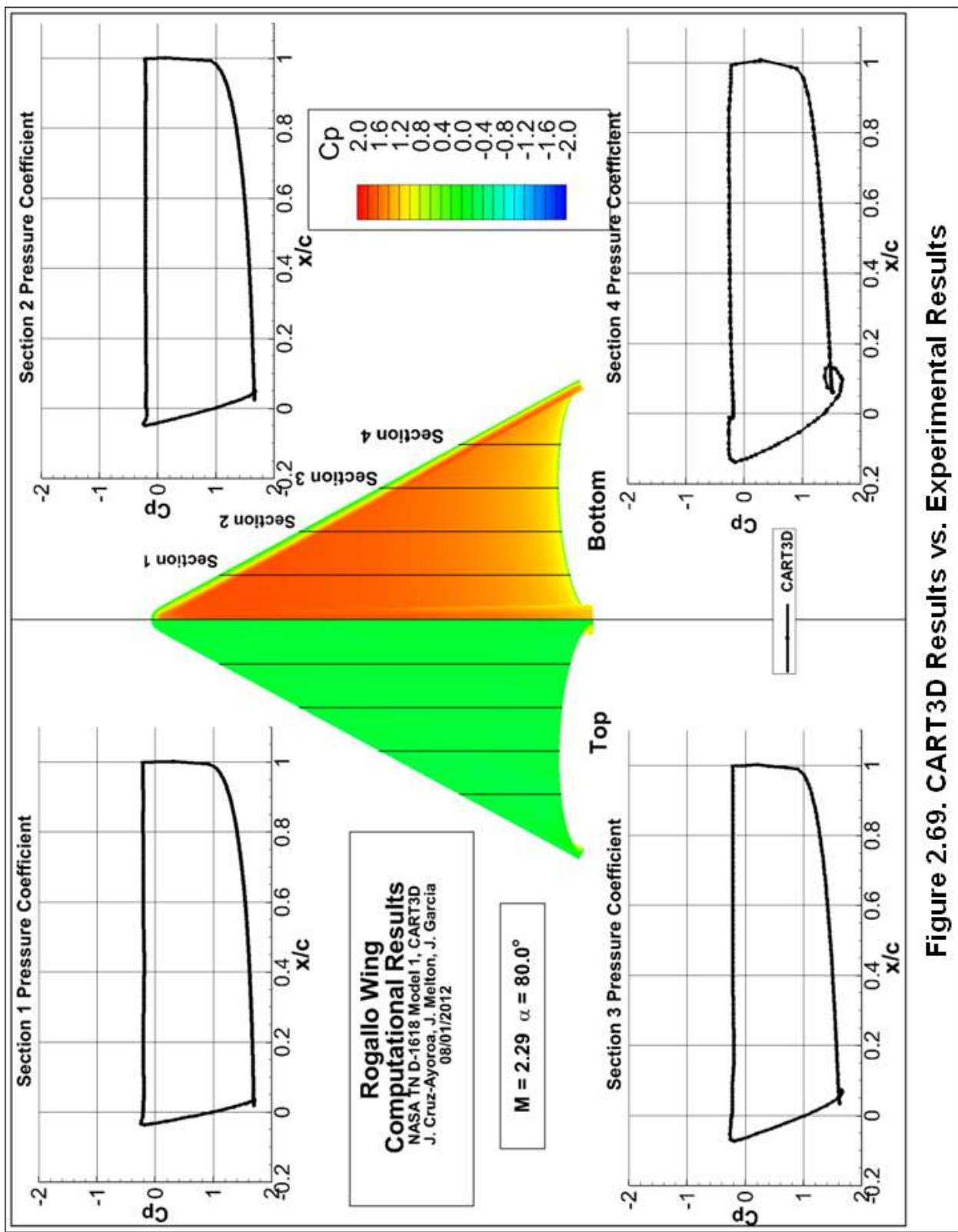


Figure 2.69. CART3D Results vs. Experimental Results

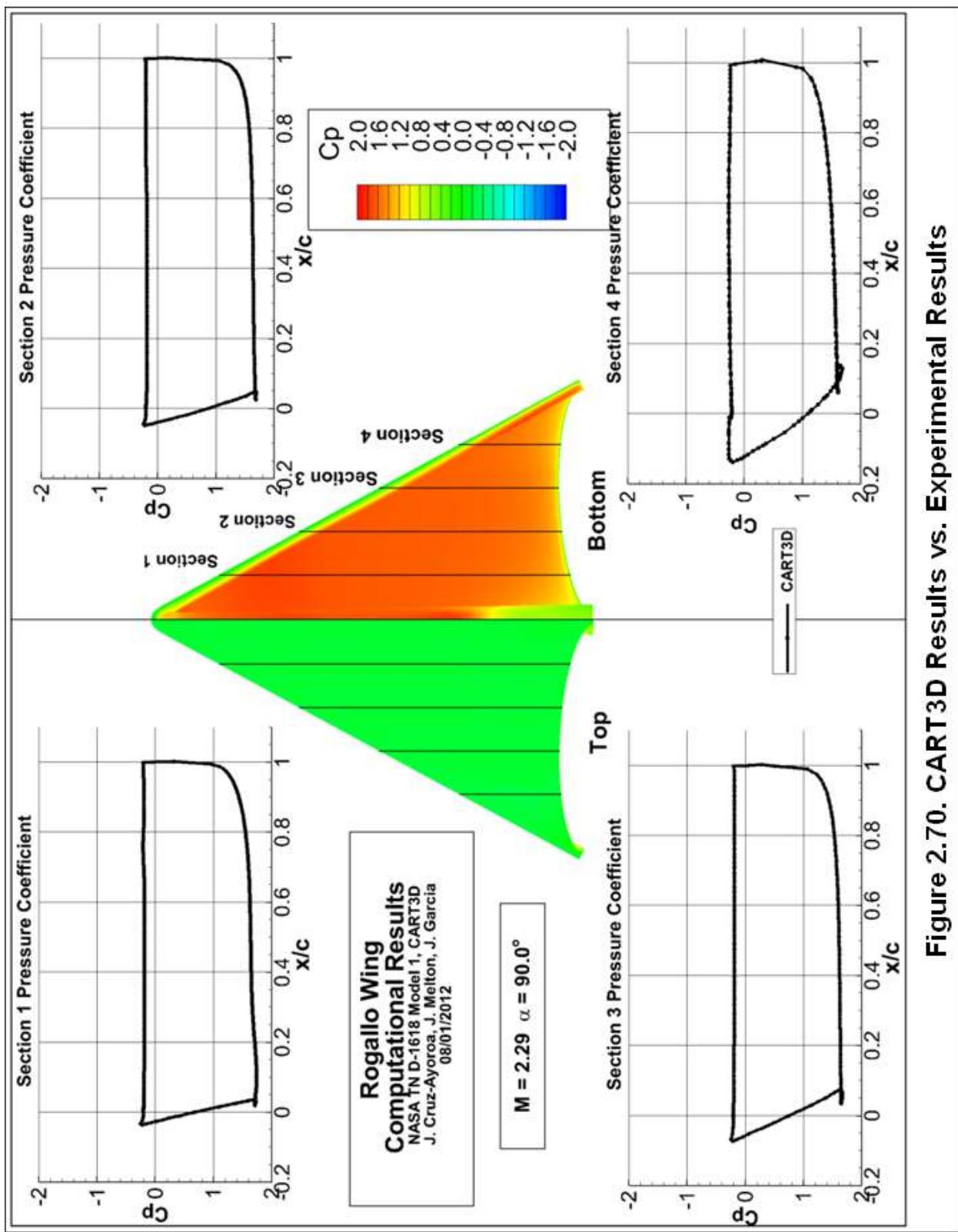


Figure 2.70. CART3D Results vs. Experimental Results

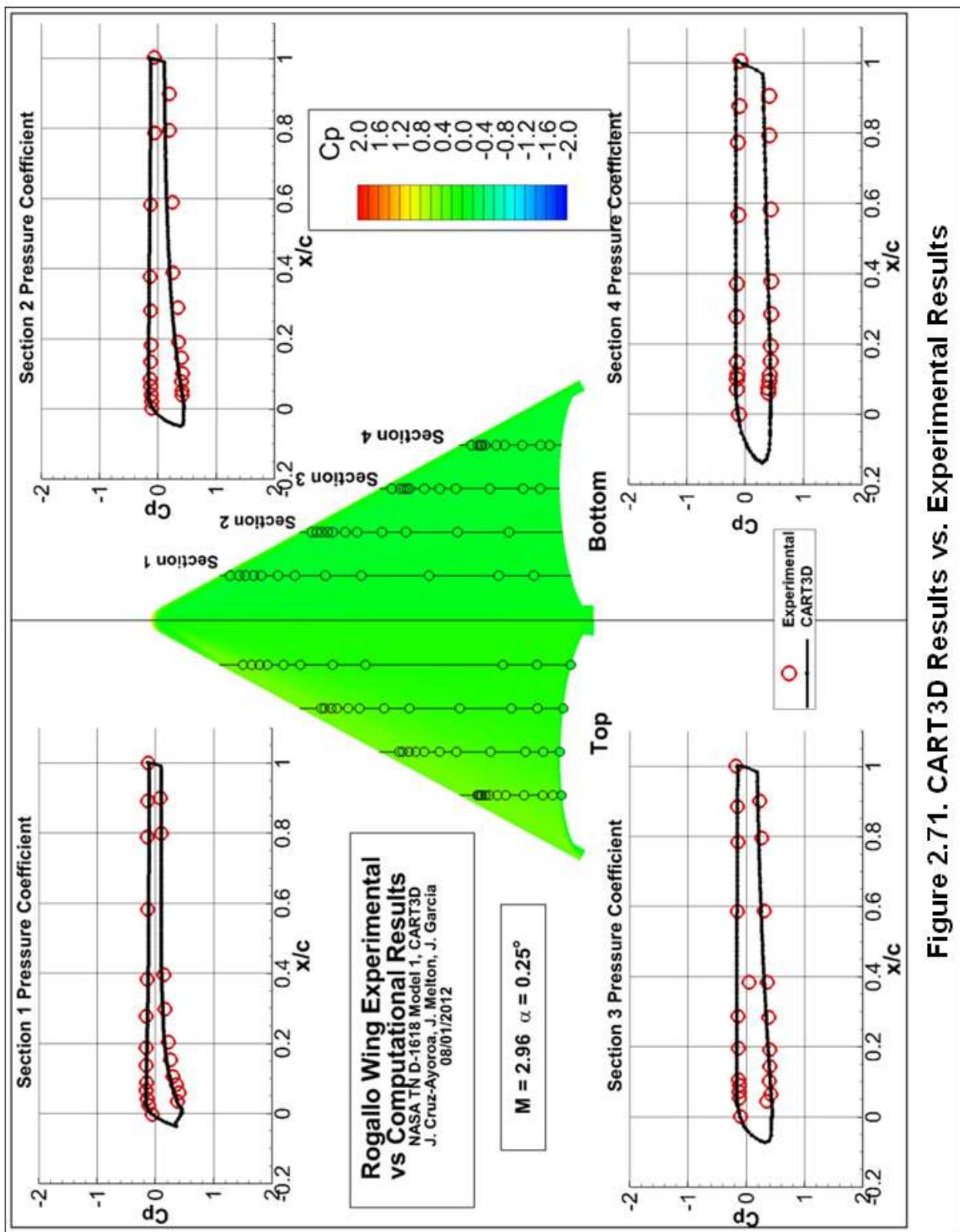


Figure 2.71. CART3D Results vs. Experimental Results

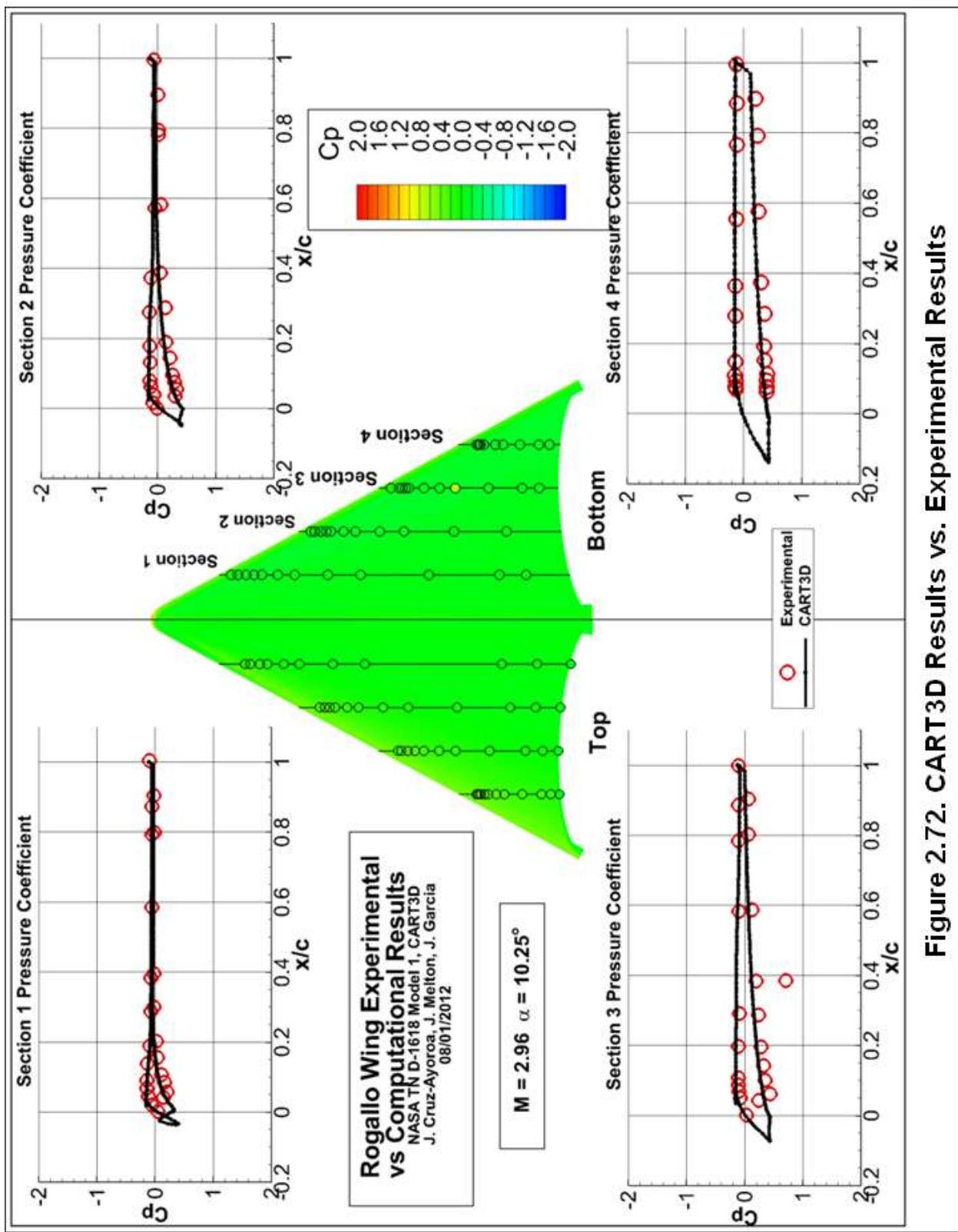


Figure 2.72. CART3D Results vs. Experimental Results

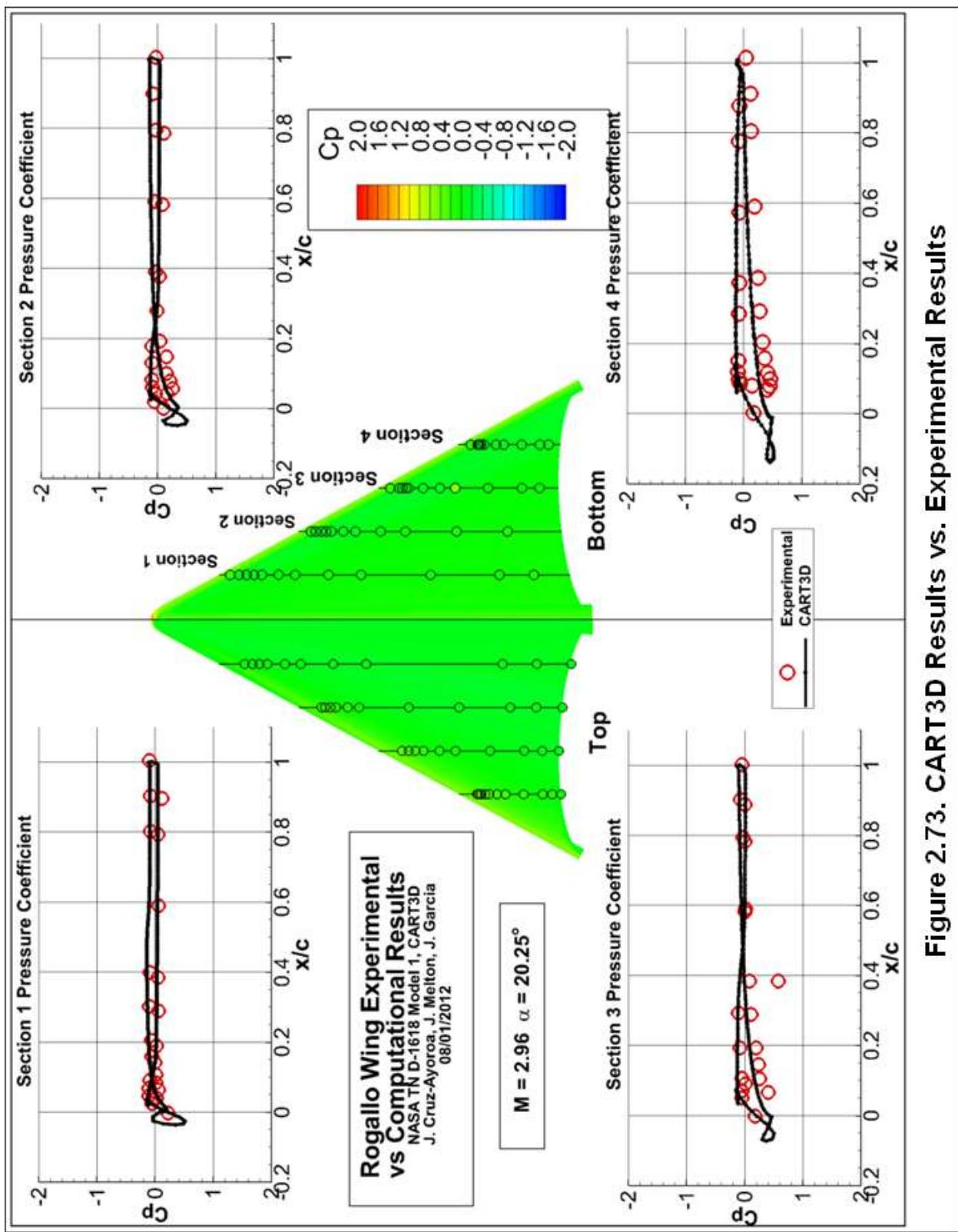


Figure 2.73. CART3D Results vs. Experimental Results

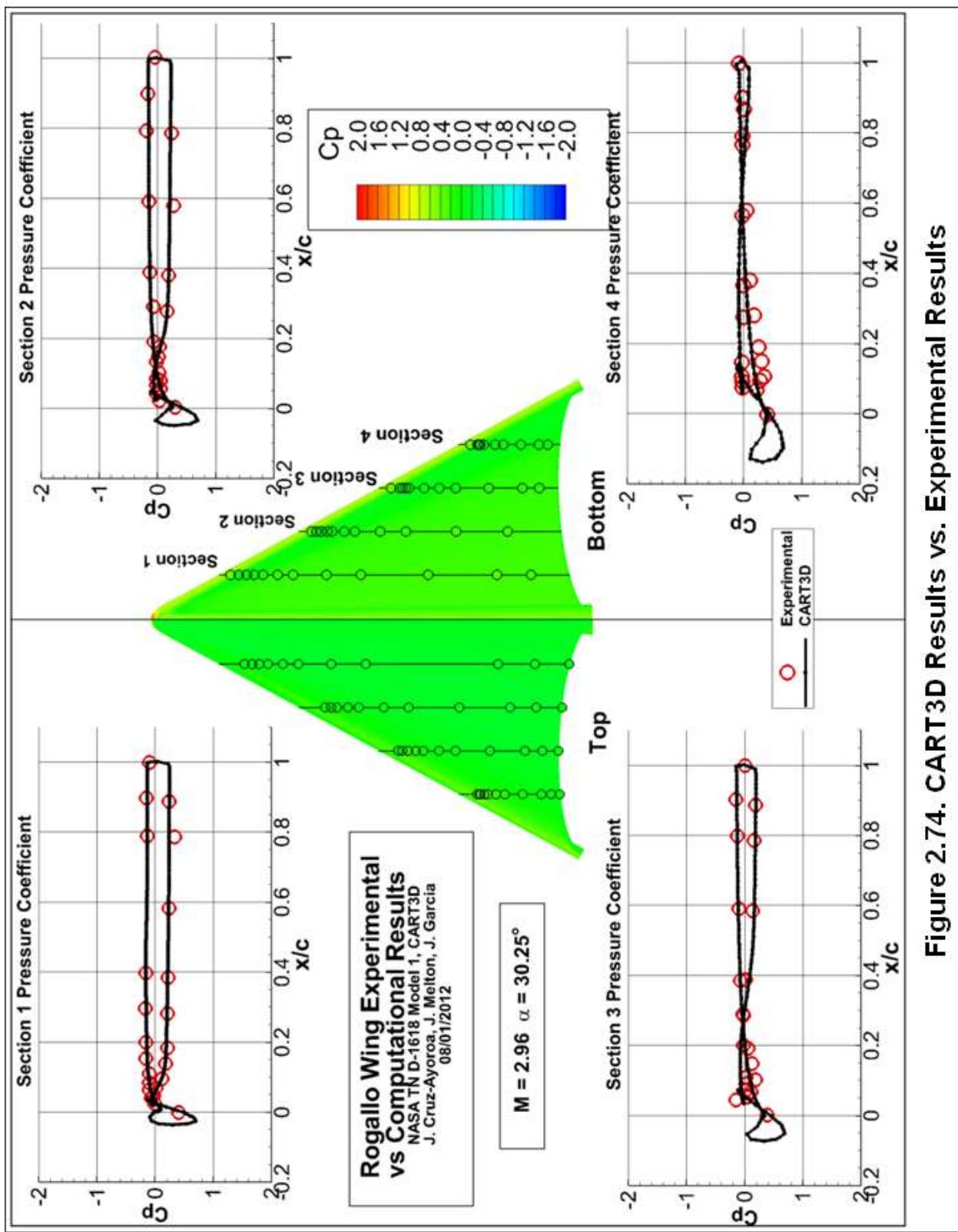


Figure 2.74. CART3D Results vs. Experimental Results

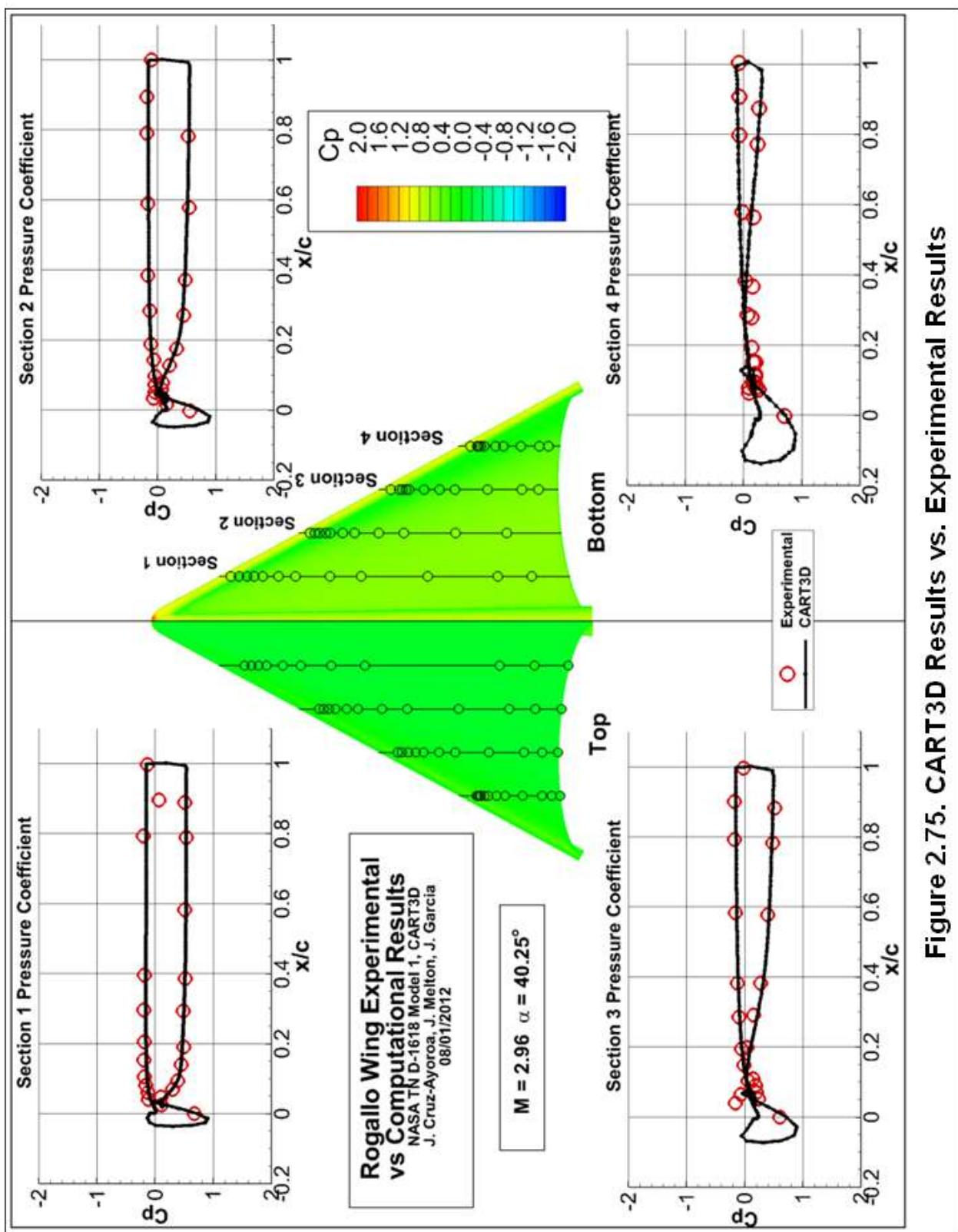


Figure 2.75. CART3D Results vs. Experimental Results

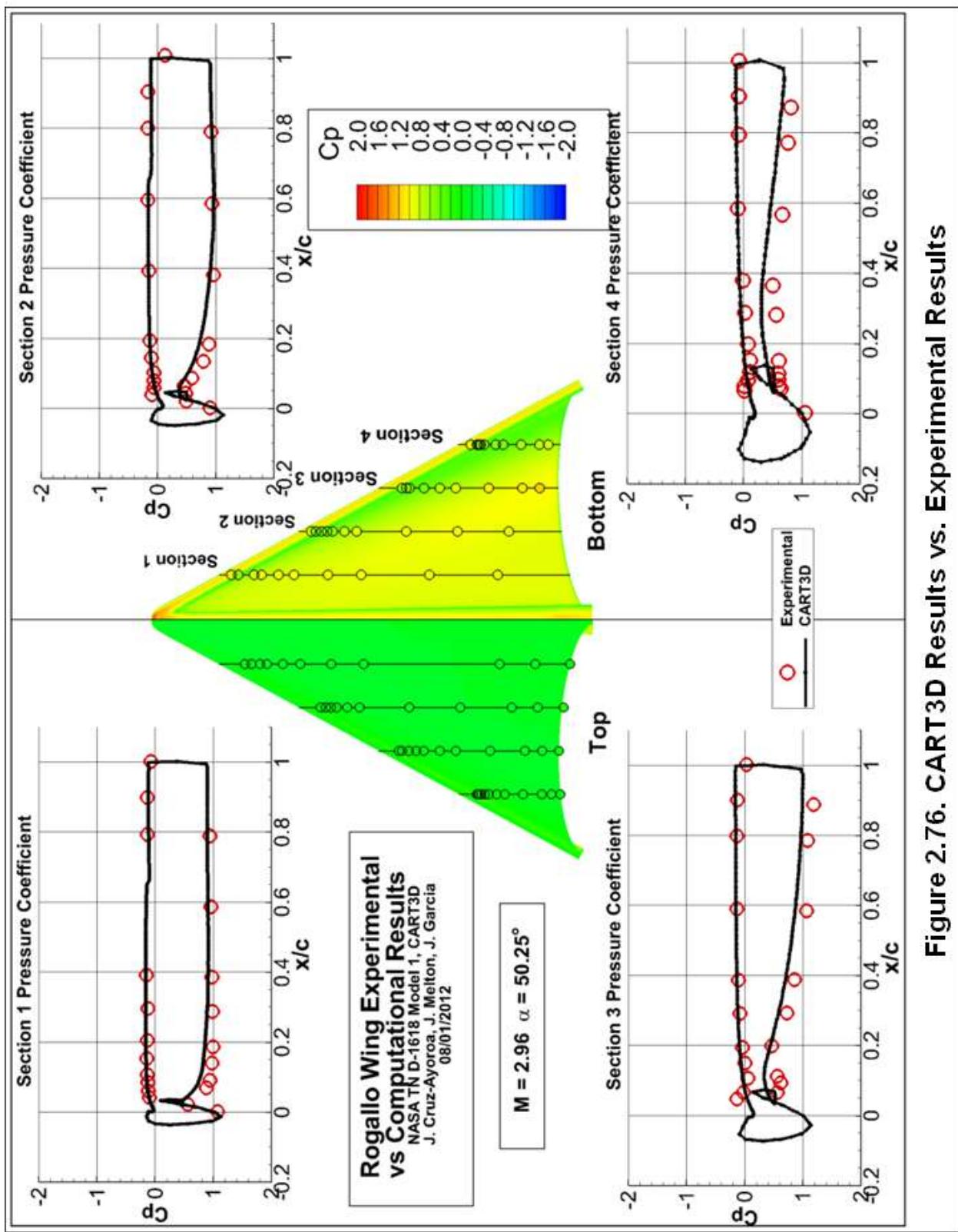


Figure 2.76. CART3D Results vs. Experimental Results

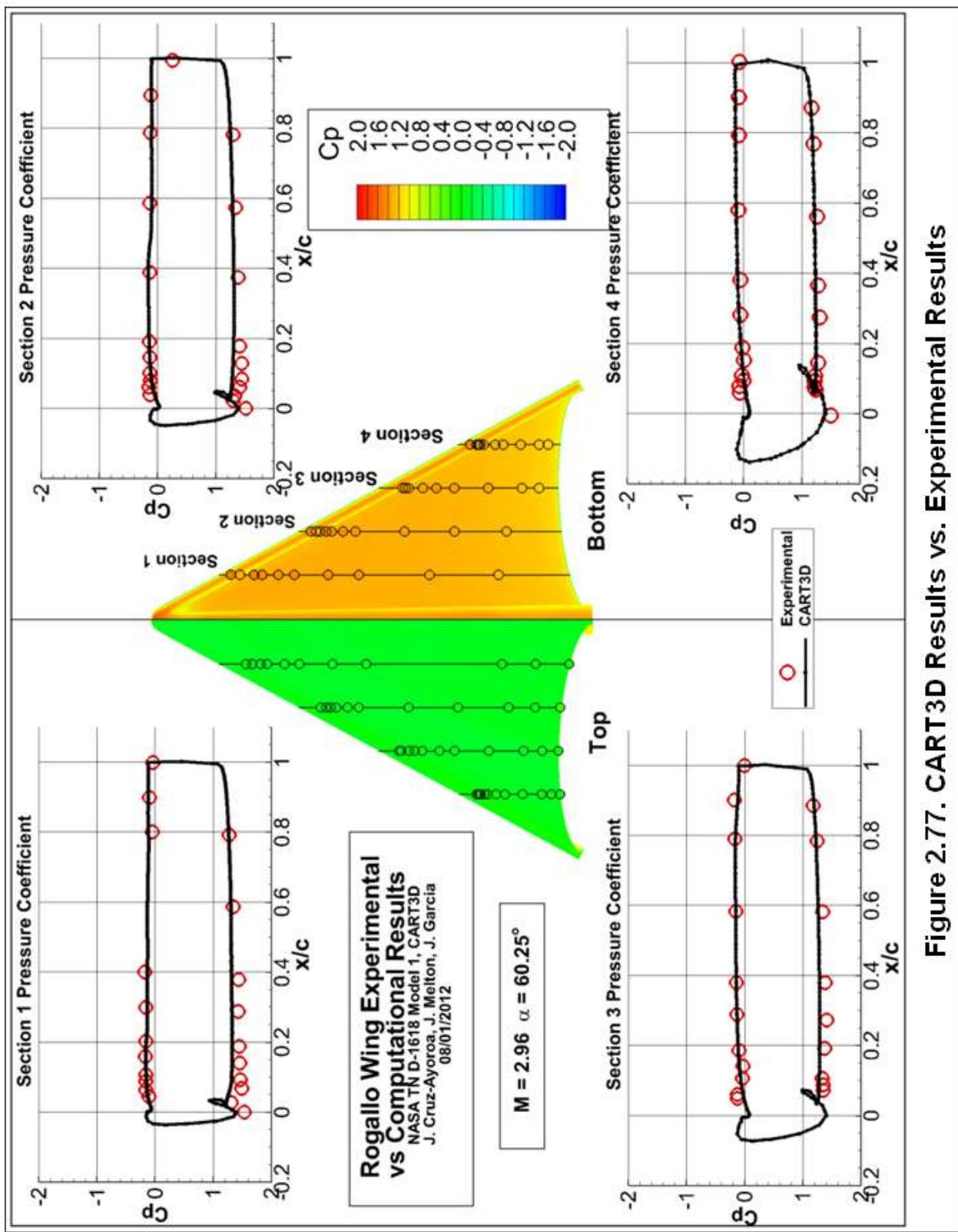


Figure 2.77. CART3D Results vs. Experimental Results

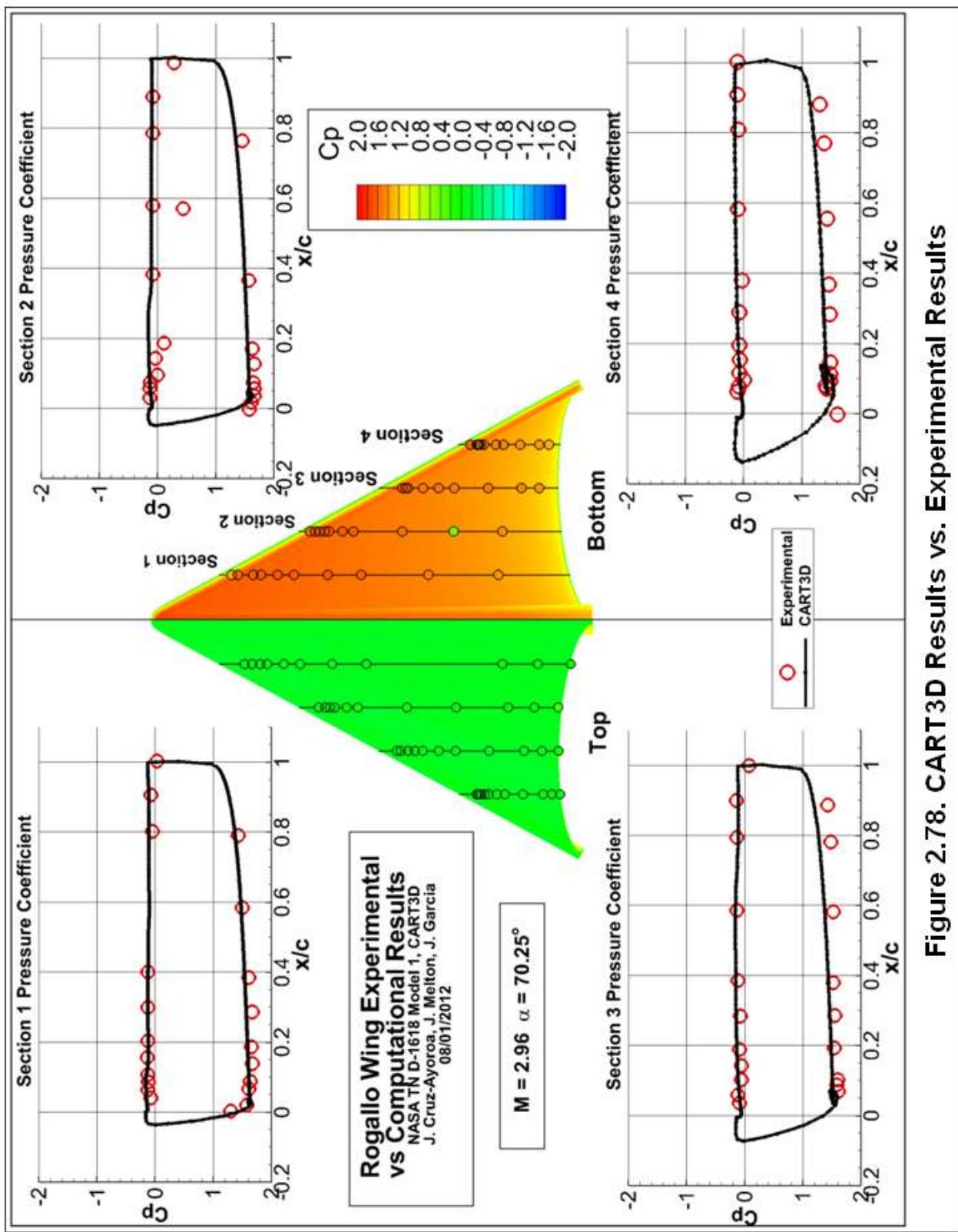


Figure 2.78. CART3D Results vs. Experimental Results

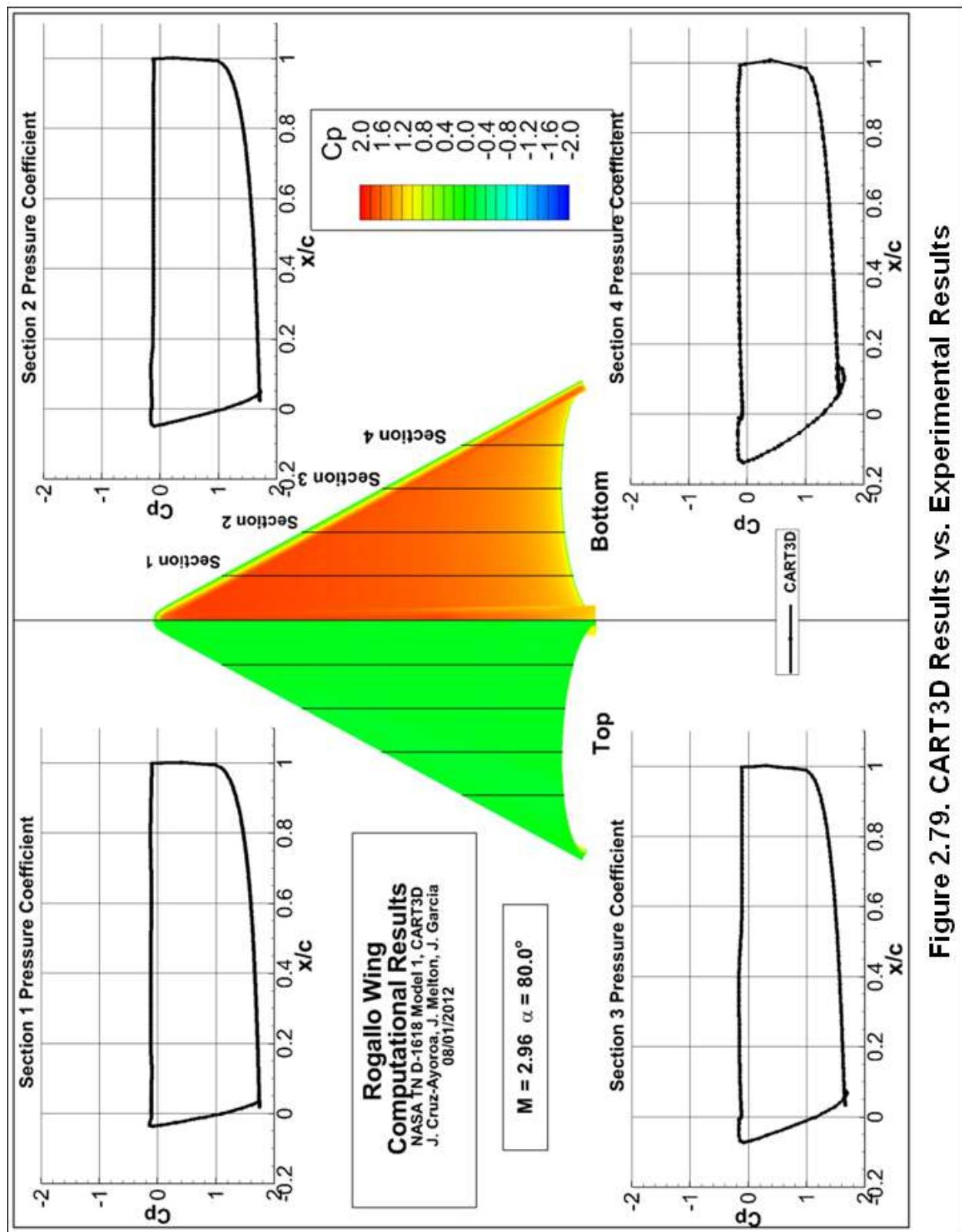


Figure 2.79. CART3D Results vs. Experimental Results

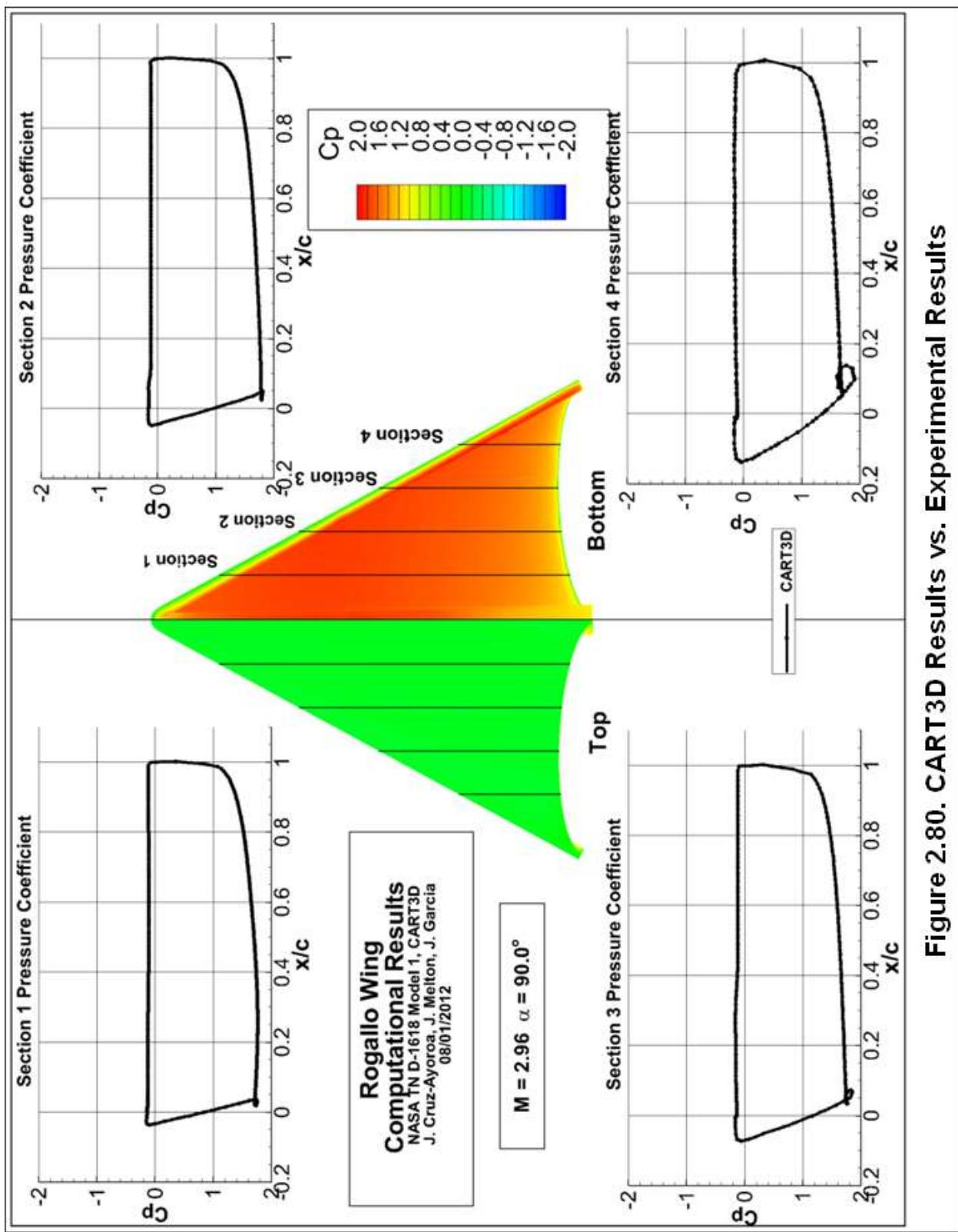


Figure 2.80. CART3D Results vs. Experimental Results

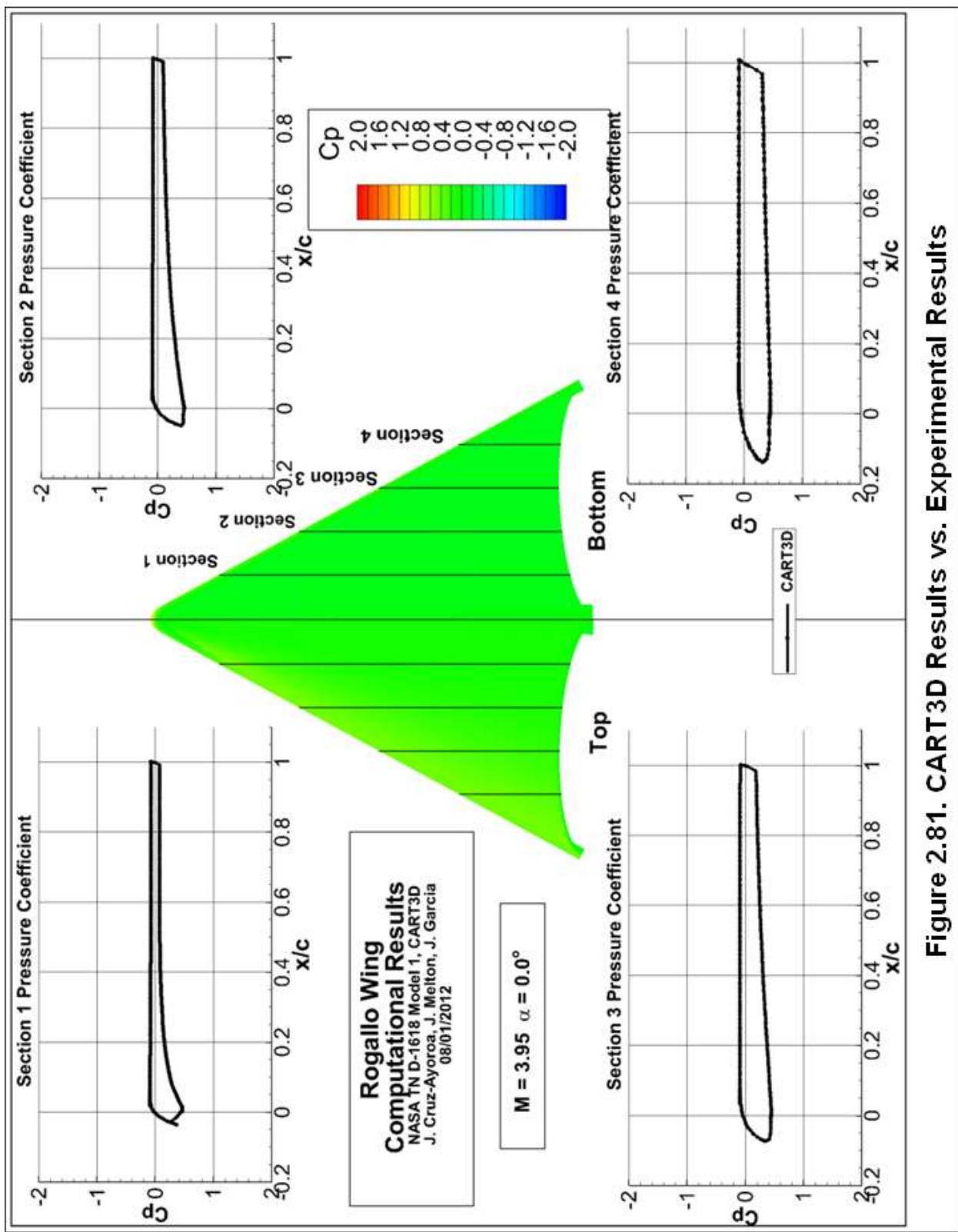


Figure 2.81. CART3D Results vs. Experimental Results

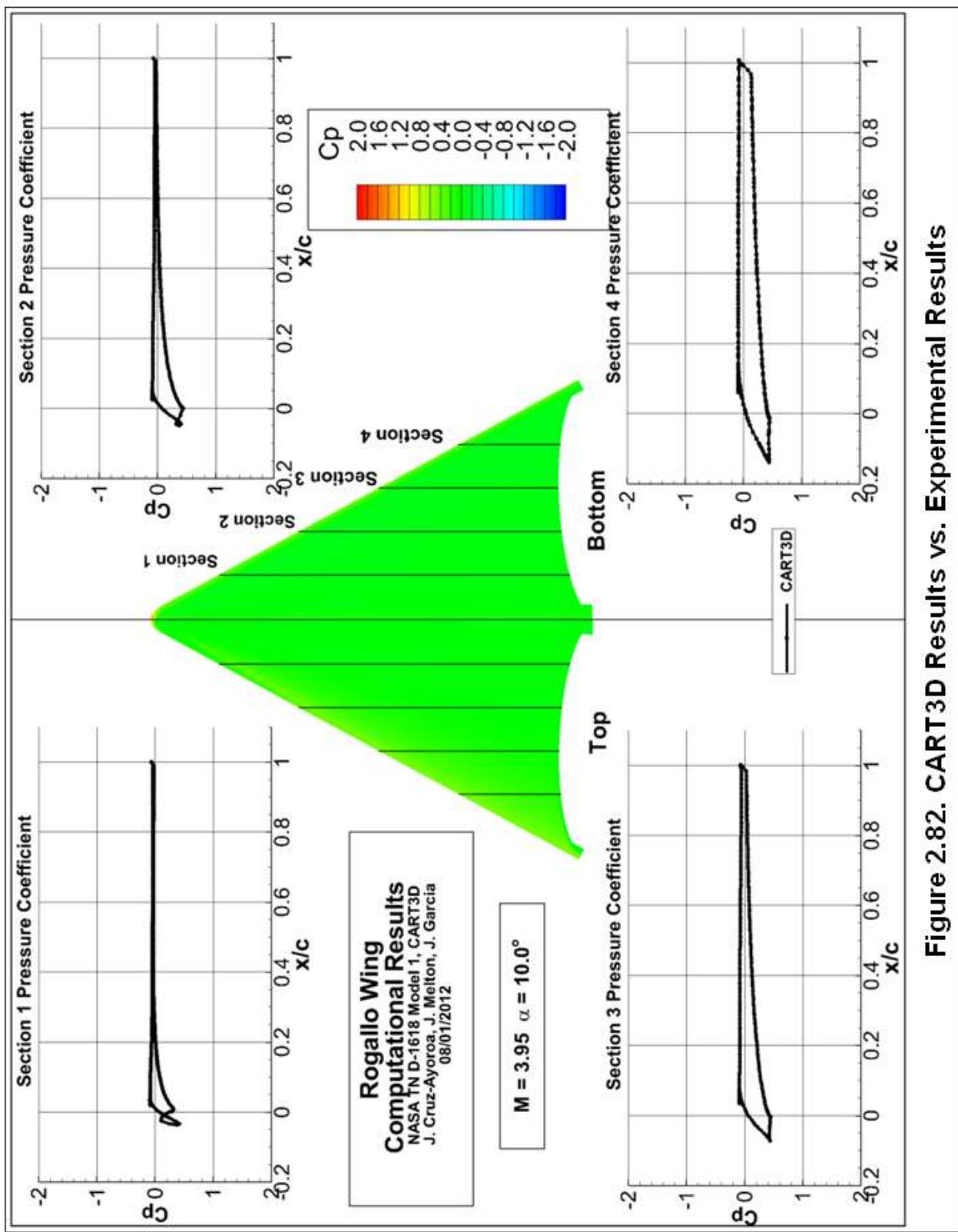


Figure 2.82. CART3D Results vs. Experimental Results

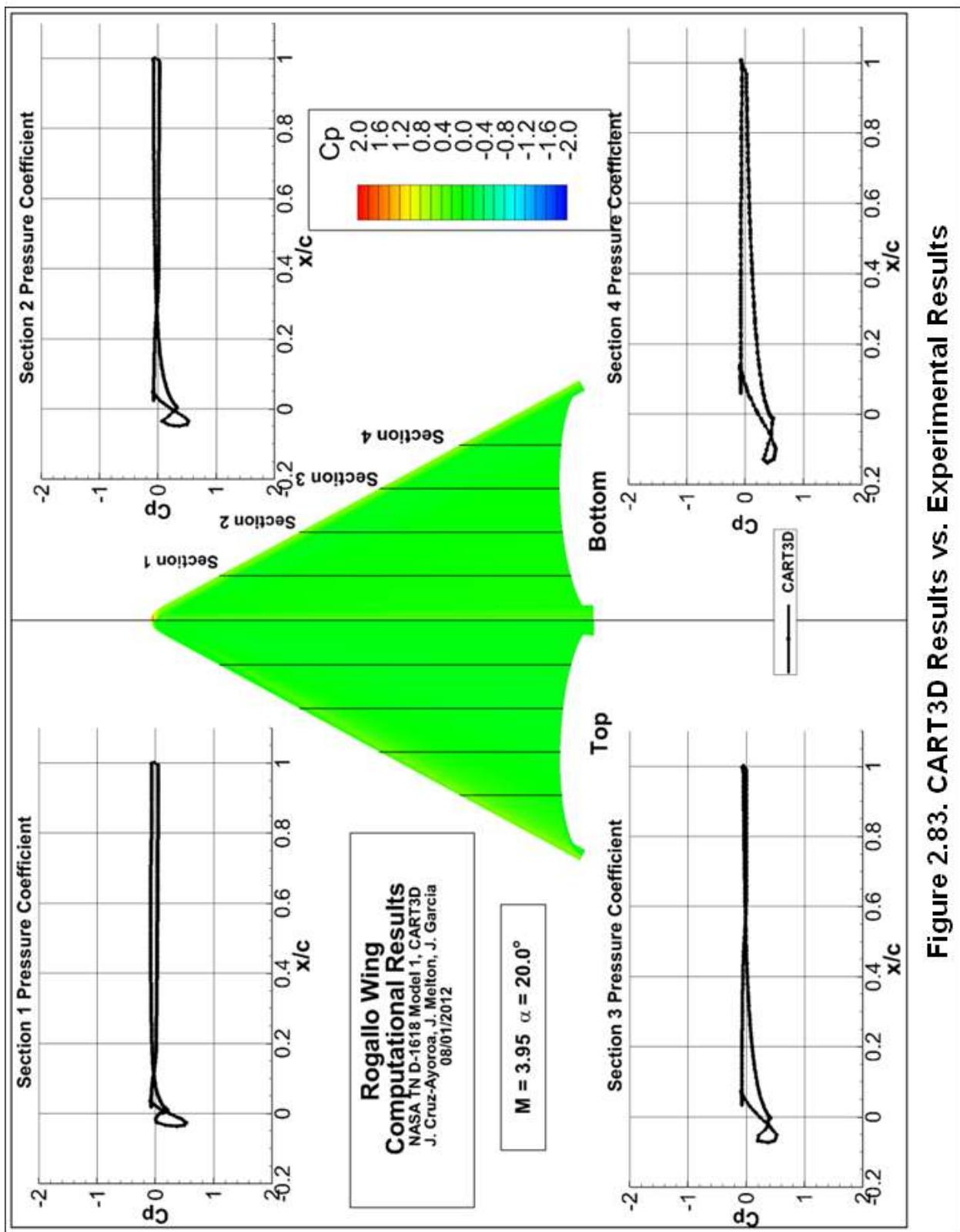


Figure 2.83. CART3D Results vs. Experimental Results

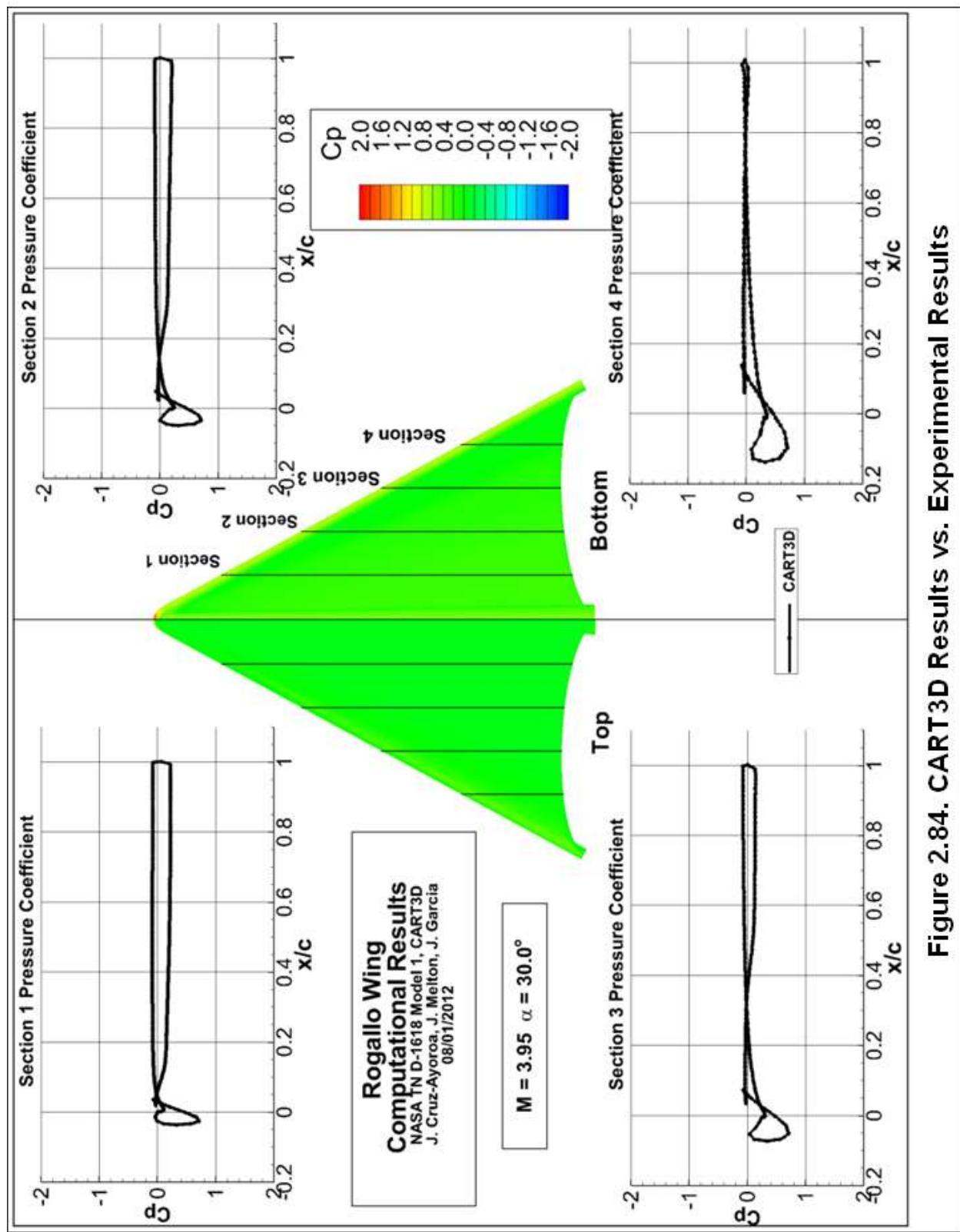


Figure 2.84. CART3D Results vs. Experimental Results

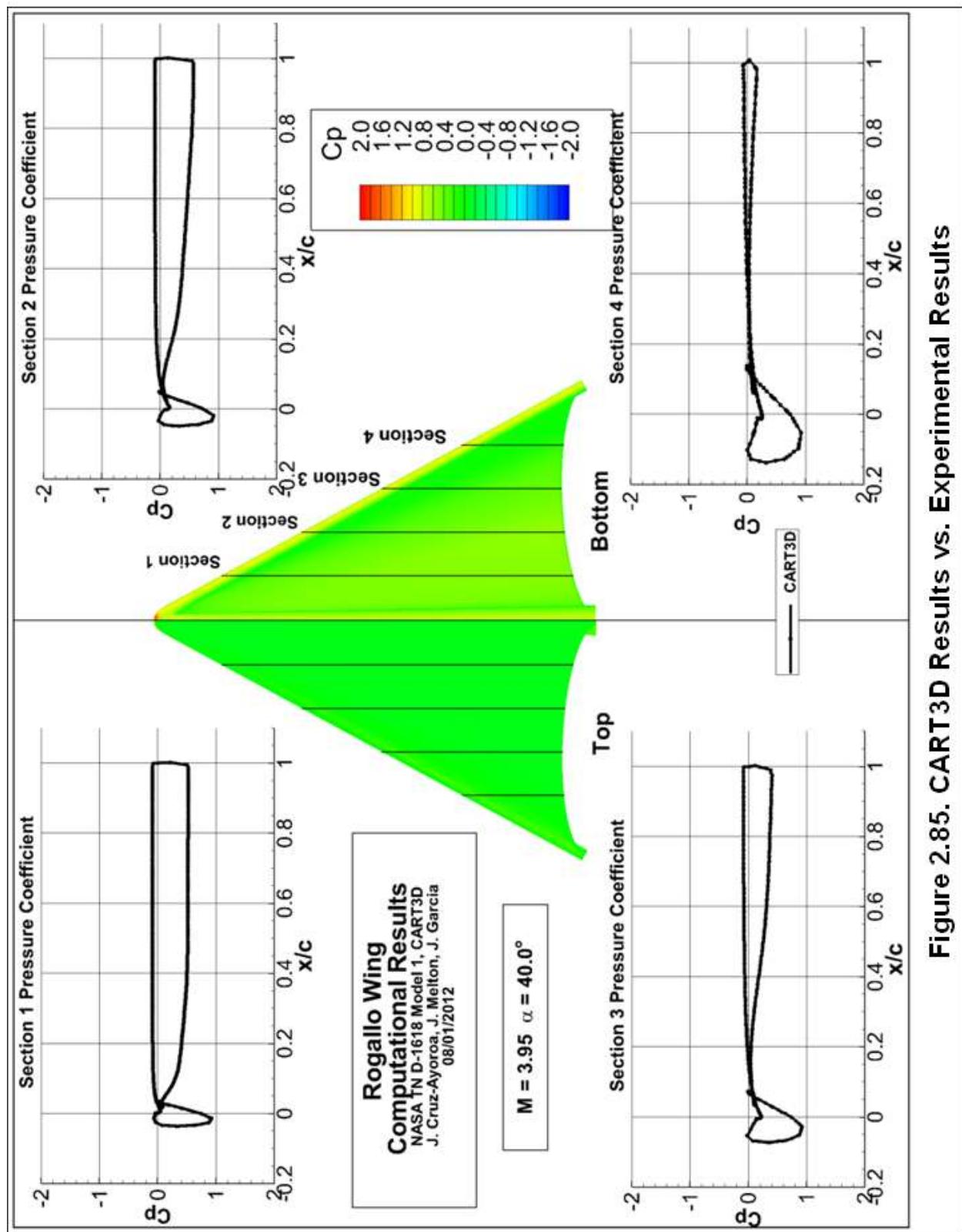


Figure 2.85. CART3D Results vs. Experimental Results

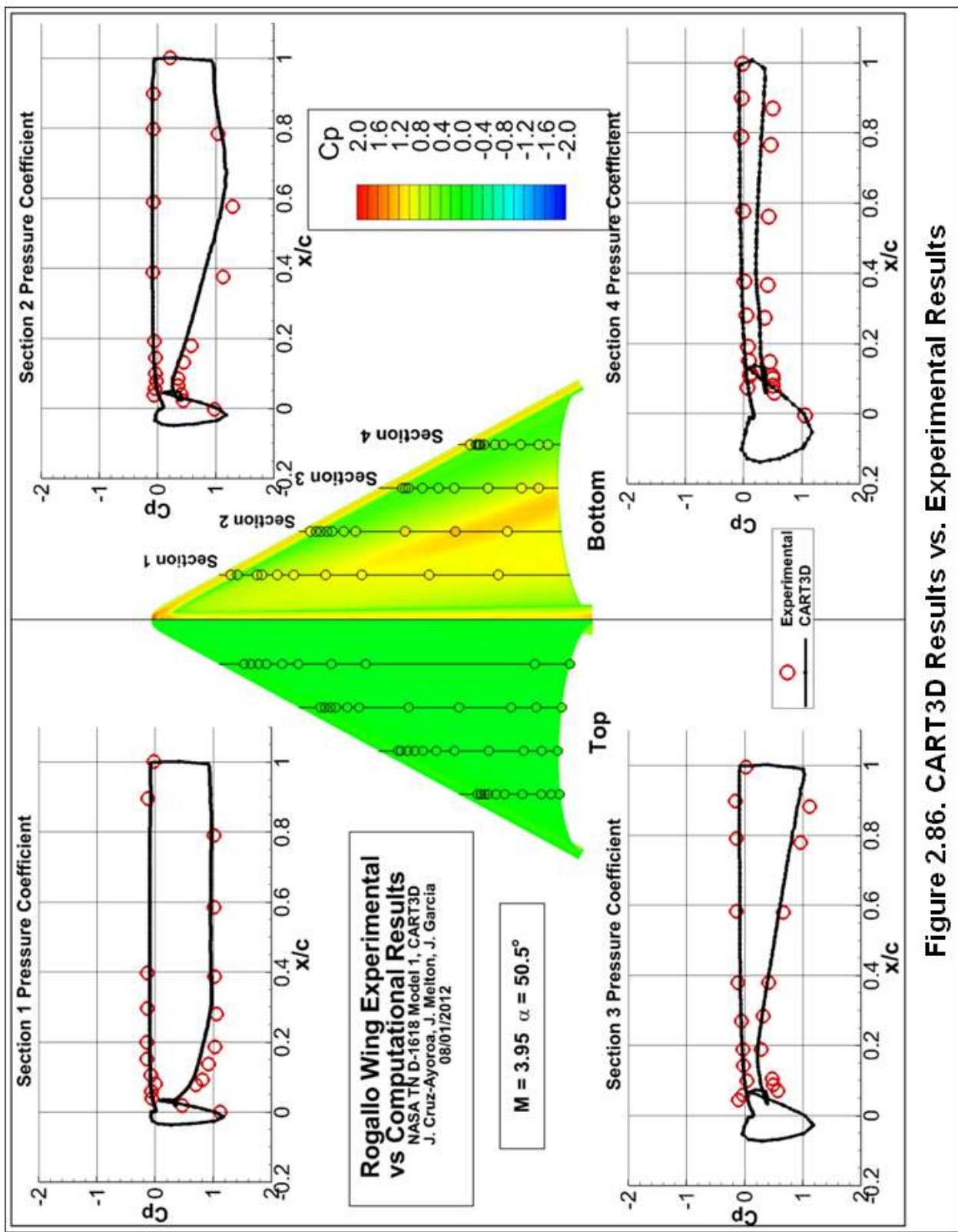


Figure 2.86. CART3D Results vs. Experimental Results

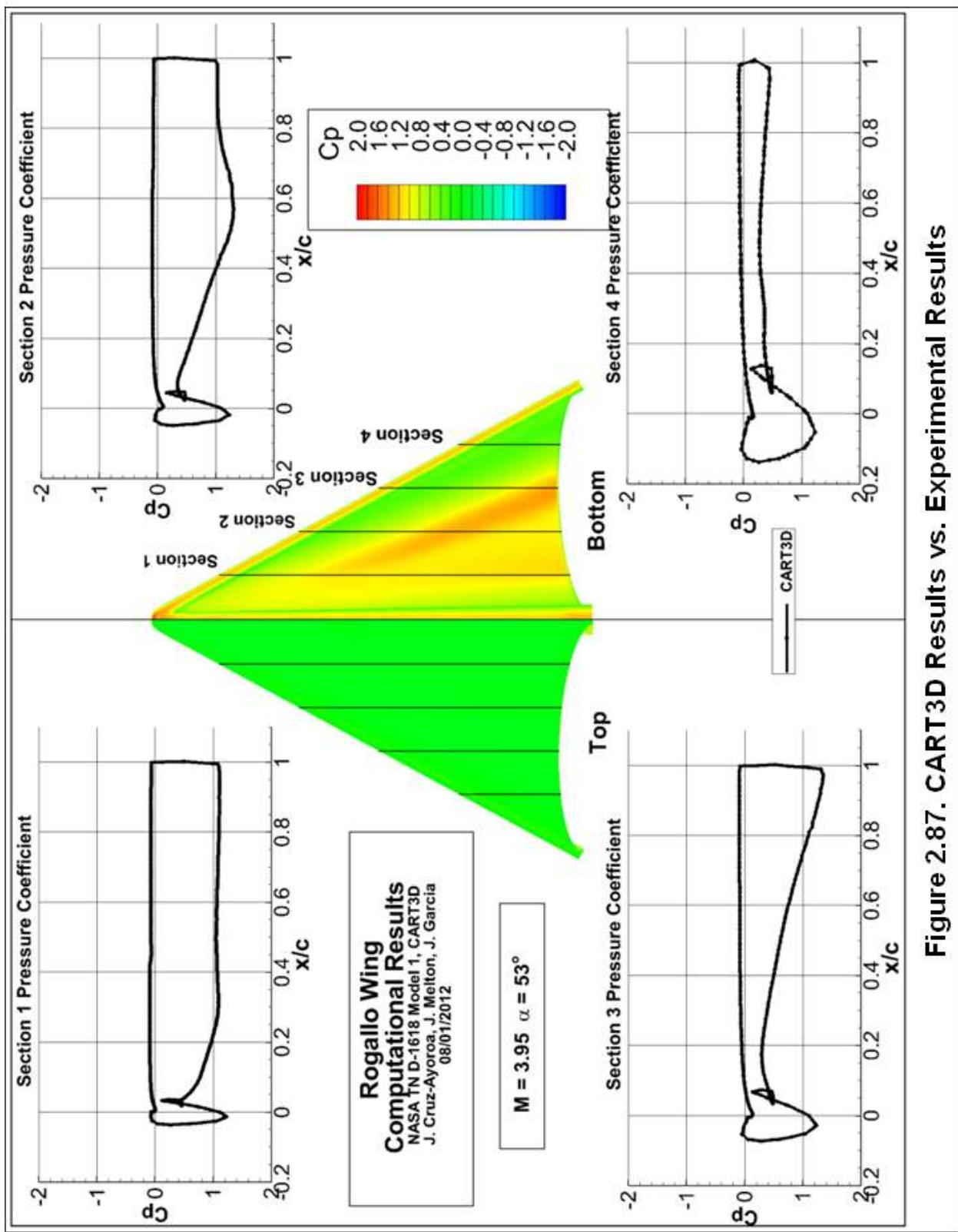


Figure 2.87. CART3D Results vs. Experimental Results

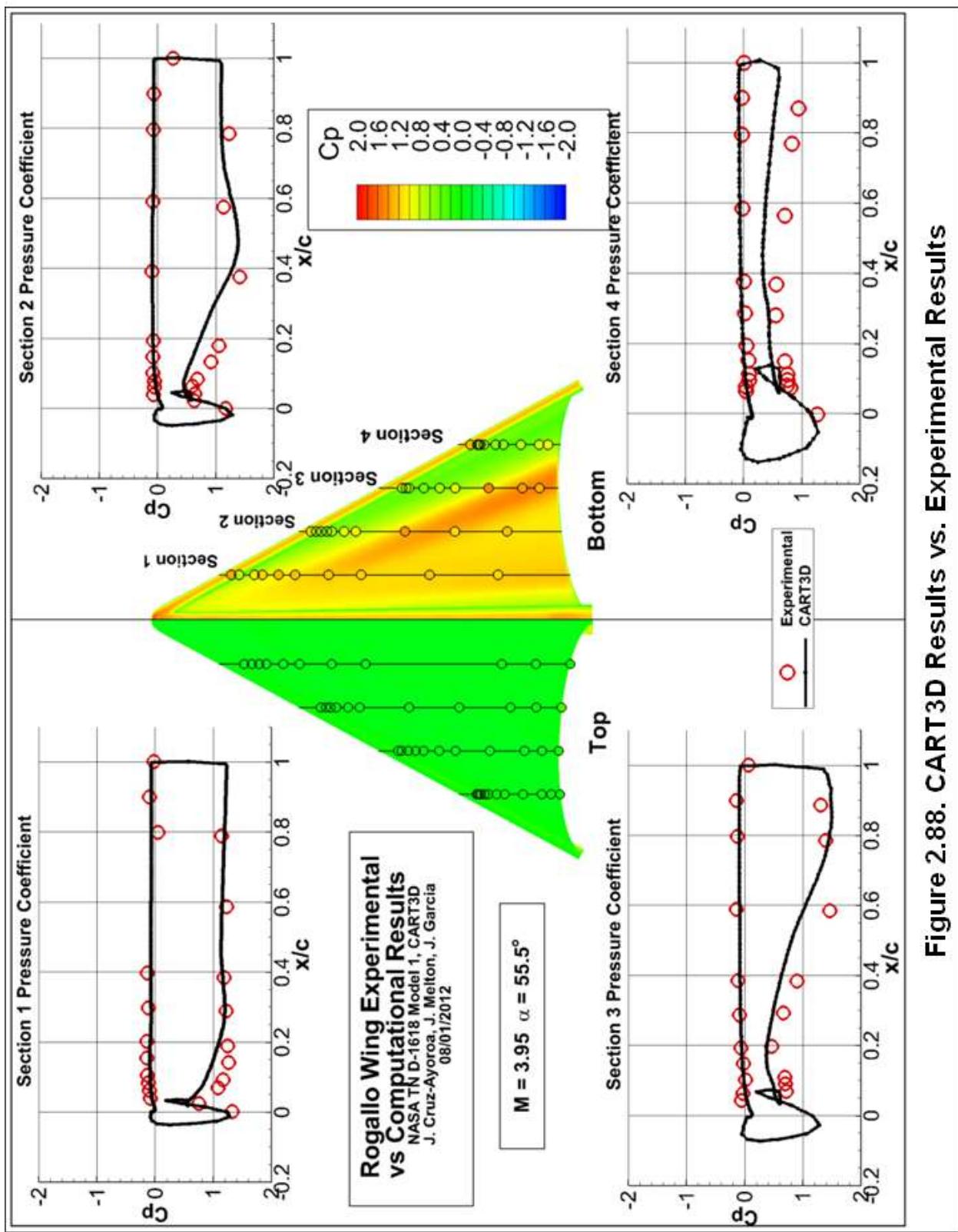


Figure 2.88. CART3D Results vs. Experimental Results

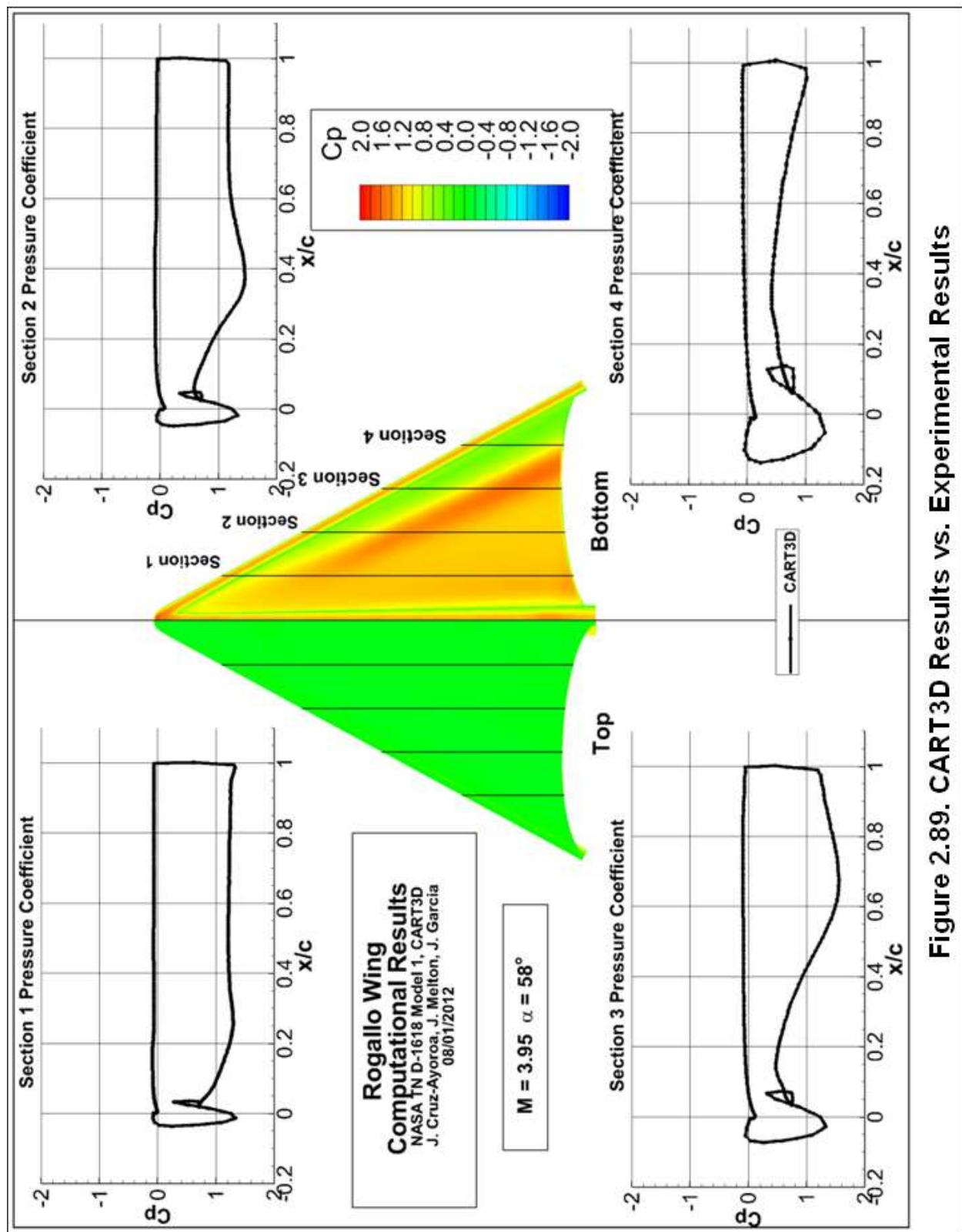


Figure 2.89. CART3D Results vs. Experimental Results

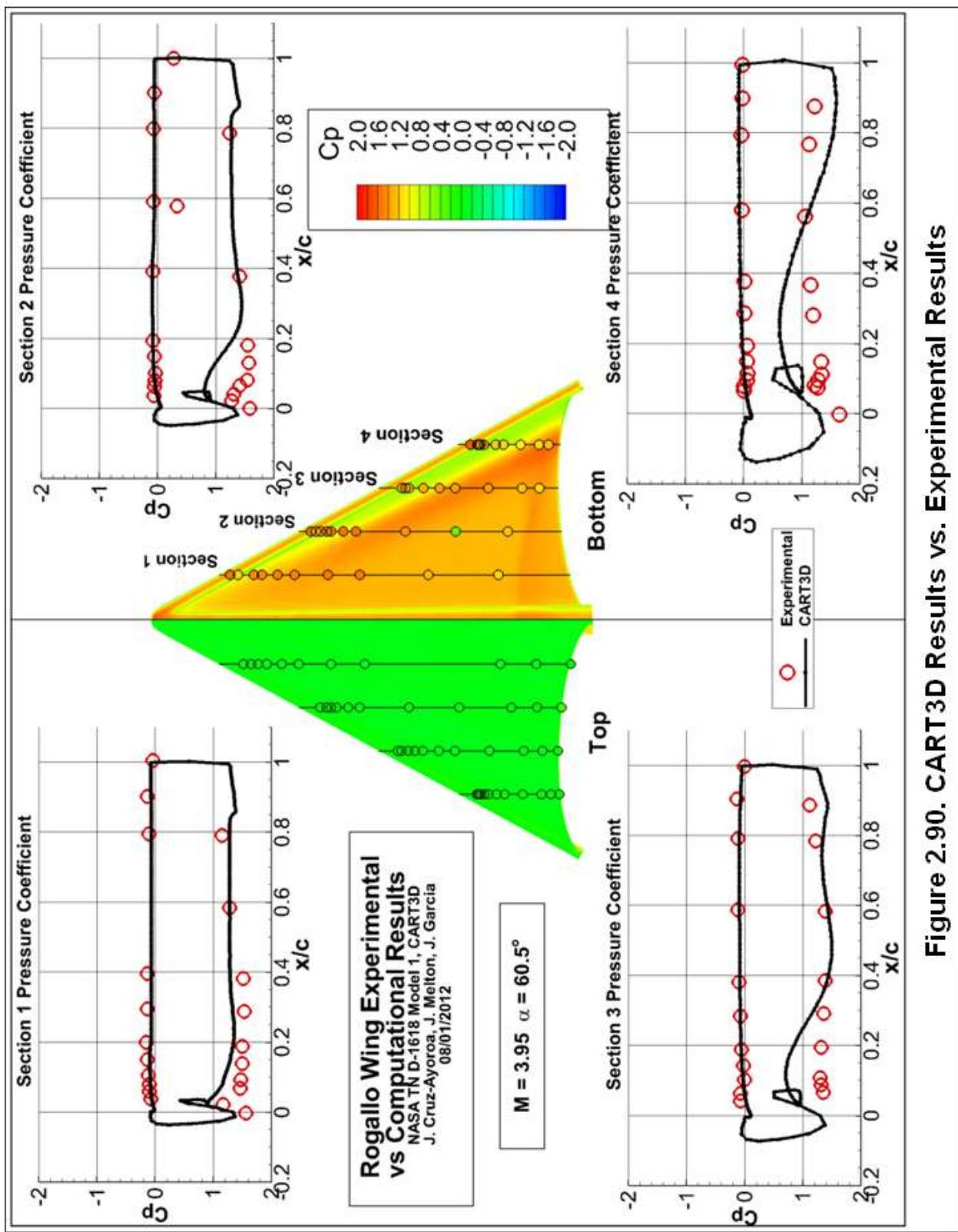


Figure 2.90. CART3D Results vs. Experimental Results

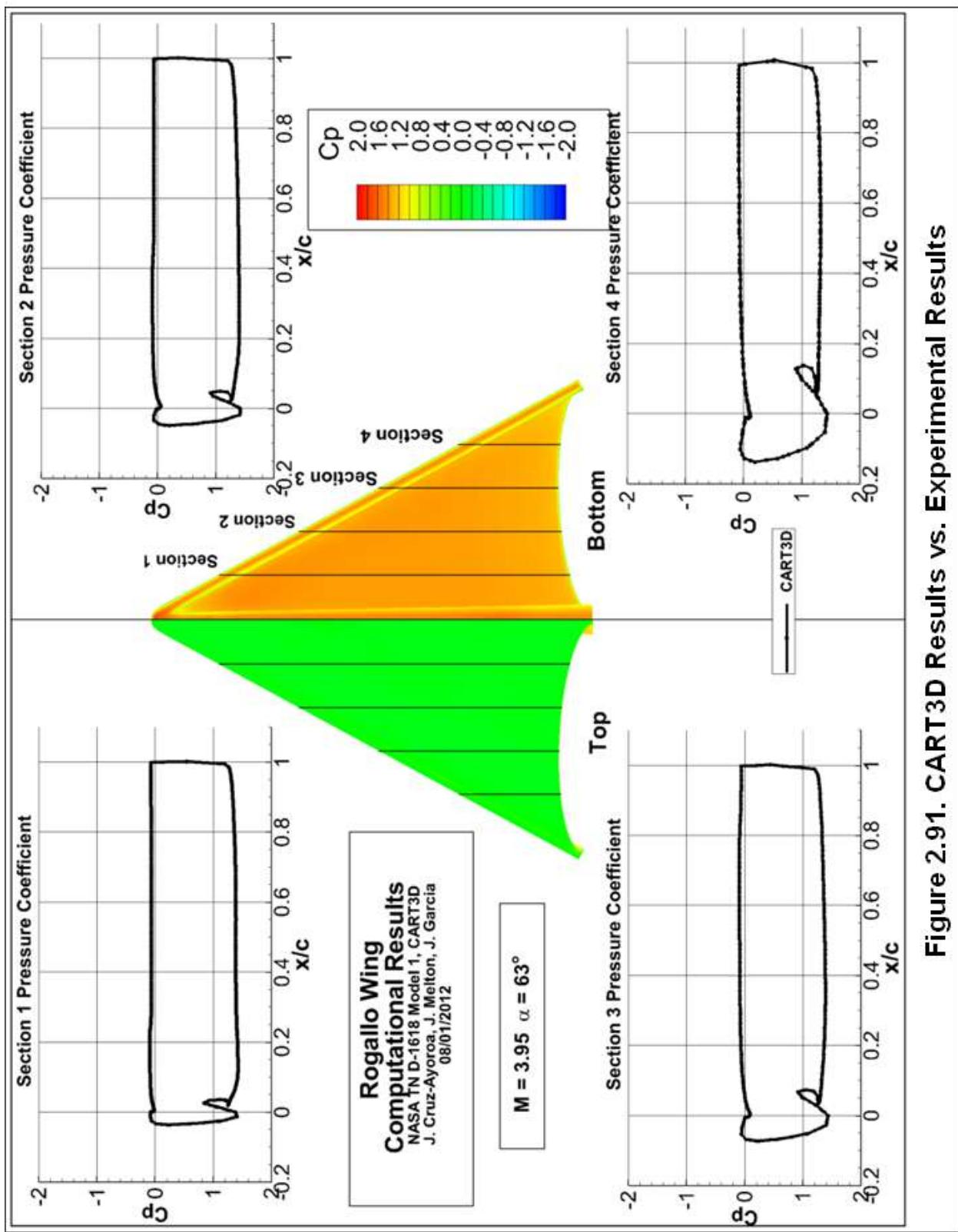


Figure 2.91. CART3D Results vs. Experimental Results

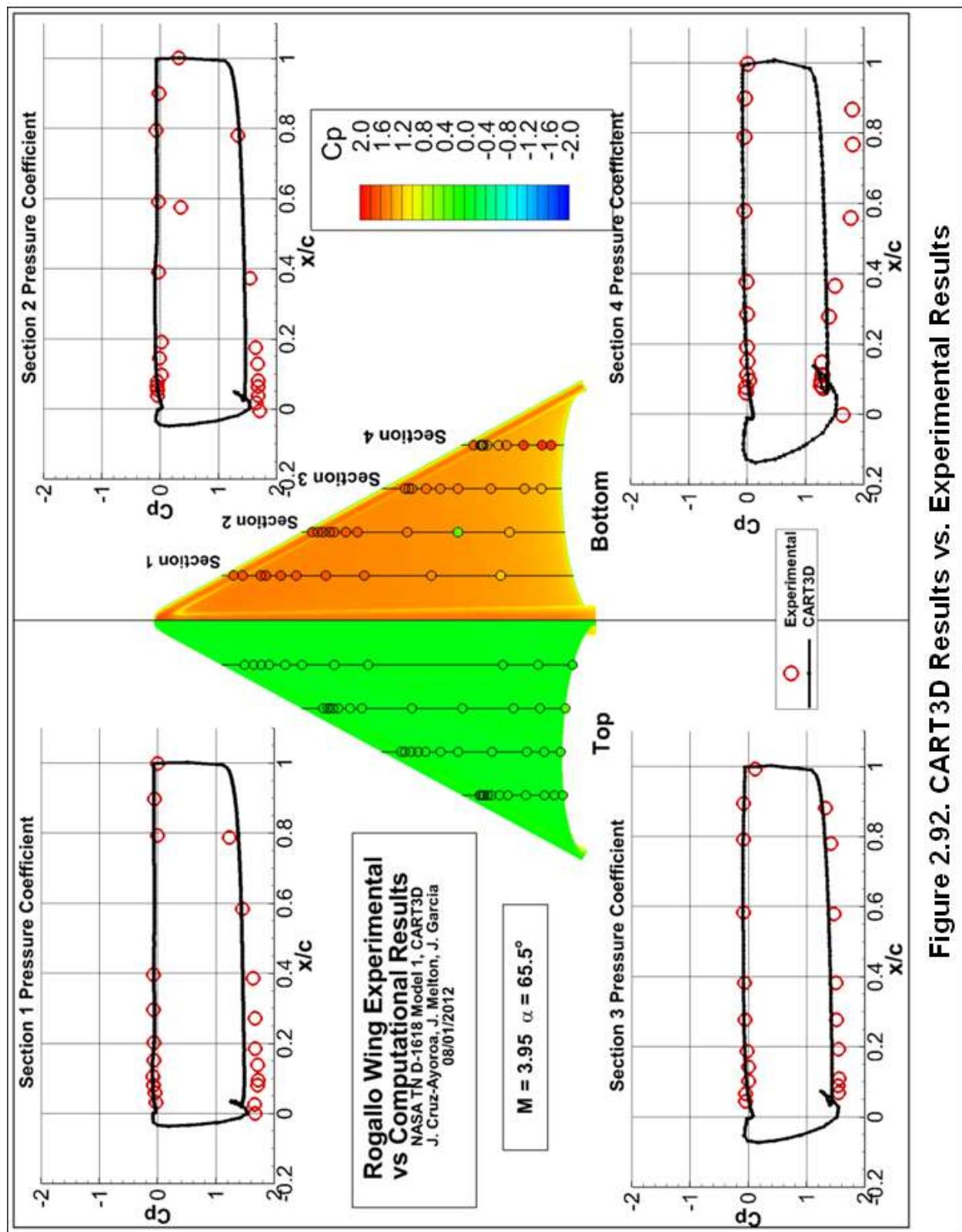


Figure 2.92. CART3D Results vs. Experimental Results

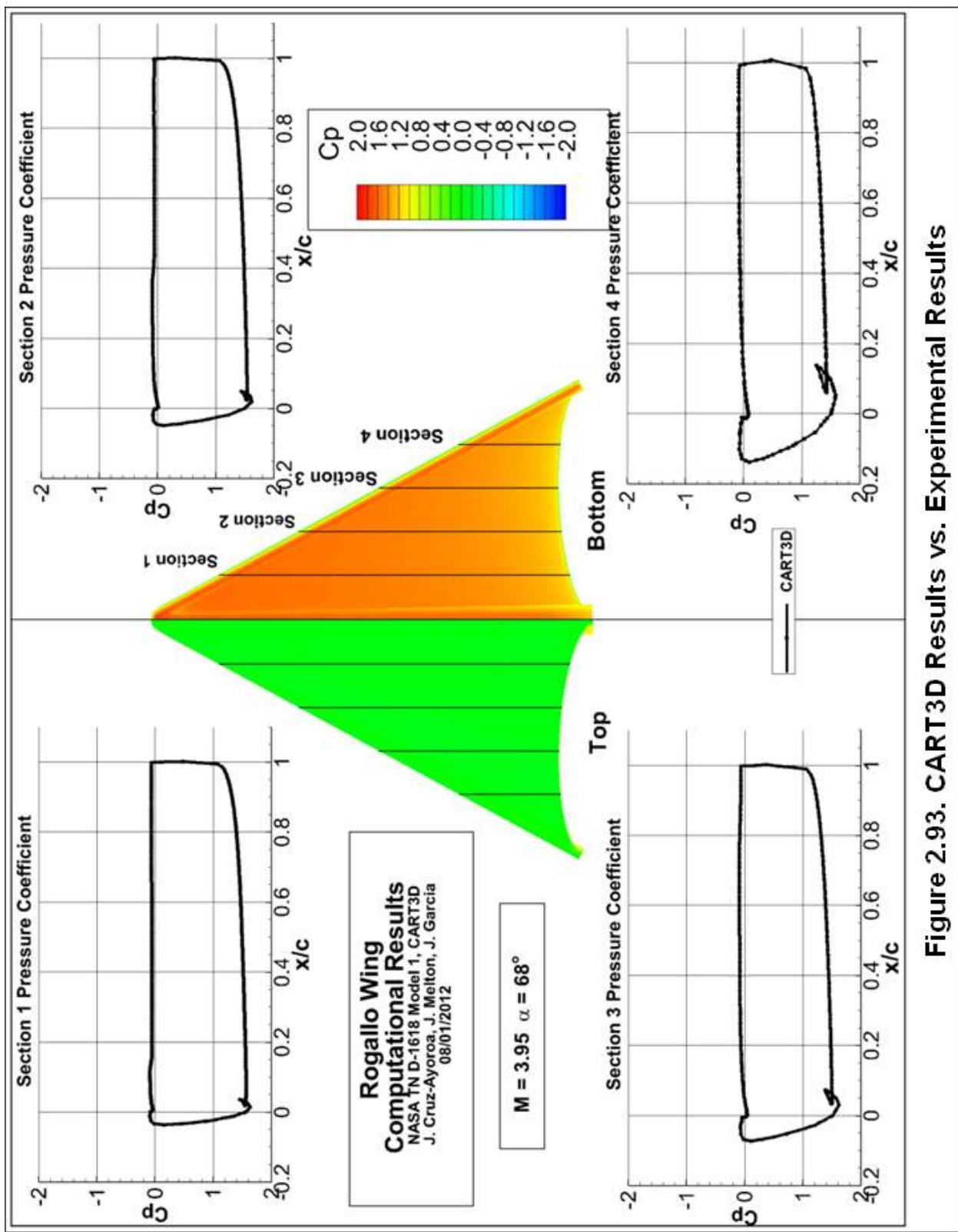


Figure 2.93. CART3D Results vs. Experimental Results

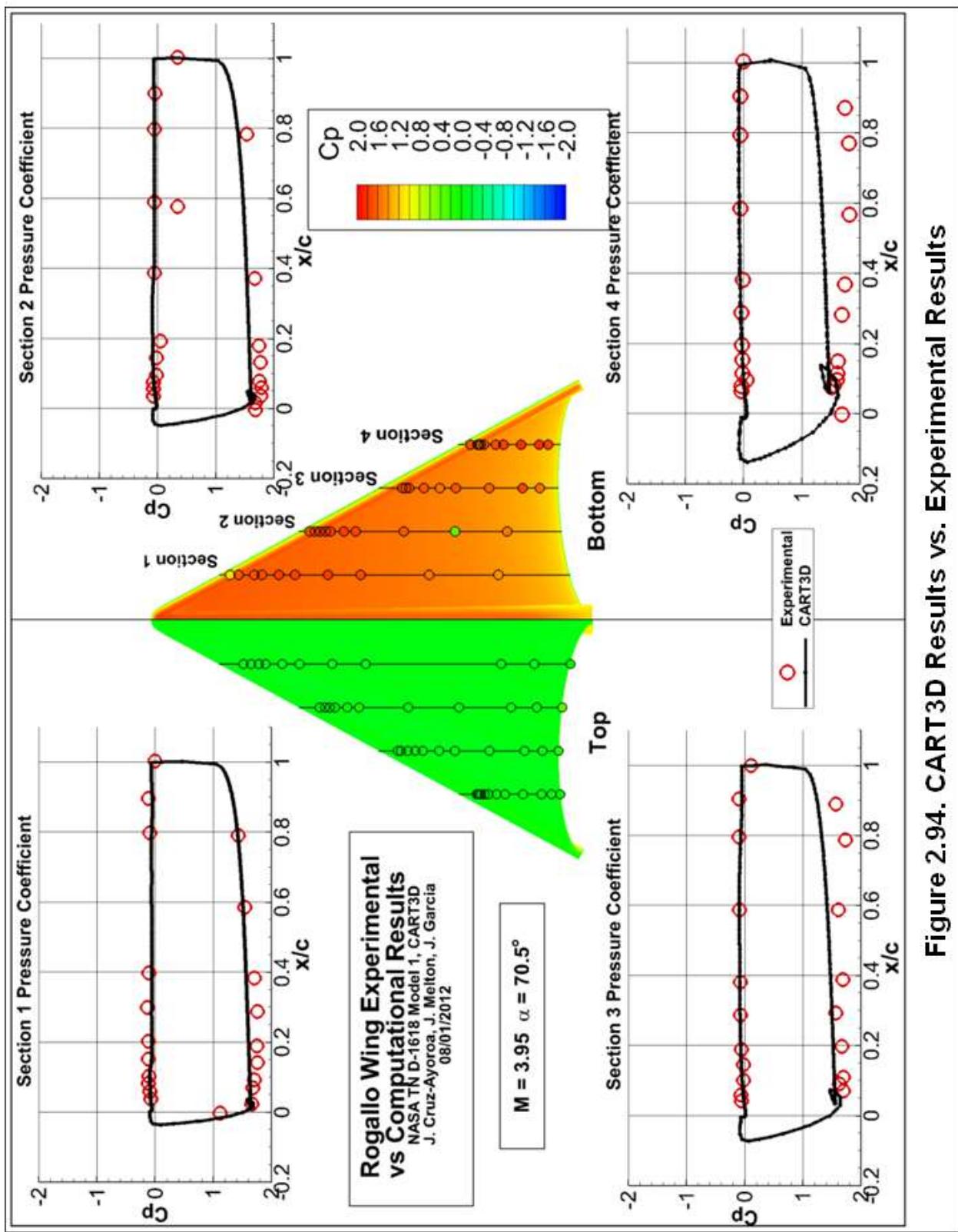


Figure 2.94. CART3D Results vs. Experimental Results

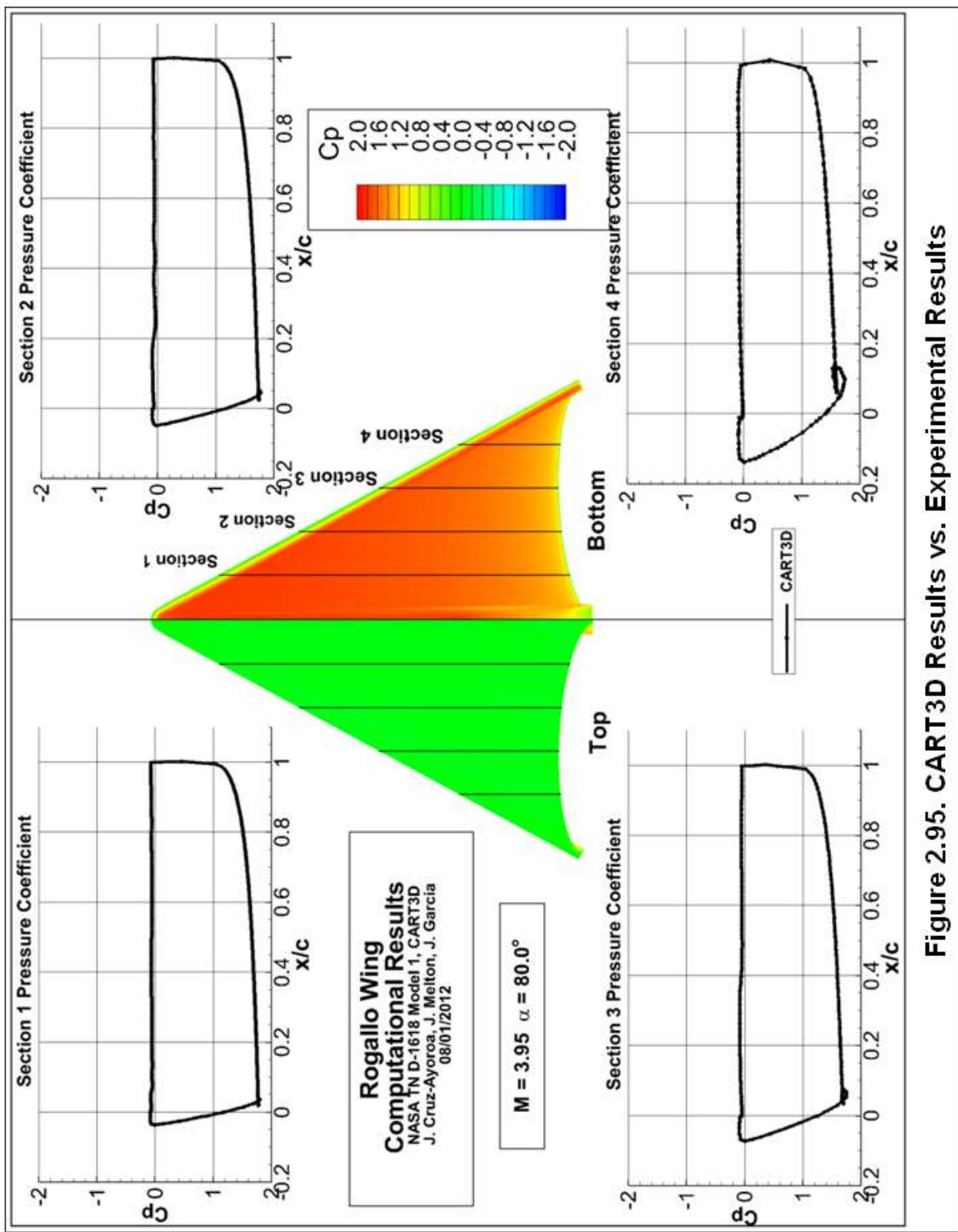


Figure 2.95. CART3D Results vs. Experimental Results

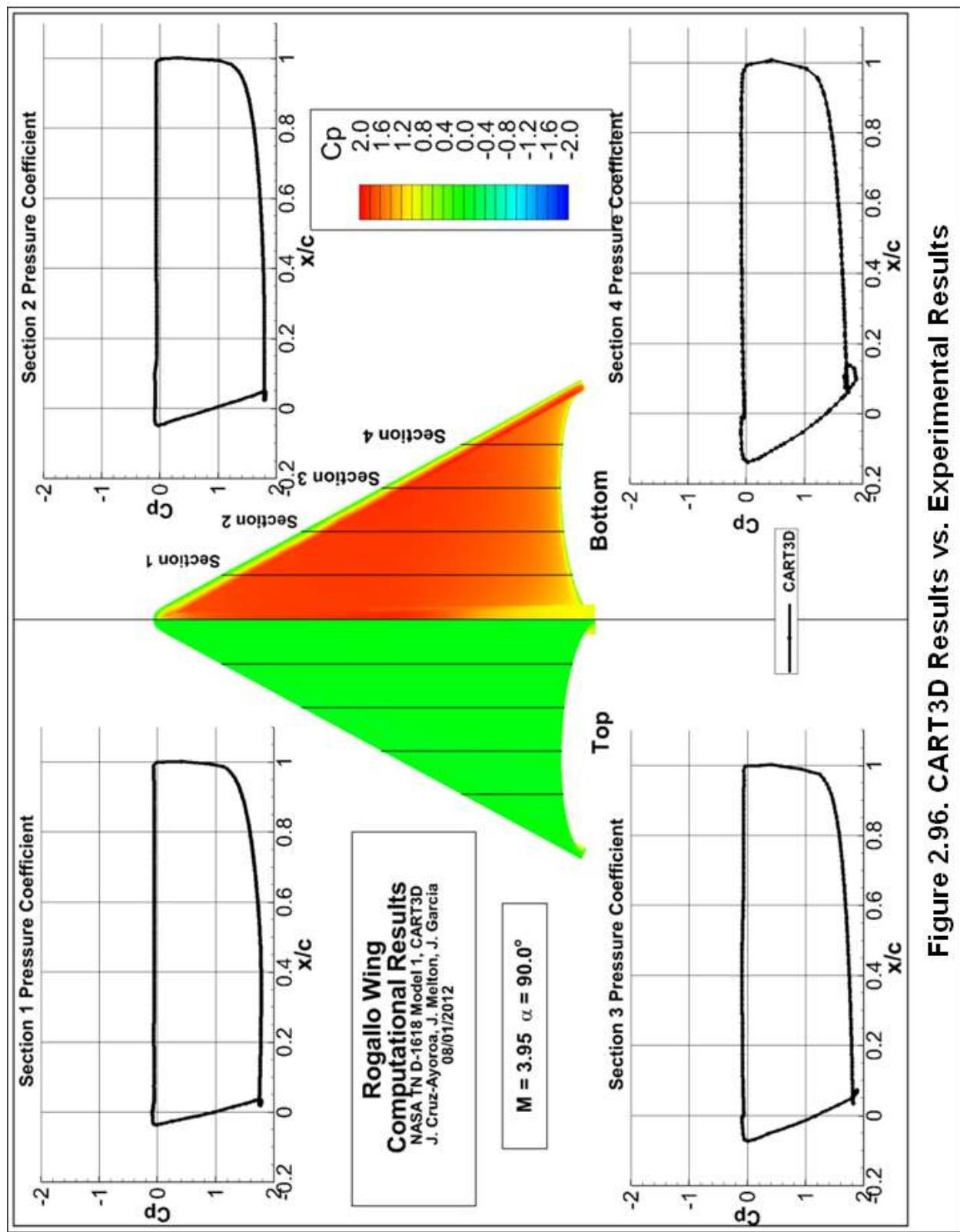


Figure 2.96. CART3D Results vs. Experimental Results

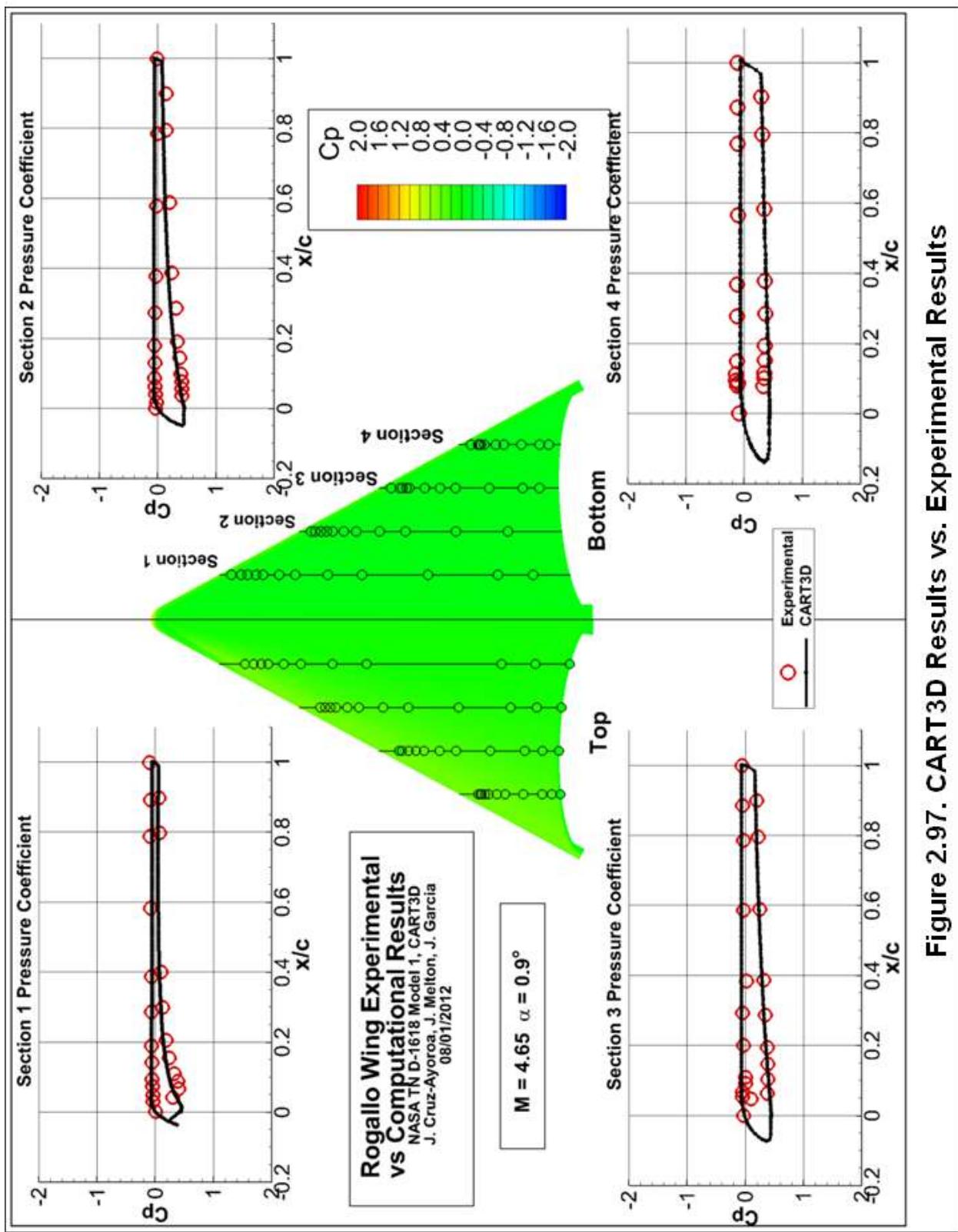


Figure 2.97. CART3D Results vs. Experimental Results

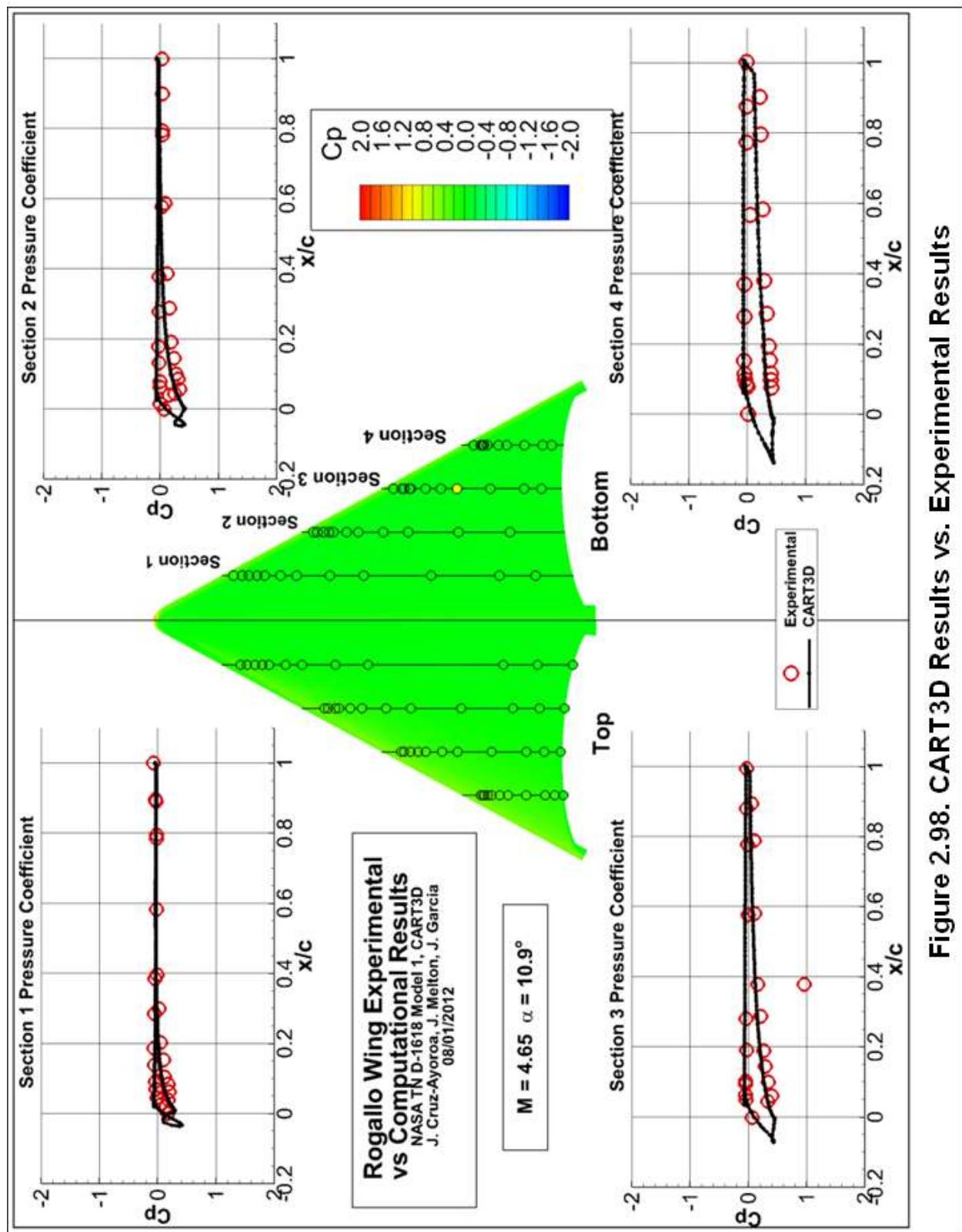


Figure 2.98. CART3D Results vs. Experimental Results

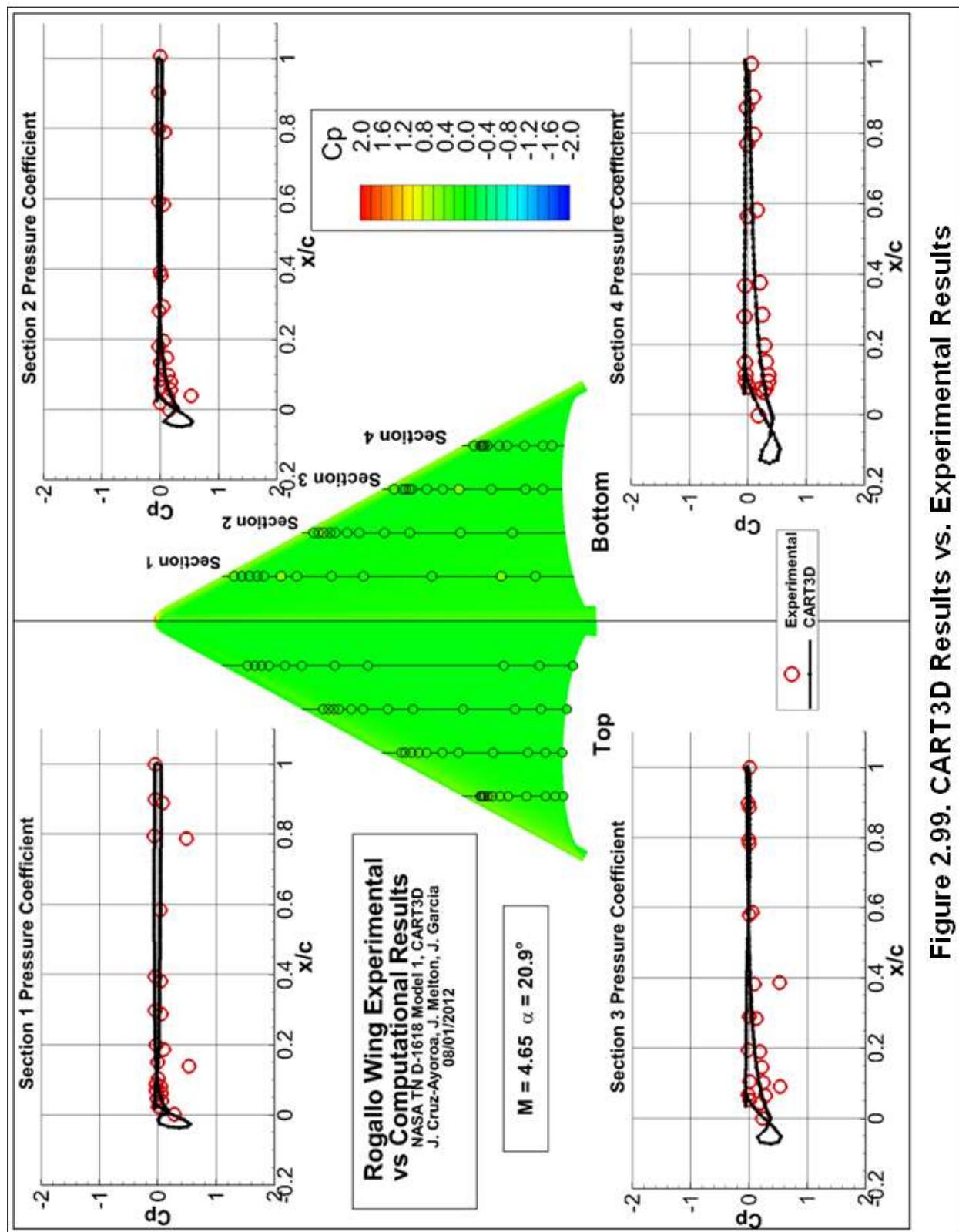


Figure 2.99. CART3D Results vs. Experimental Results

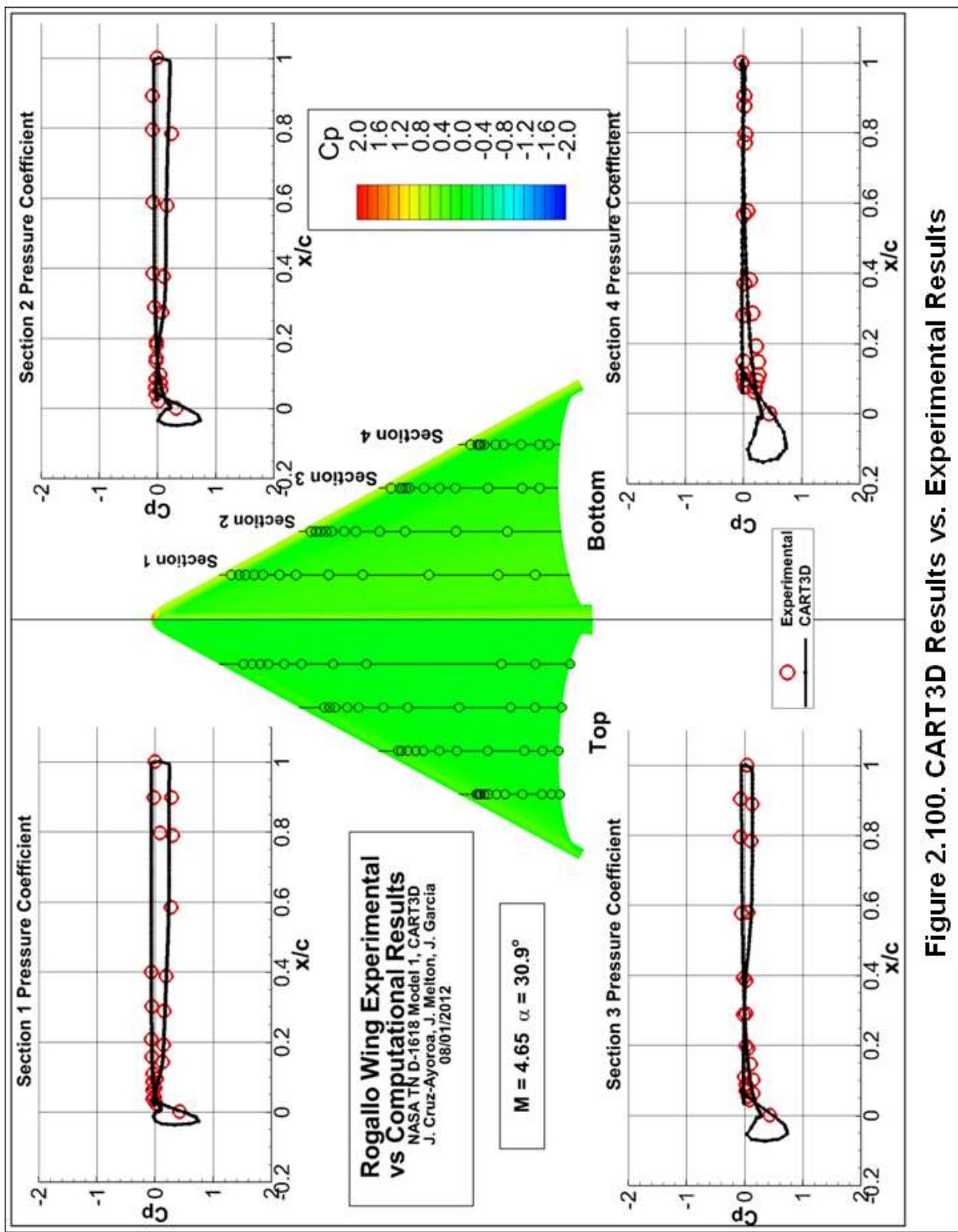


Figure 2.100. CART3D Results vs. Experimental Results

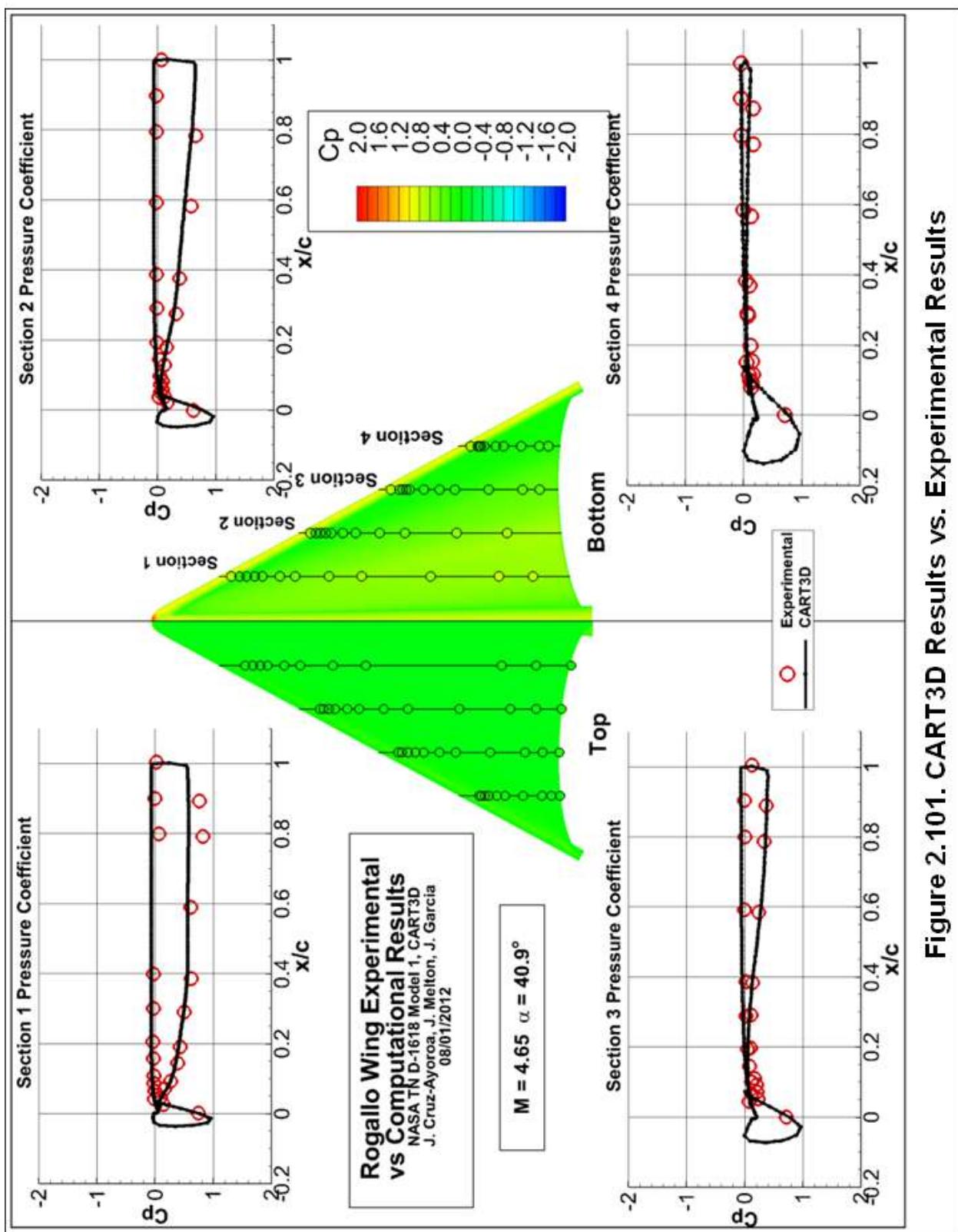


Figure 2.101. CART3D Results vs. Experimental Results

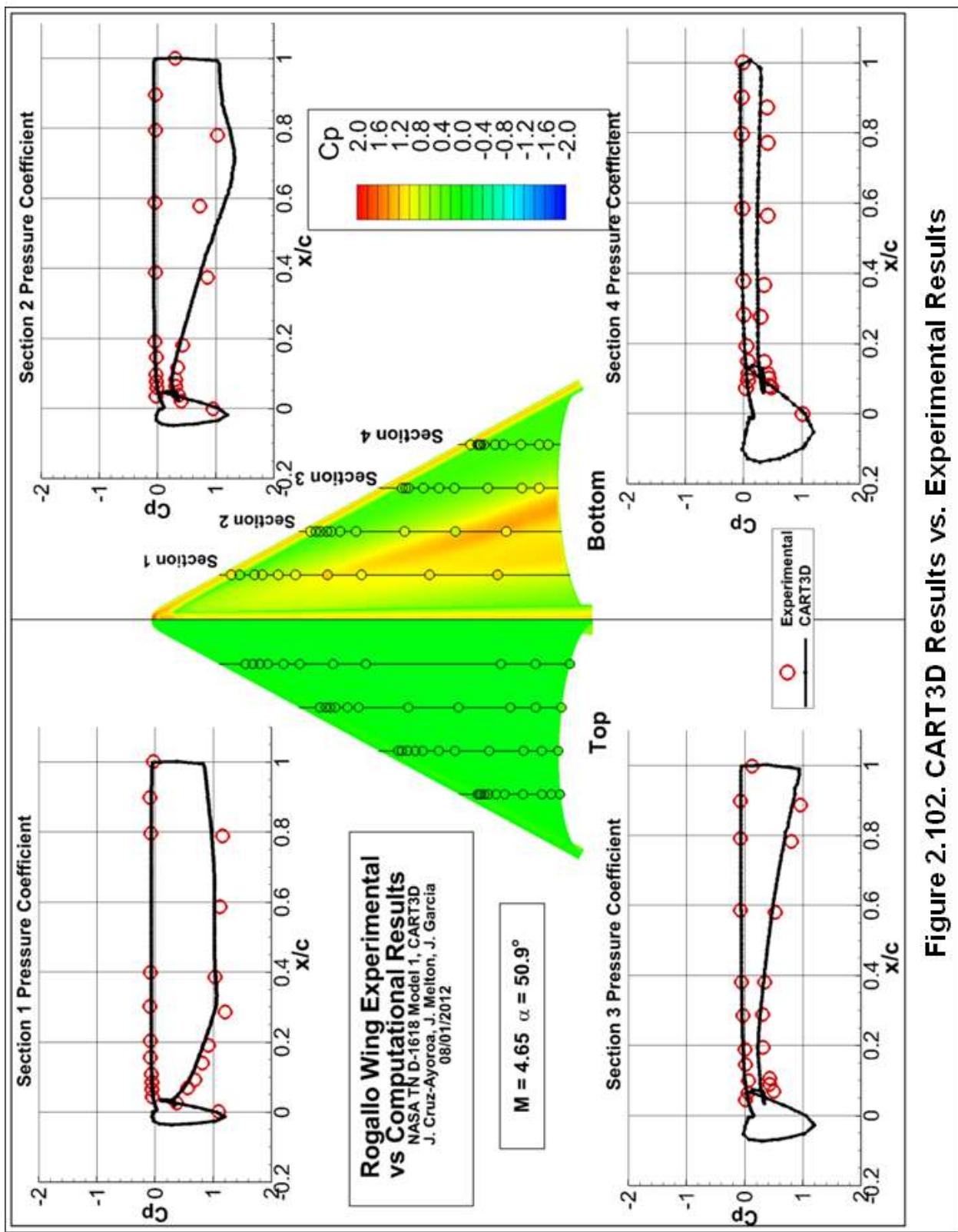


Figure 2.102. CART3D Results vs. Experimental Results

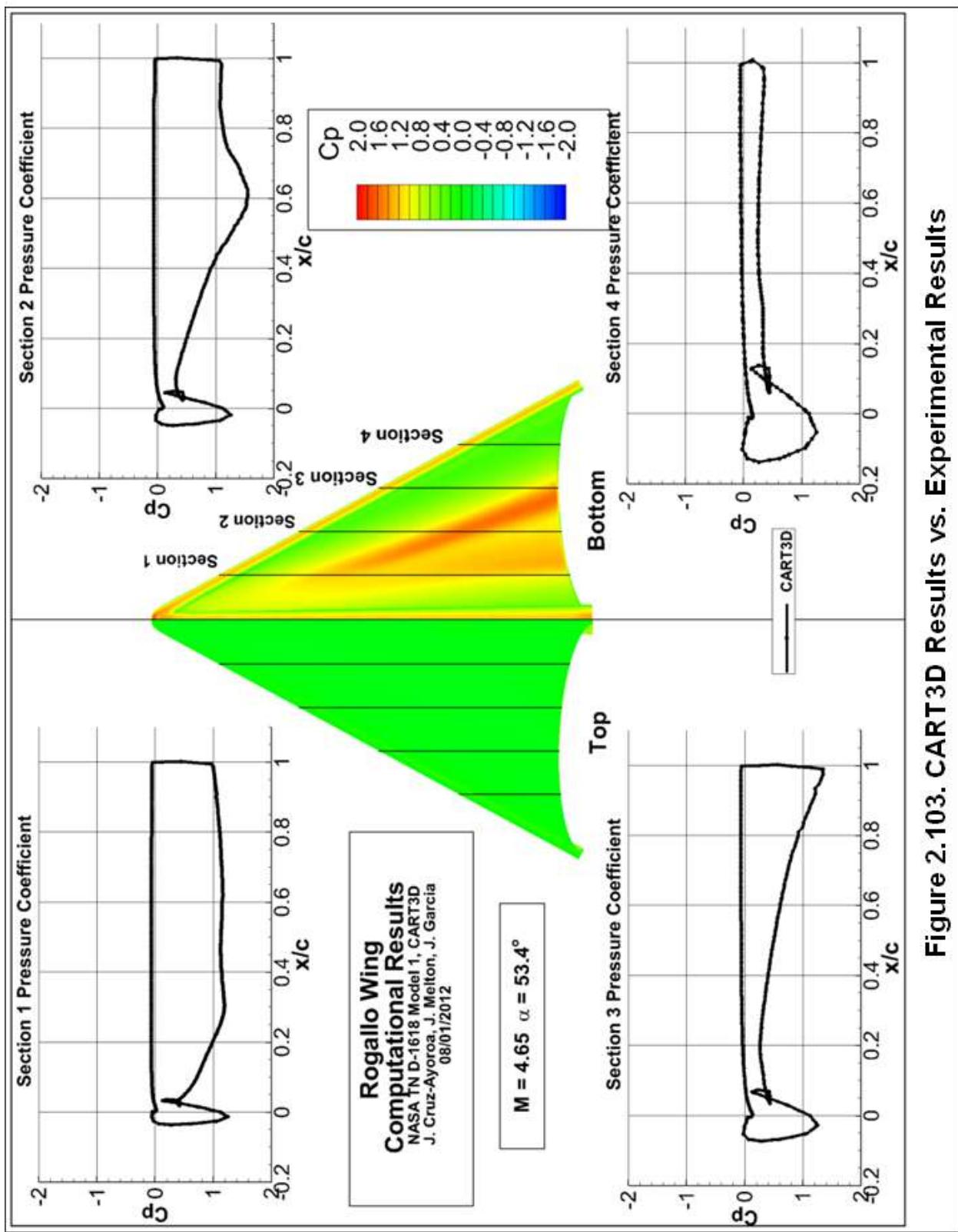


Figure 2.103. CART3D Results vs. Experimental Results

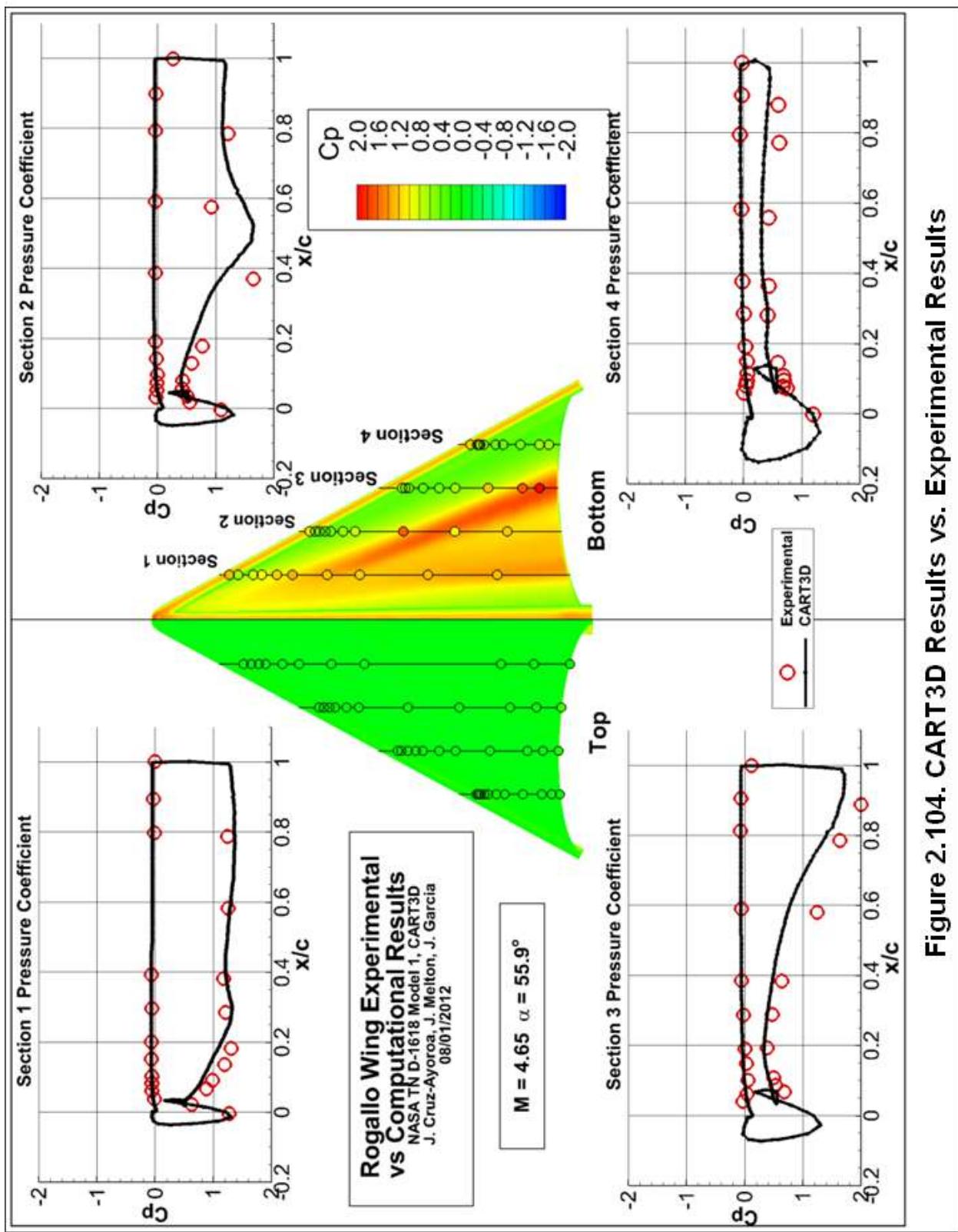


Figure 2.104. CART3D Results vs. Experimental Results

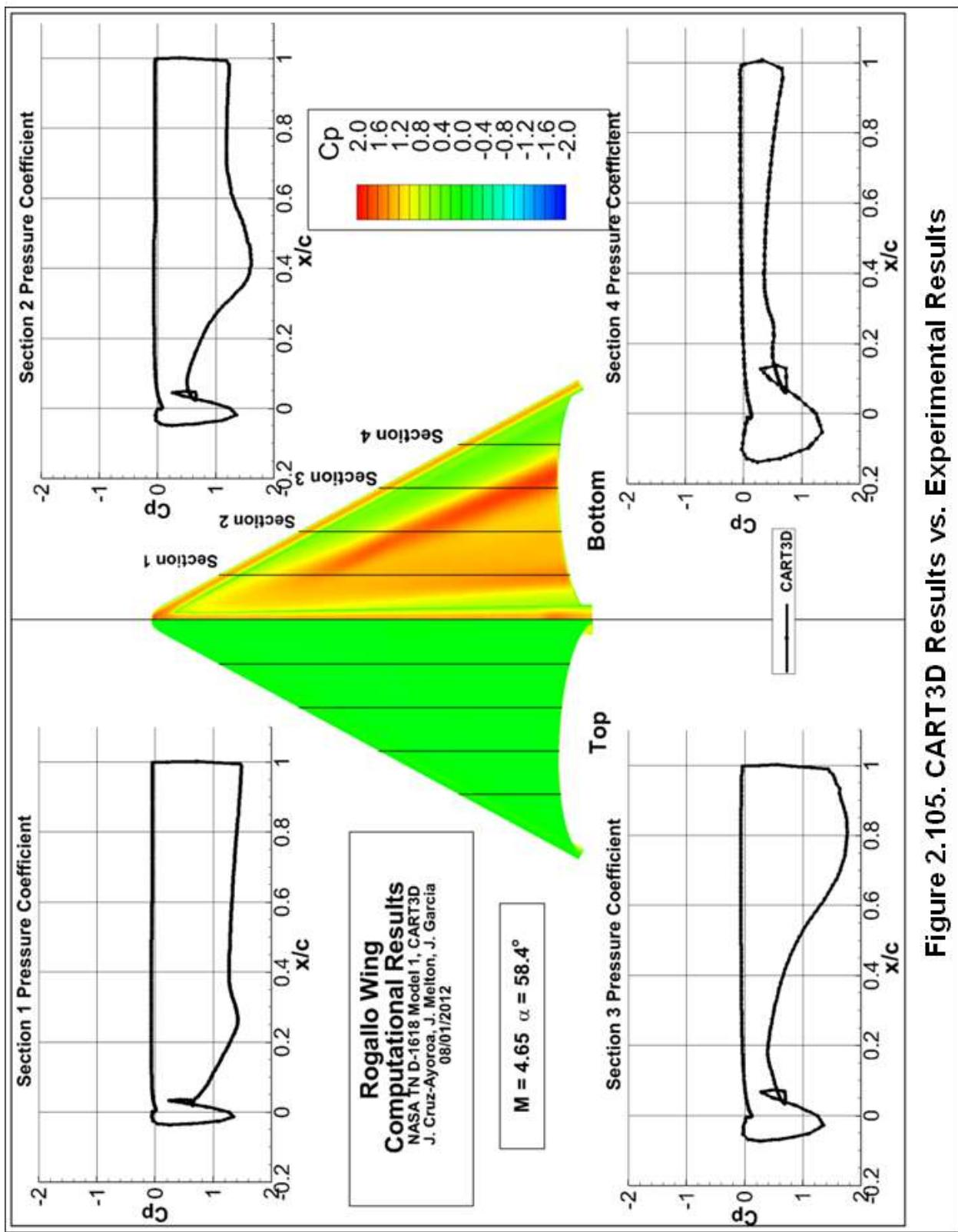


Figure 2.105. CART3D Results vs. Experimental Results

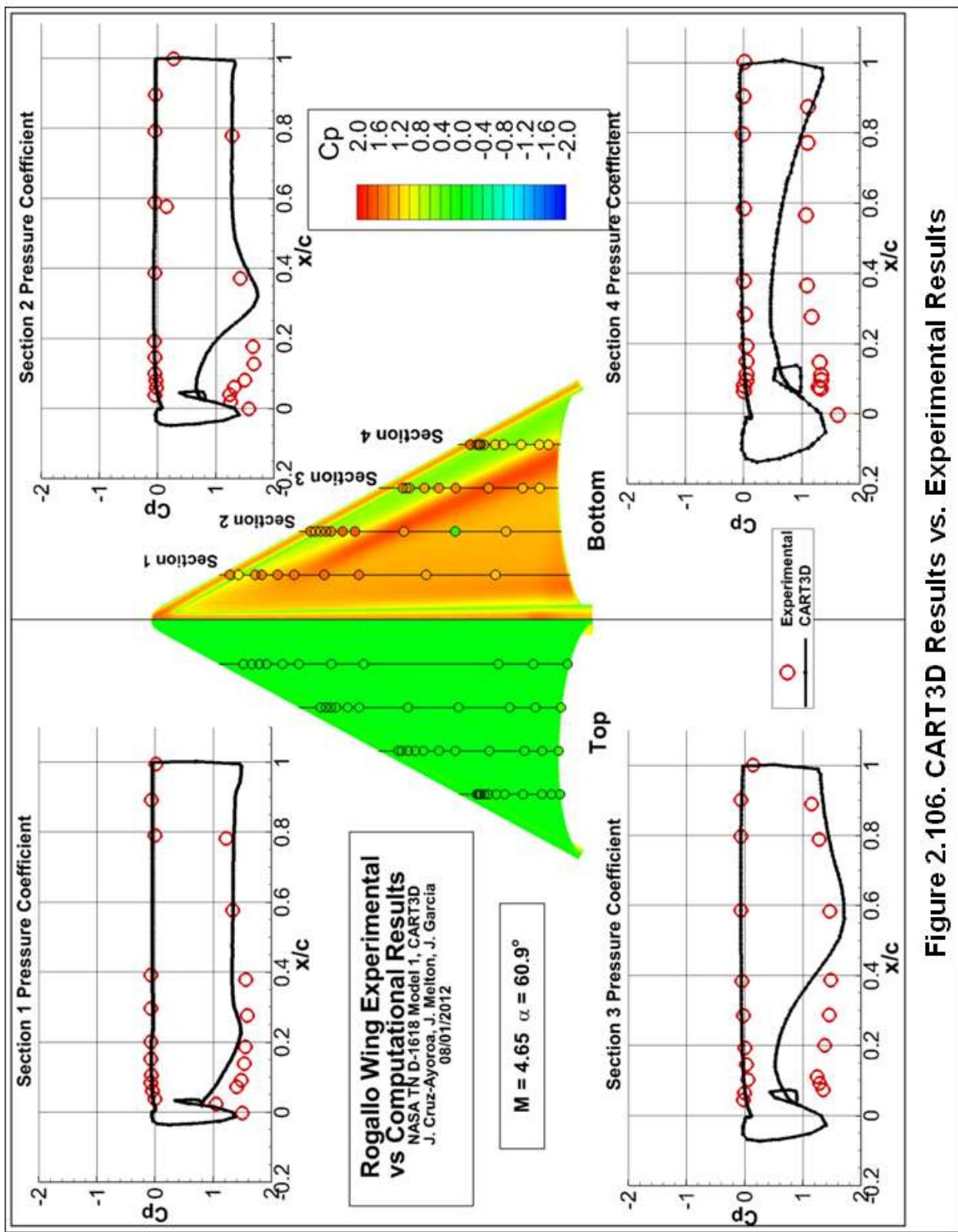


Figure 2.106. CART3D Results vs. Experimental Results

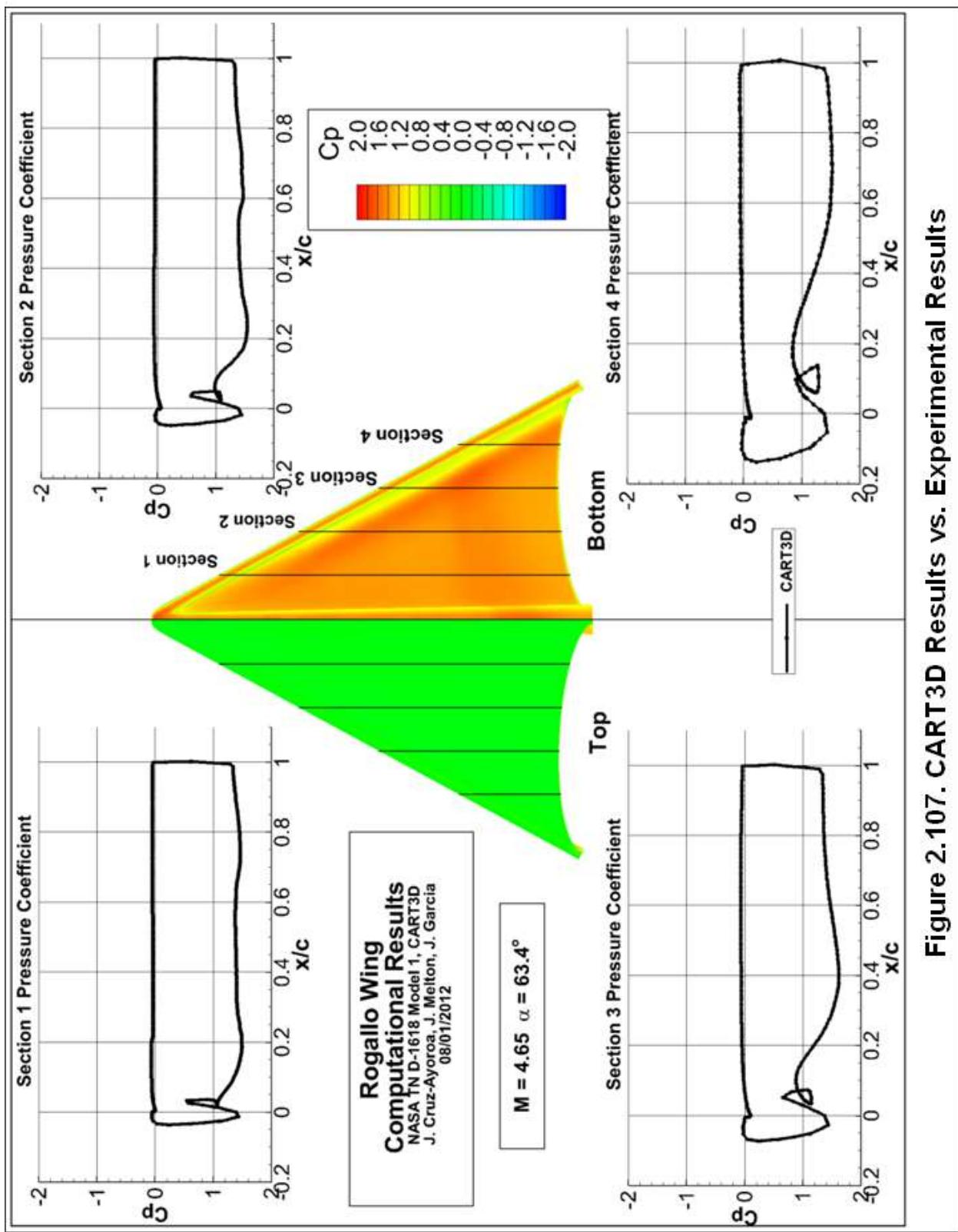


Figure 2.107. CART3D Results vs. Experimental Results

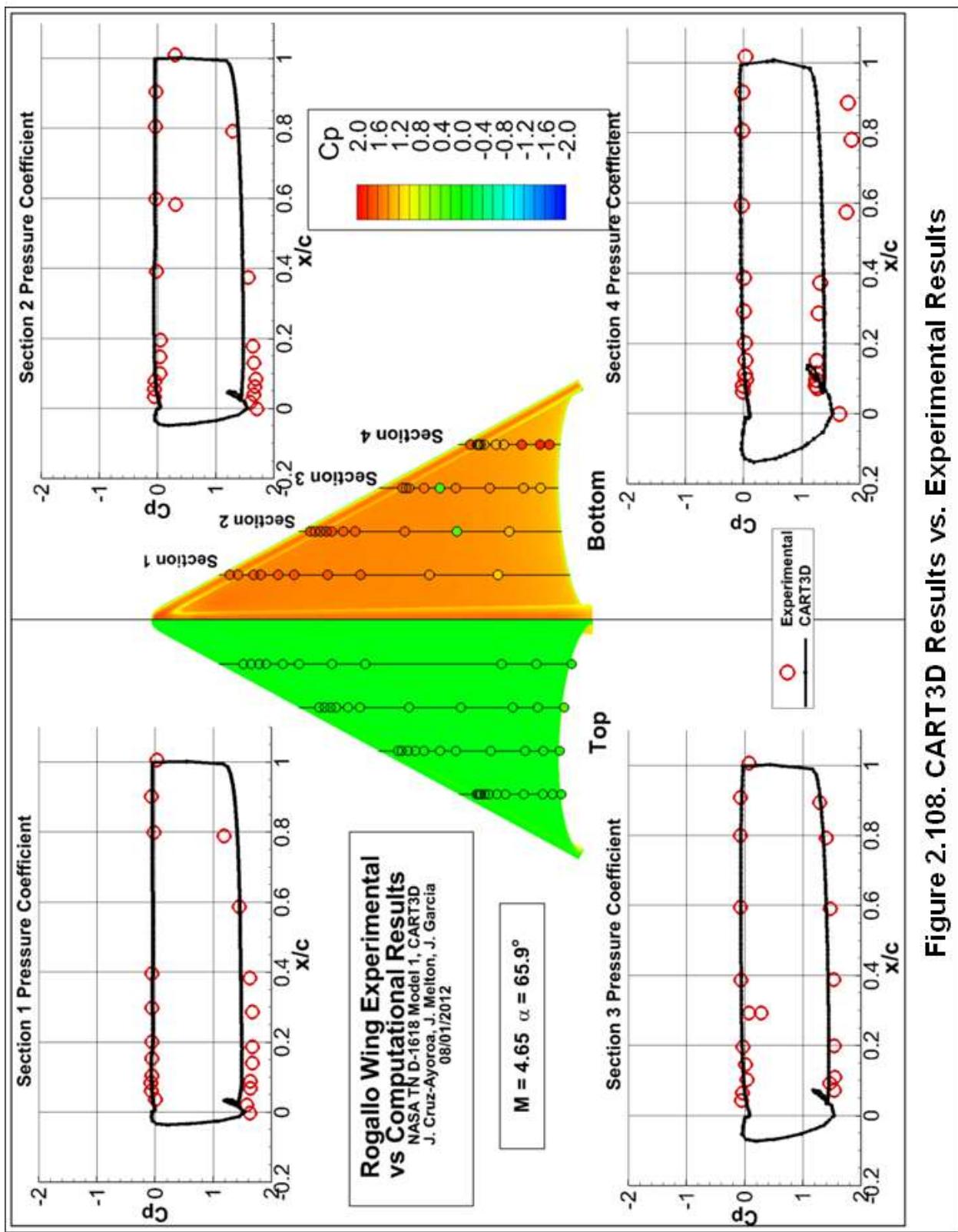


Figure 2.108. CART3D Results vs. Experimental Results

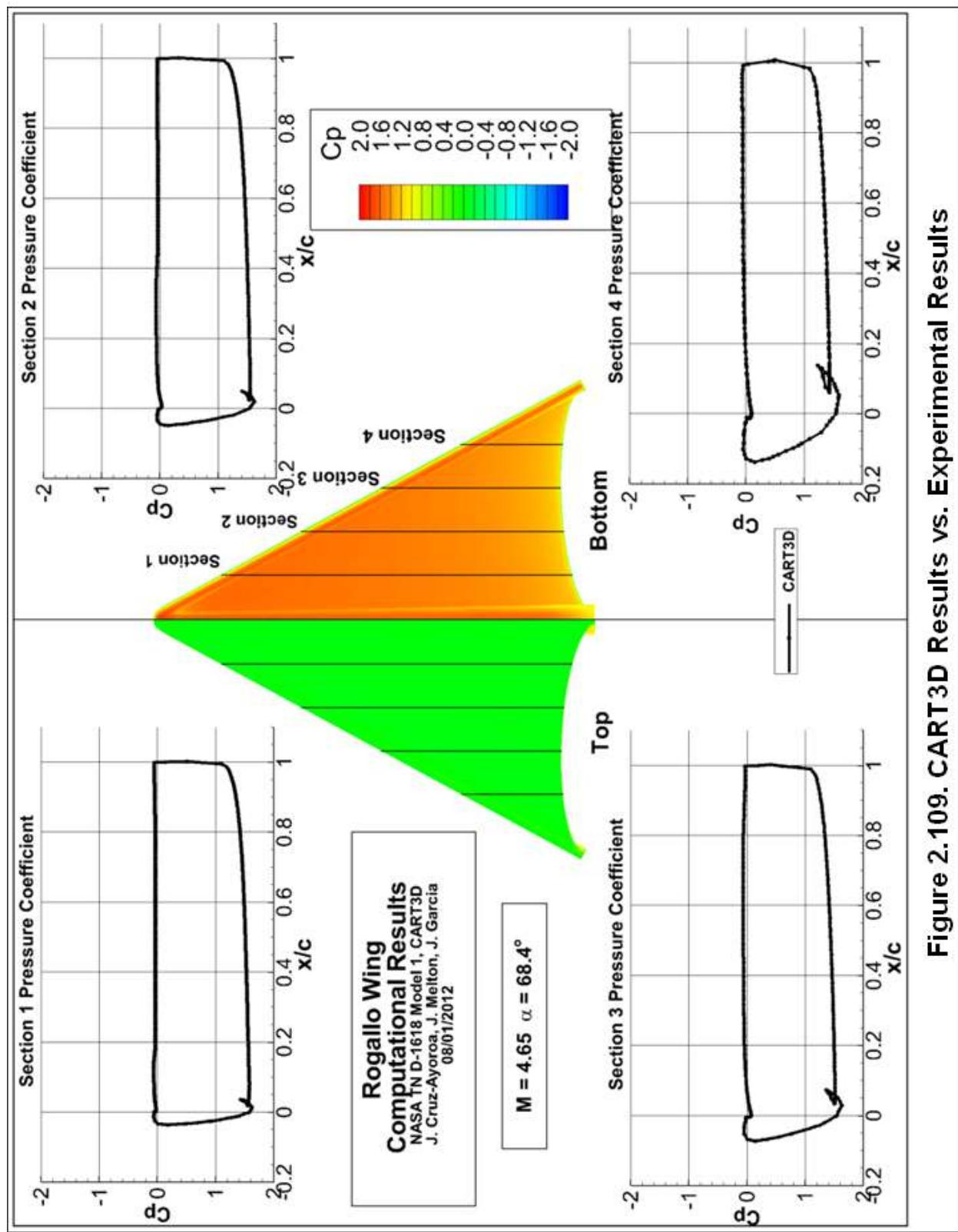


Figure 2.109. CART3D Results vs. Experimental Results

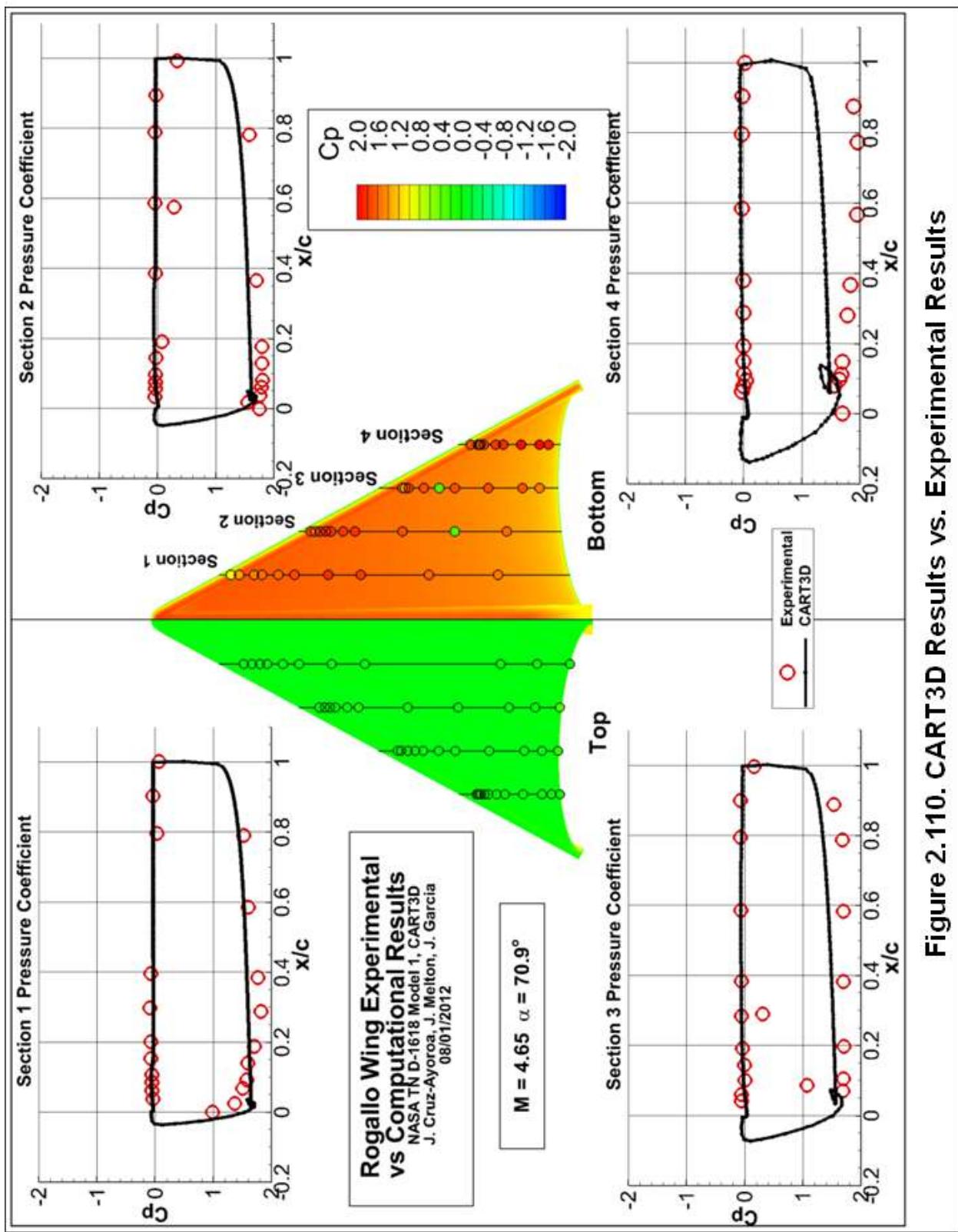


Figure 2.110. CART3D Results vs. Experimental Results

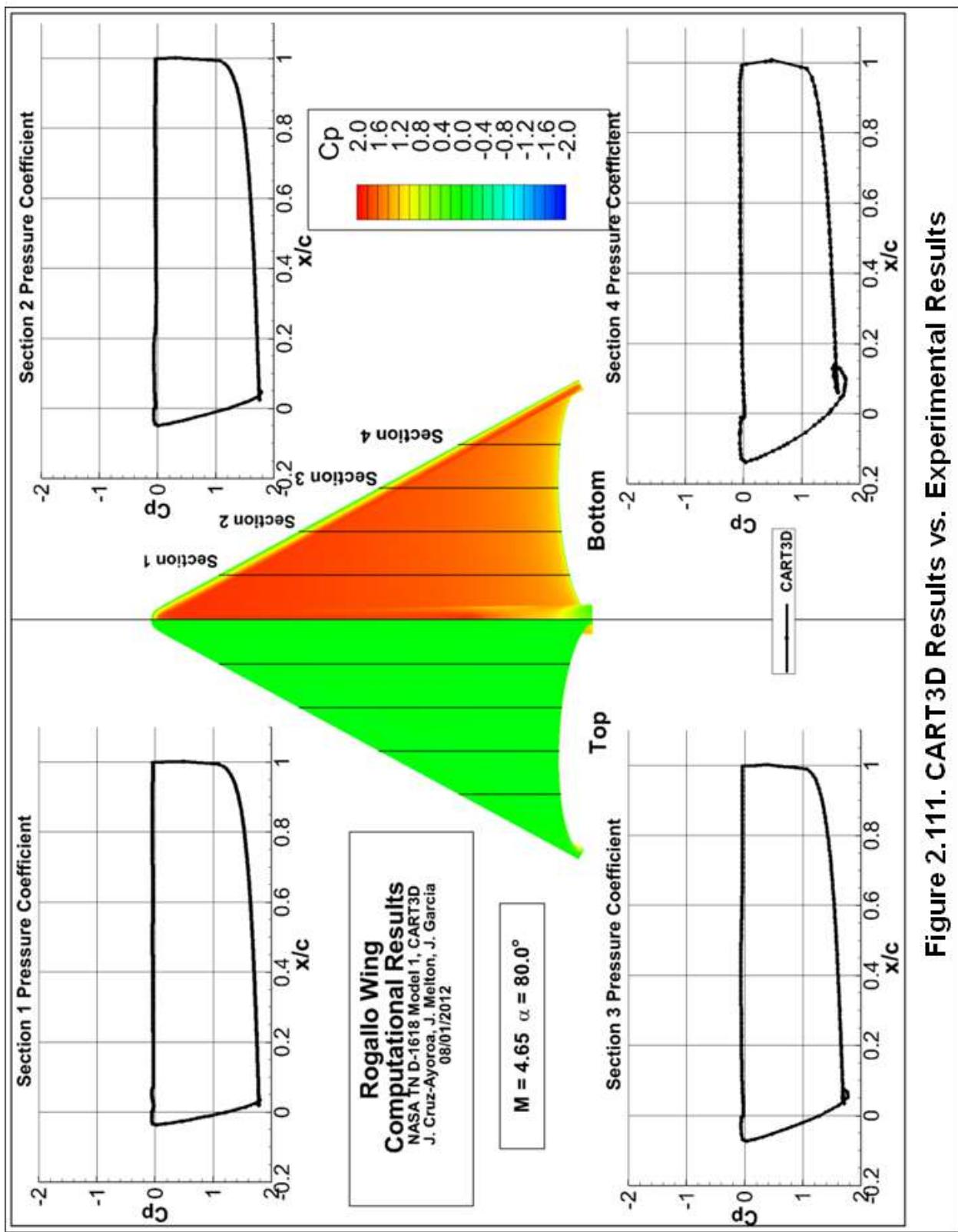


Figure 2.111. CART3D Results vs. Experimental Results

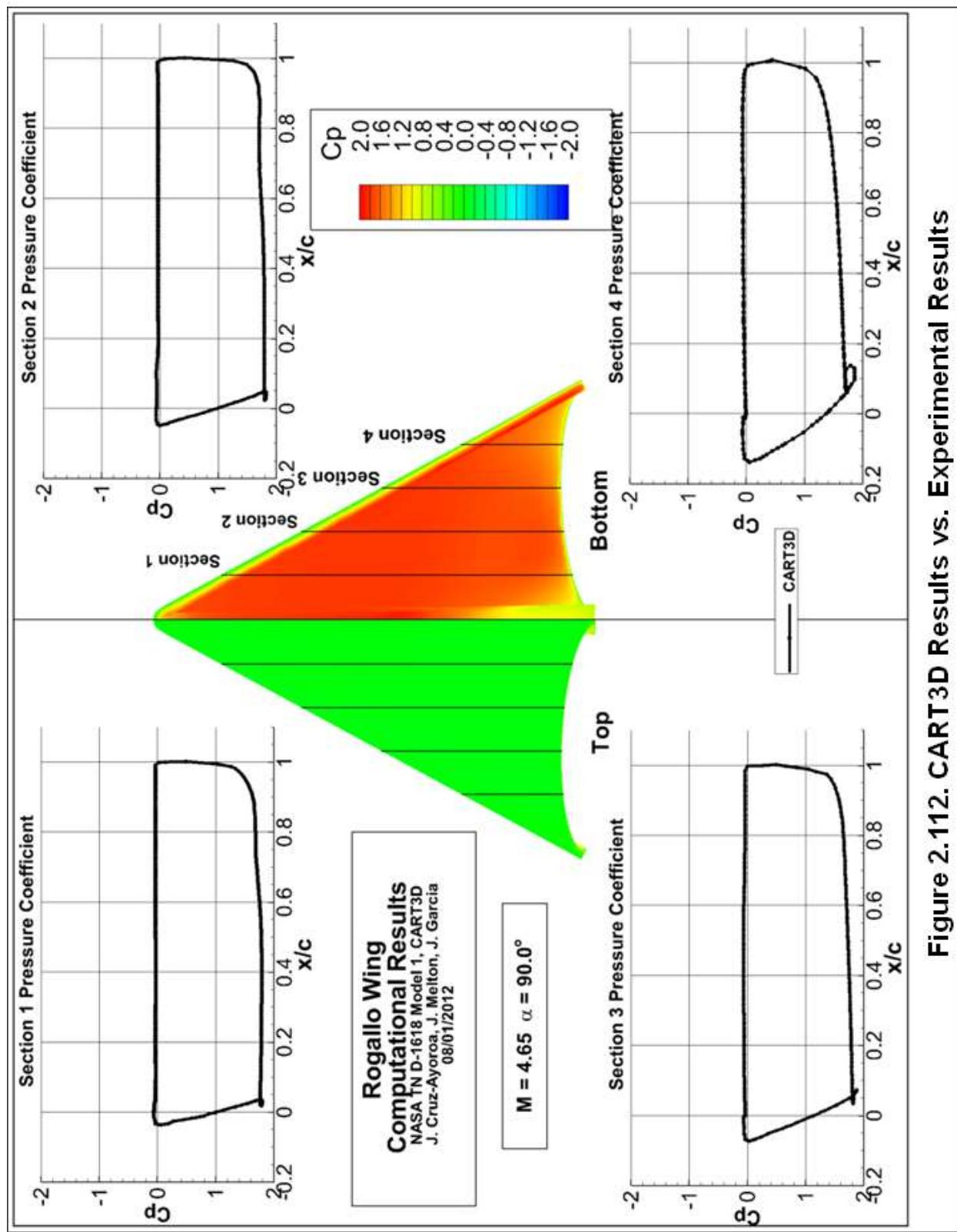
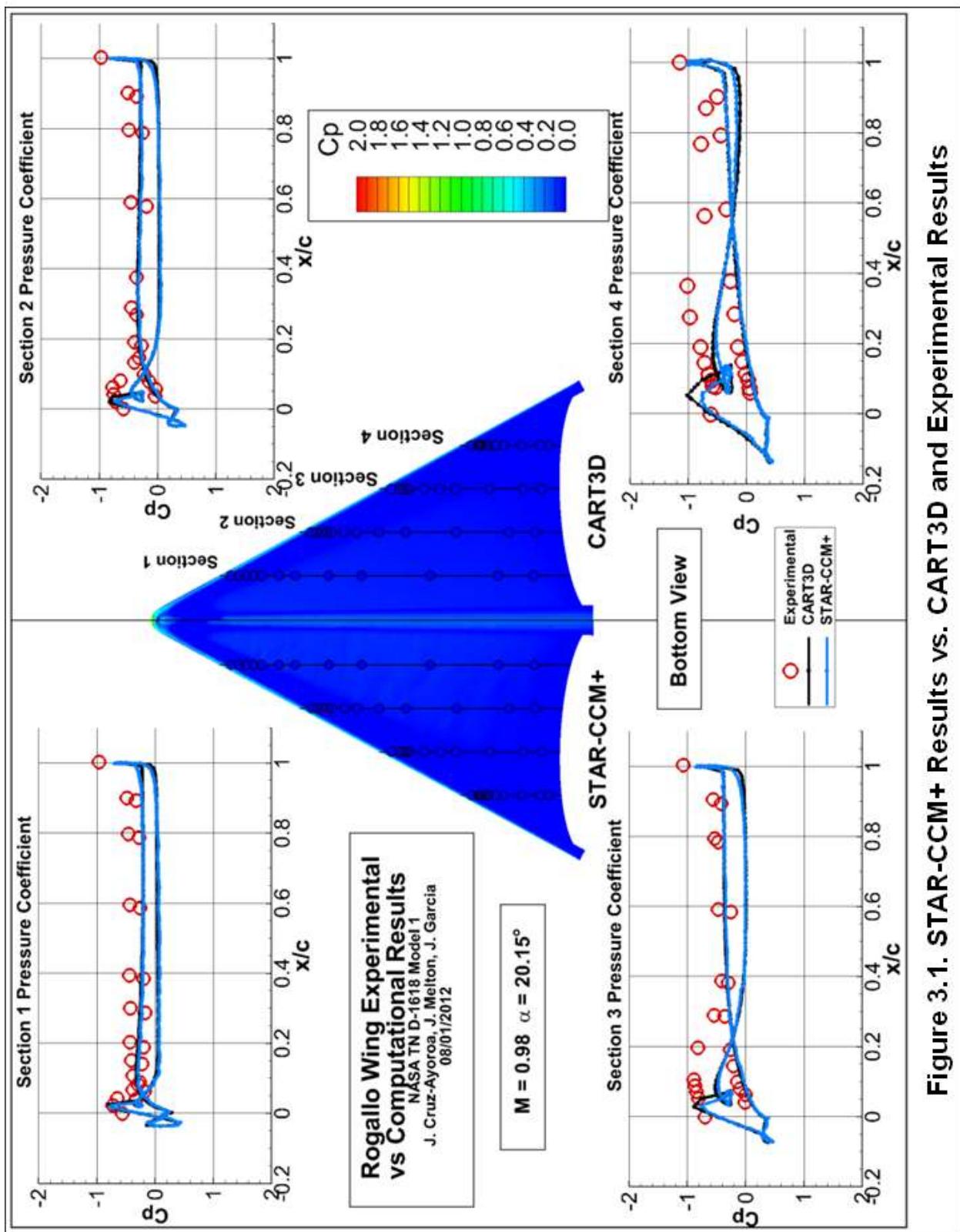


Figure 2.112. CART3D Results vs. Experimental Results



**Figure 3.1. STAR-CCM+ Results vs. CART3D and Experimental Results**

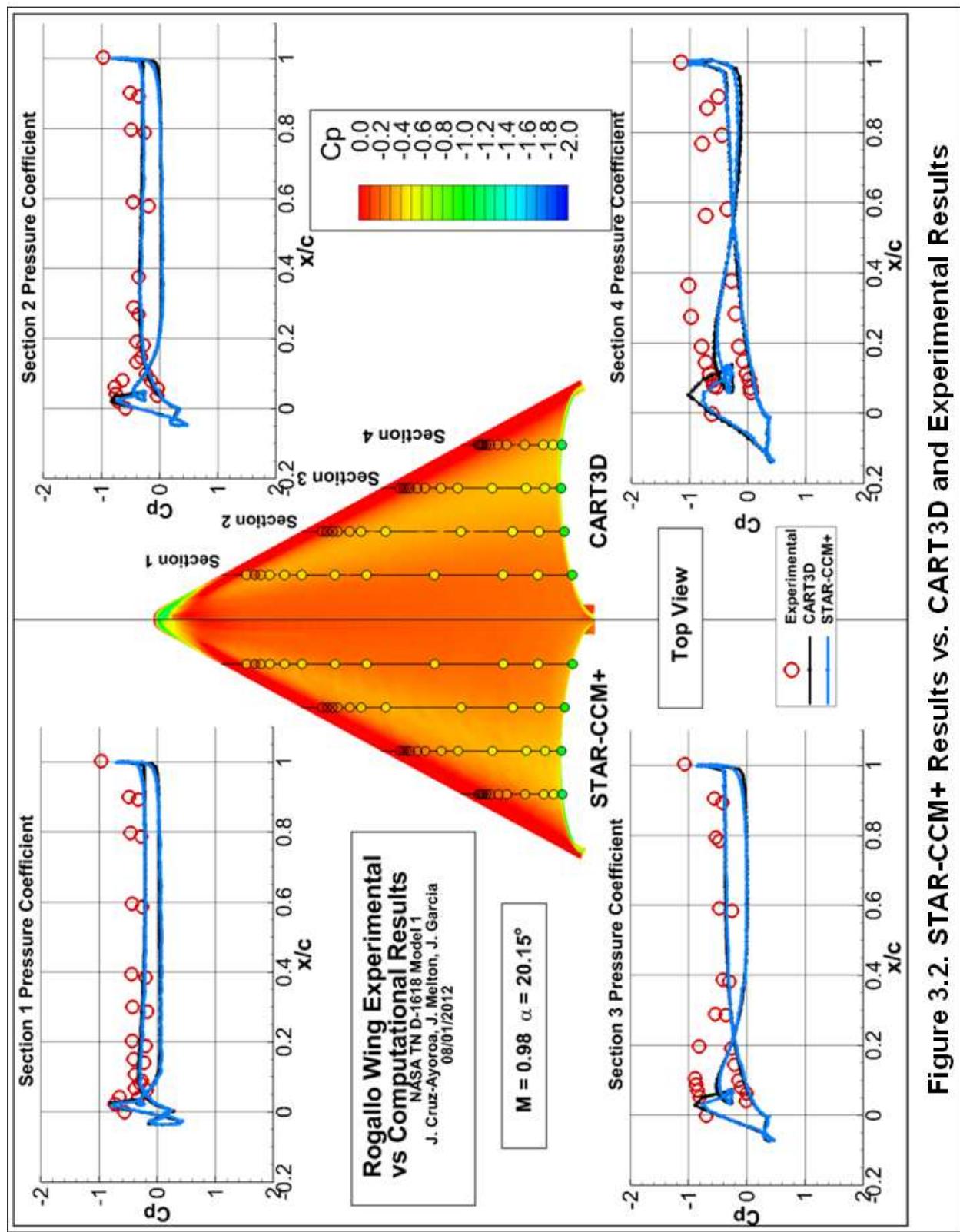


Figure 3.2. STAR-CCM+ Results vs. CART3D and Experimental Results

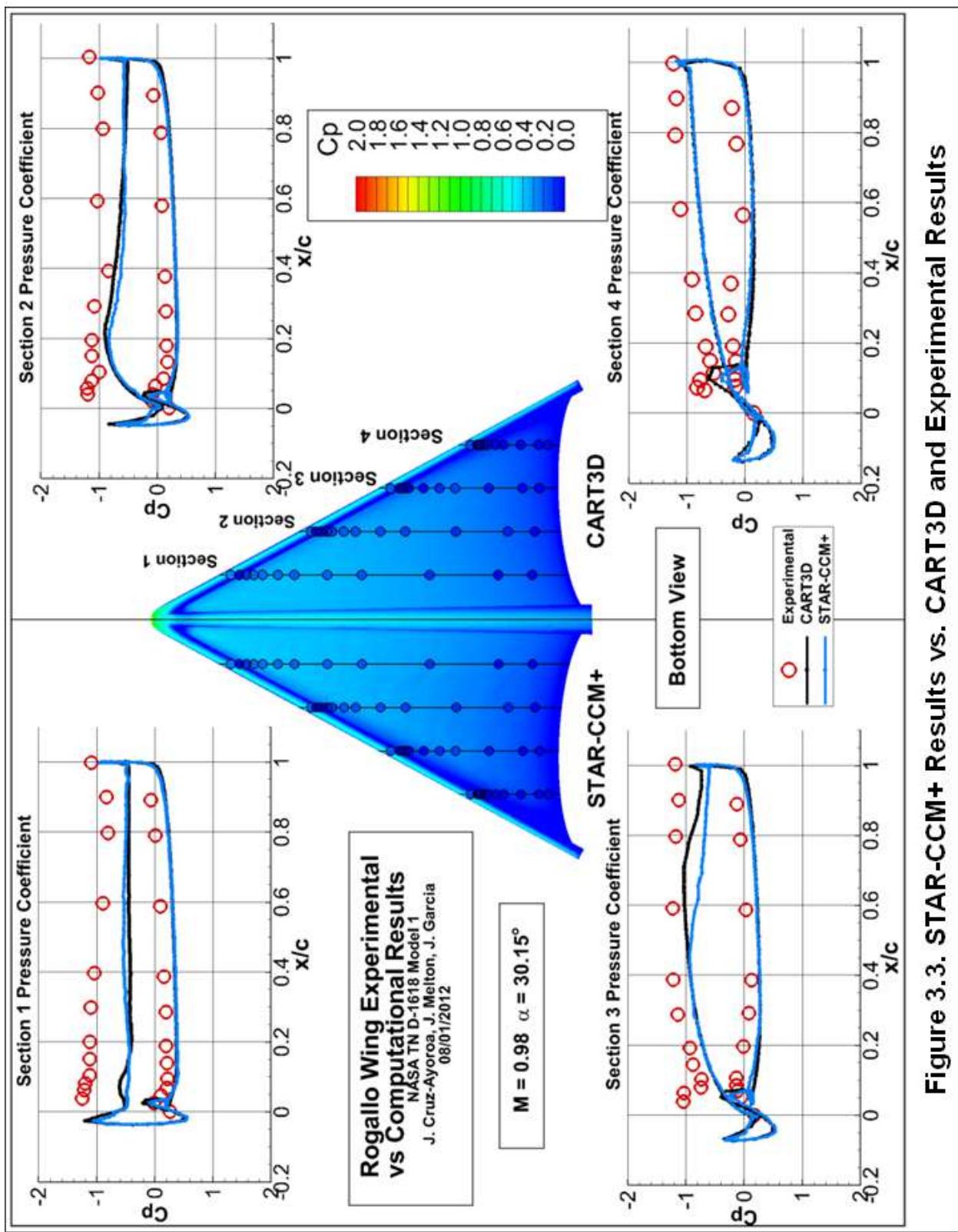


Figure 3.3. STAR-CCM+ Results vs. CART3D and Experimental Results

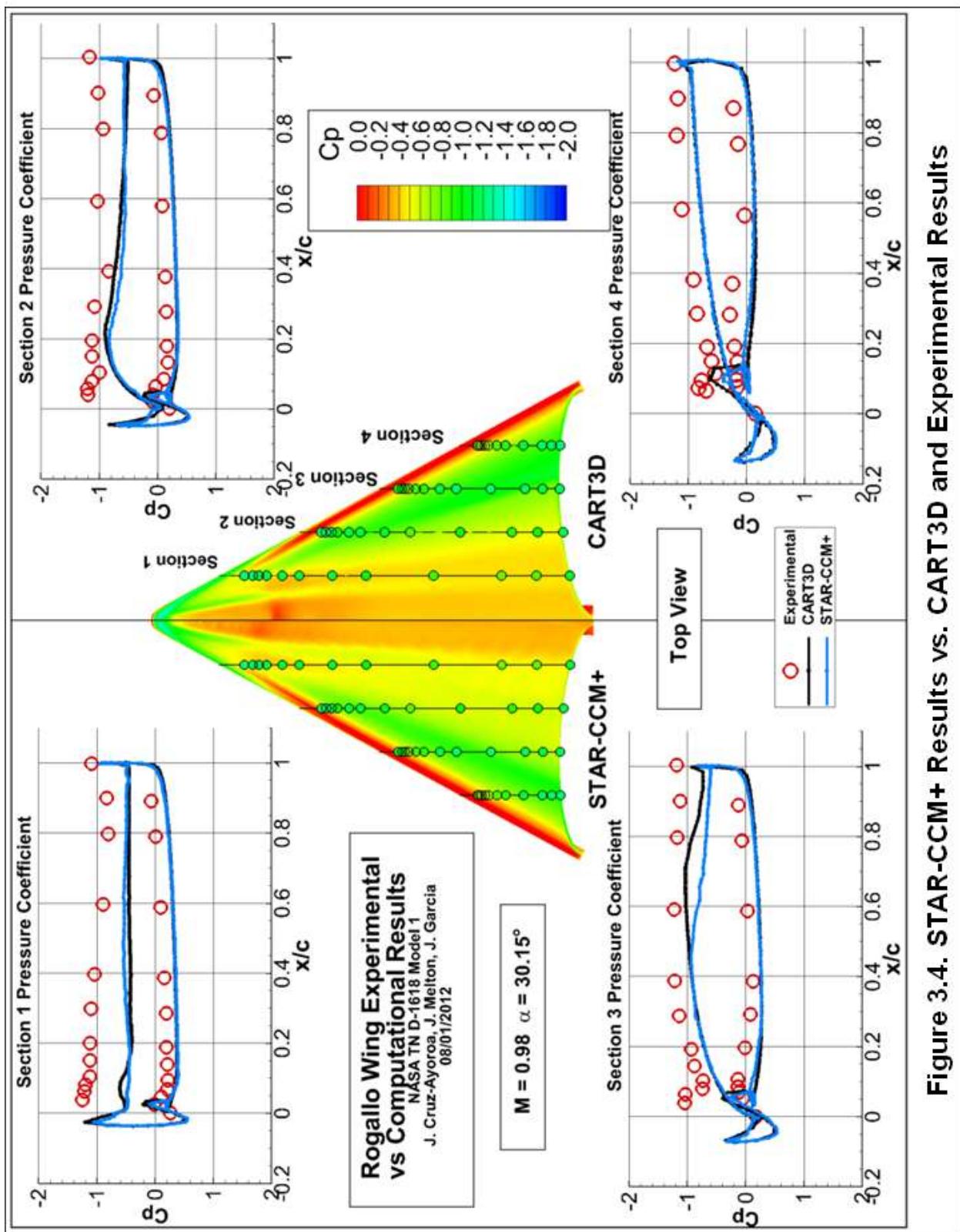


Figure 3.4. STAR-CCM+ Results vs. CART3D and Experimental Results

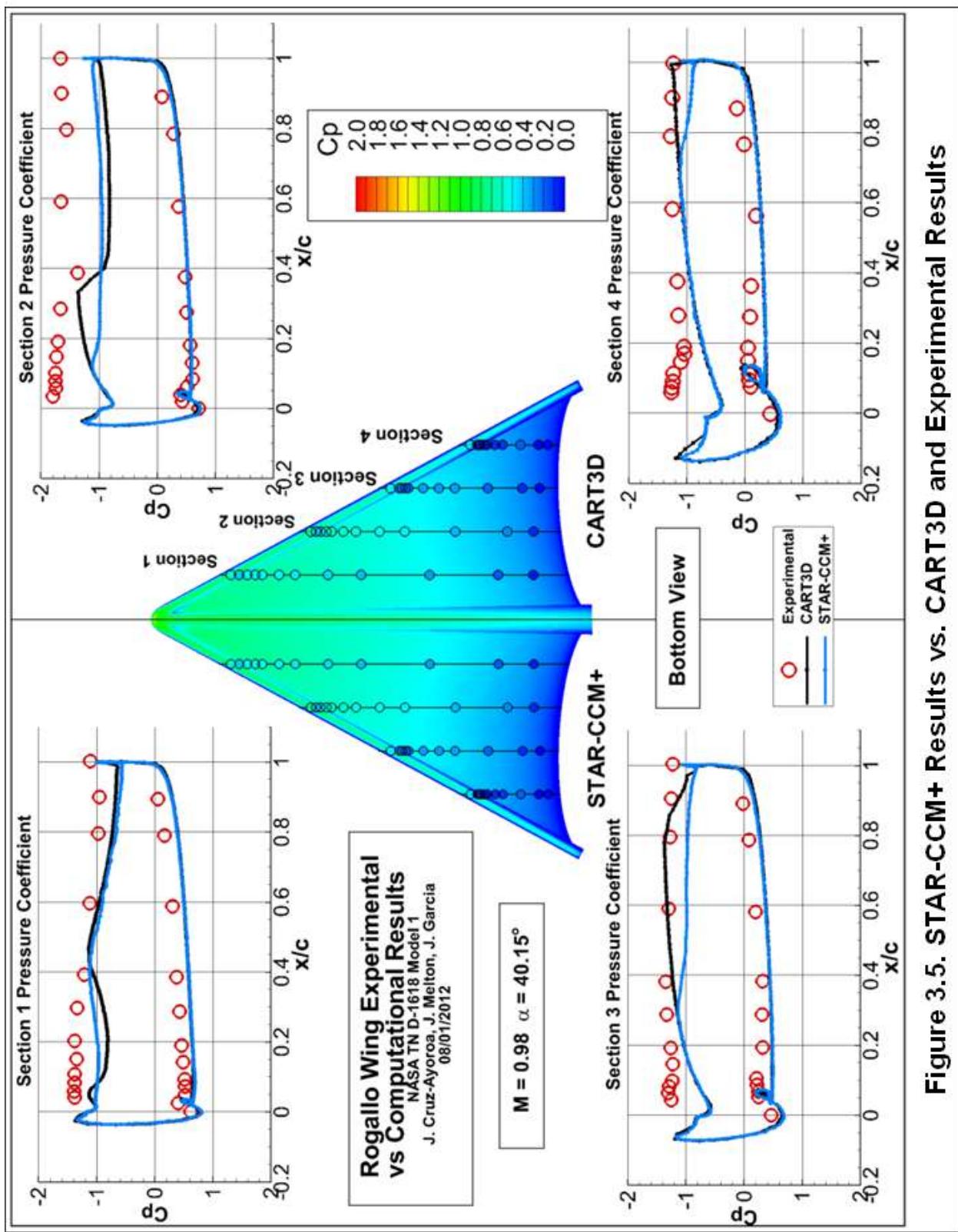


Figure 3.5. STAR-CCM+ Results vs. CART3D and Experimental Results

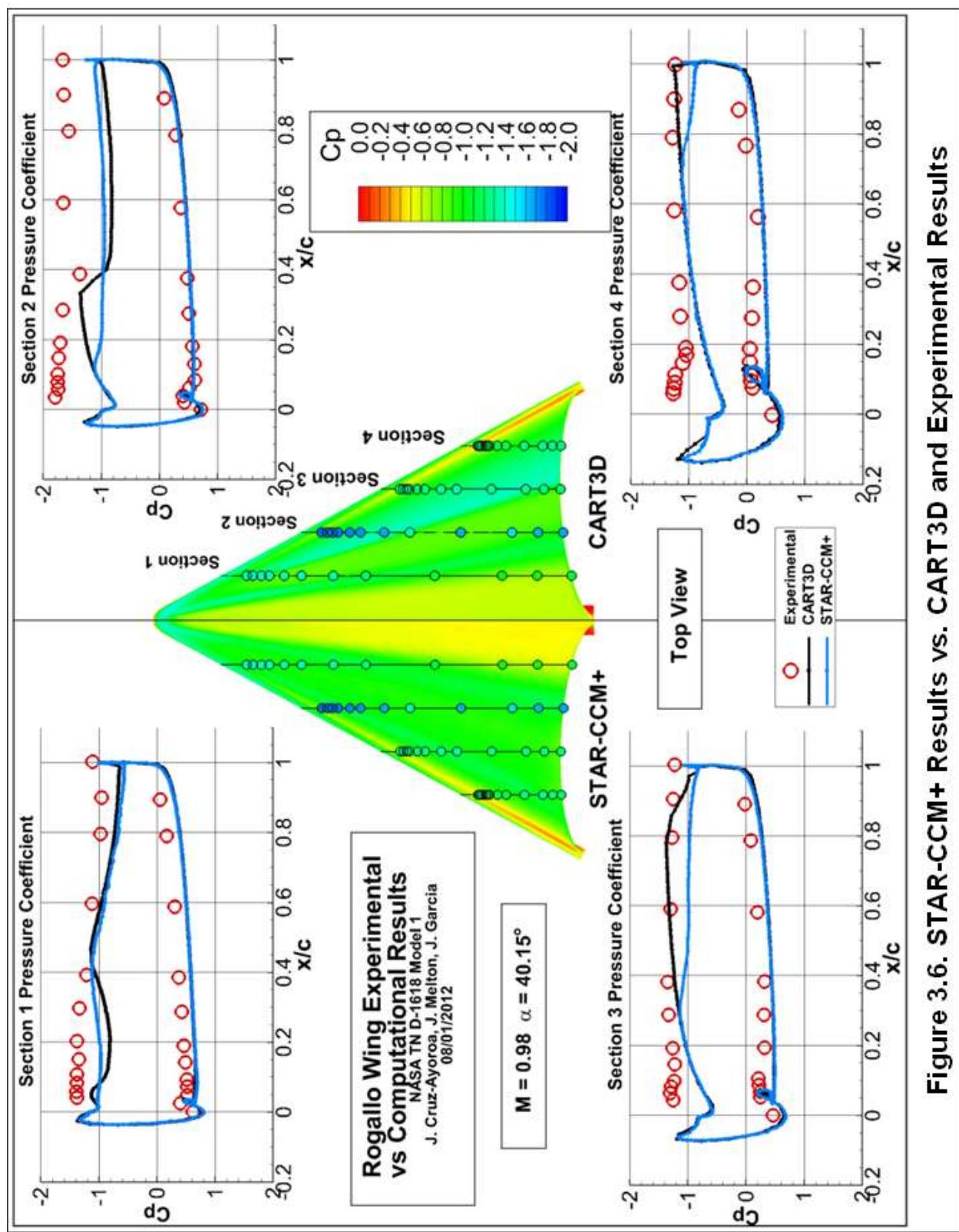
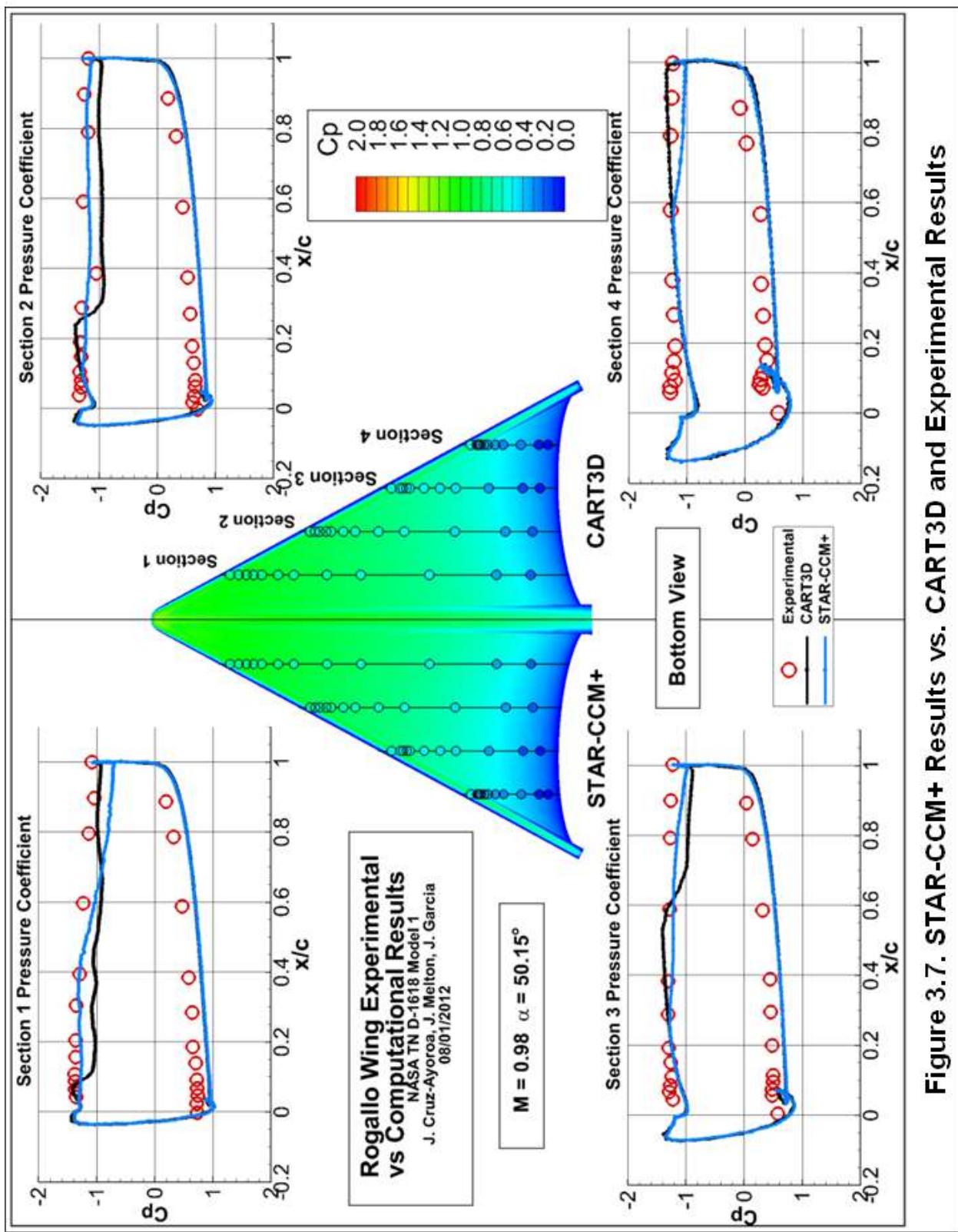


Figure 3.6. STAR-CCM+ Results vs. CART3D and Experimental Results



**Figure 3.7. STAR-CCM+ Results vs. CART3D and Experimental Results**

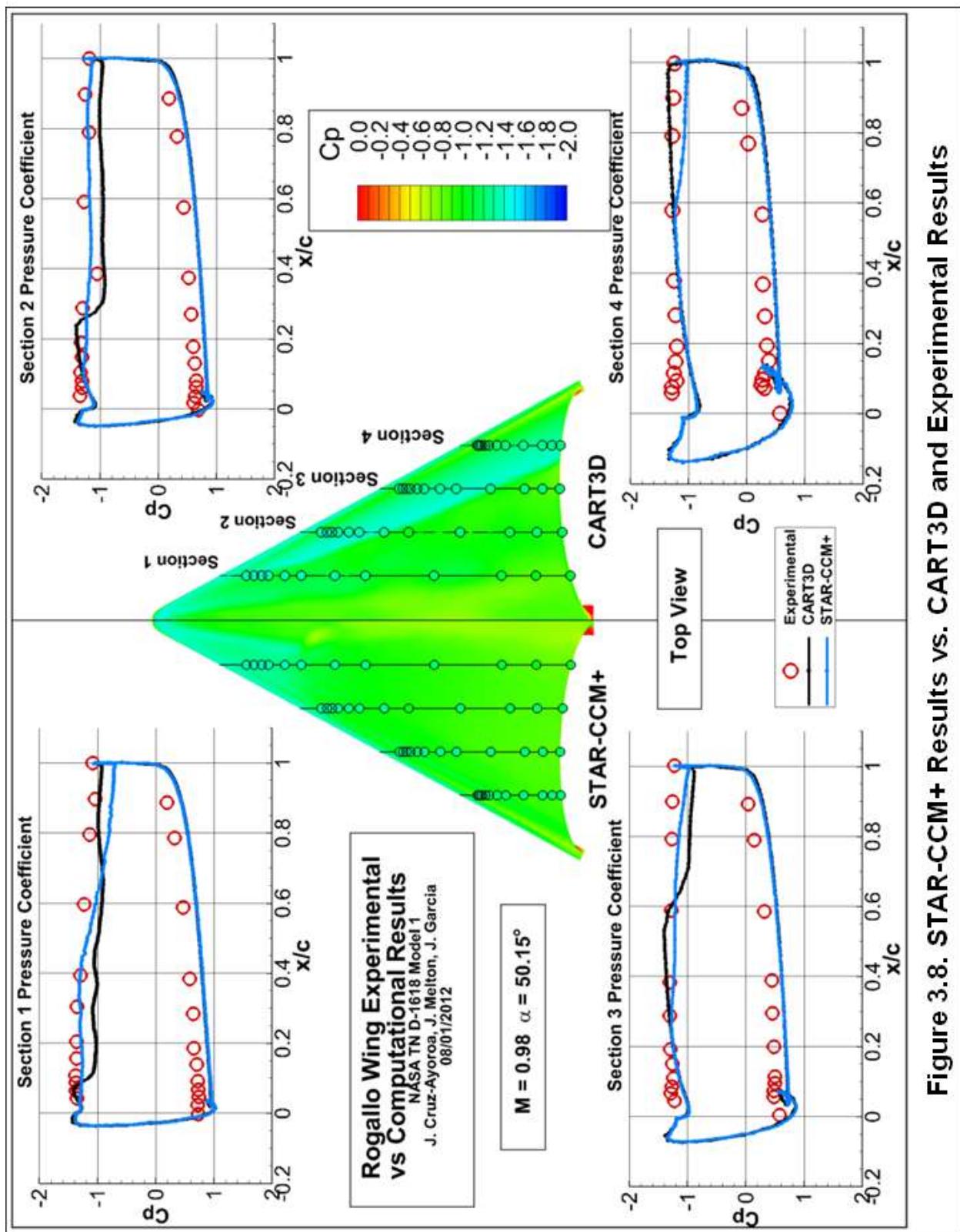


Figure 3.8. STAR-CCM+ Results vs. CART3D and Experimental Results

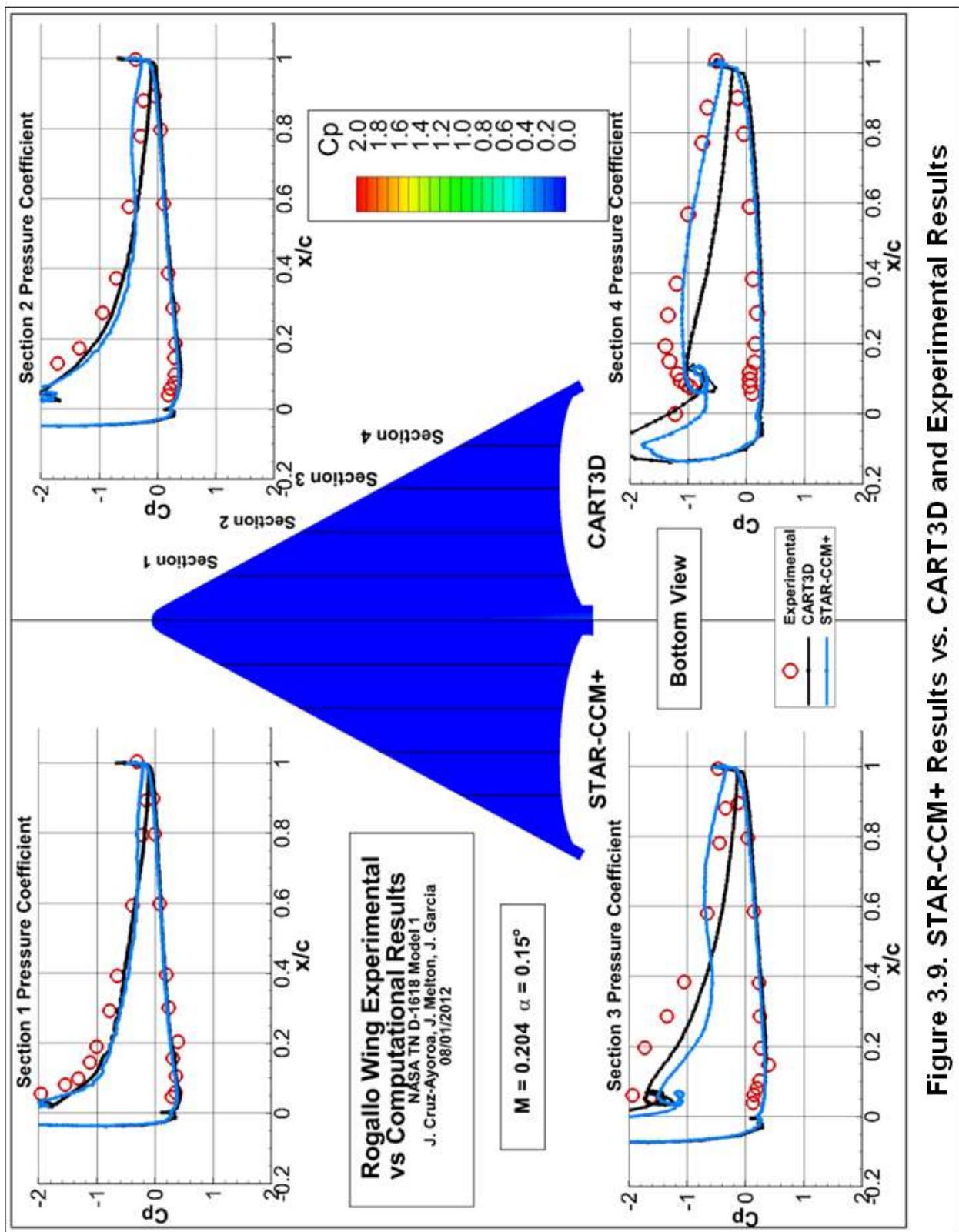
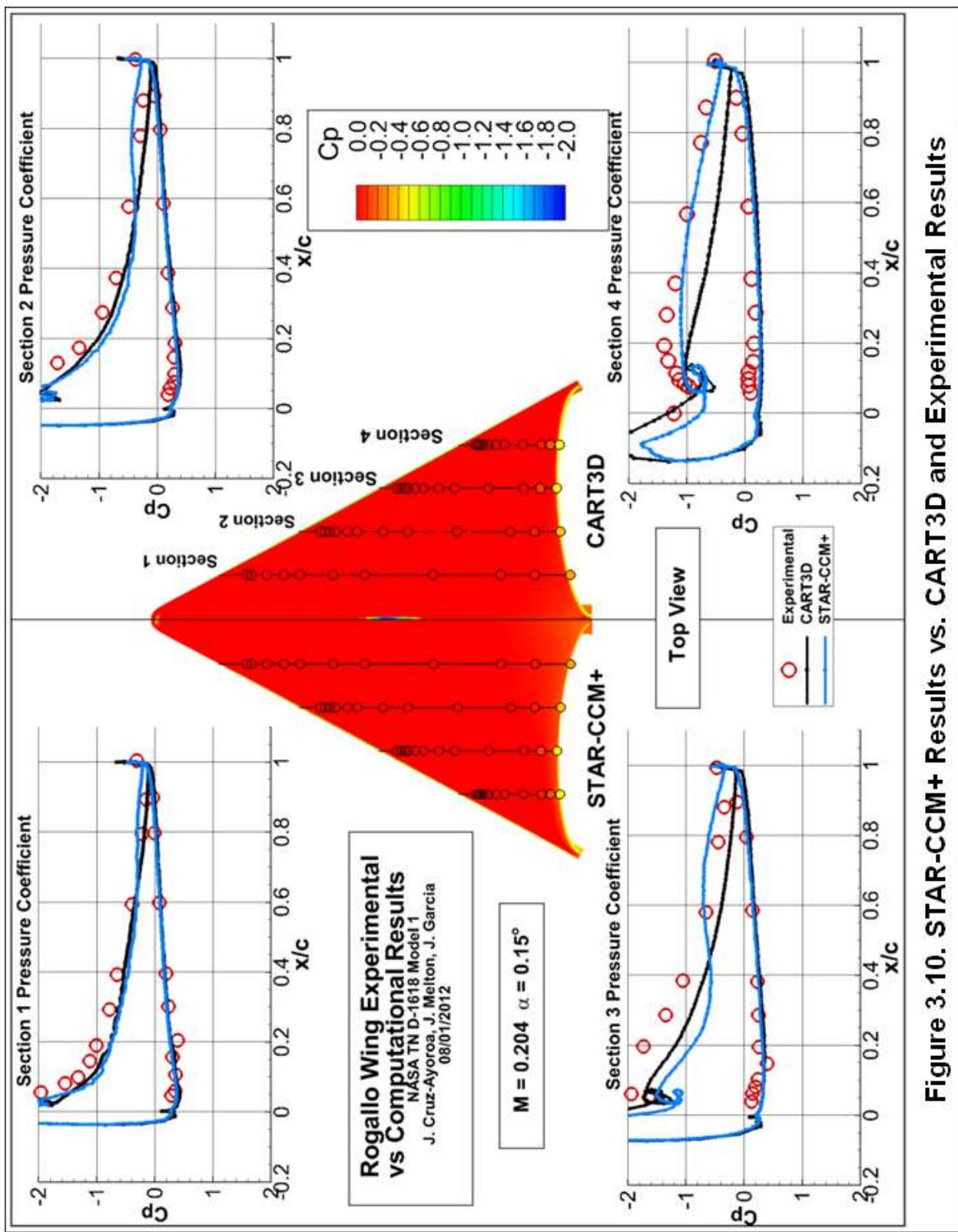
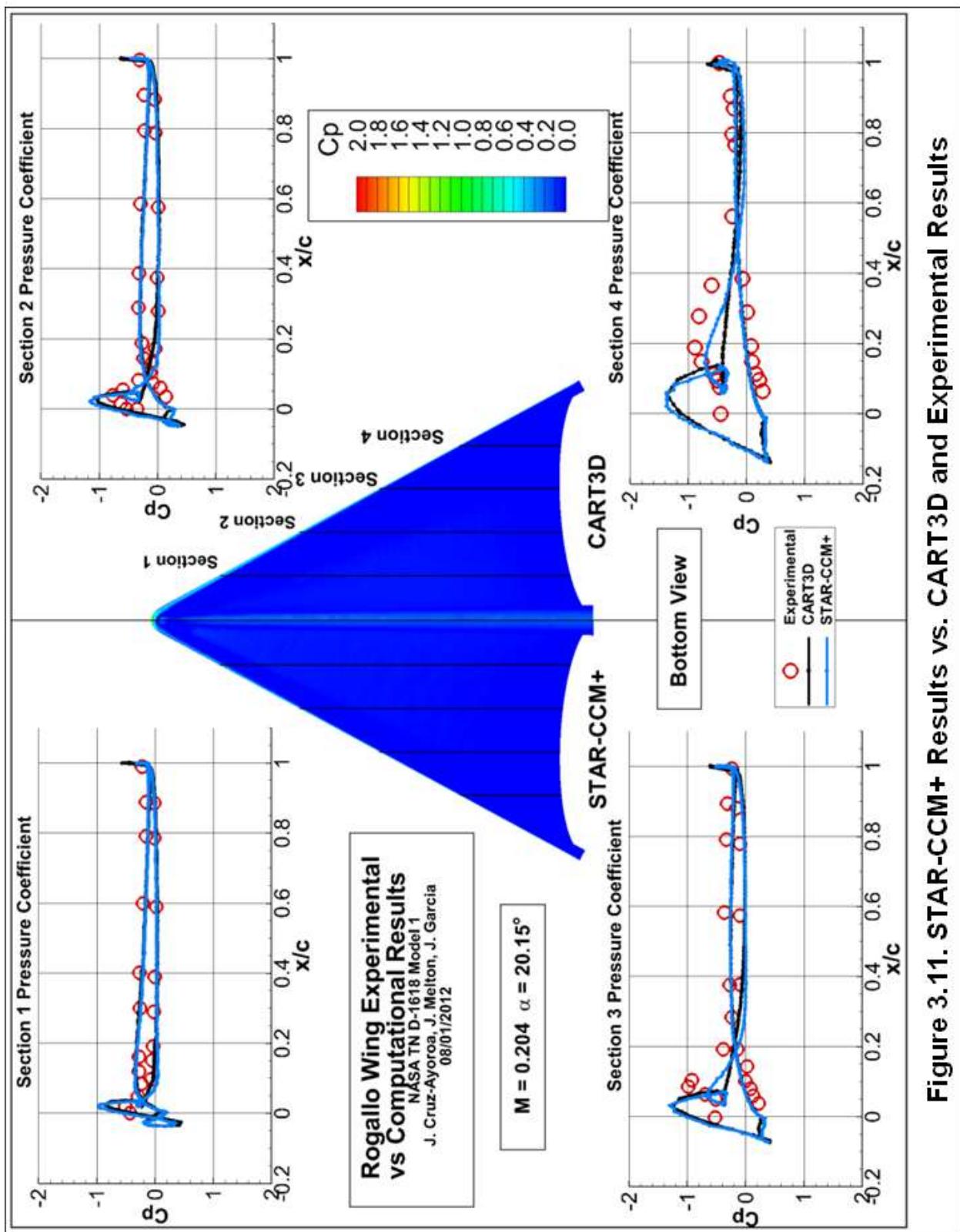


Figure 3.9. STAR-CCM+ Results vs. CART3D and Experimental Results



**Figure 3.10. STAR-CCM+ Results vs. CART3D and Experimental Results**



**Figure 3.11. STAR-CCM+ Results vs. CART3D and Experimental Results**

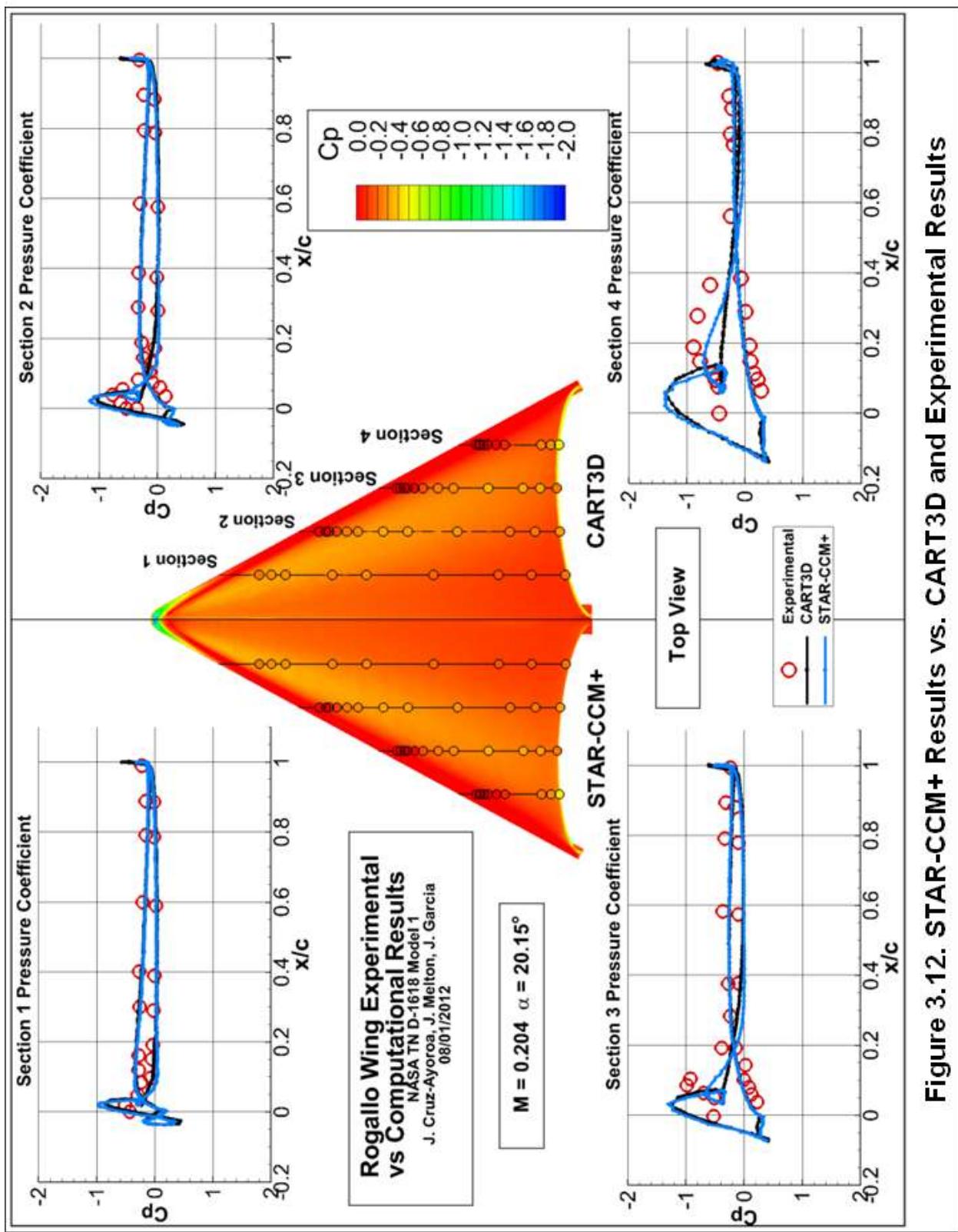


**Figure 3.12. STAR-CCM+ Results vs. CART3D and Experimental Results**

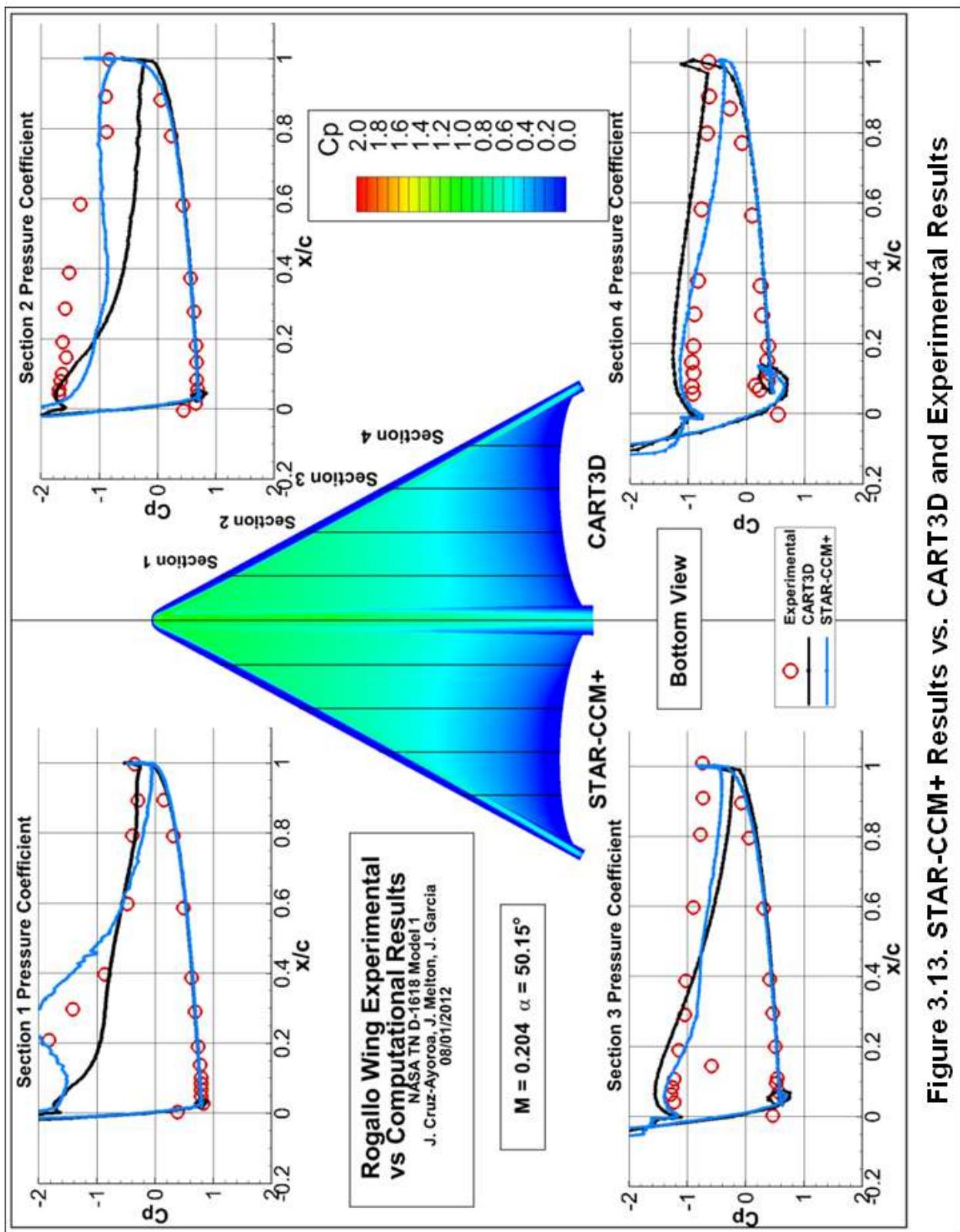


**Figure 3.13. STAR-CCM+ Results vs. CART3D and Experimental Results**

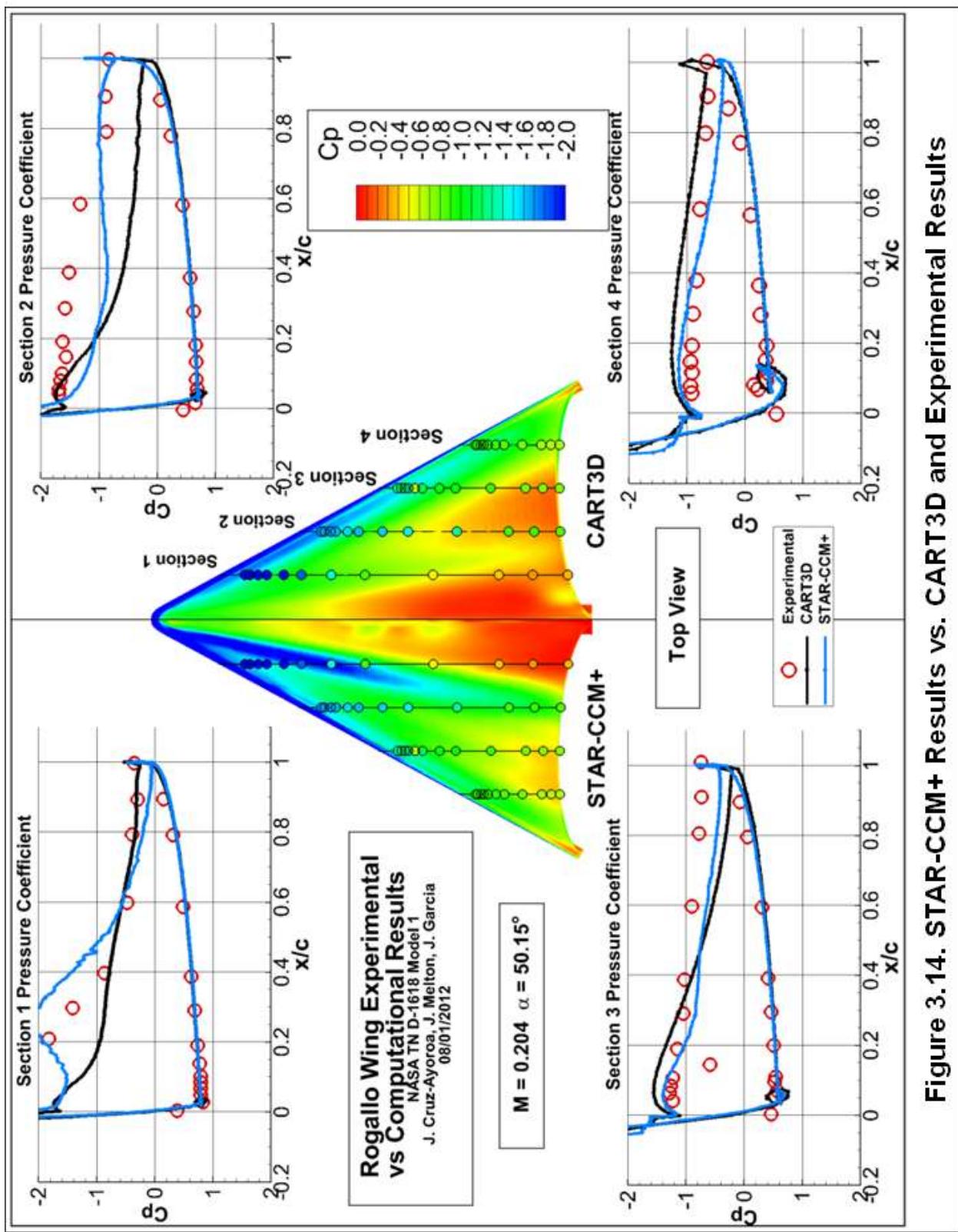


**Figure 3.14. STAR-CCM+ Results vs. CART3D and Experimental Results**

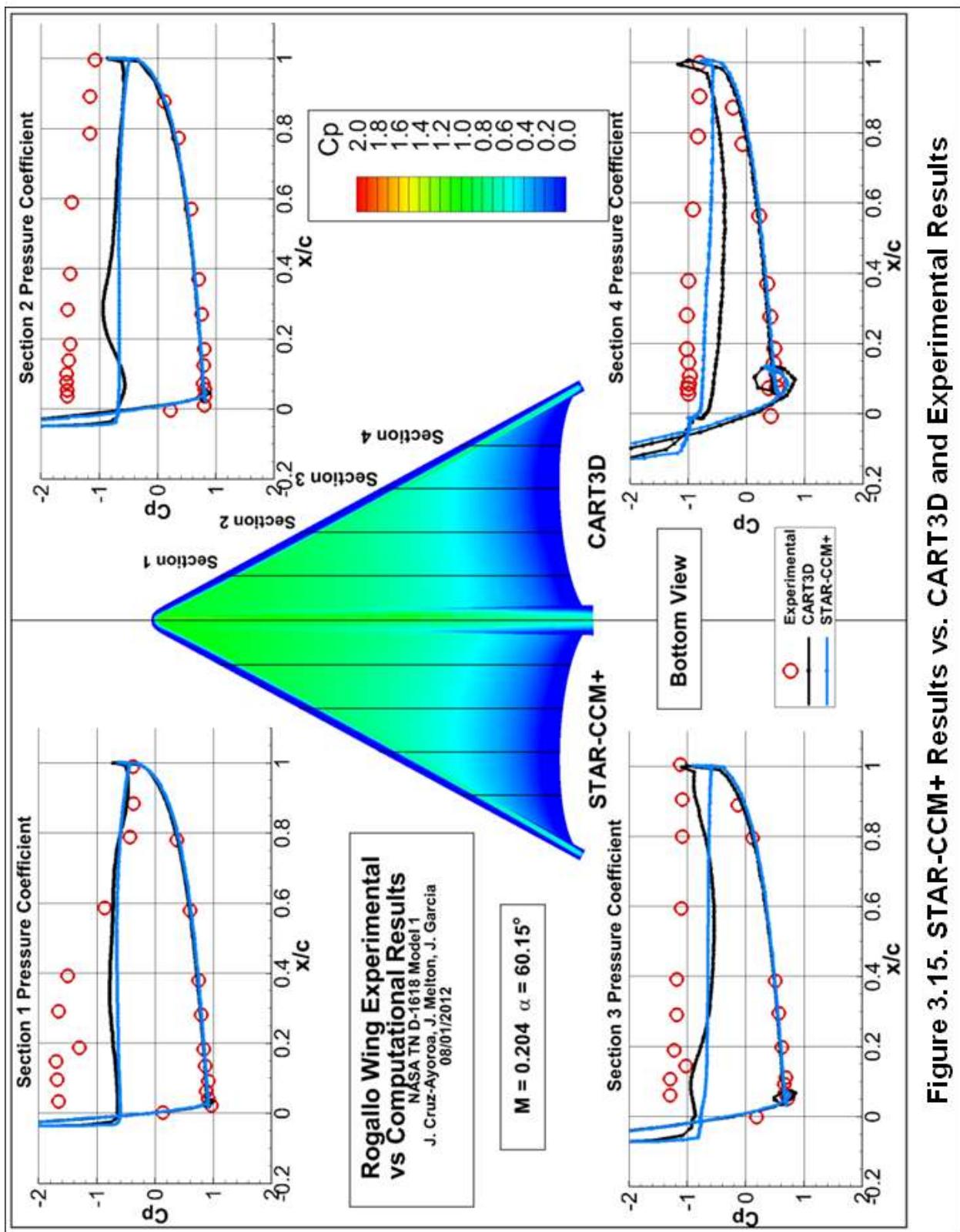


**Figure 3.15. STAR-CCM+ Results vs. CART3D and Experimental Results**

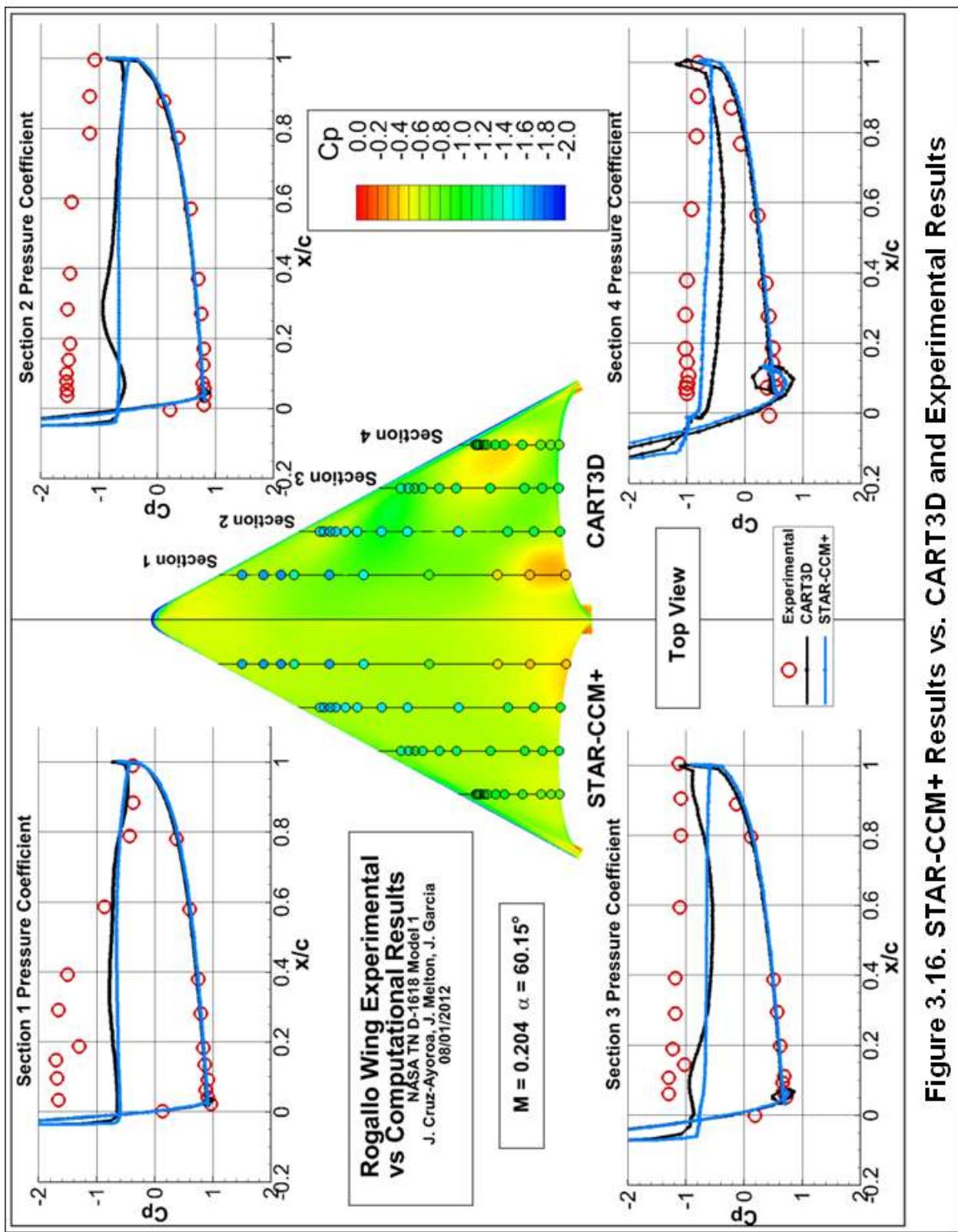


**Figure 3.16. STAR-CCM+ Results vs. CART3D and Experimental Results**

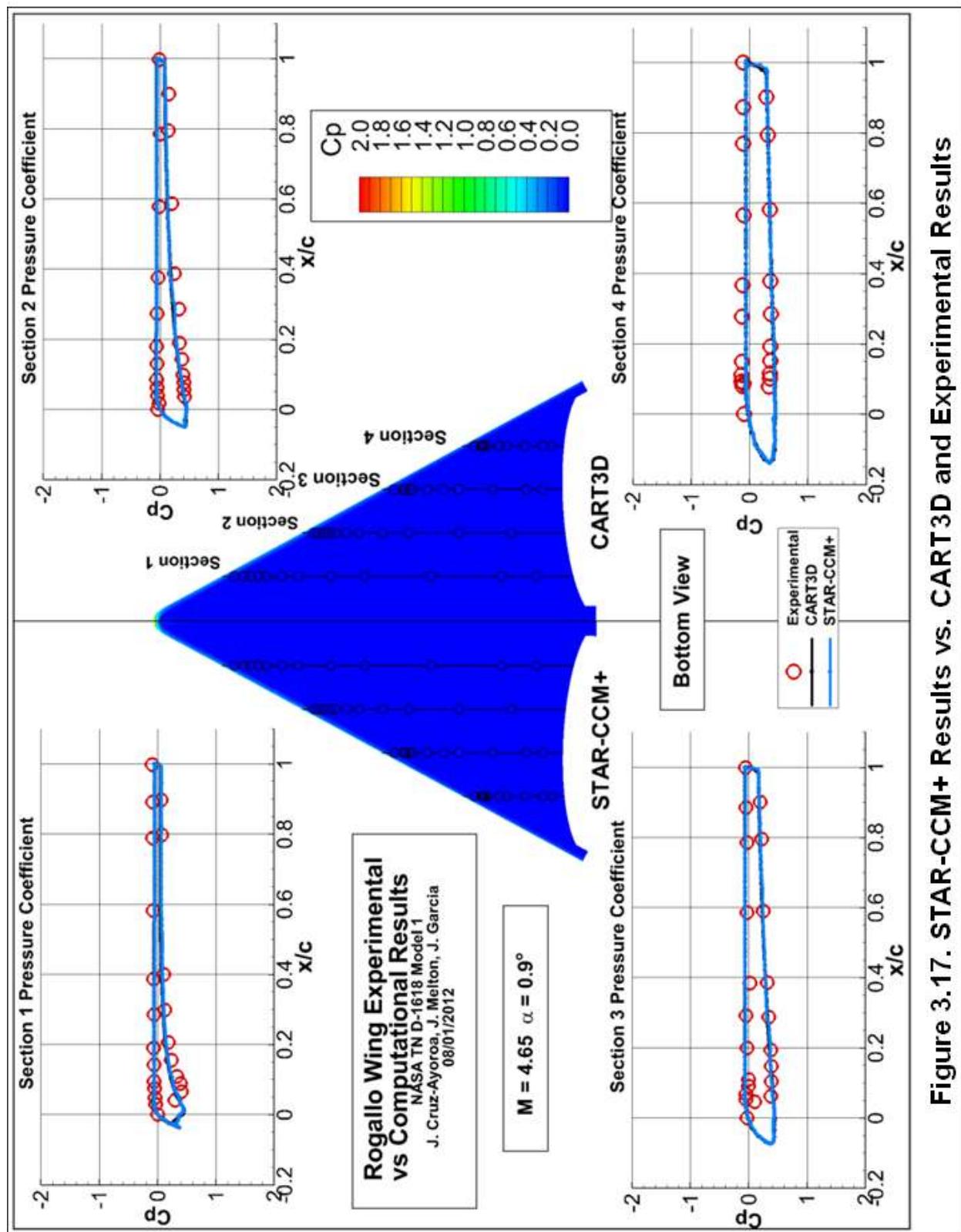
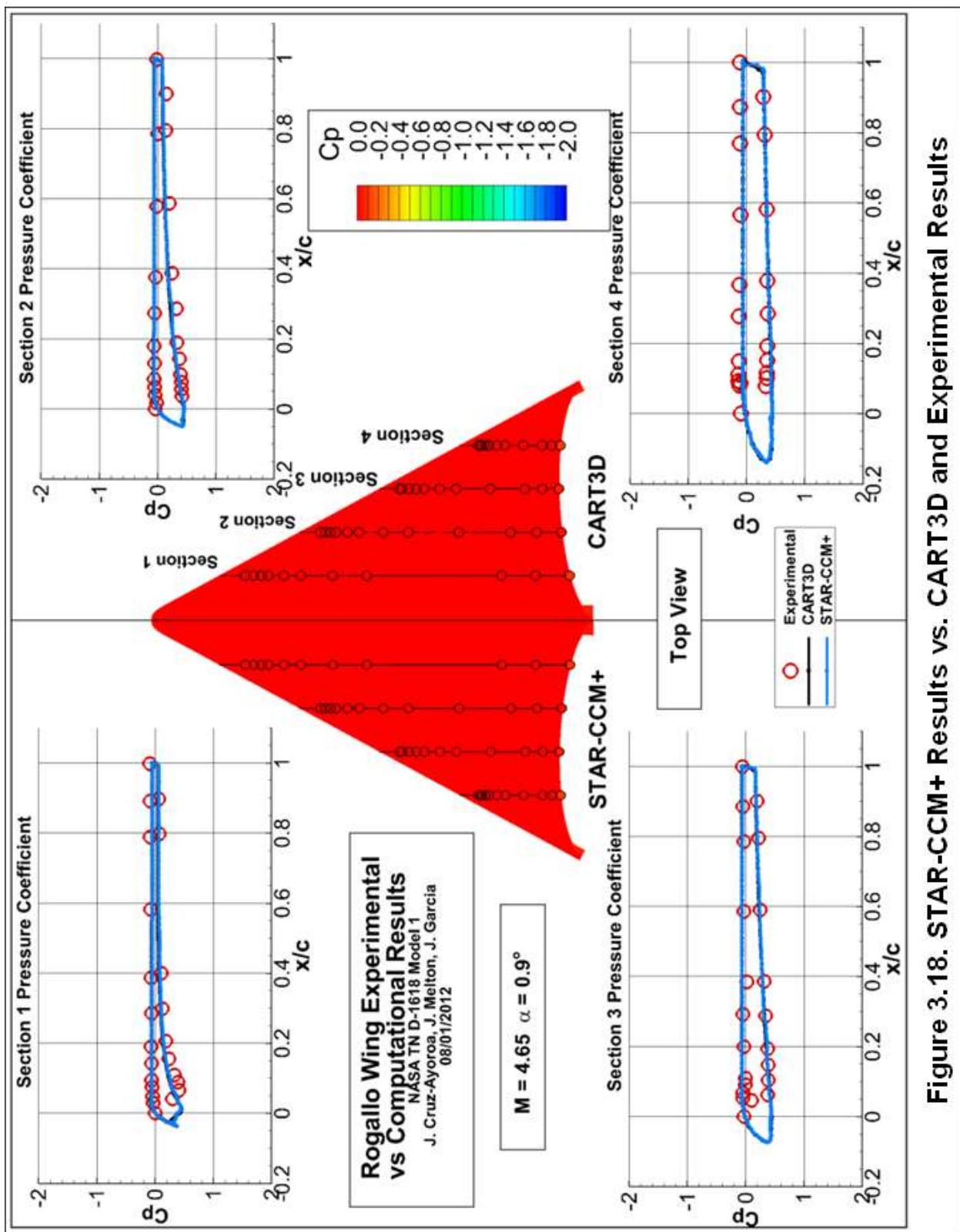


Figure 3.17. STAR-CCM+ Results vs. CART3D and Experimental Results



**Figure 3.18. STAR-CCM+ Results vs. CART3D and Experimental Results**

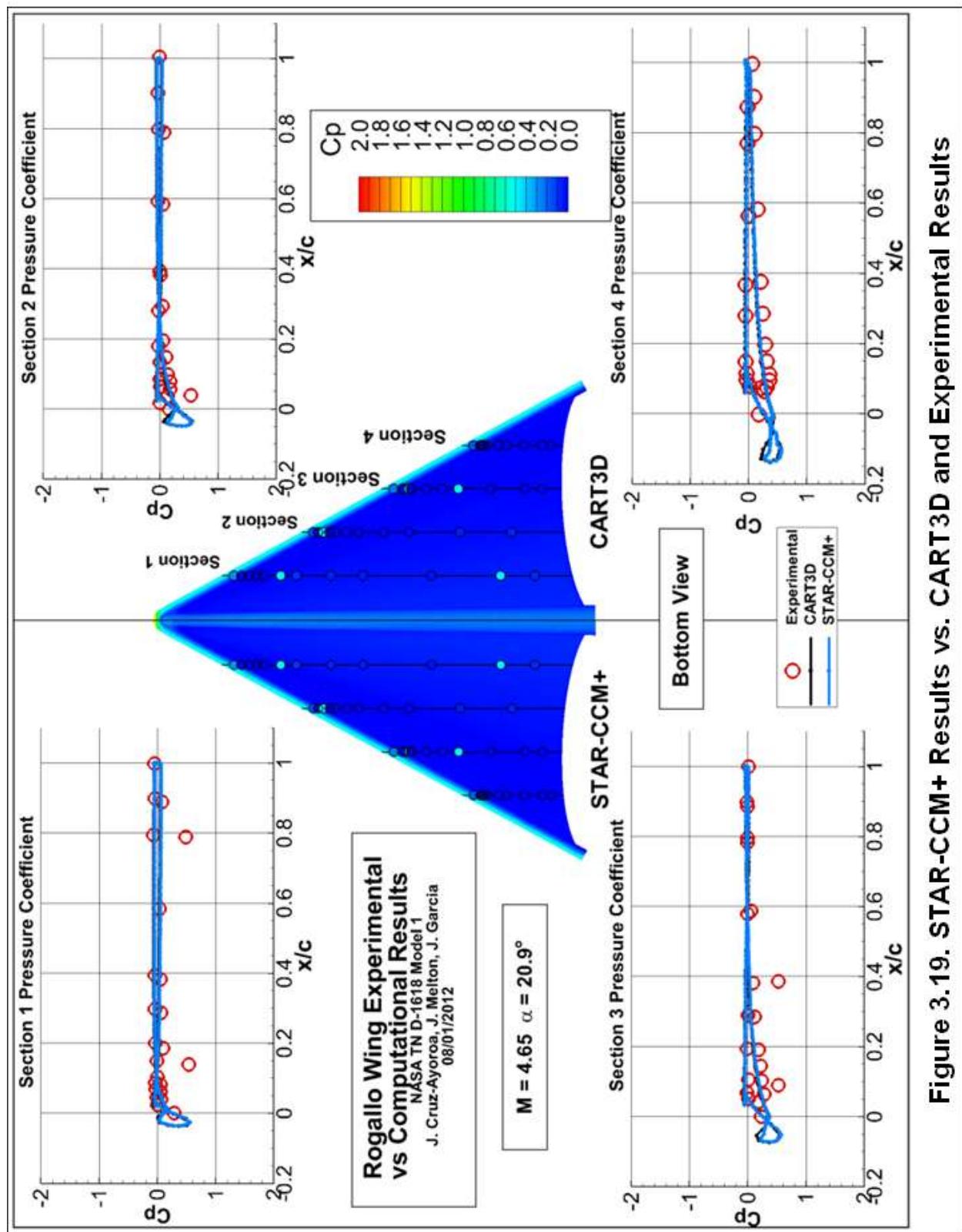
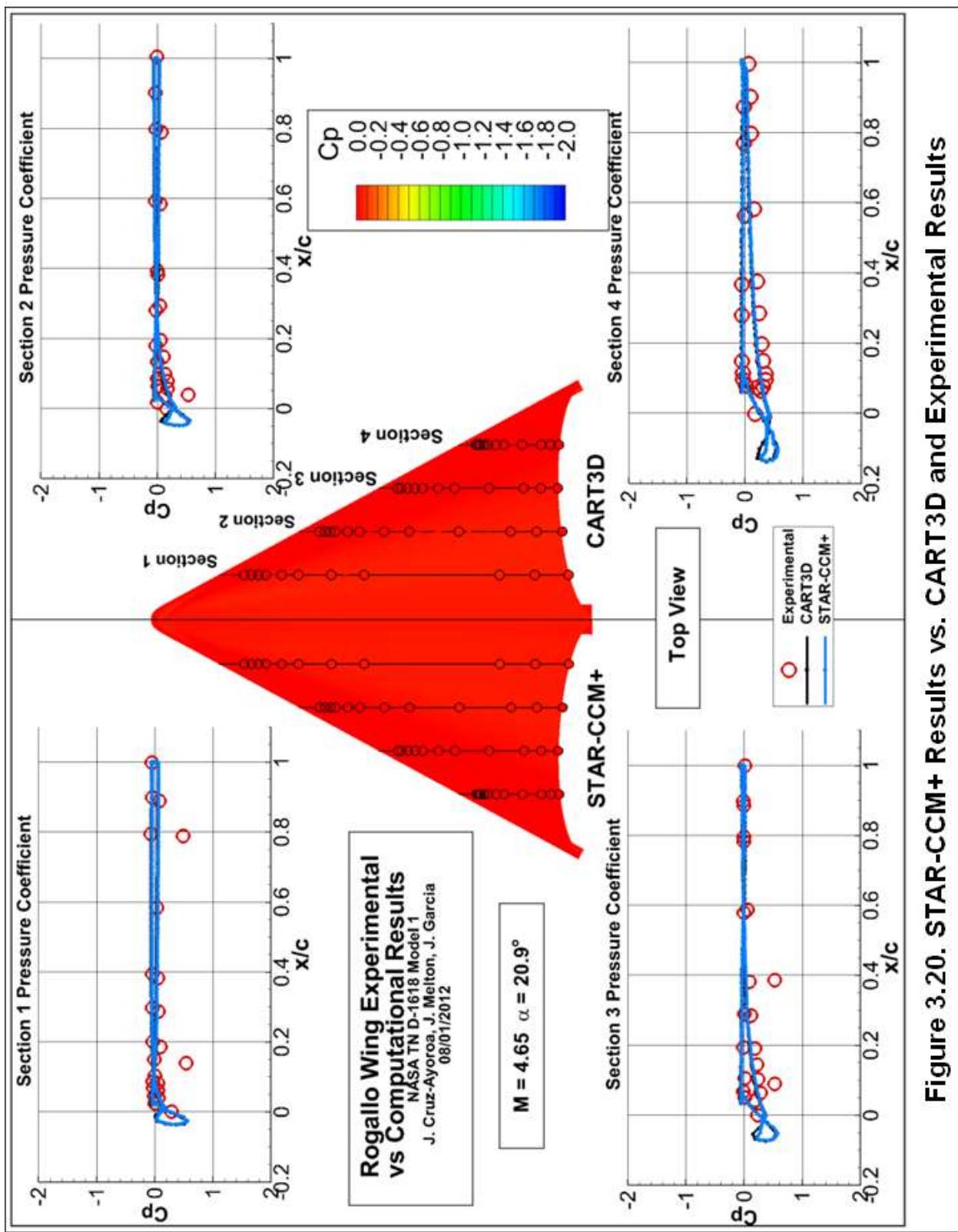
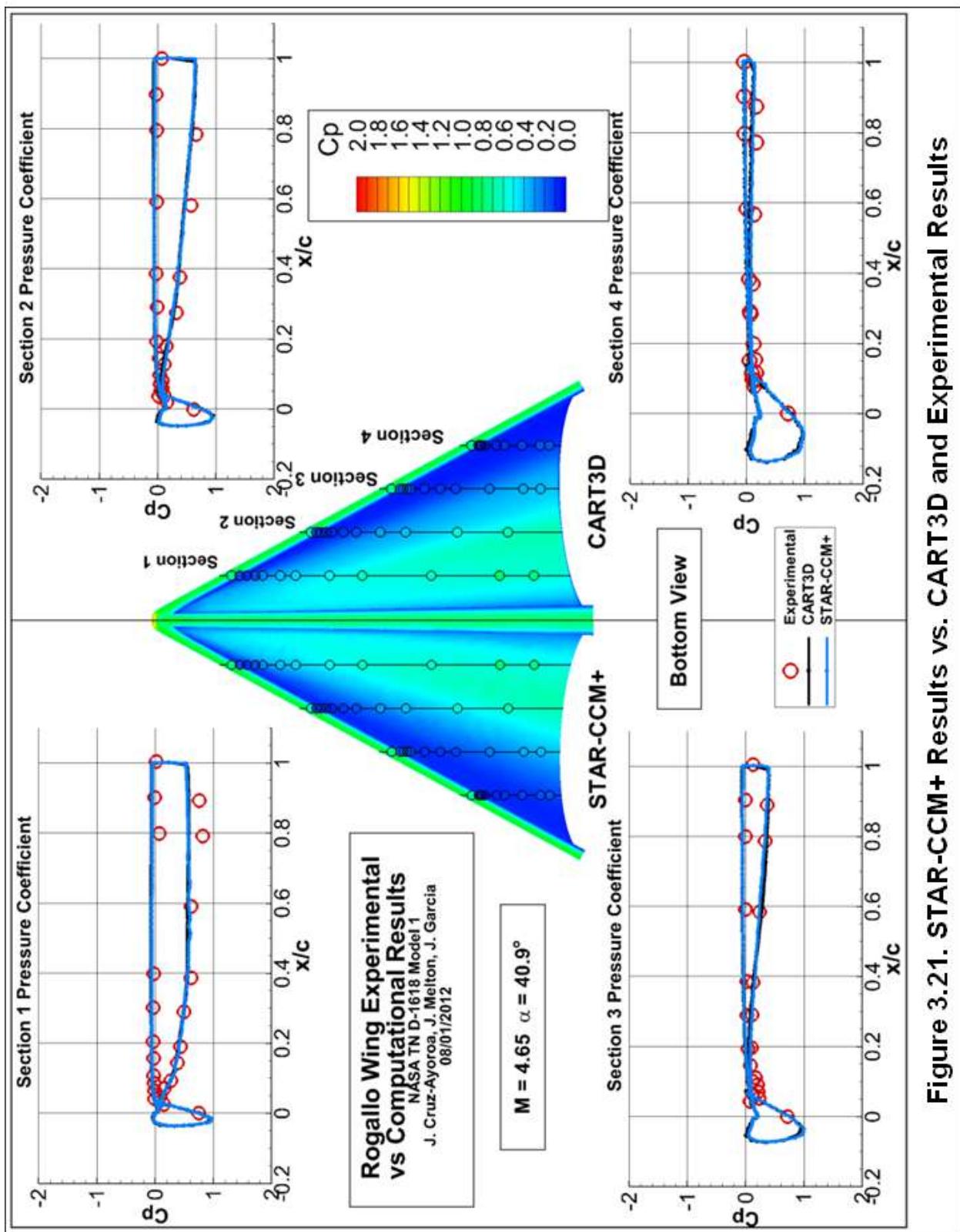


Figure 3.19. STAR-CCM+ Results vs. CART3D and Experimental Results



**Figure 3.20. STAR-CCM+ Results vs. CART3D and Experimental Results**



**Figure 3.21. STAR-CCM+ Results vs. CART3D and Experimental Results**

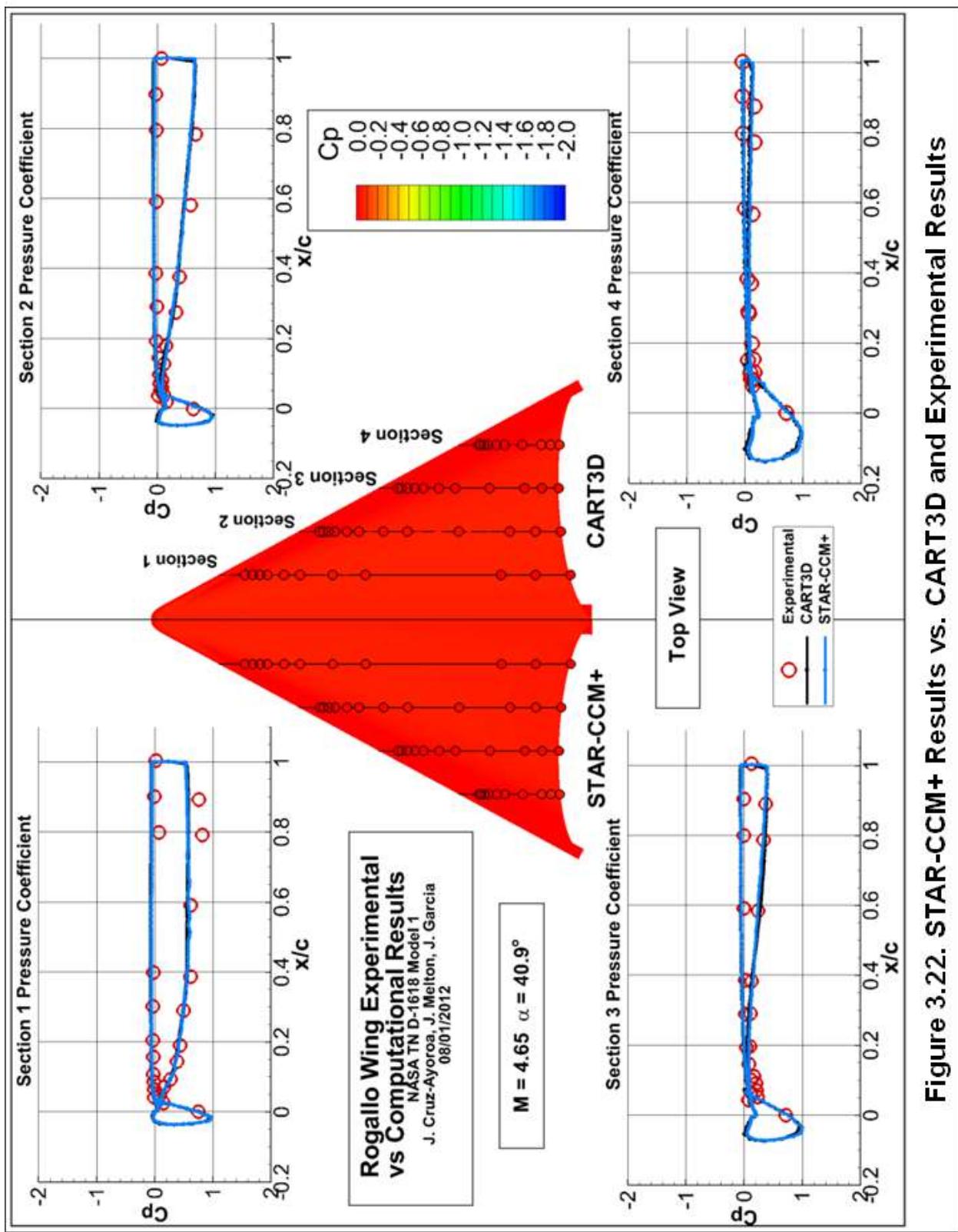


**Figure 3.22. STAR-CCM+ Results vs. CART3D and Experimental Results**

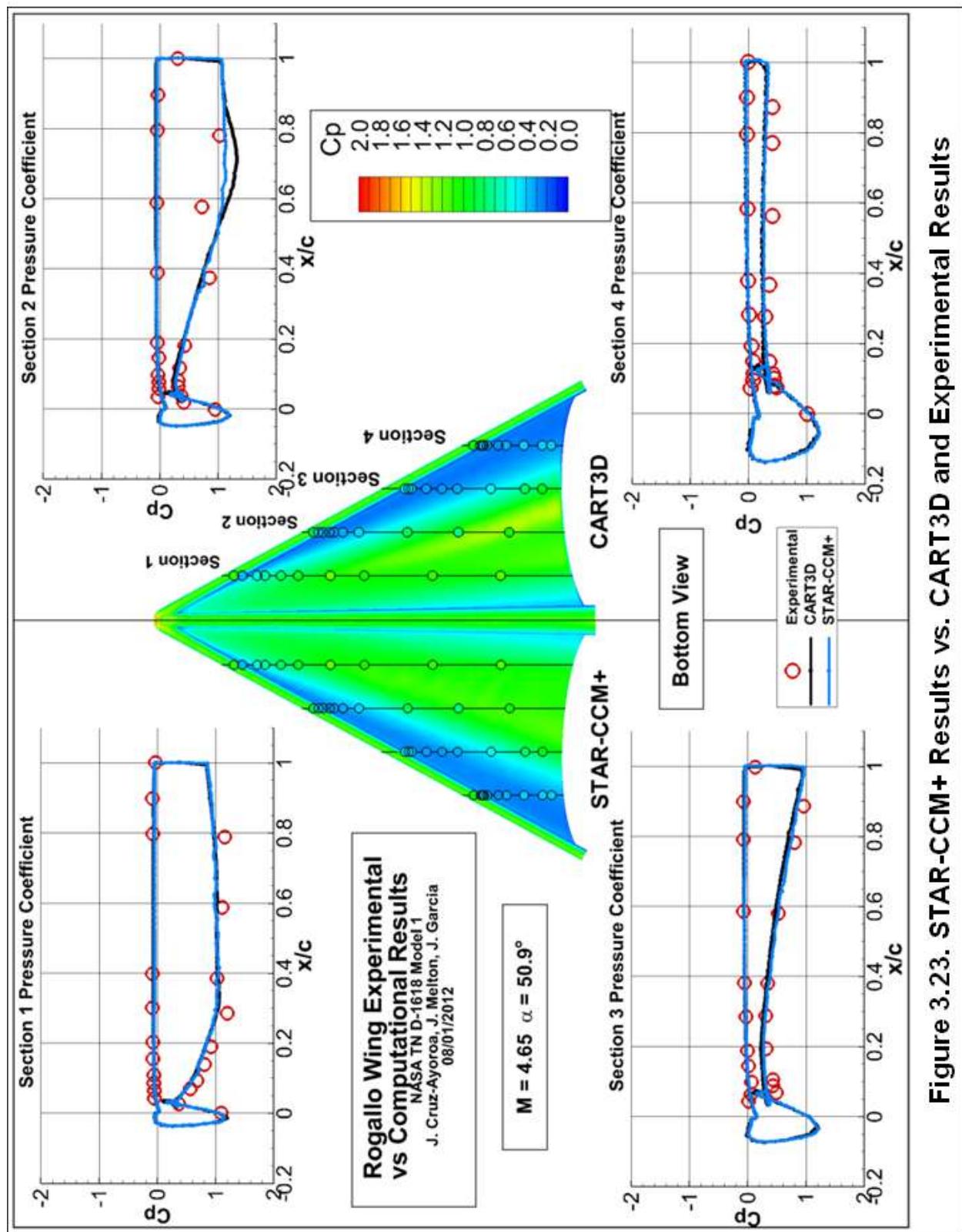
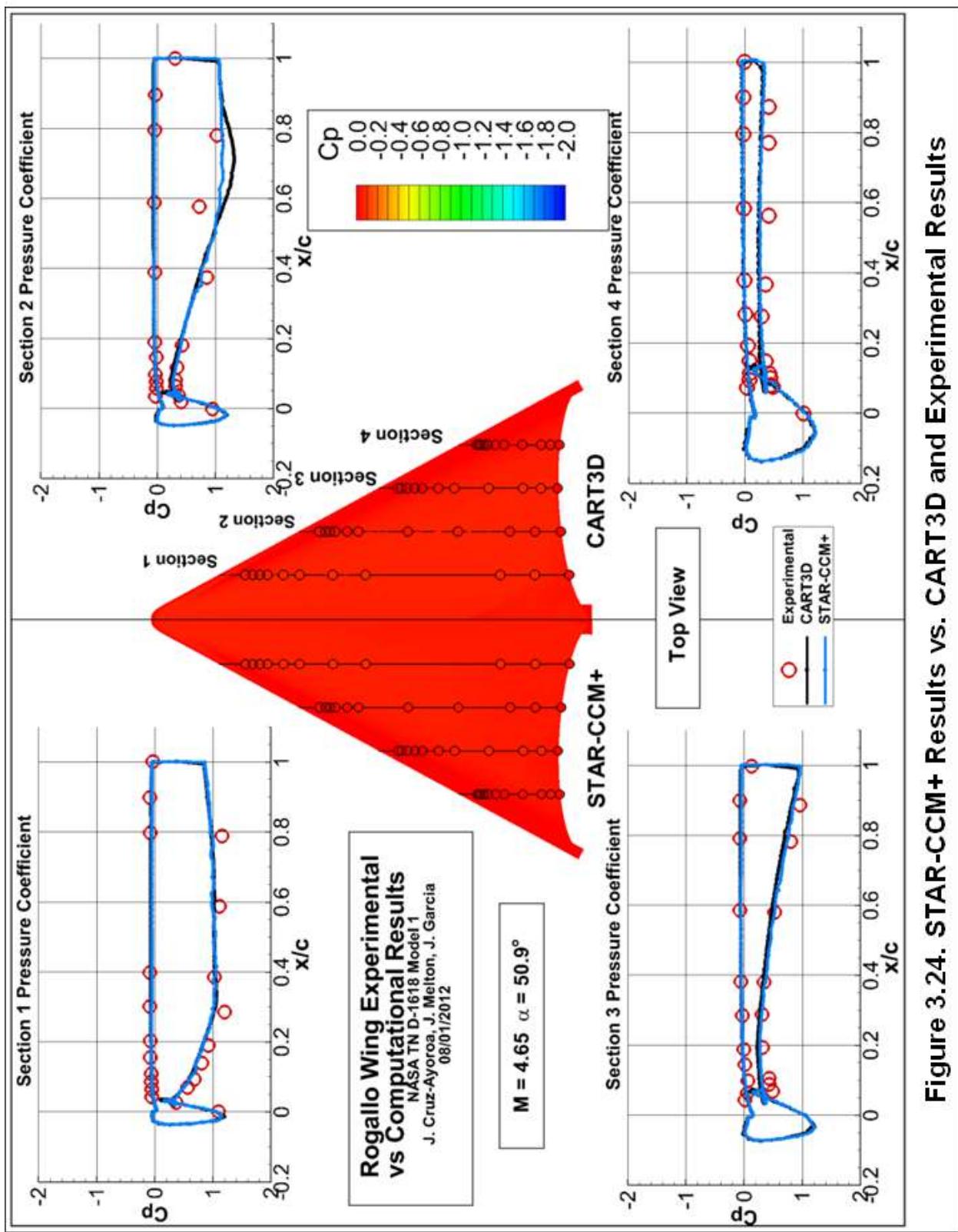
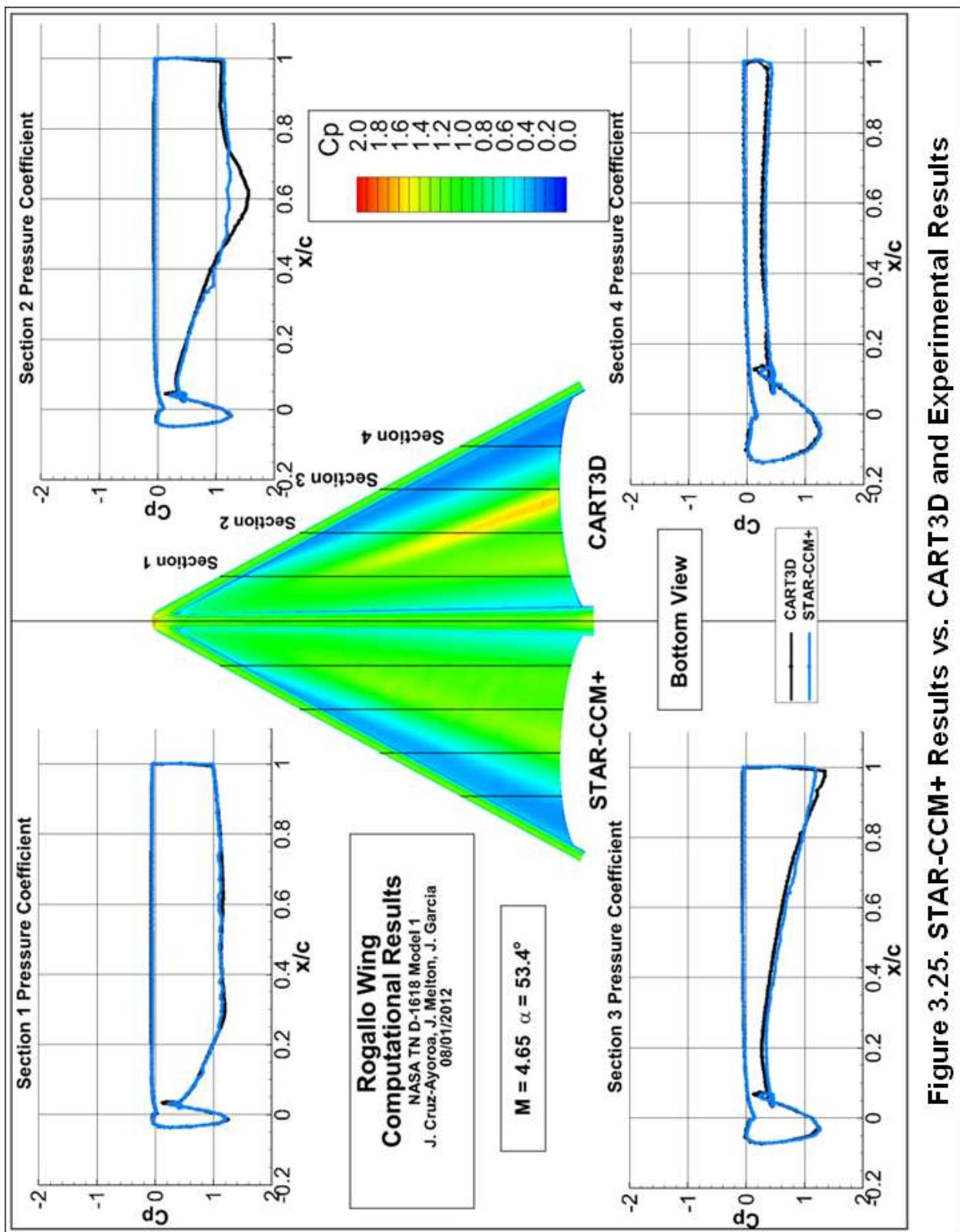


Figure 3.23. STAR-CCM+ Results vs. CART3D and Experimental Results



**Figure 3.24. STAR-CCM+ Results vs. CART3D and Experimental Results**



**Figure 3.25. STAR-CCM+ Results vs. CART3D and Experimental Results**

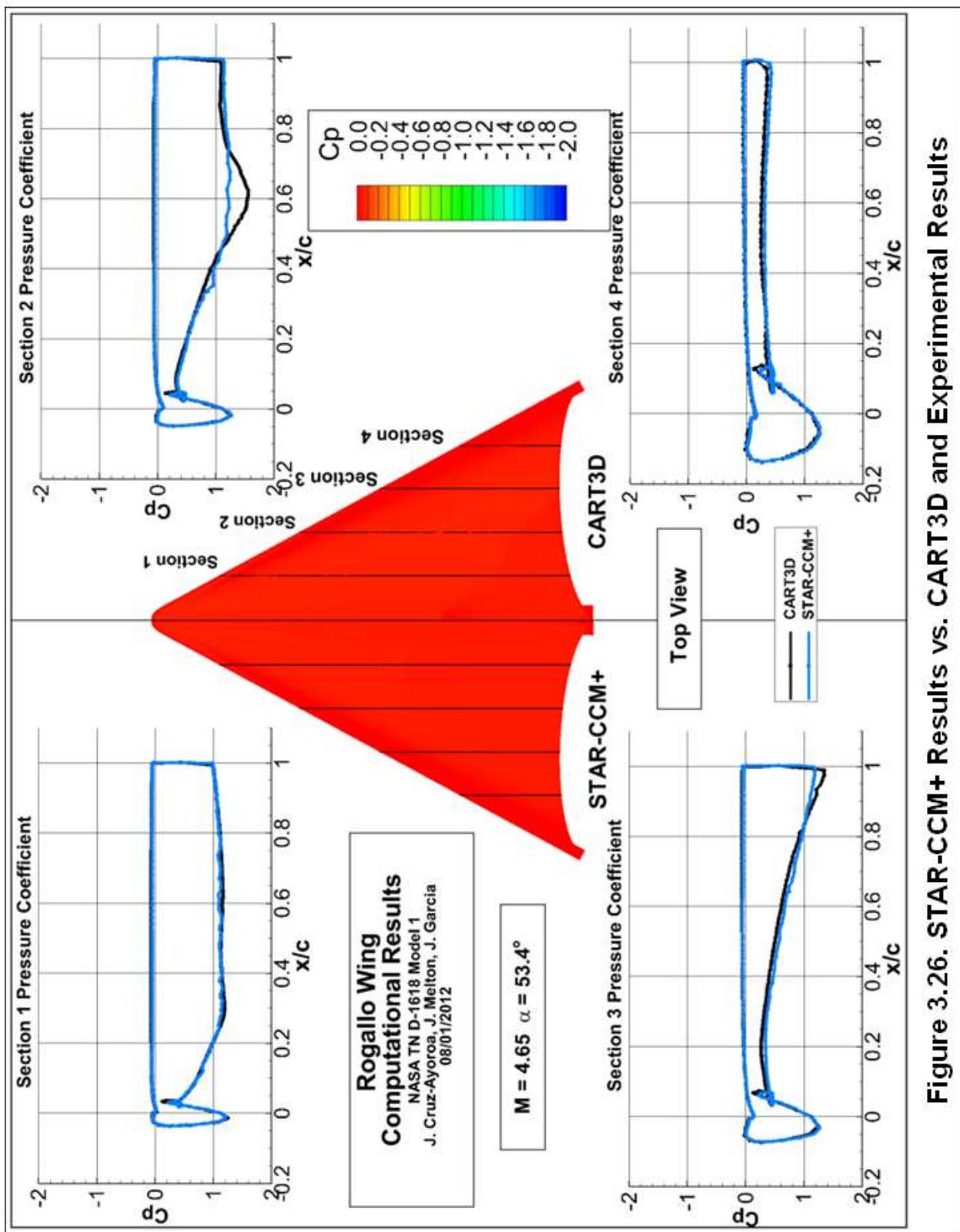


**Figure 3.26. STAR-CCM+ Results vs. CART3D and Experimental Results**

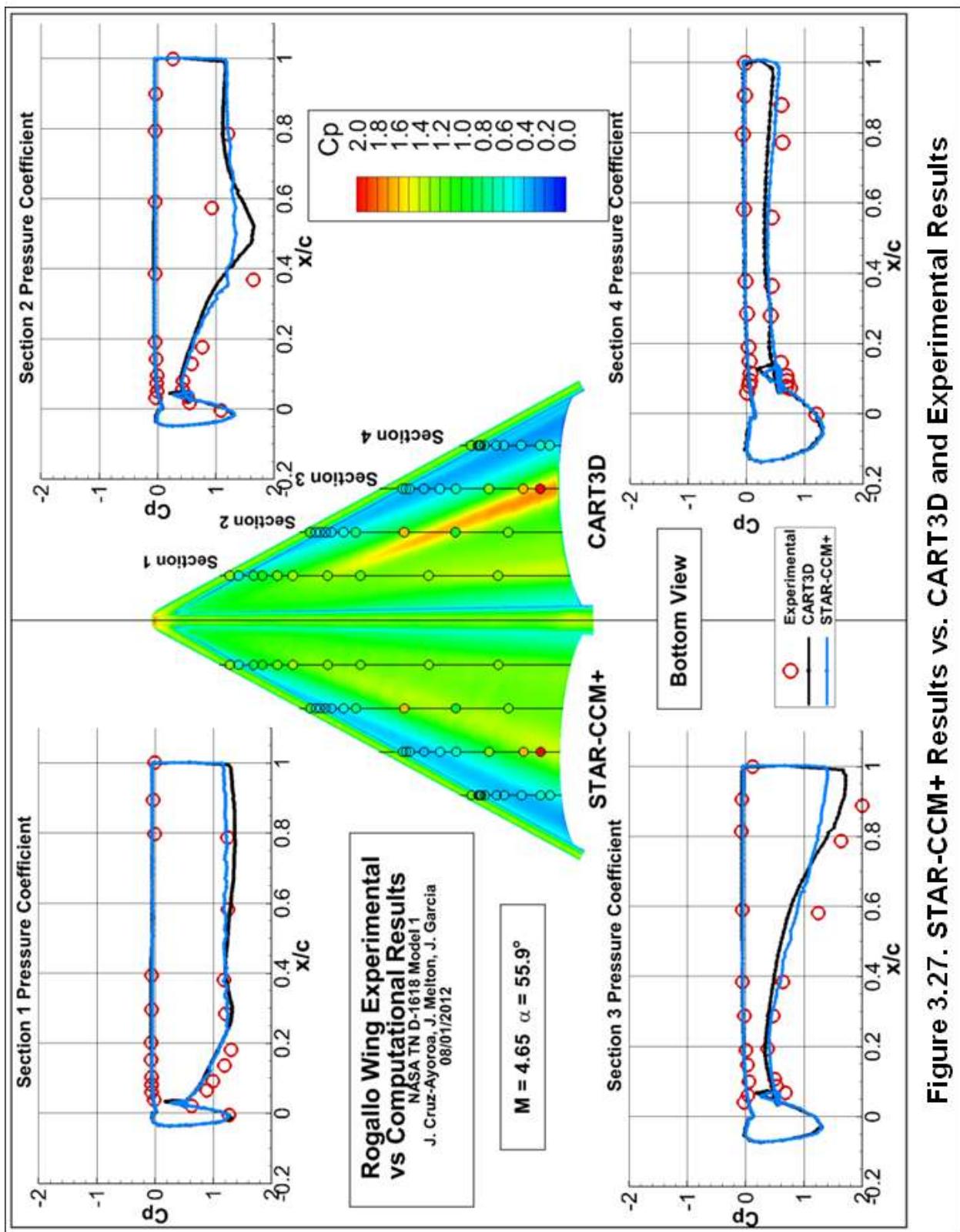


**Figure 3.27. STAR-CCM+ Results vs. CART3D and Experimental Results**

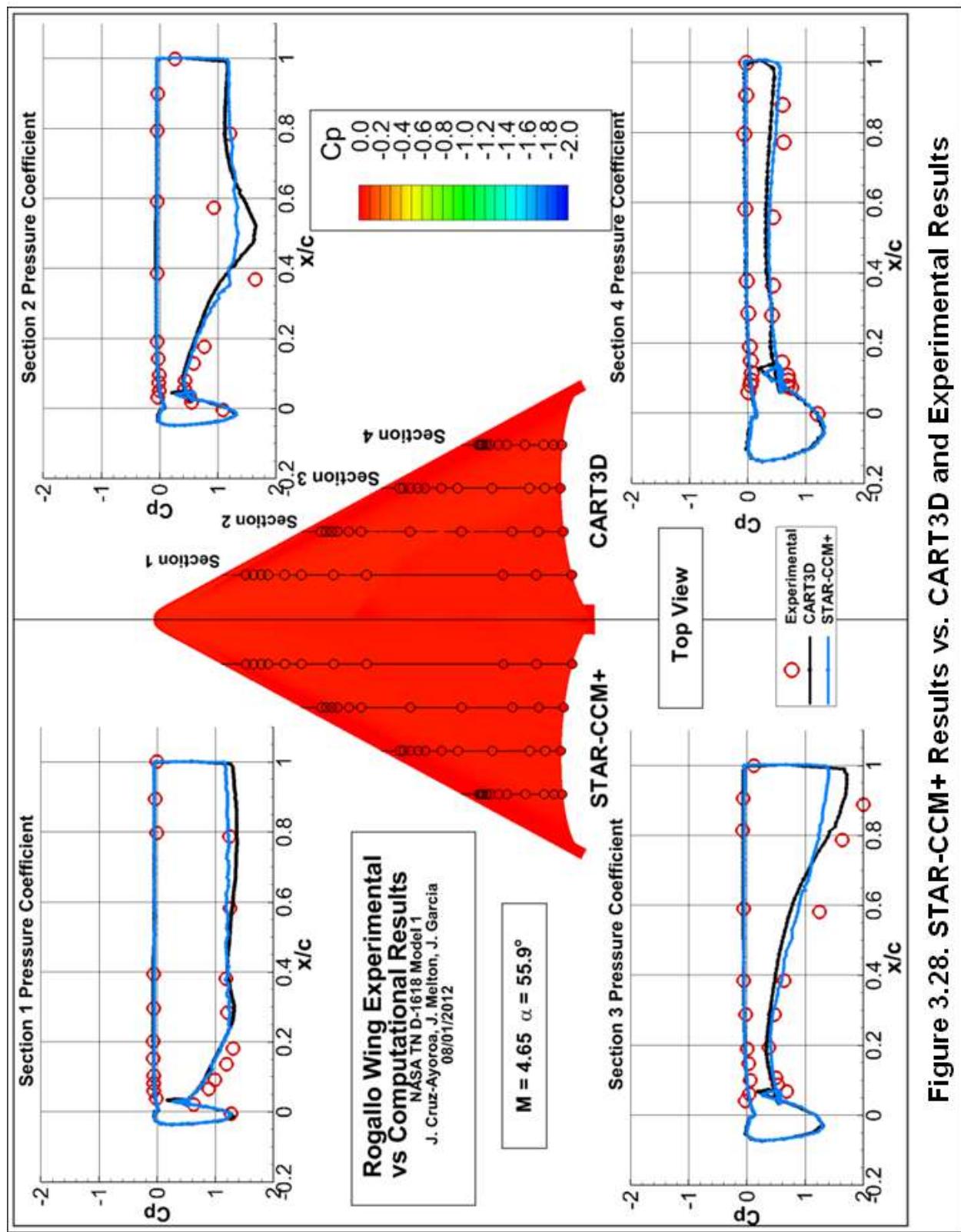
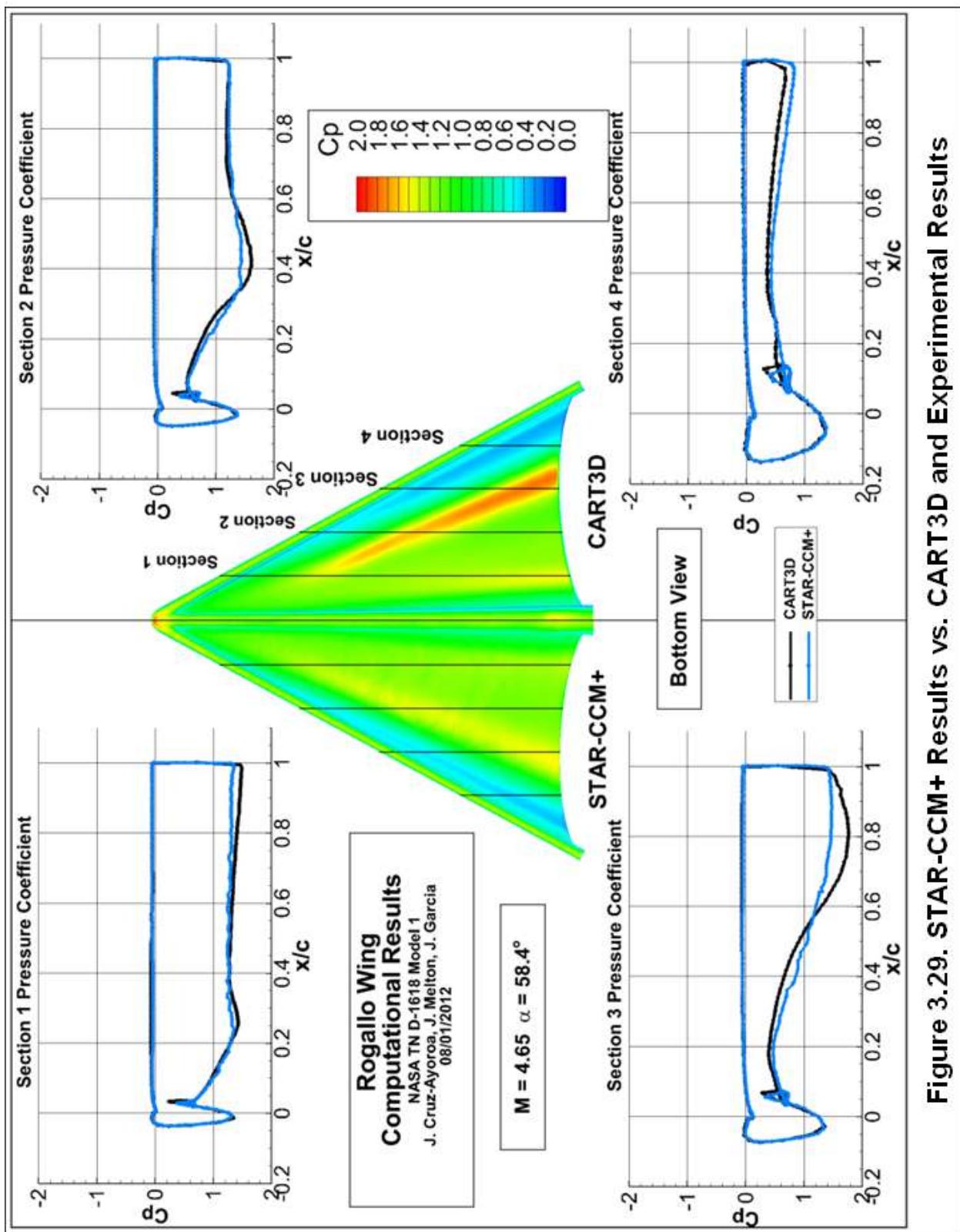
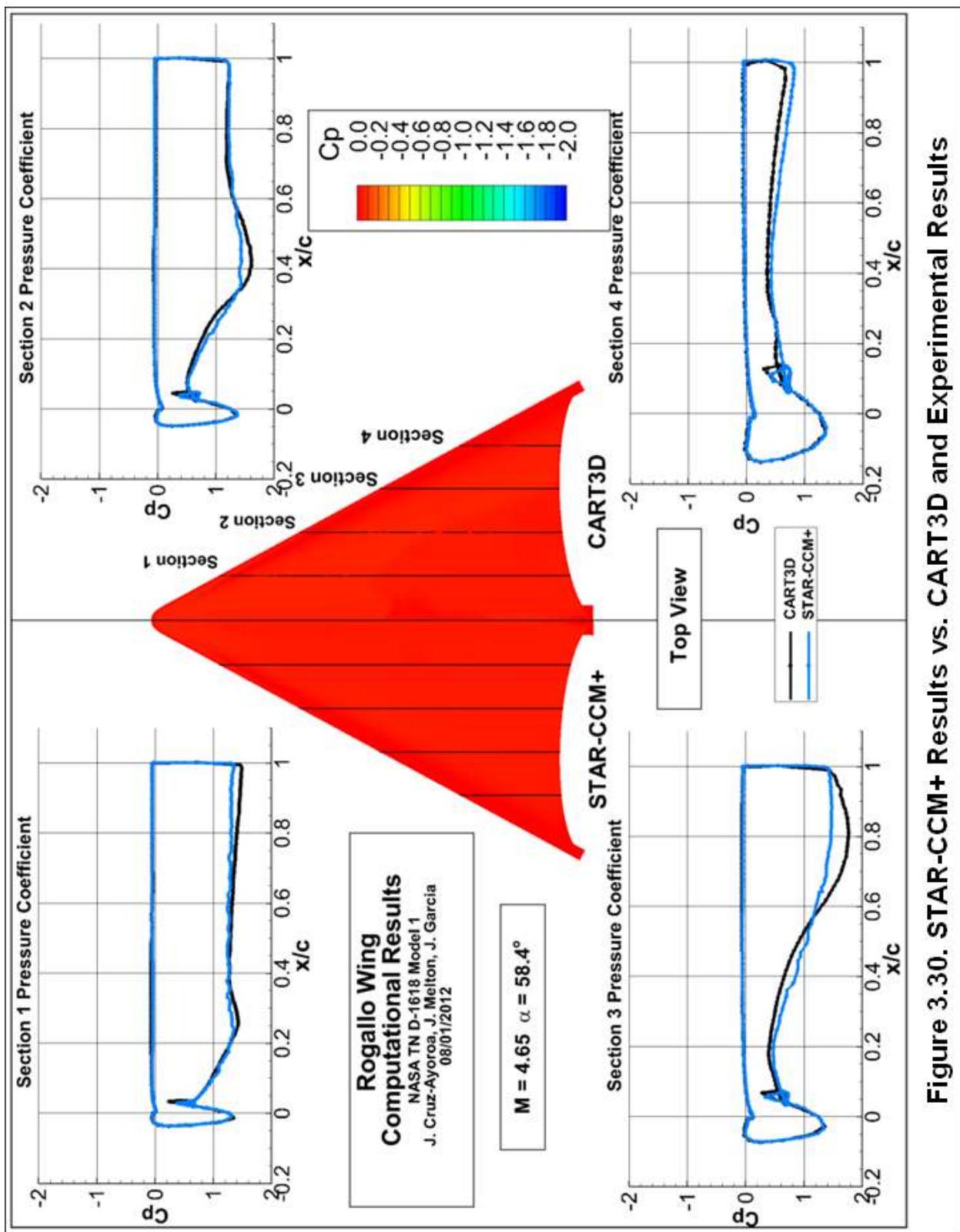


Figure 3.28. STAR-CCM+ Results vs. CART3D and Experimental Results



**Figure 3.29. STAR-CCM+ Results vs. CART3D and Experimental Results**



**Figure 3.30. STAR-CCM+ Results vs. CART3D and Experimental Results**

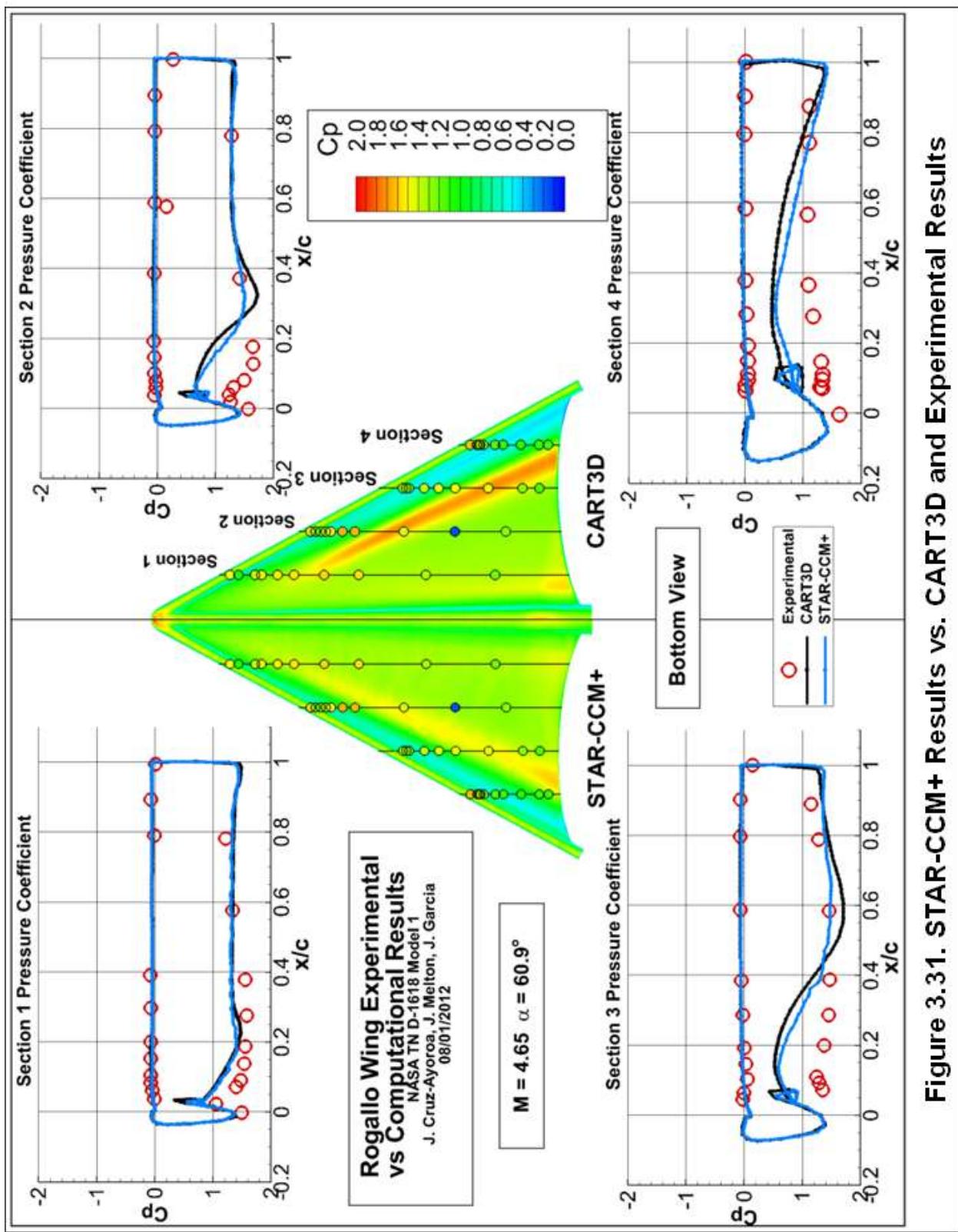


**Figure 3.31. STAR-CCM+ Results vs. CART3D and Experimental Results**

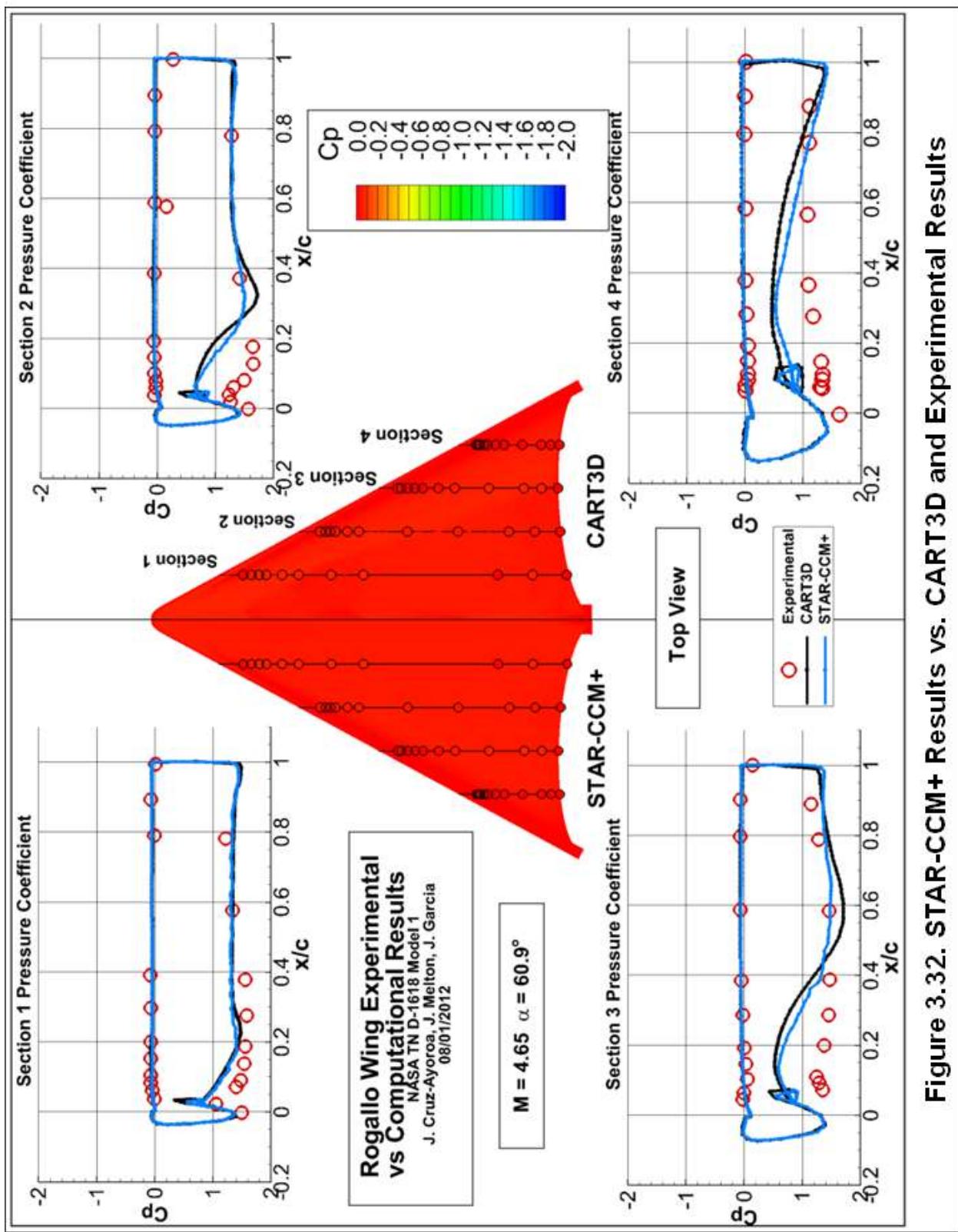


**Figure 3.32. STAR-CCM+ Results vs. CART3D and Experimental Results**

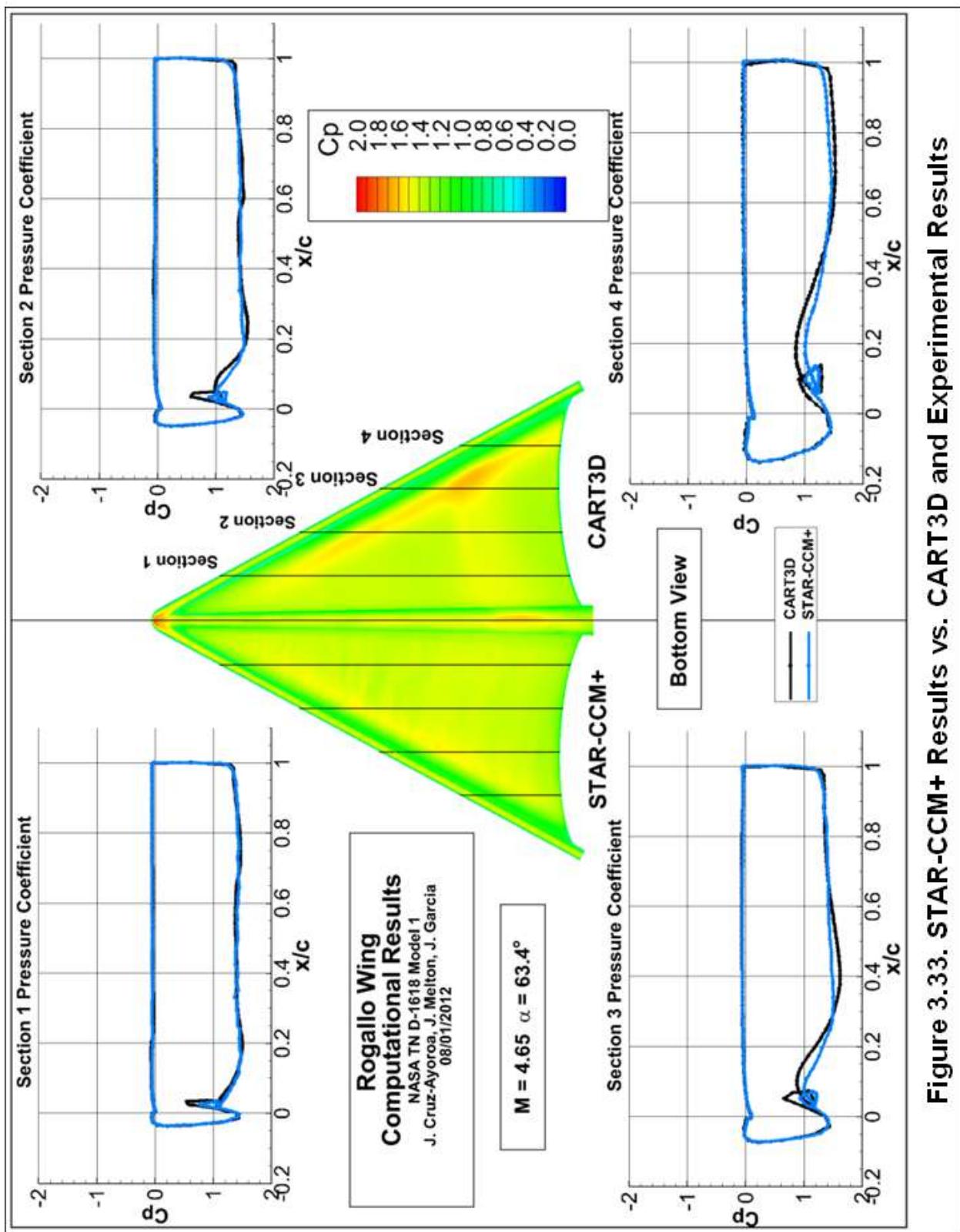


**Figure 3.33. STAR-CCM+ Results vs. CART3D and Experimental Results**

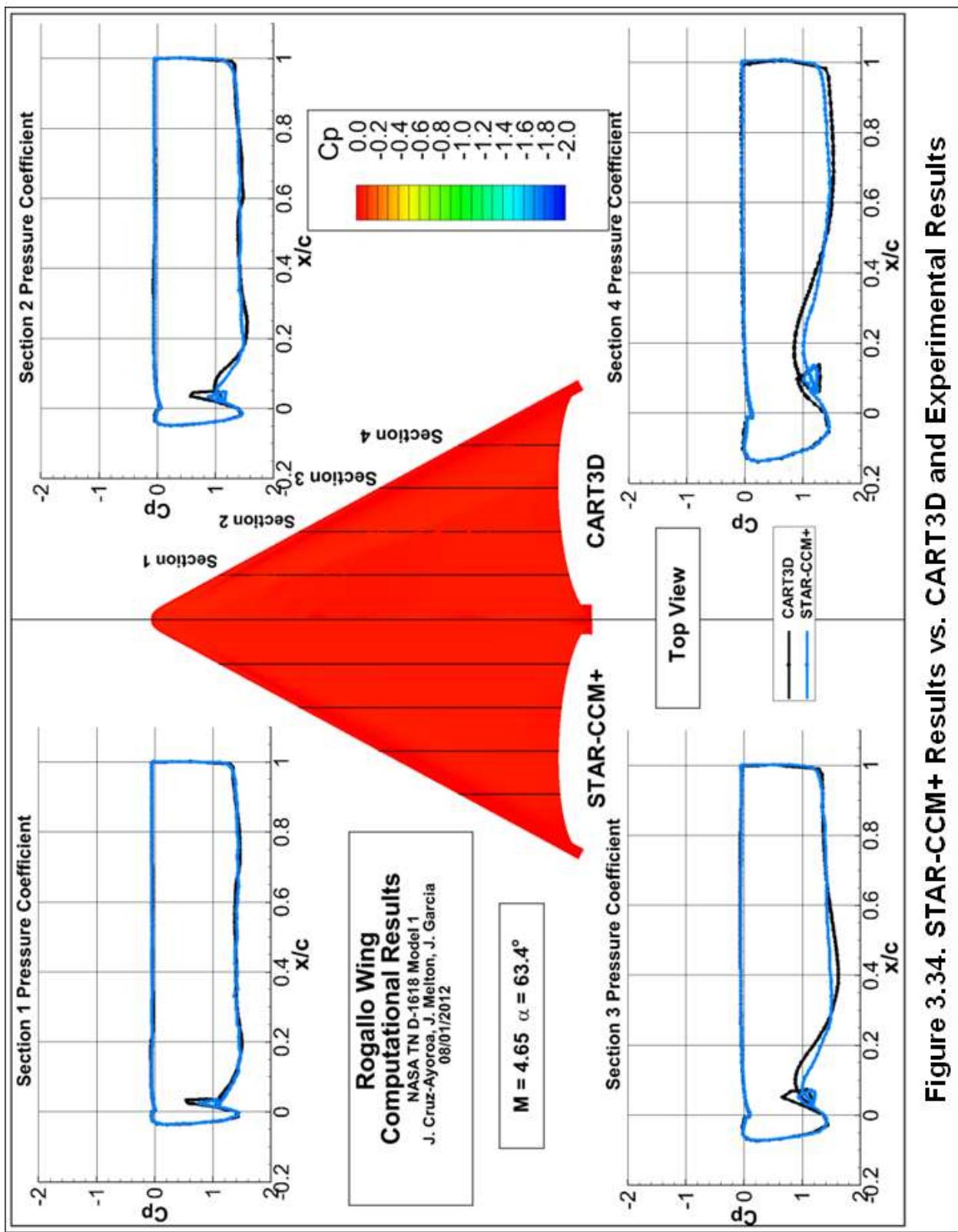


**Figure 3.34. STAR-CCM+ Results vs. CART3D and Experimental Results**

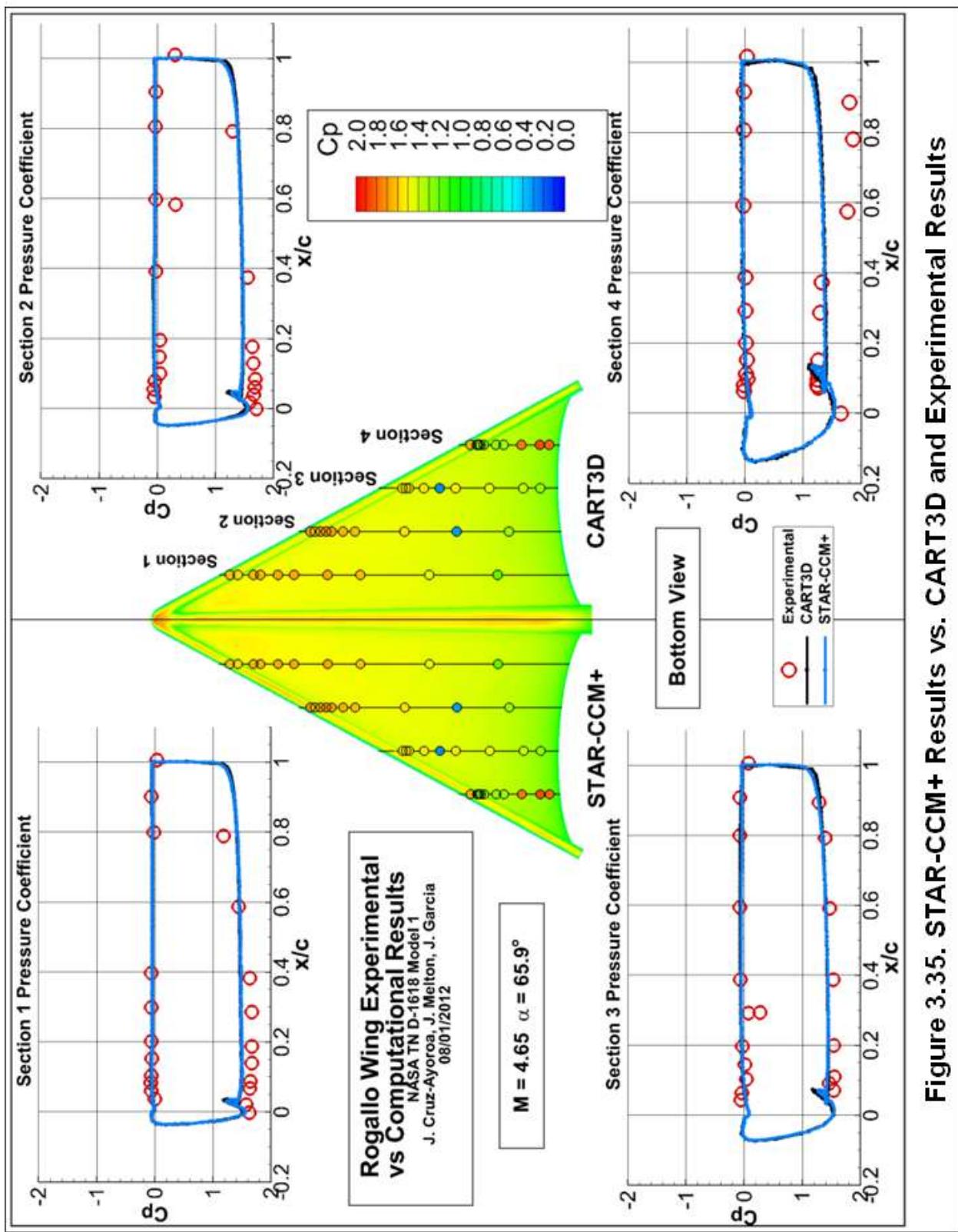


**Figure 3.35. STAR-CCM+ Results vs. CART3D and Experimental Results**

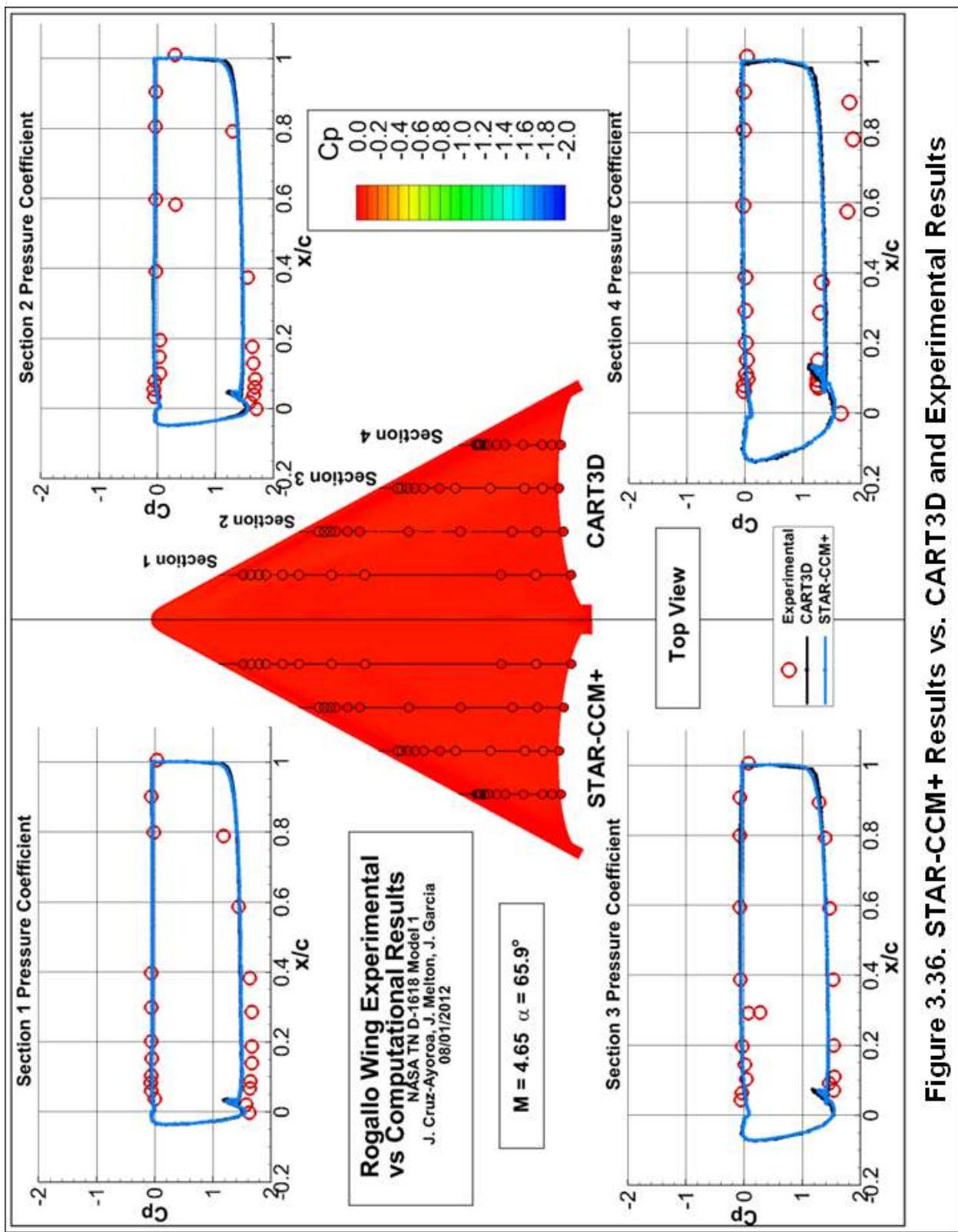


**Figure 3.36. STAR-CCM+ Results vs. CART3D and Experimental Results**

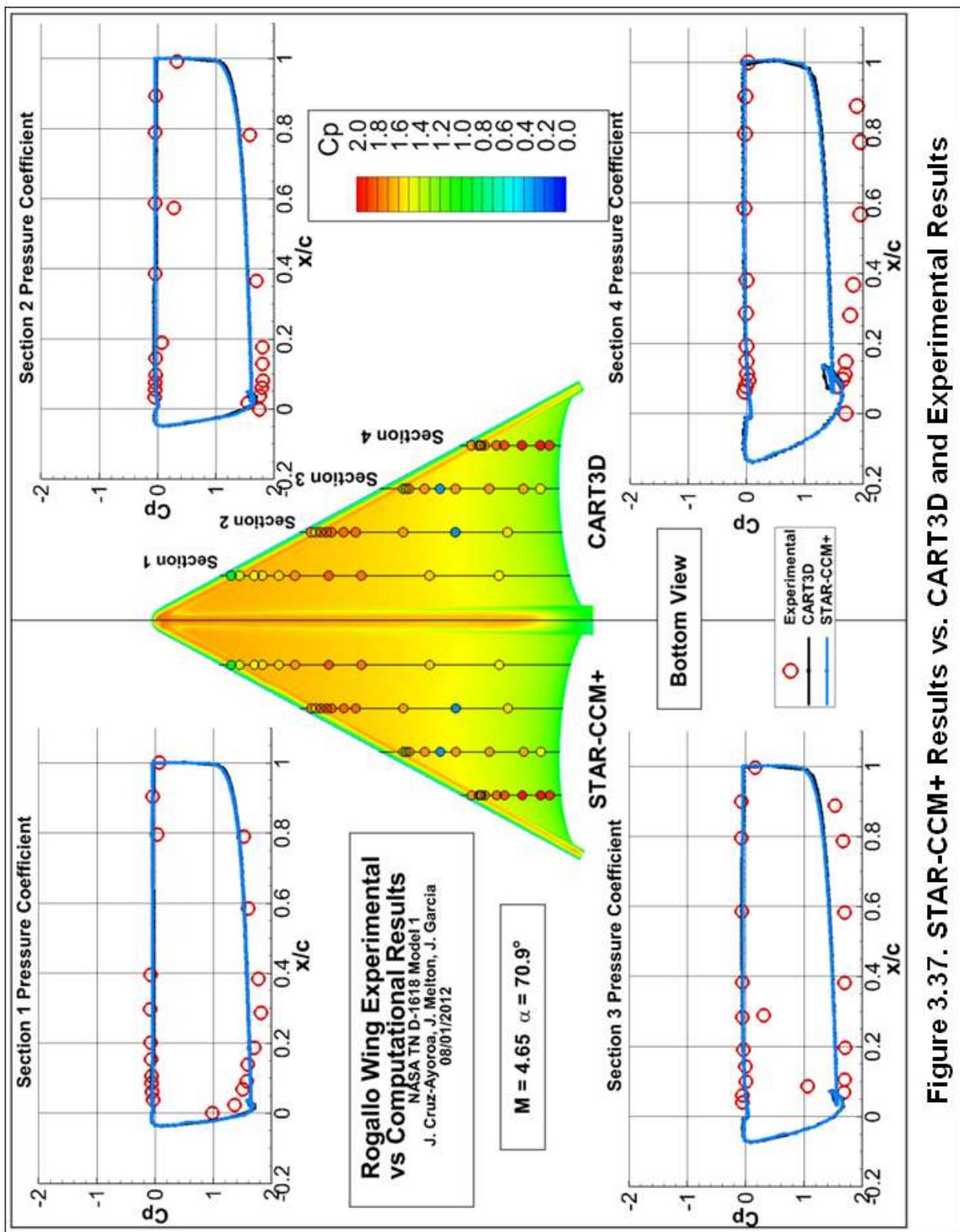


**Figure 3.37. STAR-CCM+ Results vs. CART3D and Experimental Results**

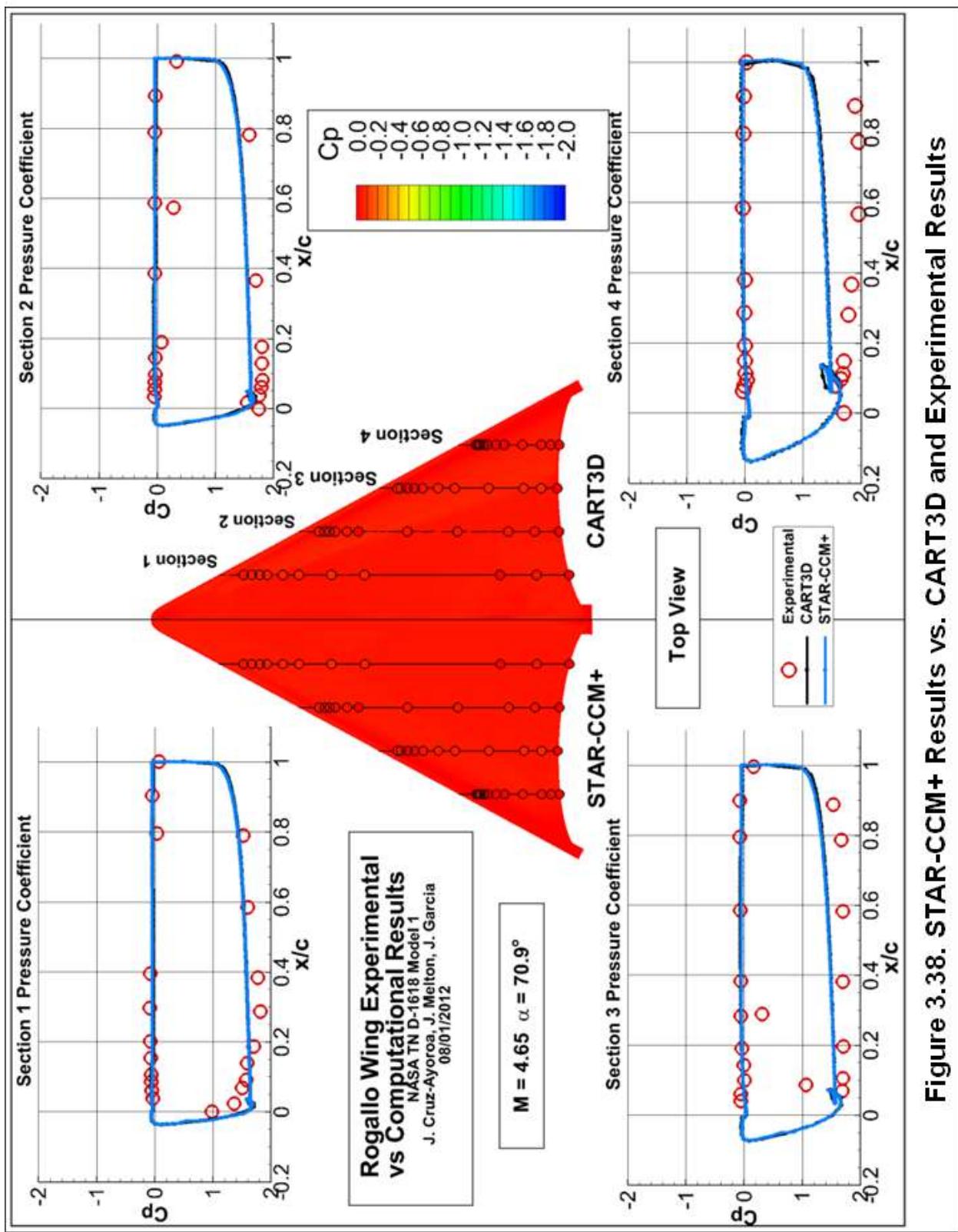


**Figure 3.38. STAR-CCM+ Results vs. CART3D and Experimental Results**

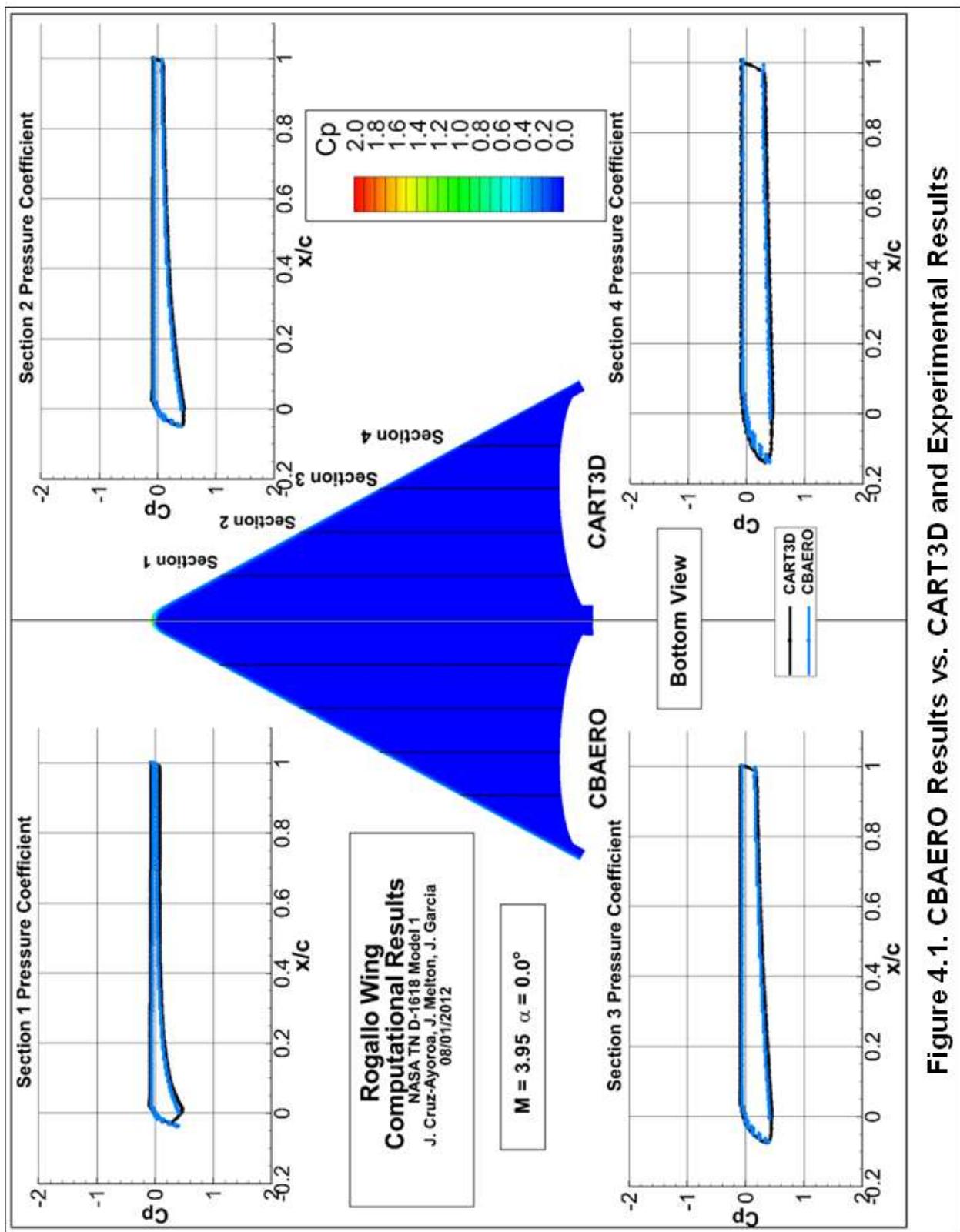


**Figure 4.1. CBAERO Results vs. CART3D and Experimental Results**

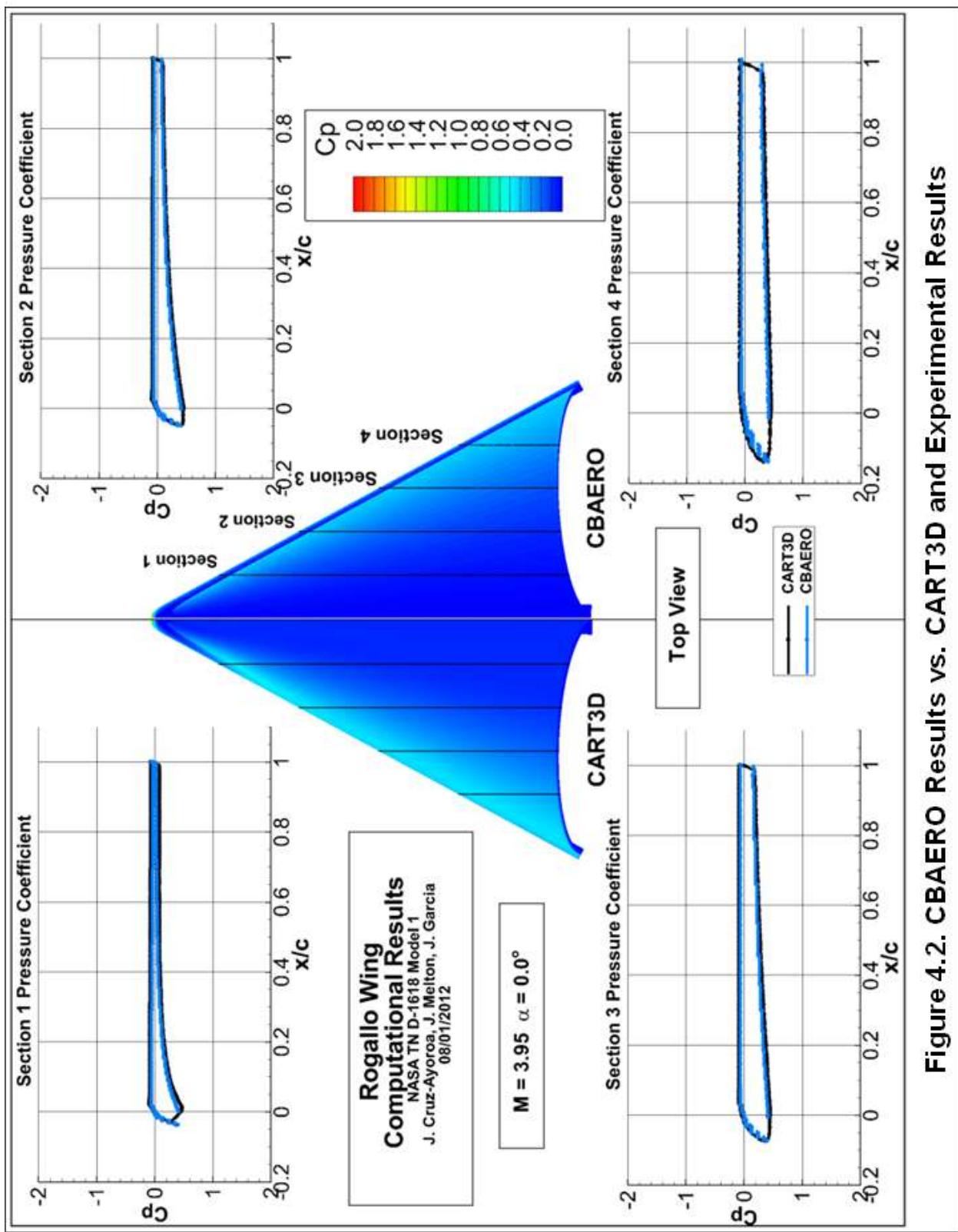


**Figure 4.2. CBAERO Results vs. CART3D and Experimental Results**

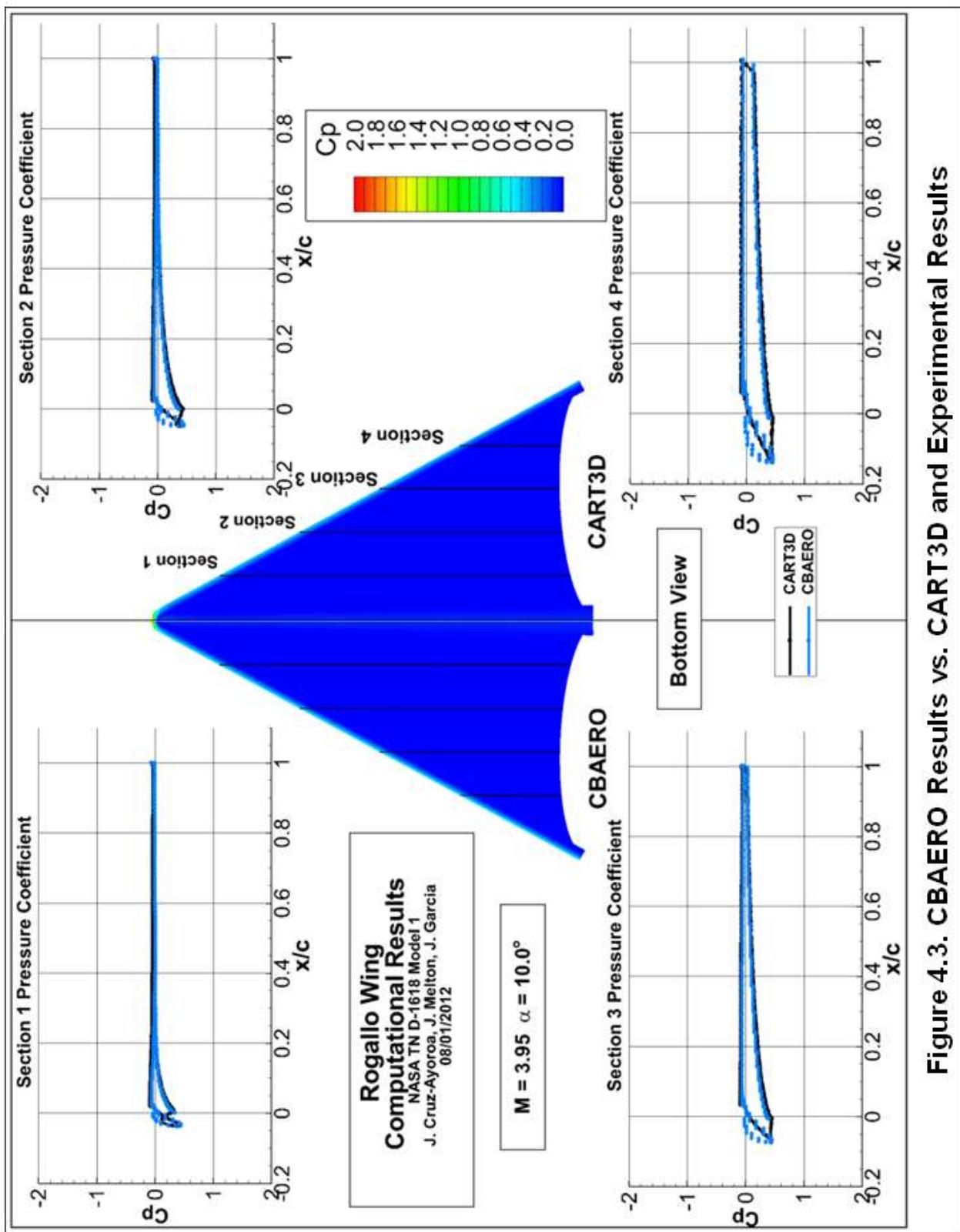


**Figure 4.3. CBAERO Results vs. CART3D and Experimental Results**

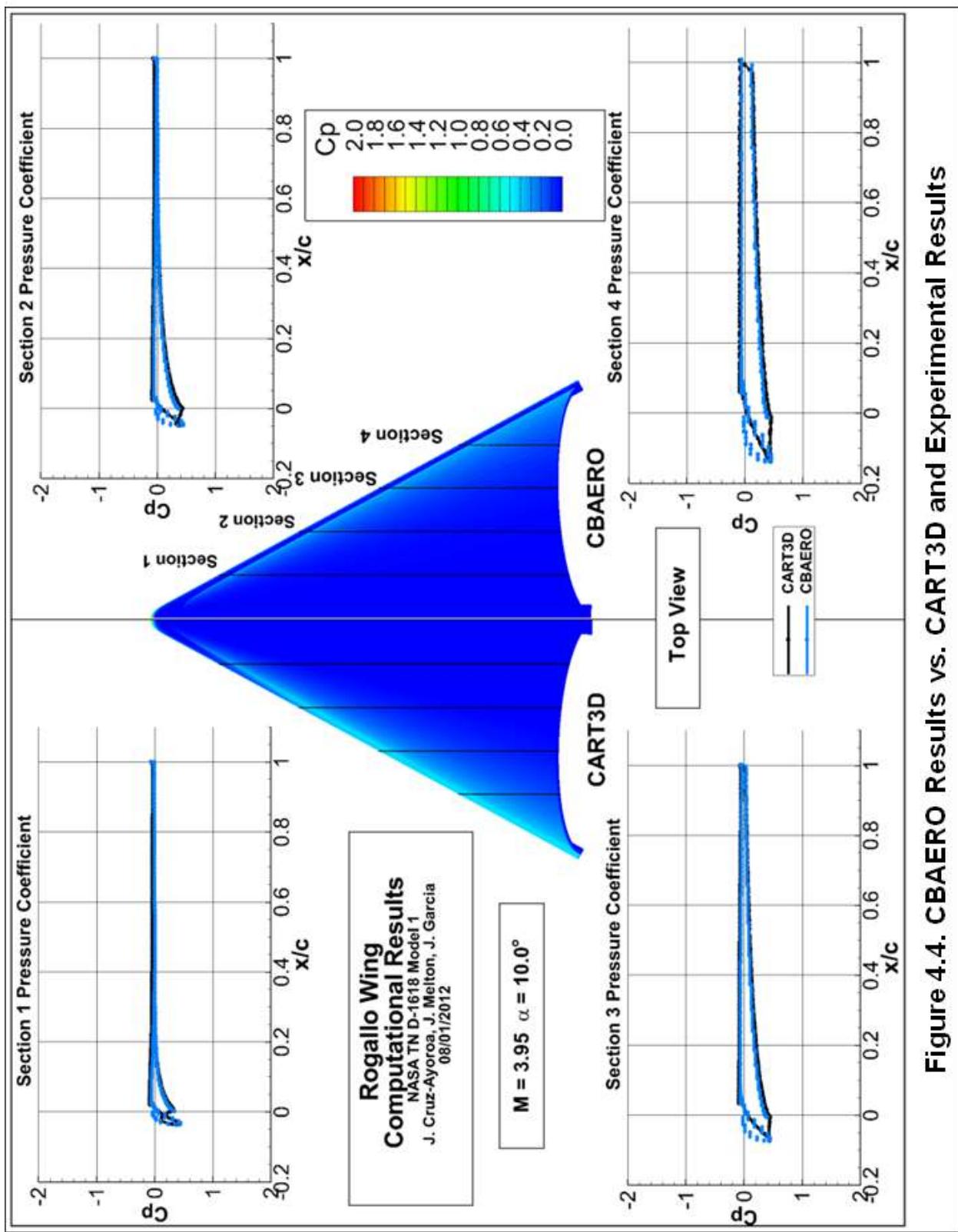


**Figure 4.4. CBAERO Results vs. CART3D and Experimental Results**

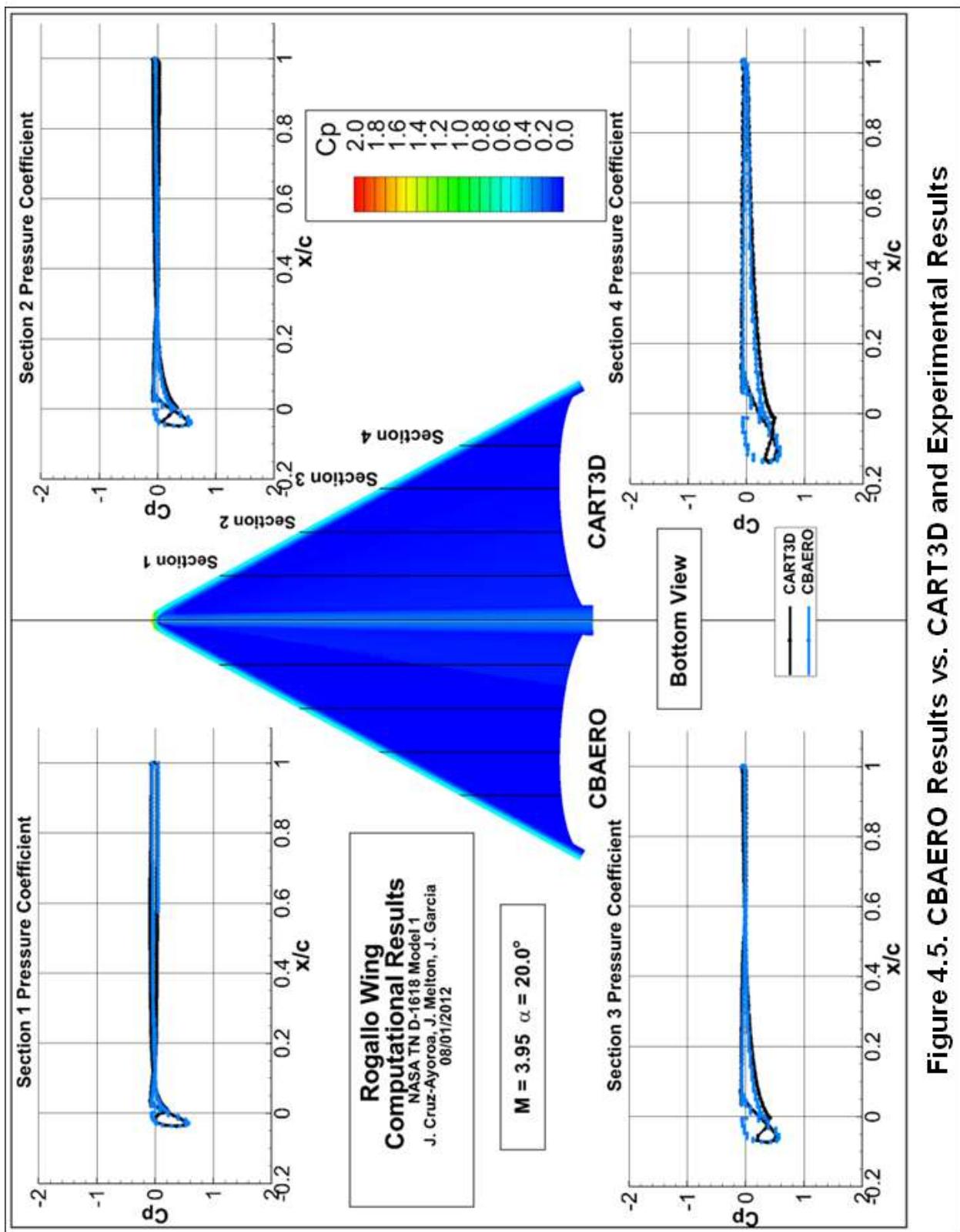


**Figure 4.5. CBAERO Results vs. CART3D and Experimental Results**

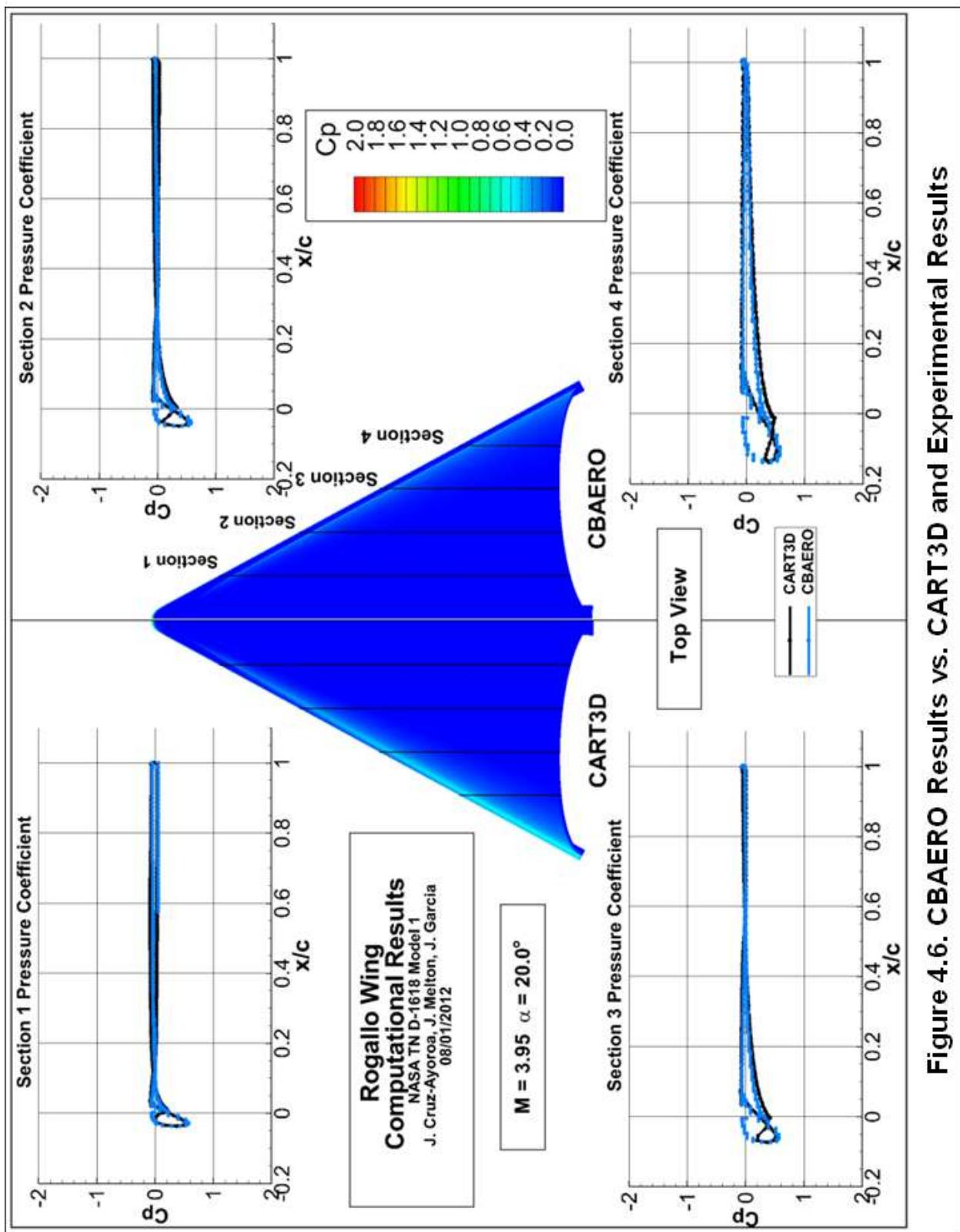


**Figure 4.6. CBAERO Results vs. CART3D and Experimental Results**

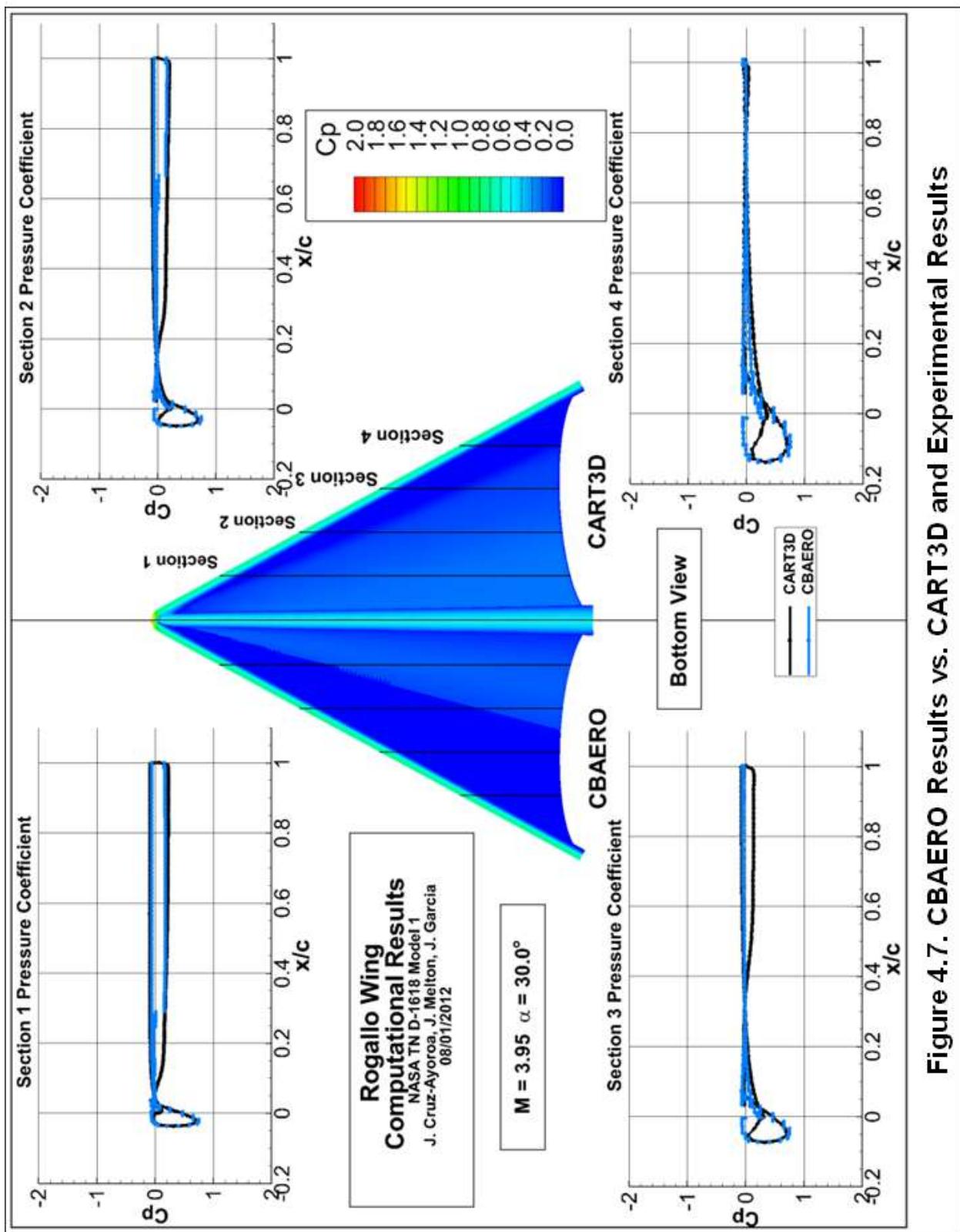


**Figure 4.7. CBAERO Results vs. CART3D and Experimental Results**

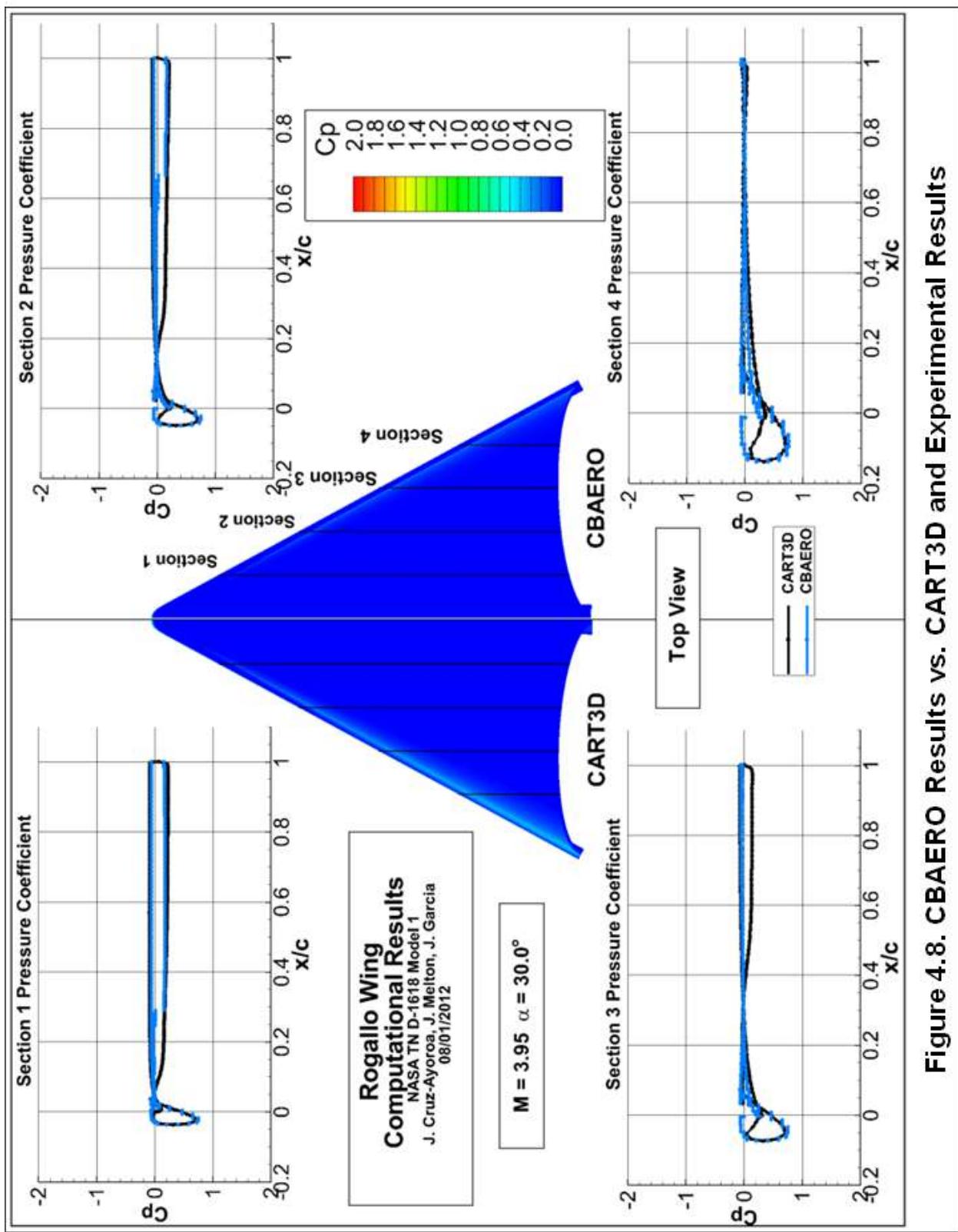


**Figure 4.8. CBAERO Results vs. CART3D and Experimental Results**

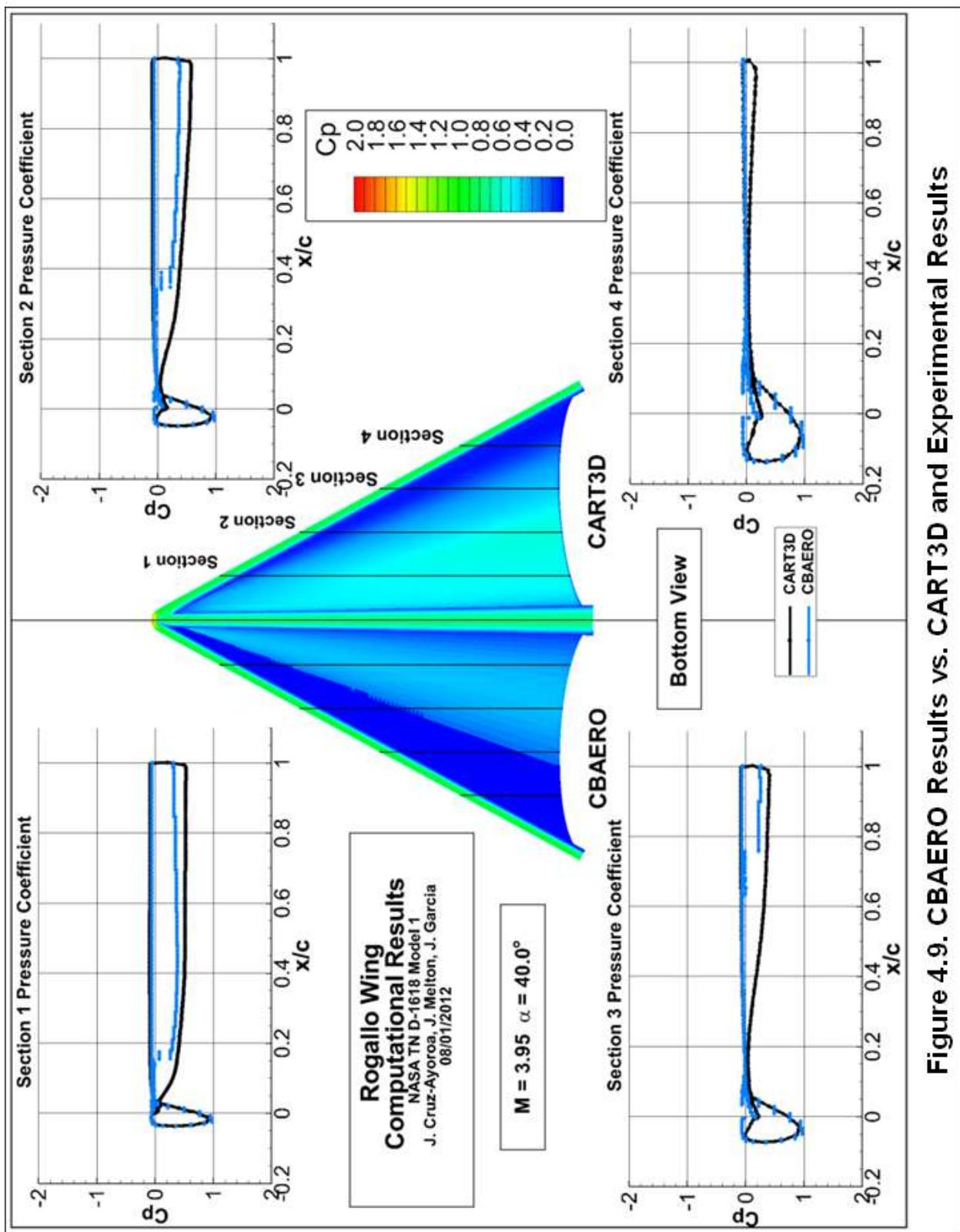
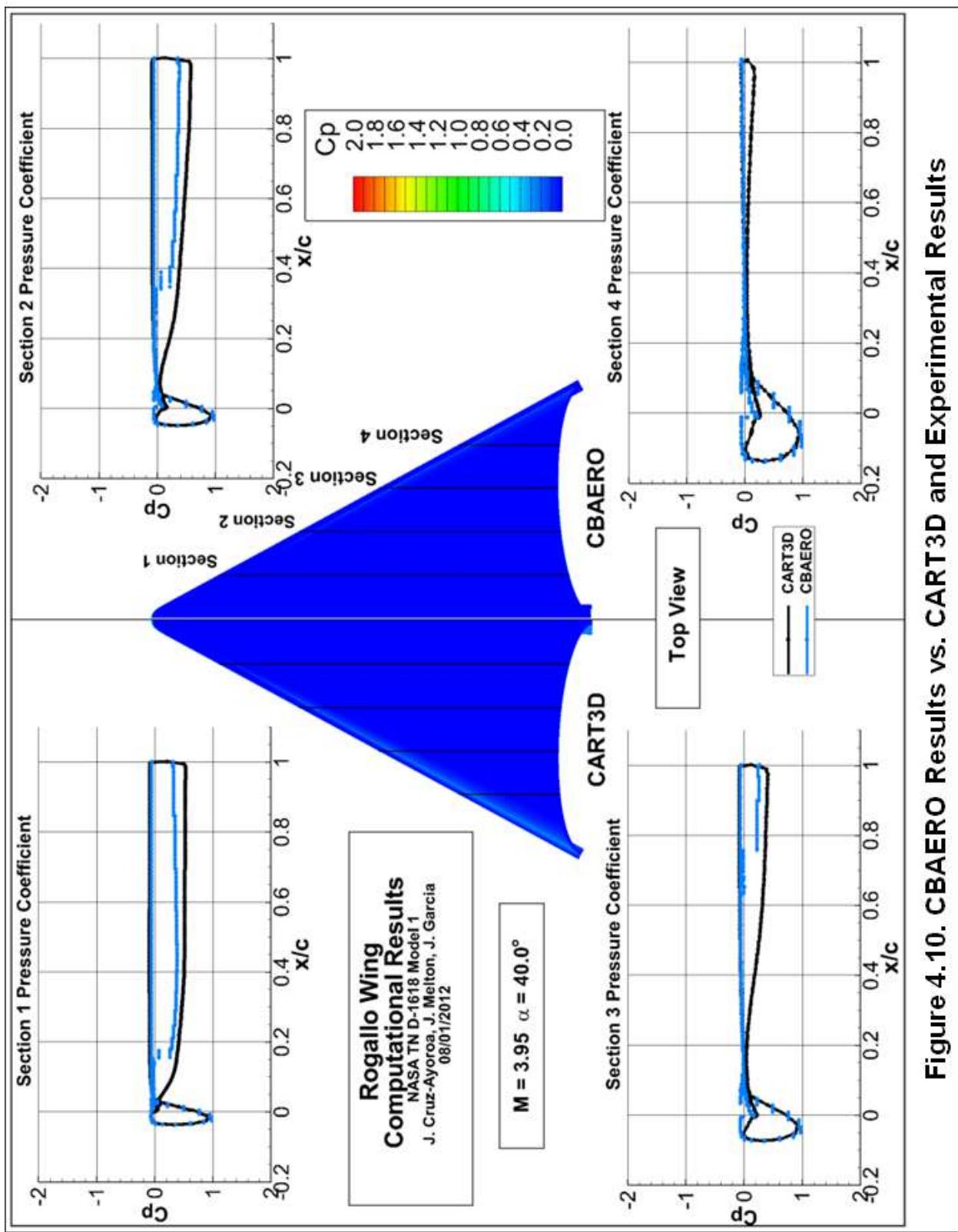
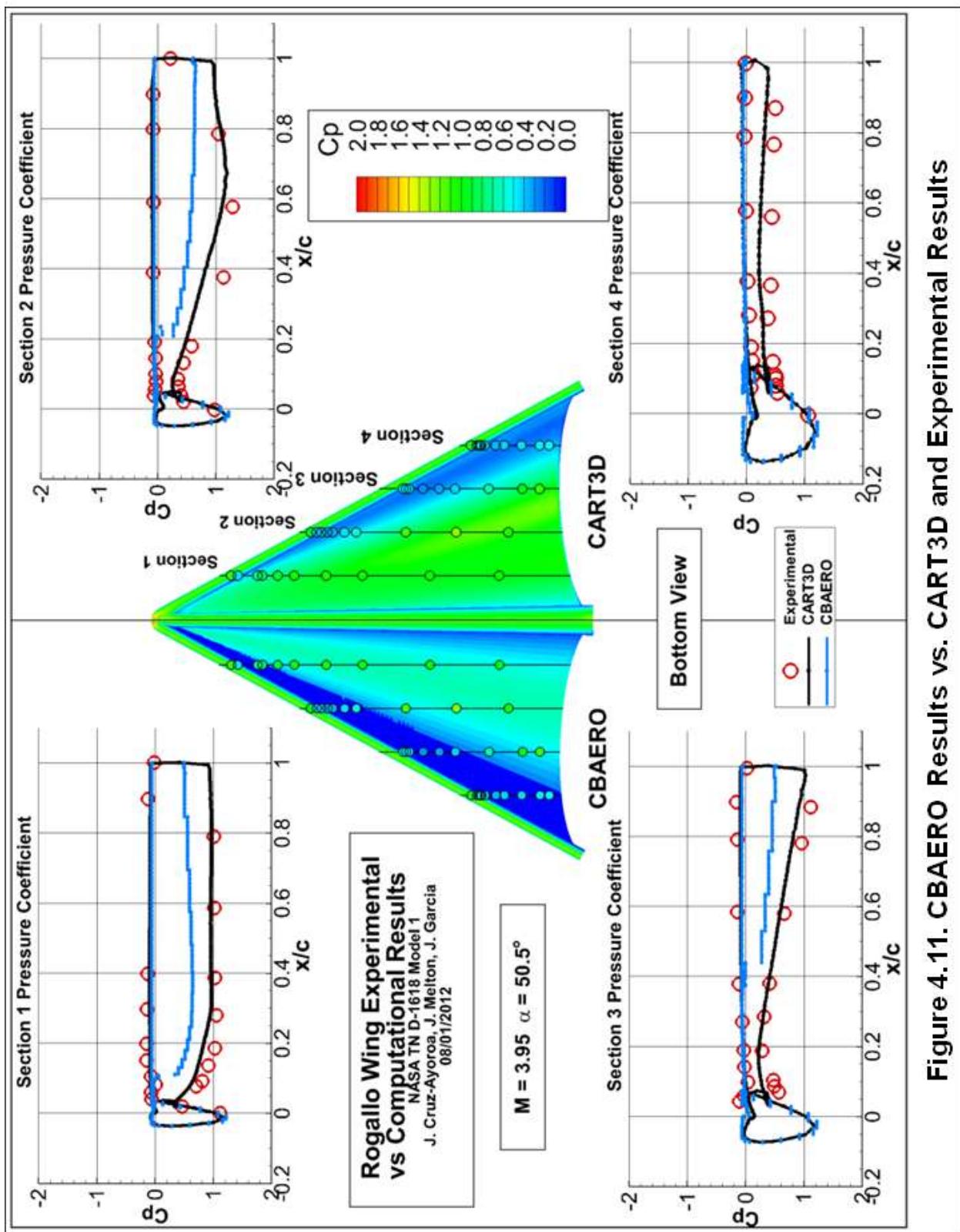


Figure 4.9. CBAERO Results vs. CART3D and Experimental Results



**Figure 4.10. CBAERO Results vs. CART3D and Experimental Results**



**Figure 4.11. CBAERO Results vs. CART3D and Experimental Results**

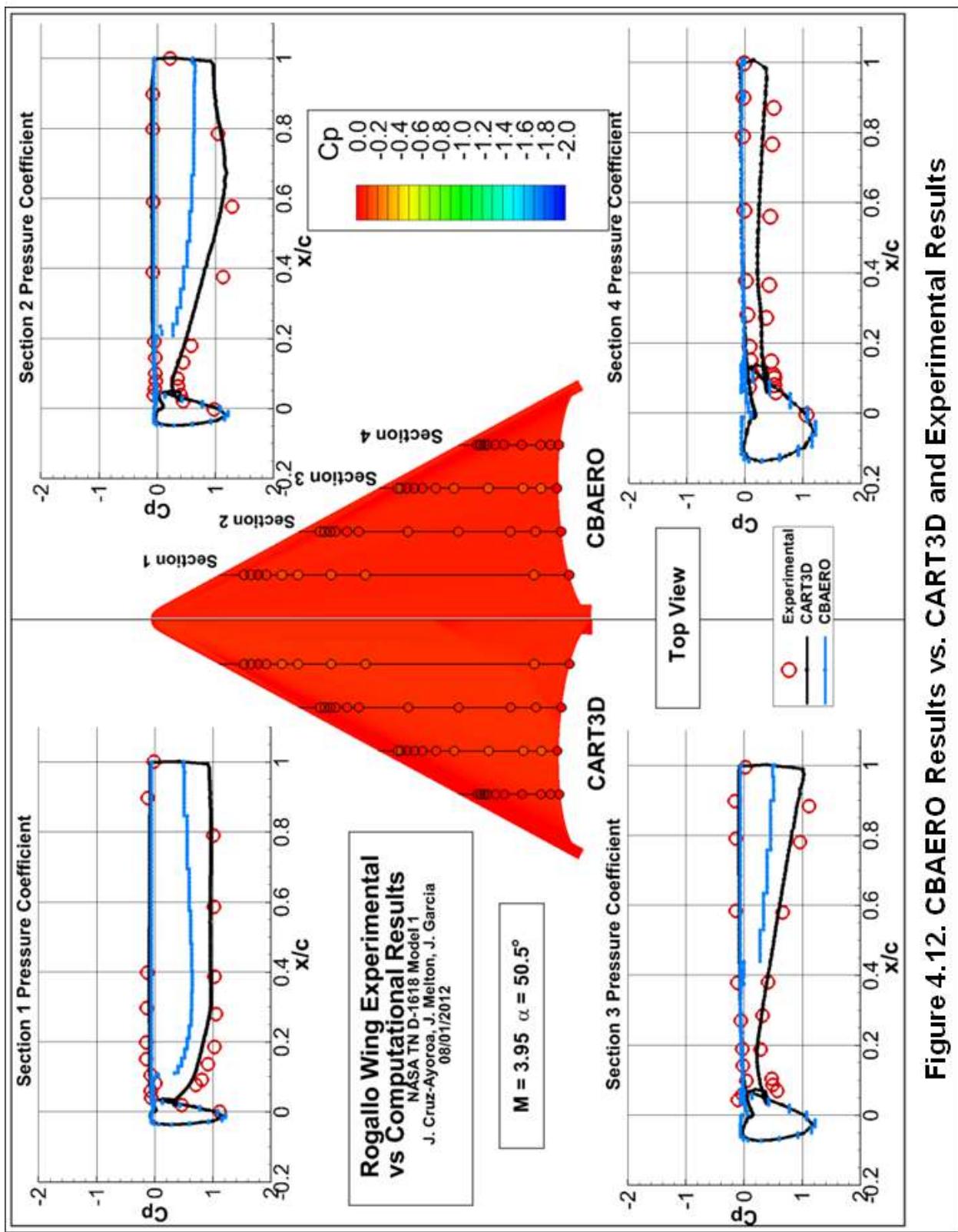


**Figure 4.12. CBAERO Results vs. CART3D and Experimental Results**

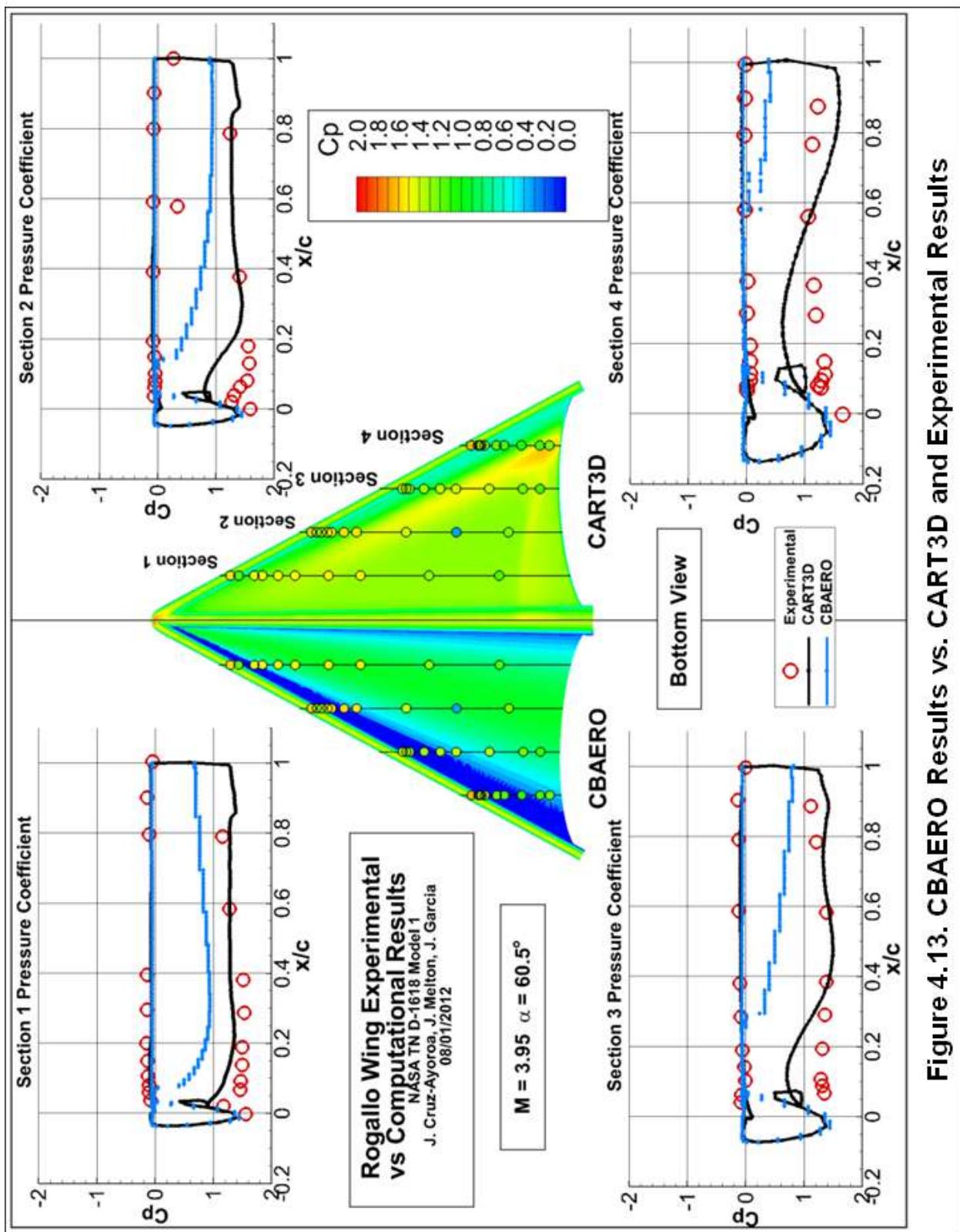
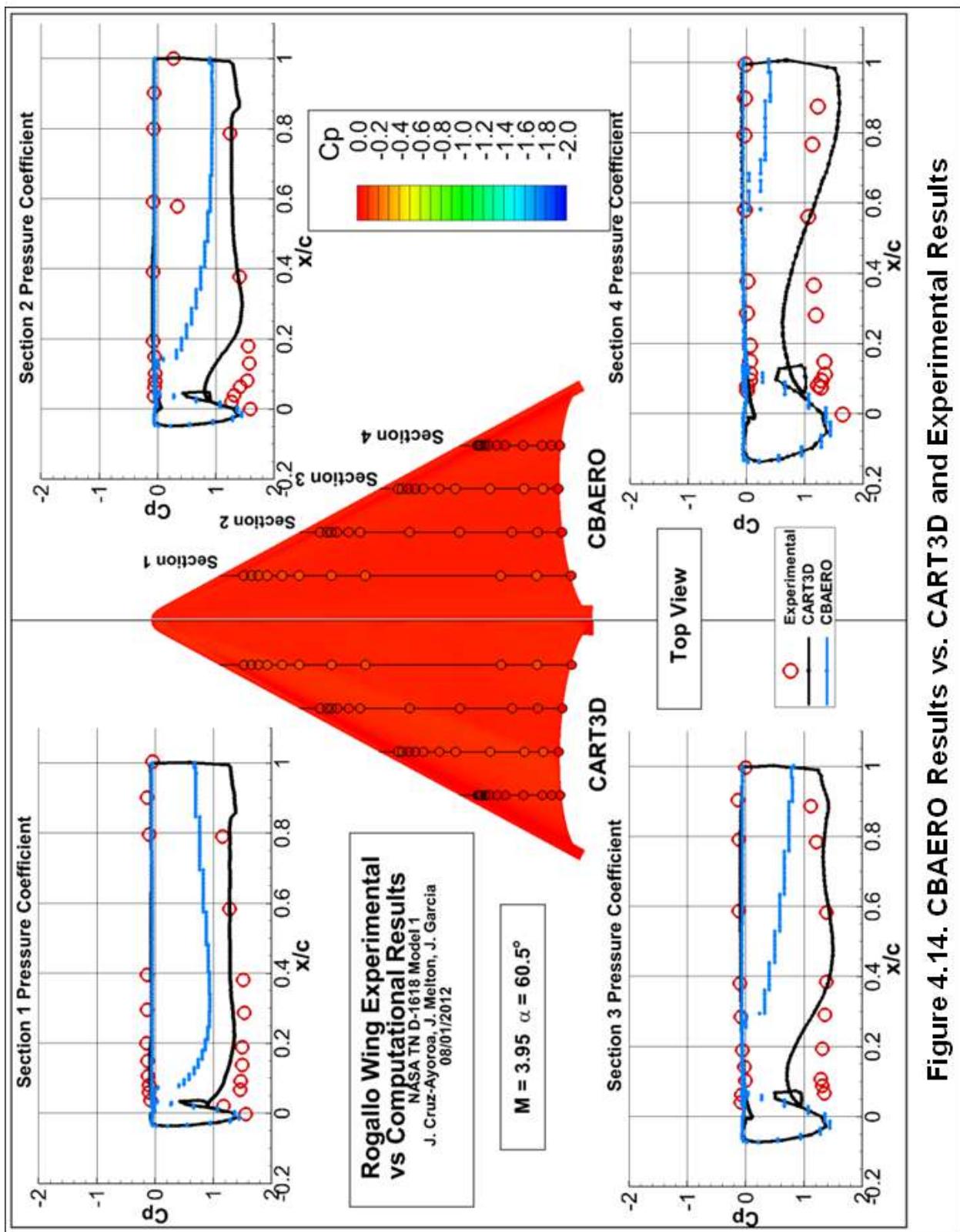
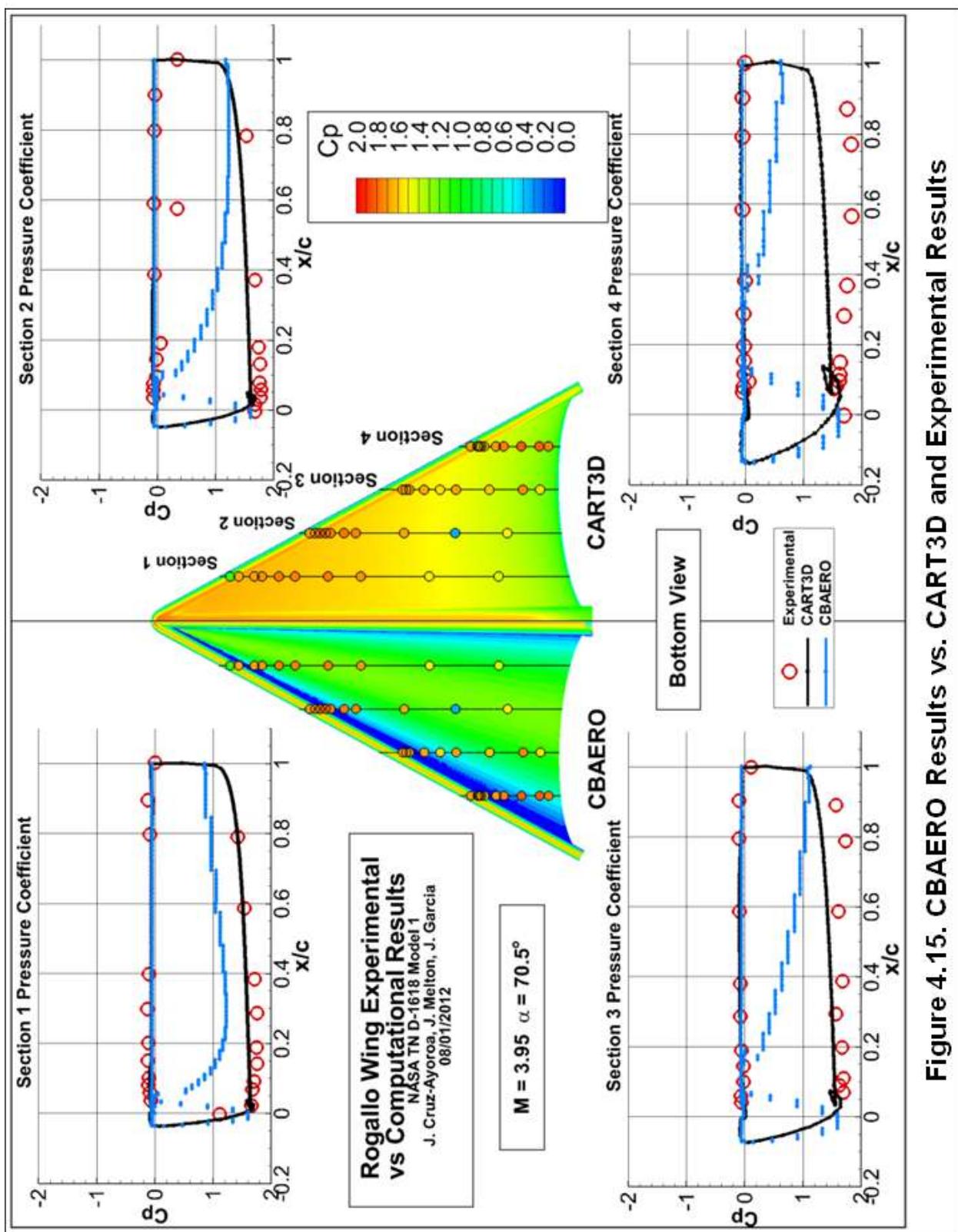


Figure 4.13. CBAERO Results vs. CART3D and Experimental Results



**Figure 4.14. CBAERO Results vs. CART3D and Experimental Results**



**Figure 4.15. CBAERO Results vs. CART3D and Experimental Results**

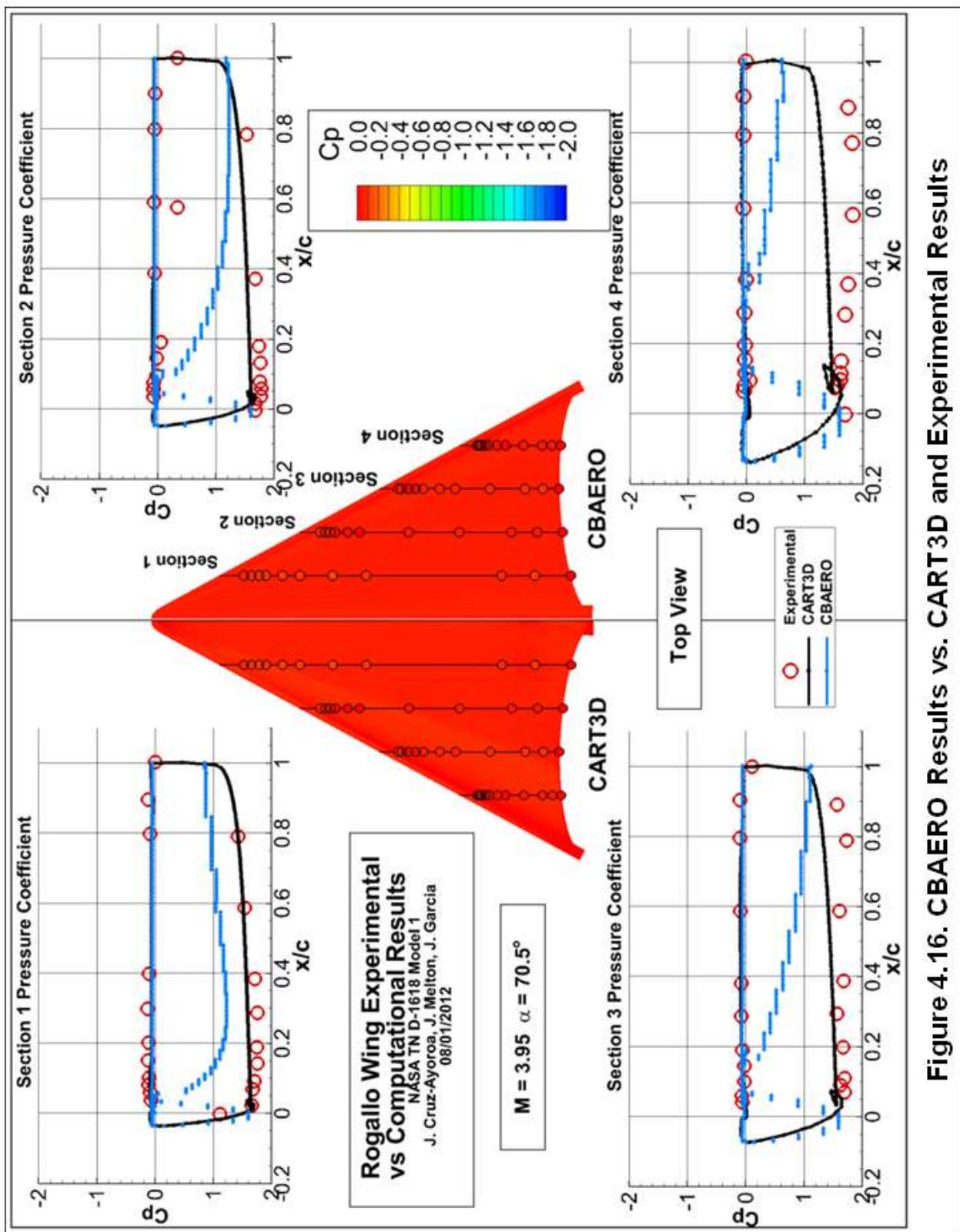


**Figure 4.16. CBAERO Results vs. CART3D and Experimental Results**

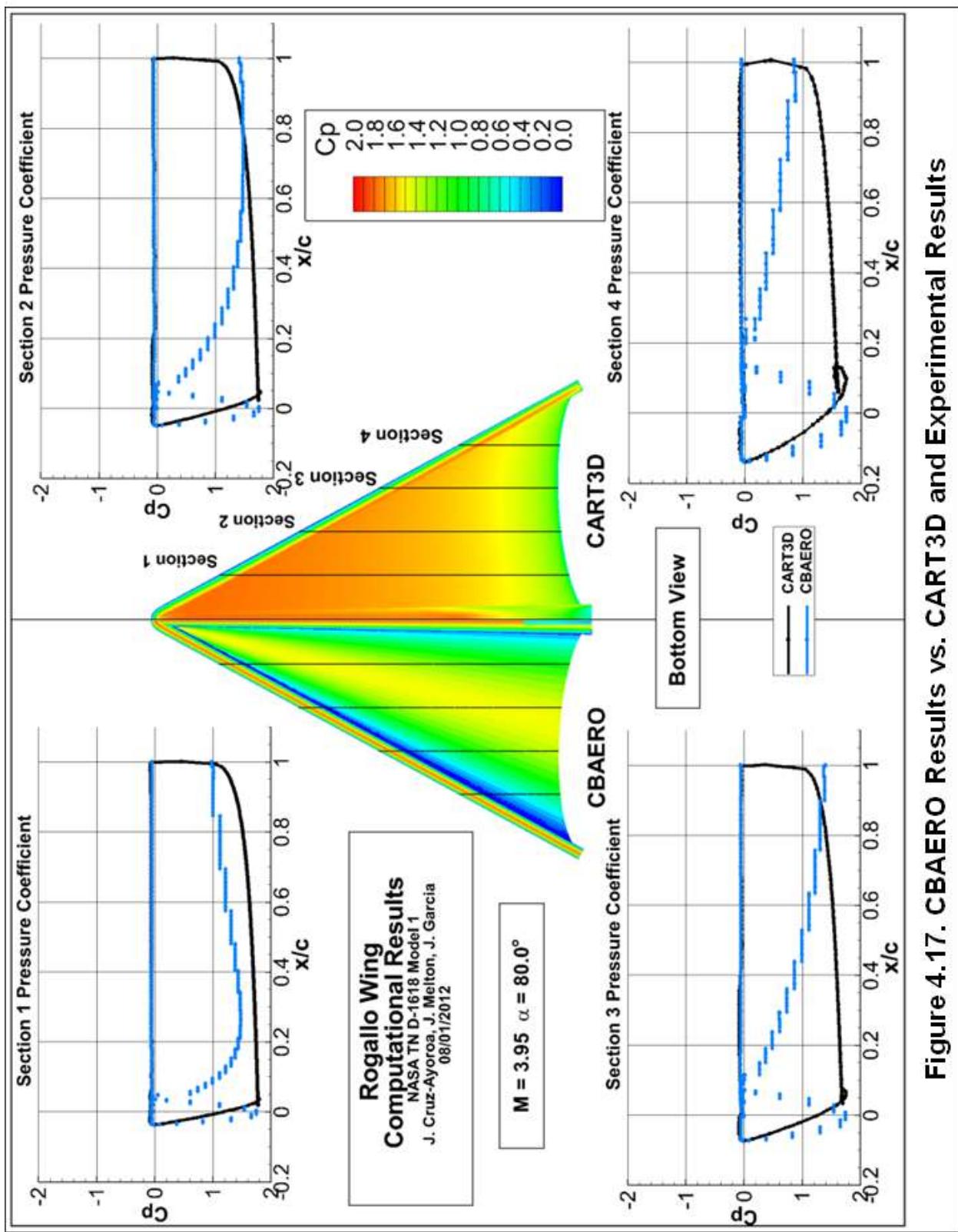


**Figure 4.17. CBAERO Results vs. CART3D and Experimental Results**

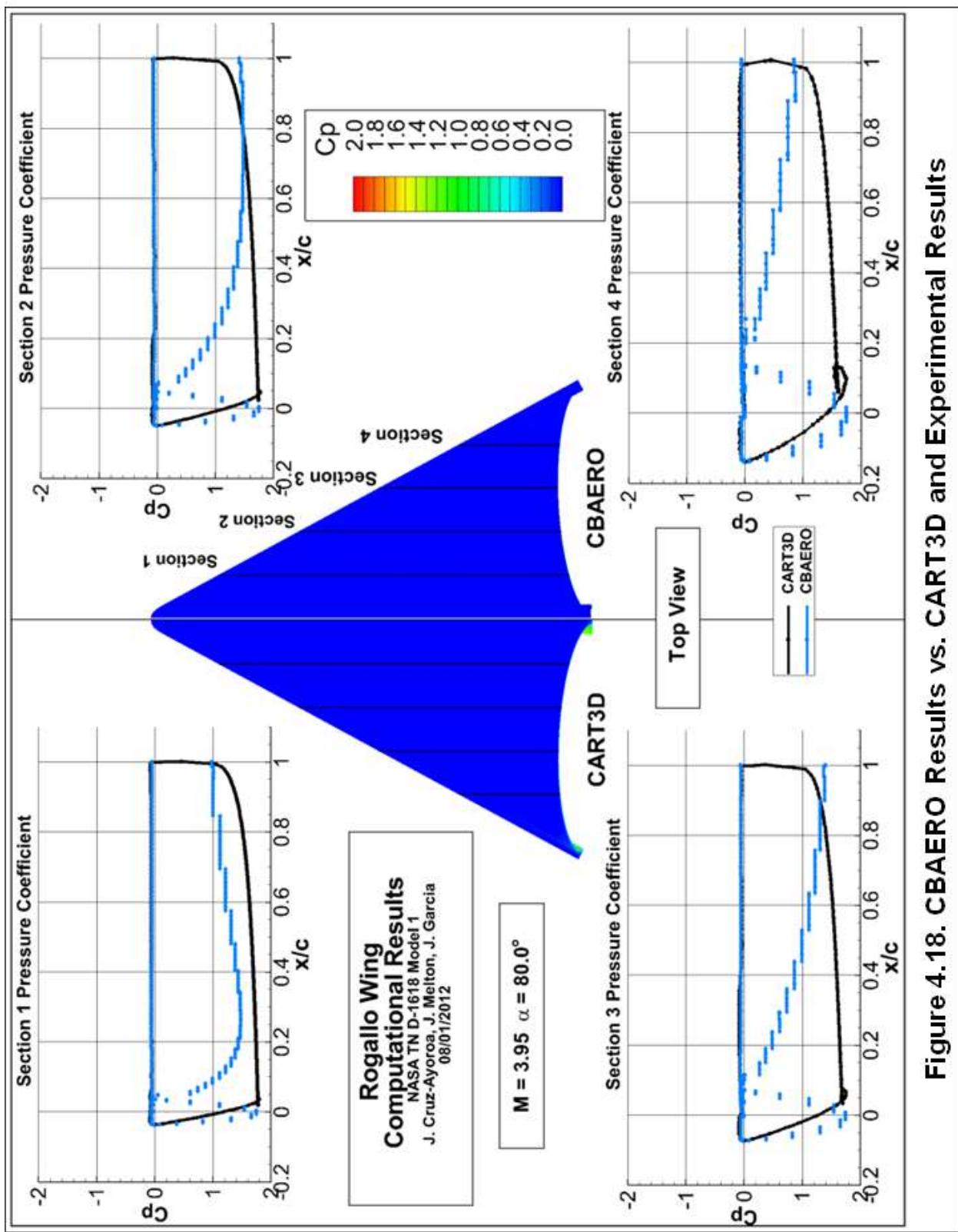


**Figure 4.18. CBAERO Results vs. CART3D and Experimental Results**

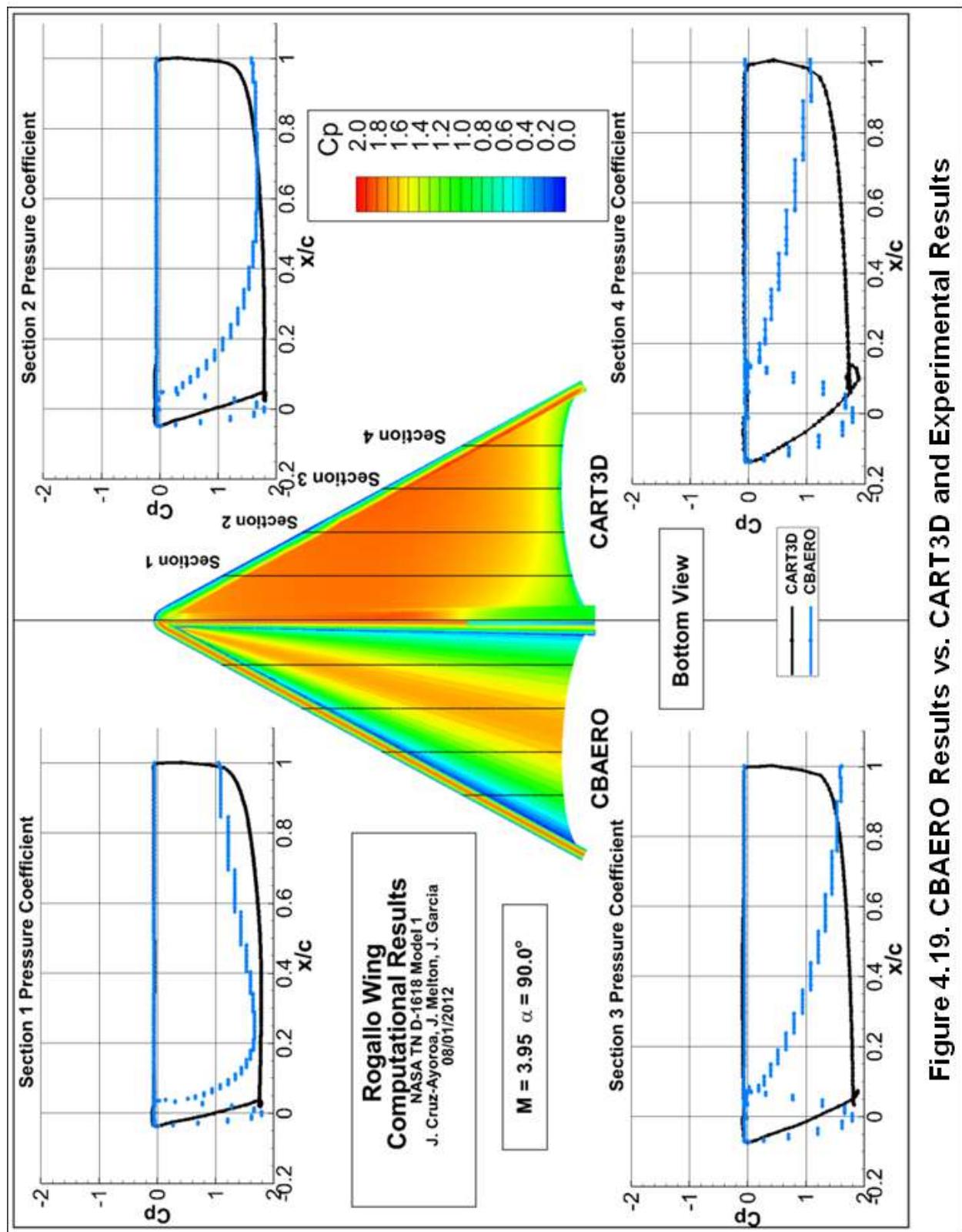
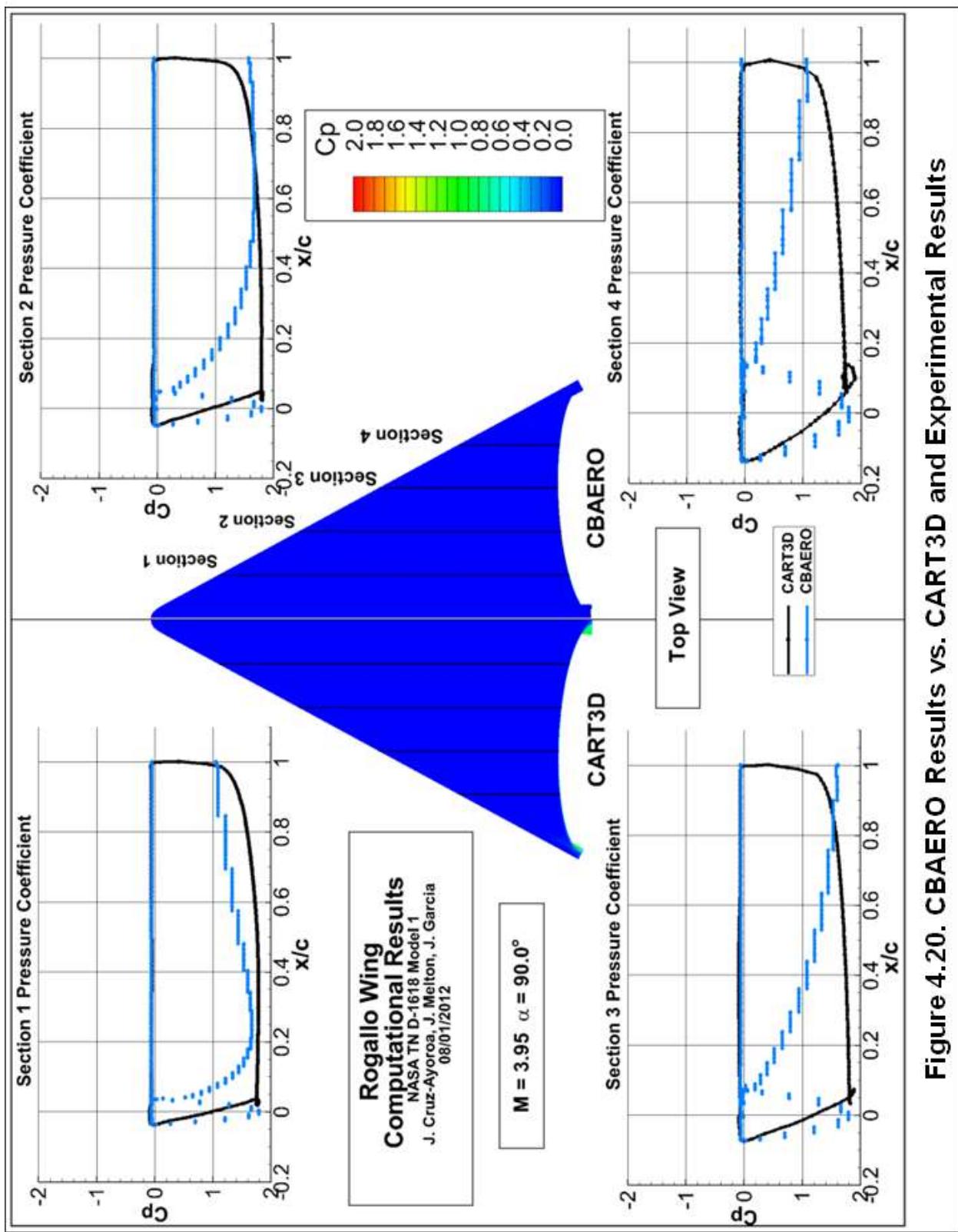


Figure 4.19. CBAERO Results vs. CART3D and Experimental Results



**Figure 4.20. CBAERO Results vs. CART3D and Experimental Results**

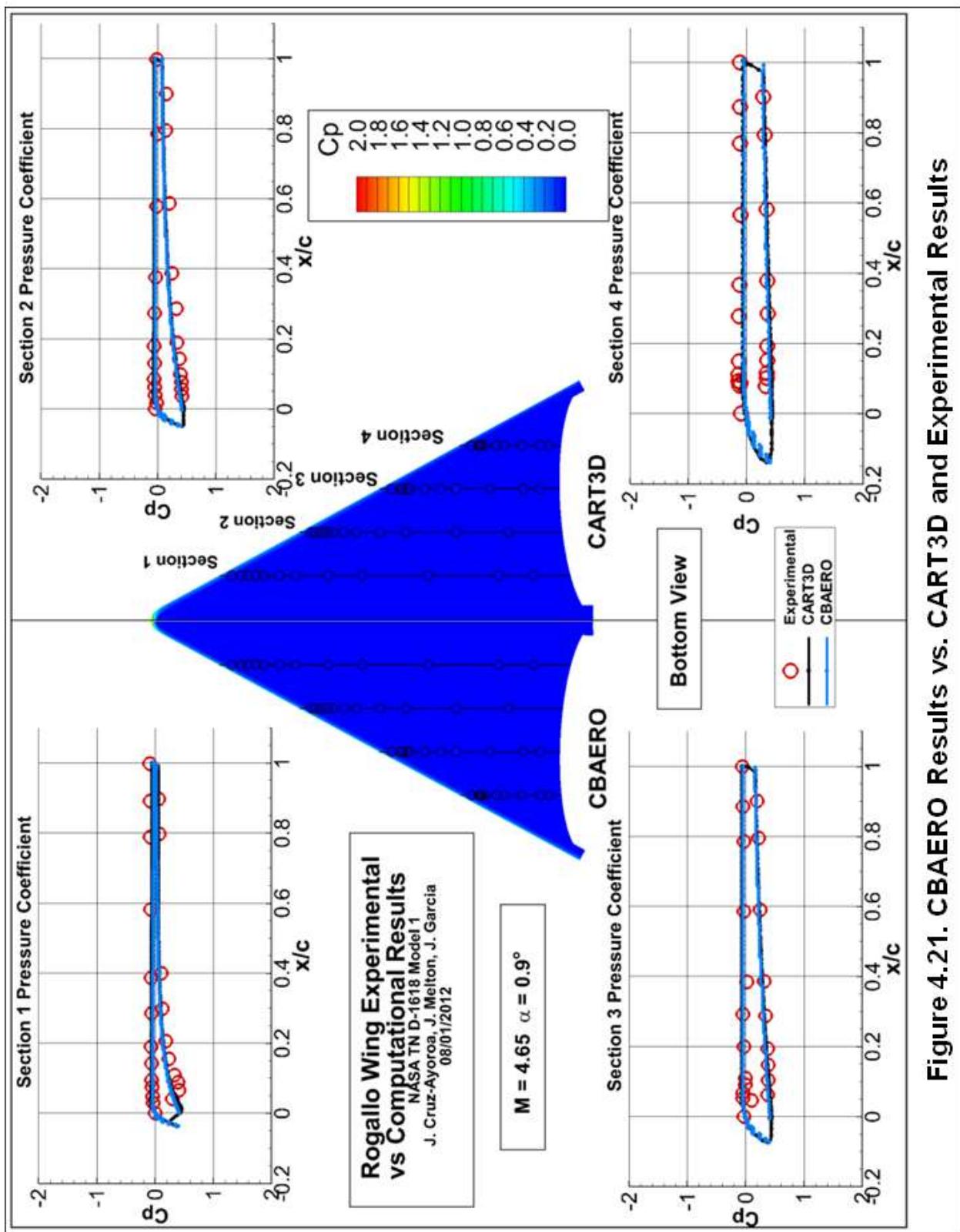
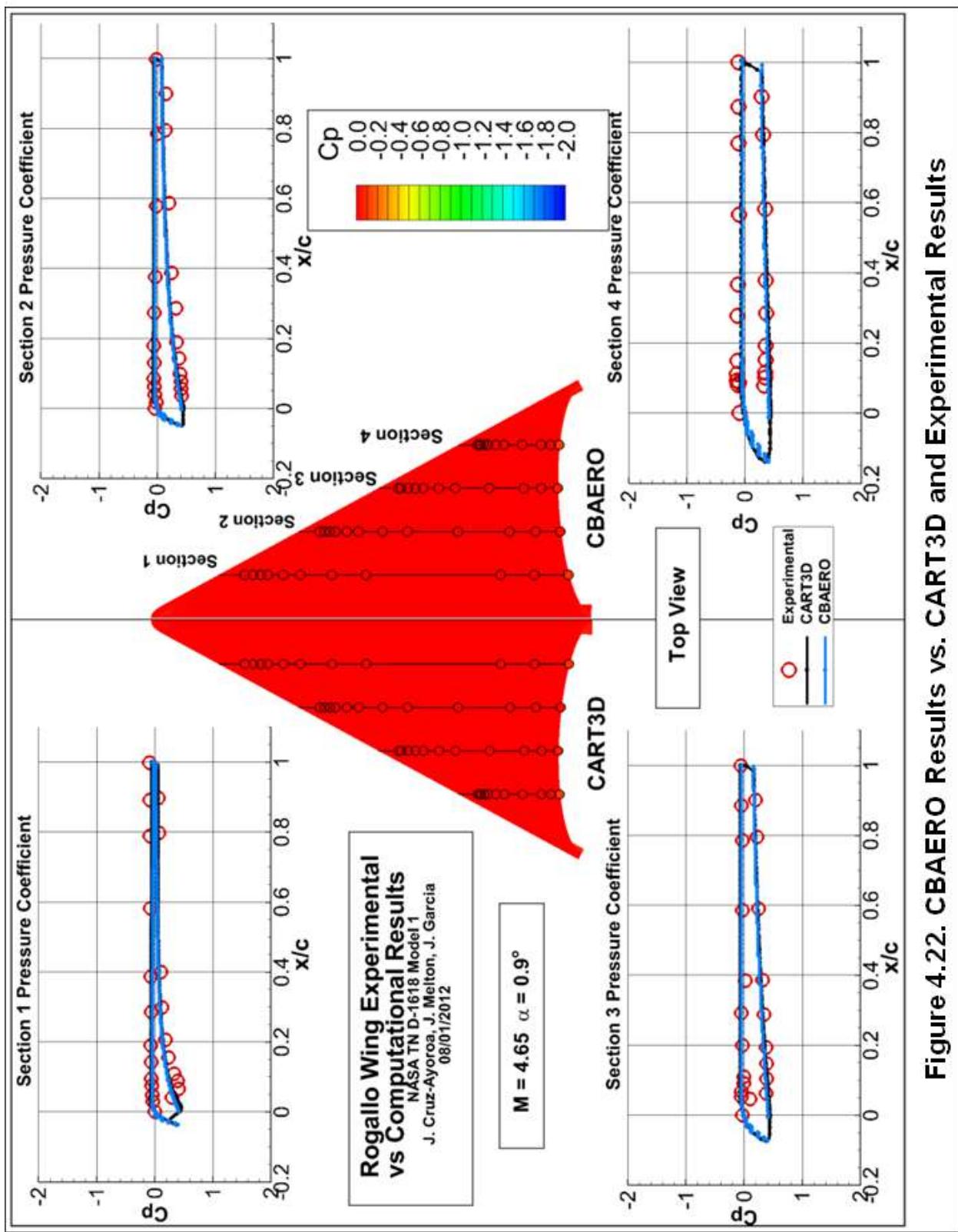
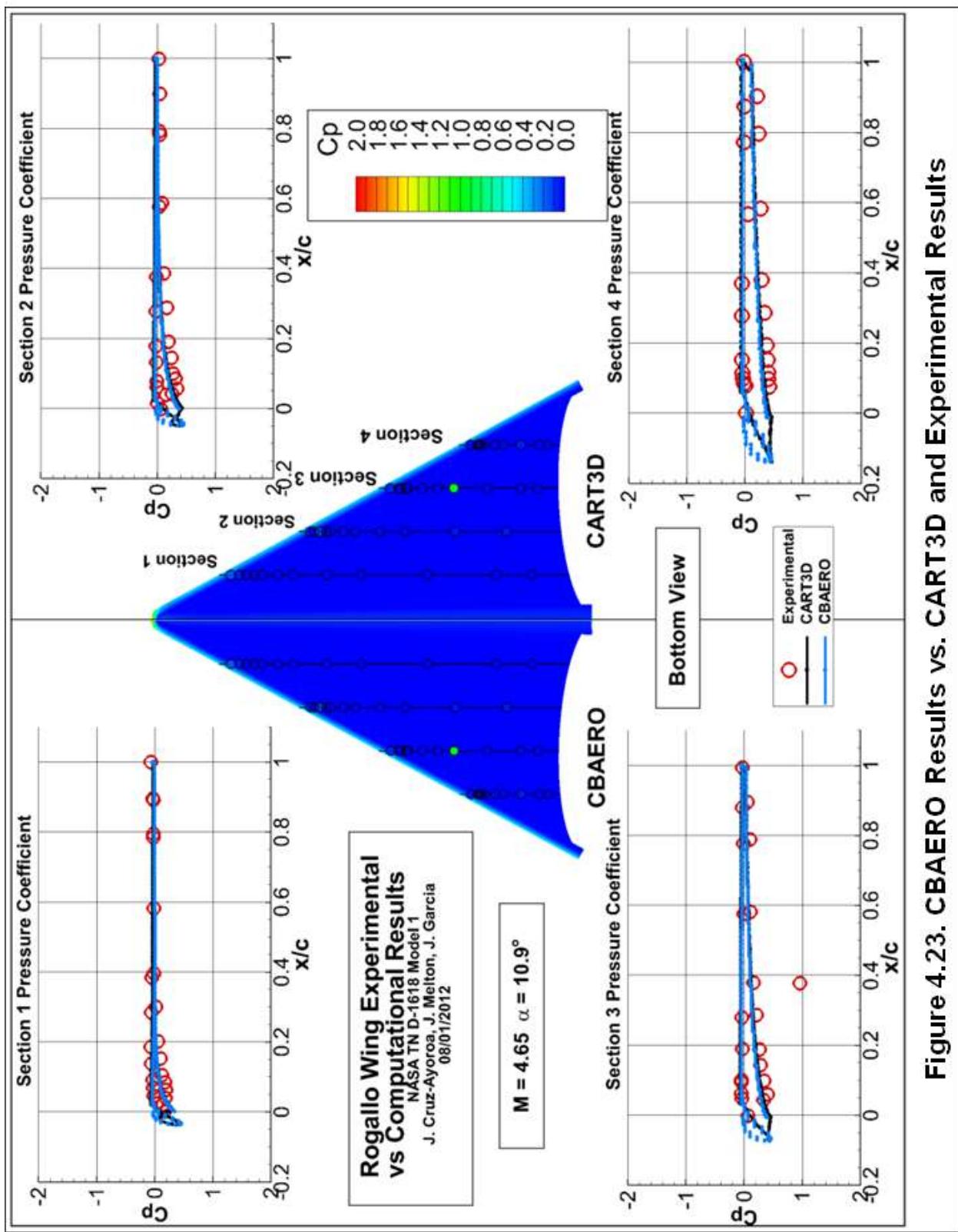


Figure 4.21. CBAERO Results vs. CART3D and Experimental Results



**Figure 4.22. CBAERO Results vs. CART3D and Experimental Results**



**Figure 4.23. CBAERO Results vs. CART3D and Experimental Results**

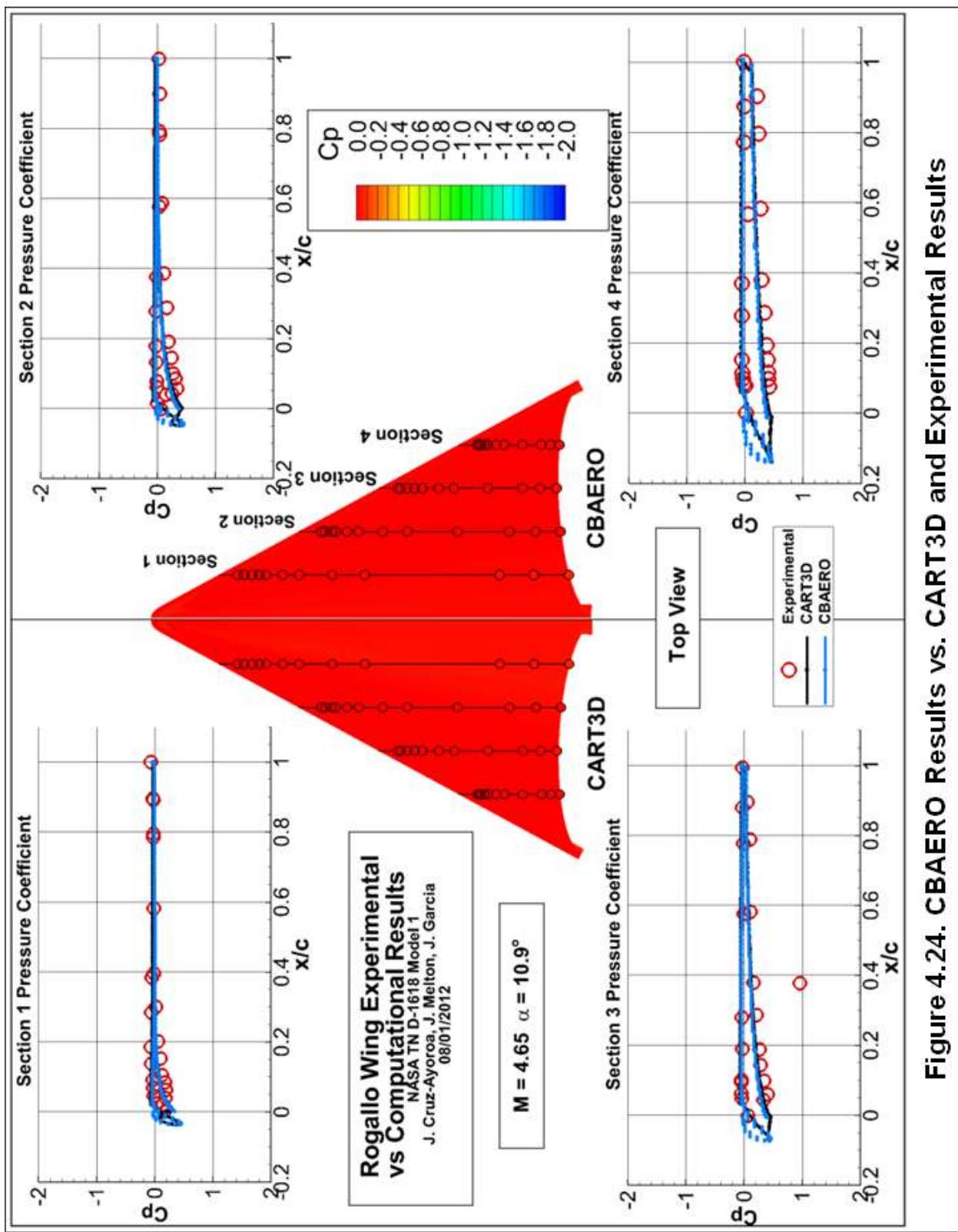


**Figure 4.24. CBAERO Results vs. CART3D and Experimental Results**

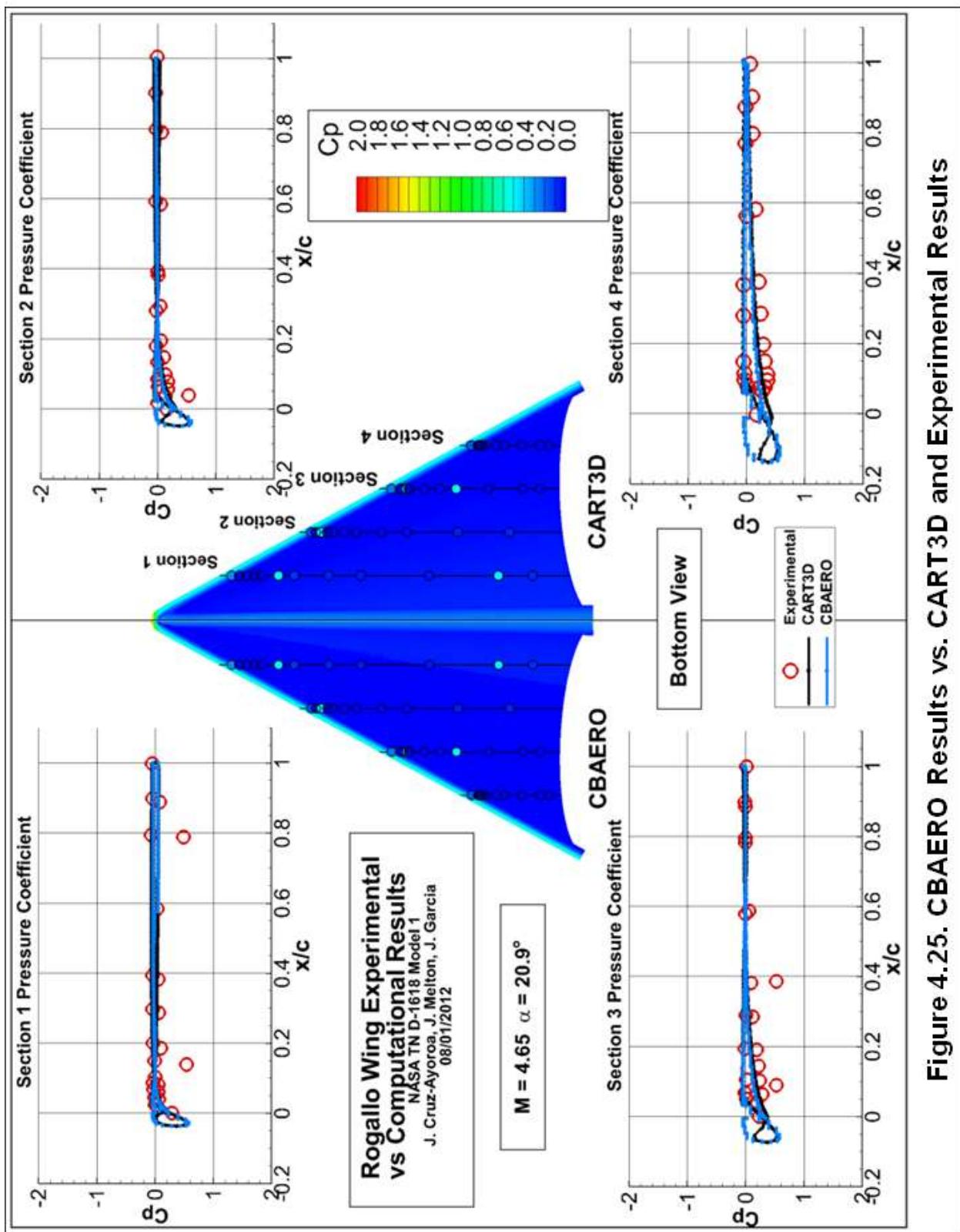


**Figure 4.25. CBAERO Results vs. CART3D and Experimental Results**

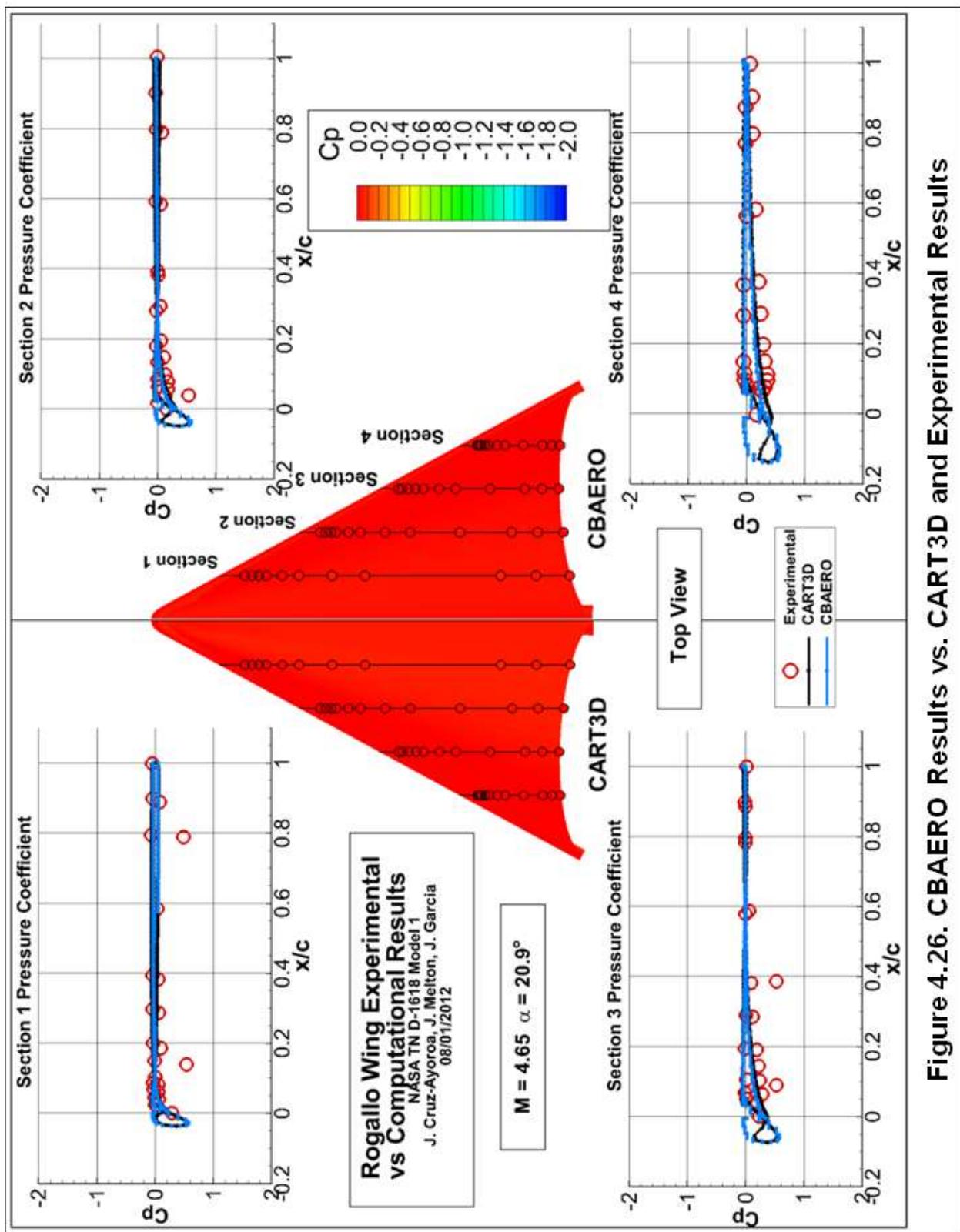


**Figure 4.26. CBAERO Results vs. CART3D and Experimental Results**

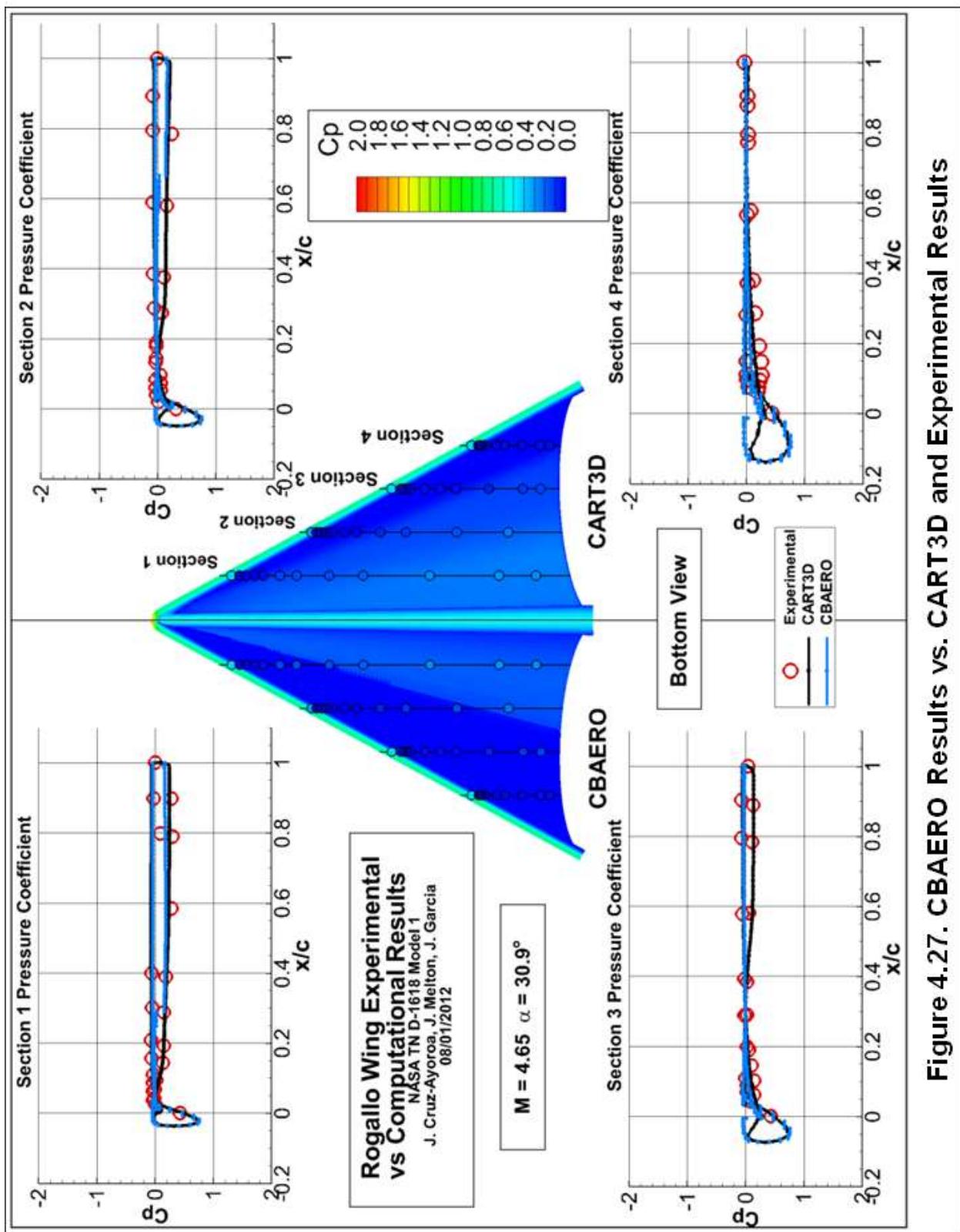
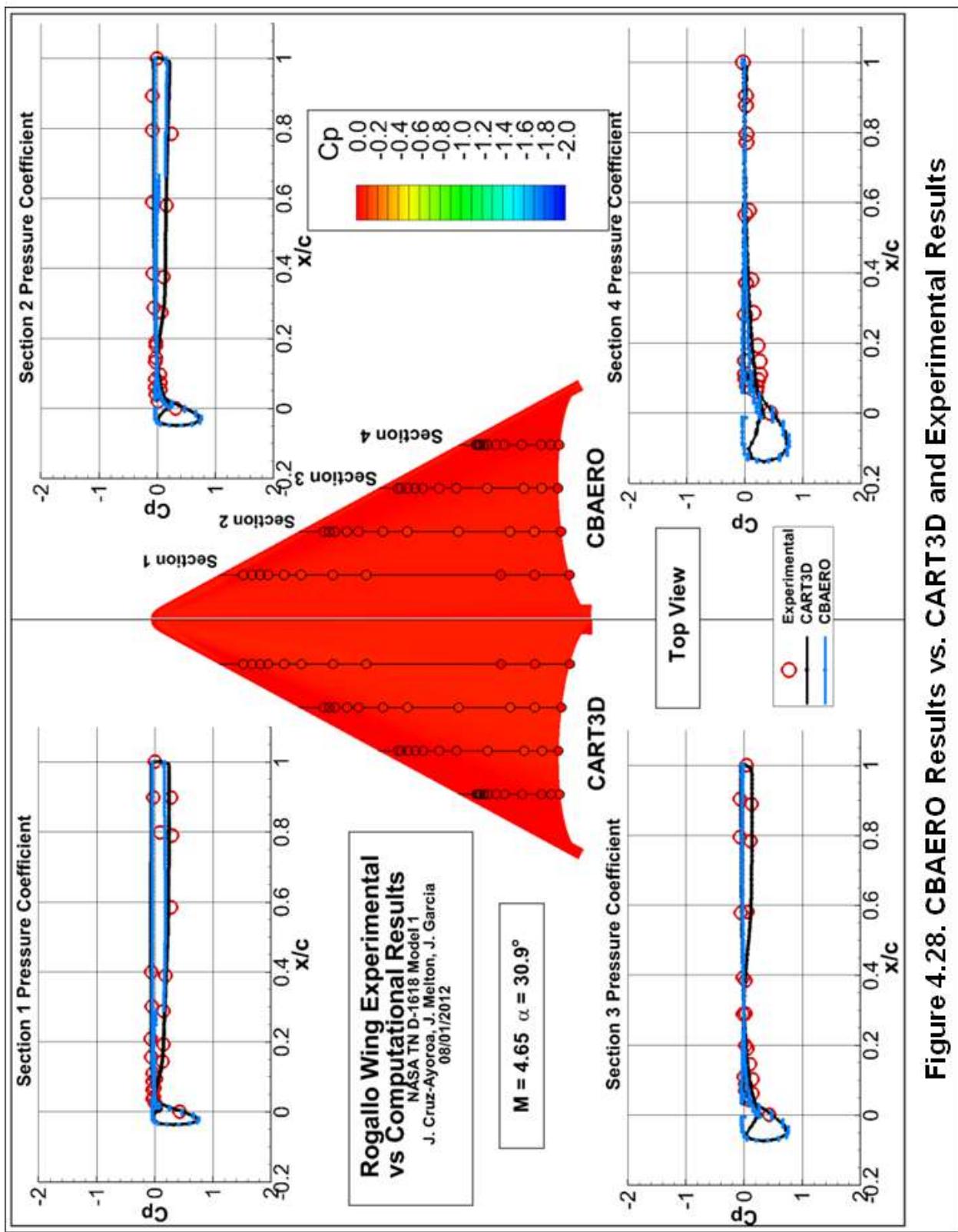


Figure 4.27. CBAERO Results vs. CART3D and Experimental Results



**Figure 4.28. CBAERO Results vs. CART3D and Experimental Results**

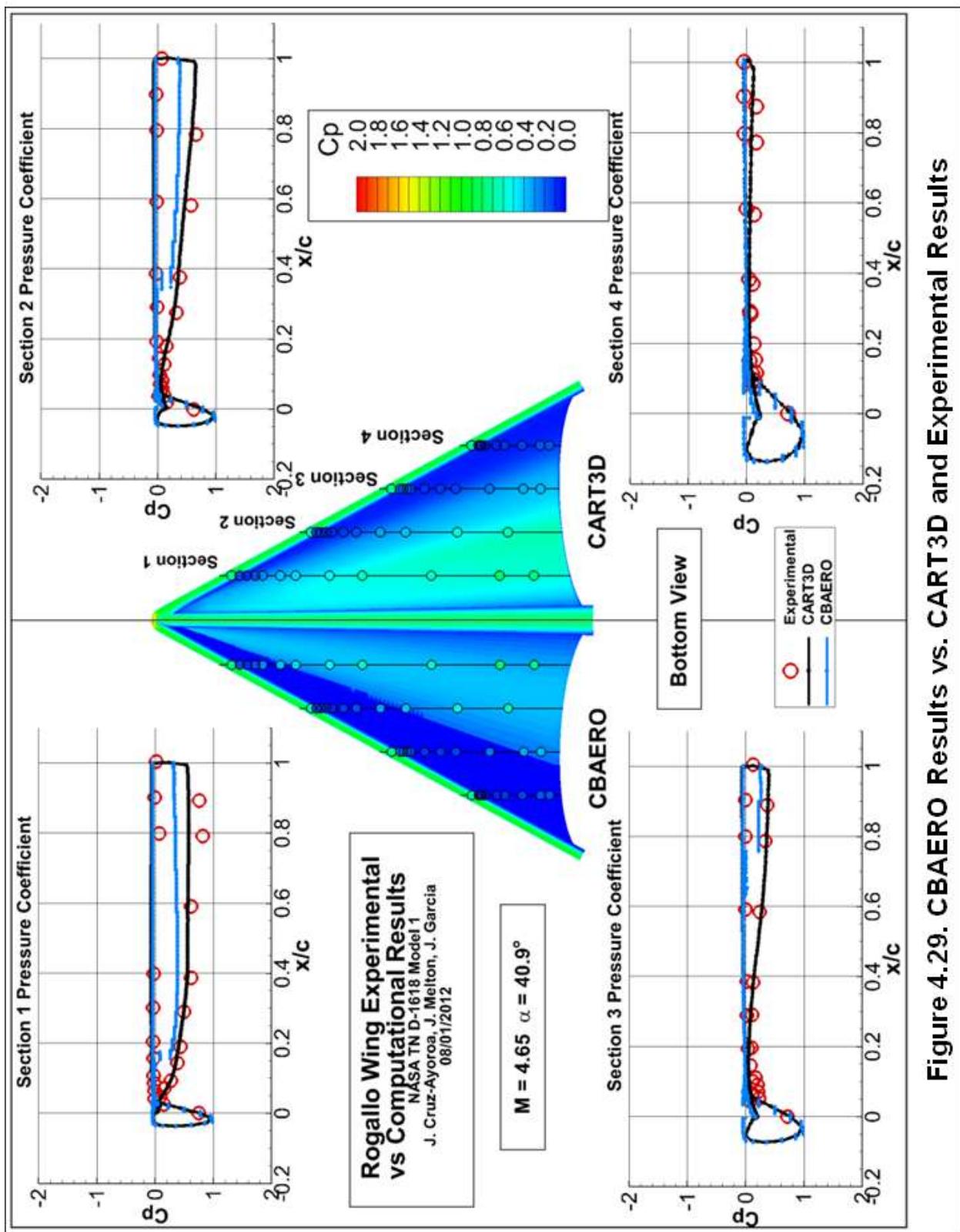


Figure 4.29. CBAERO Results vs. CART3D and Experimental Results

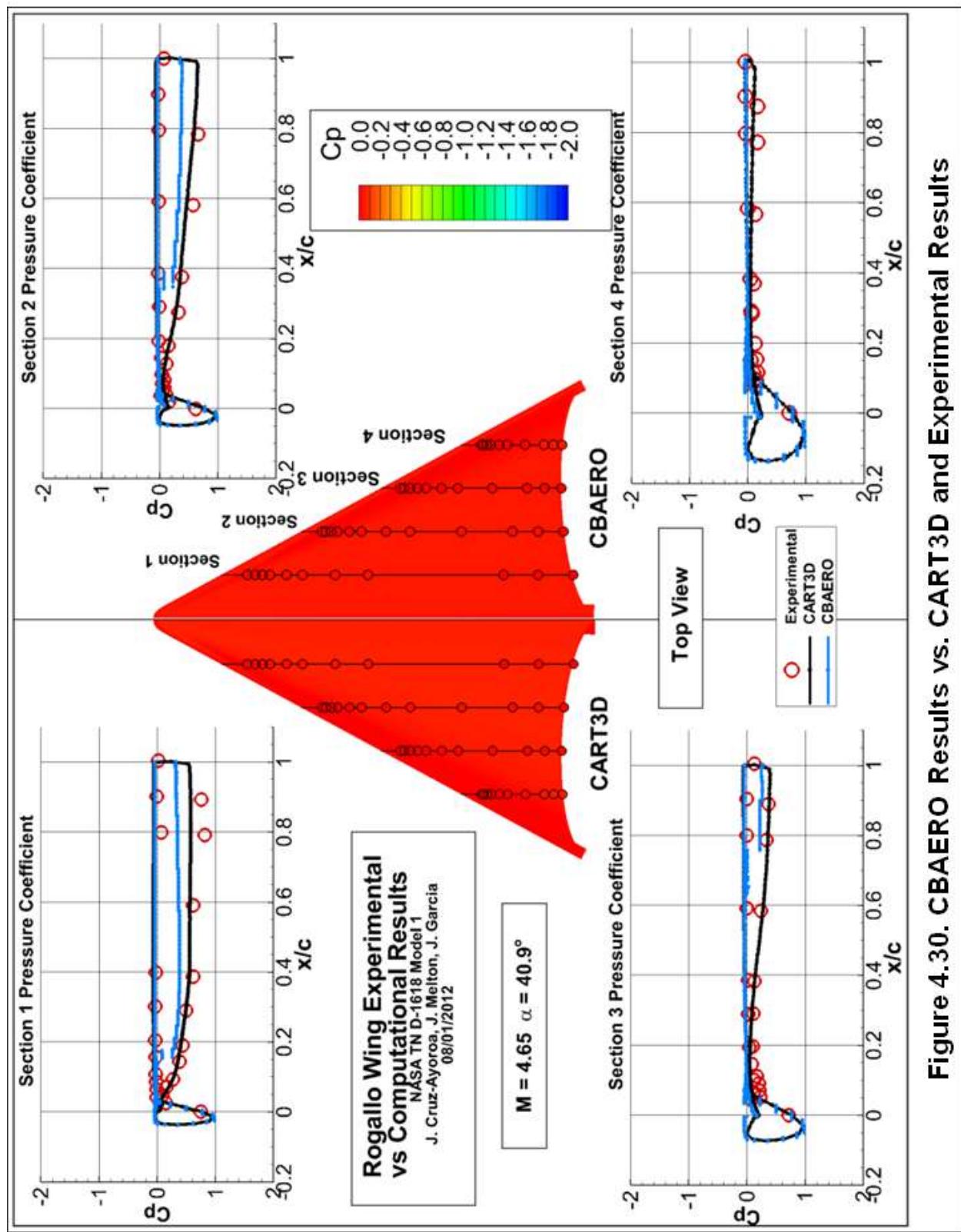


Figure 4.30. CBAERO Results vs. CART3D and Experimental Results

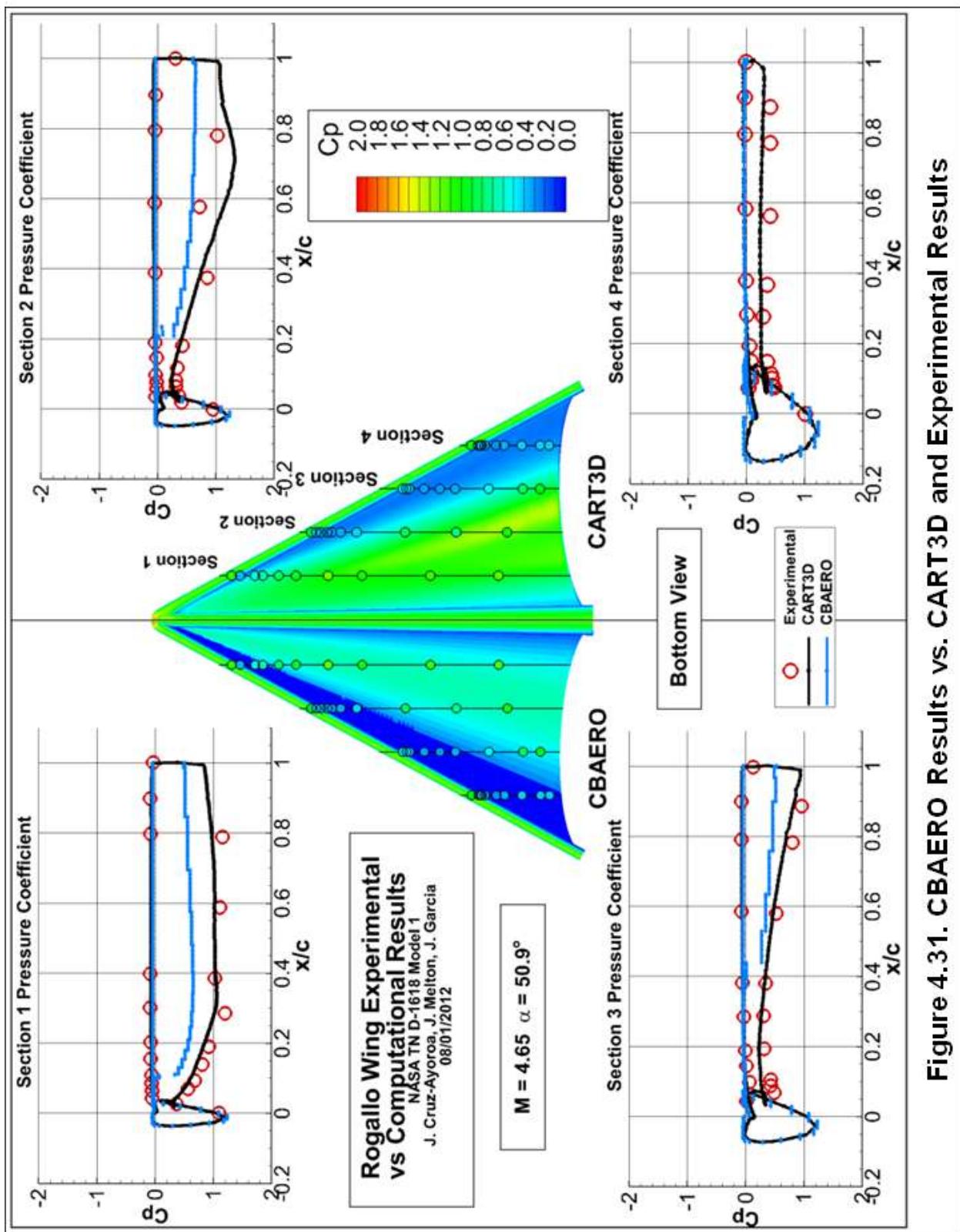
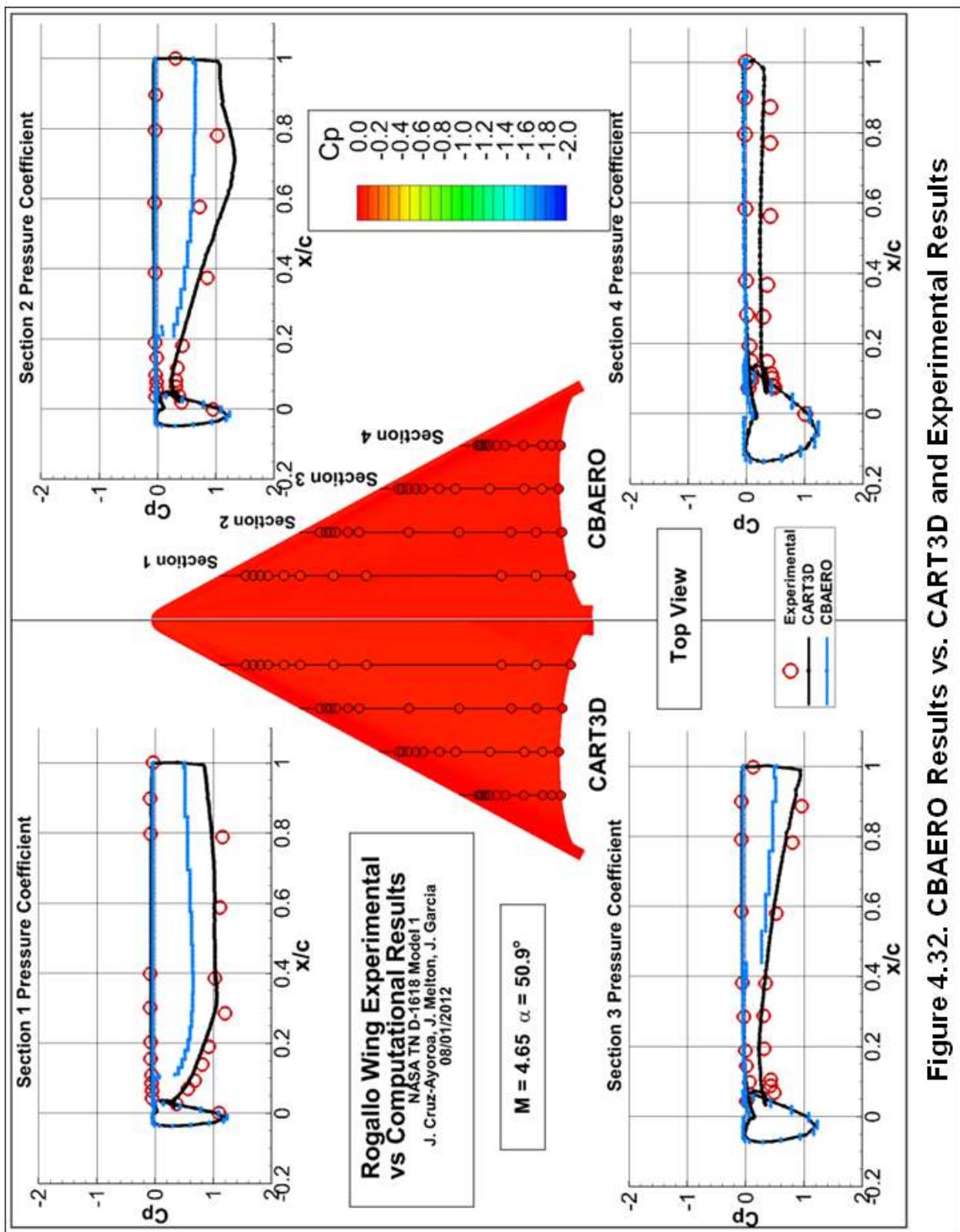
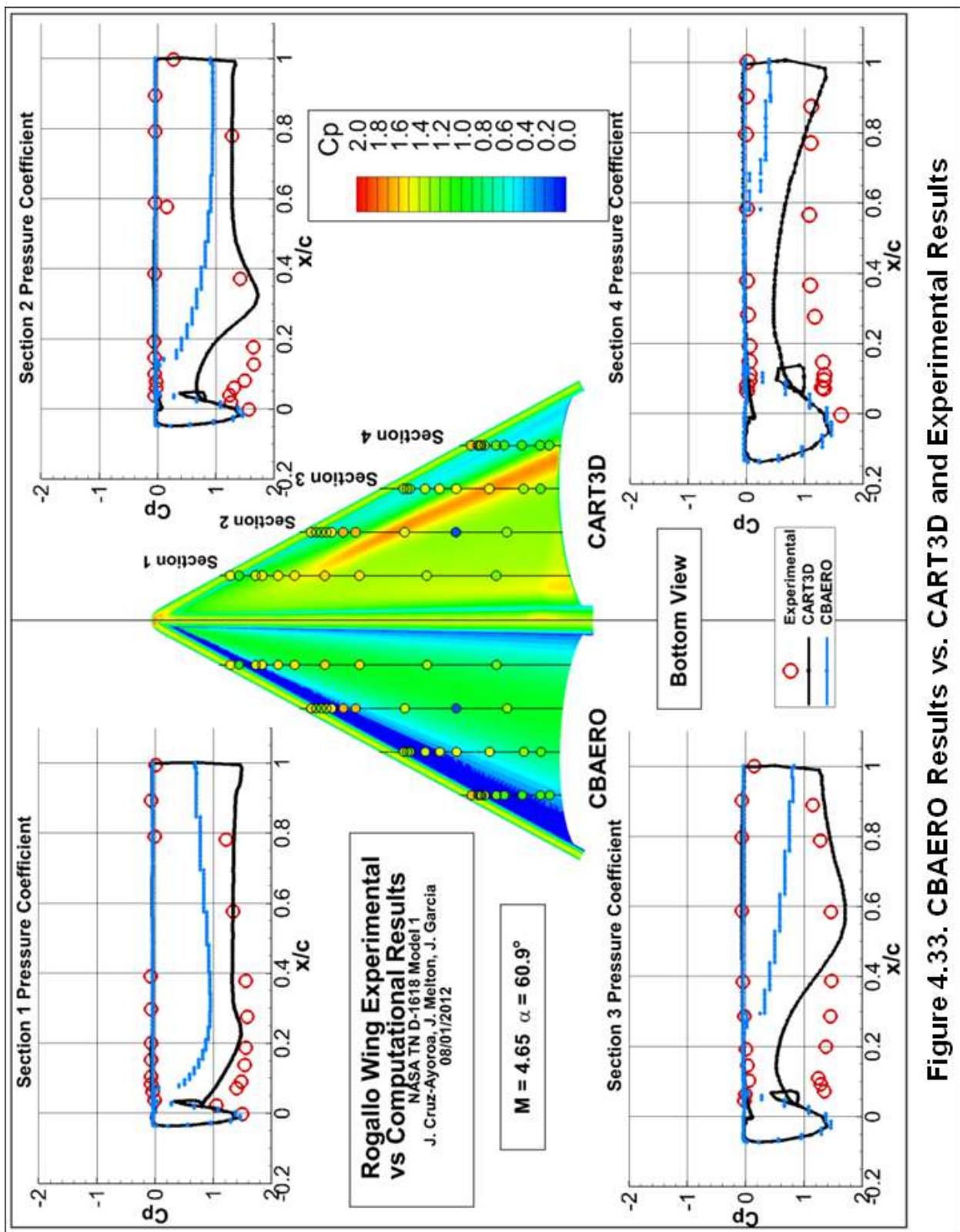


Figure 4.31. CBAERO Results vs. CART3D and Experimental Results



**Figure 4.32. CBAERO Results vs. CART3D and Experimental Results**



**Figure 4.33. CBAERO Results vs. CART3D and Experimental Results**

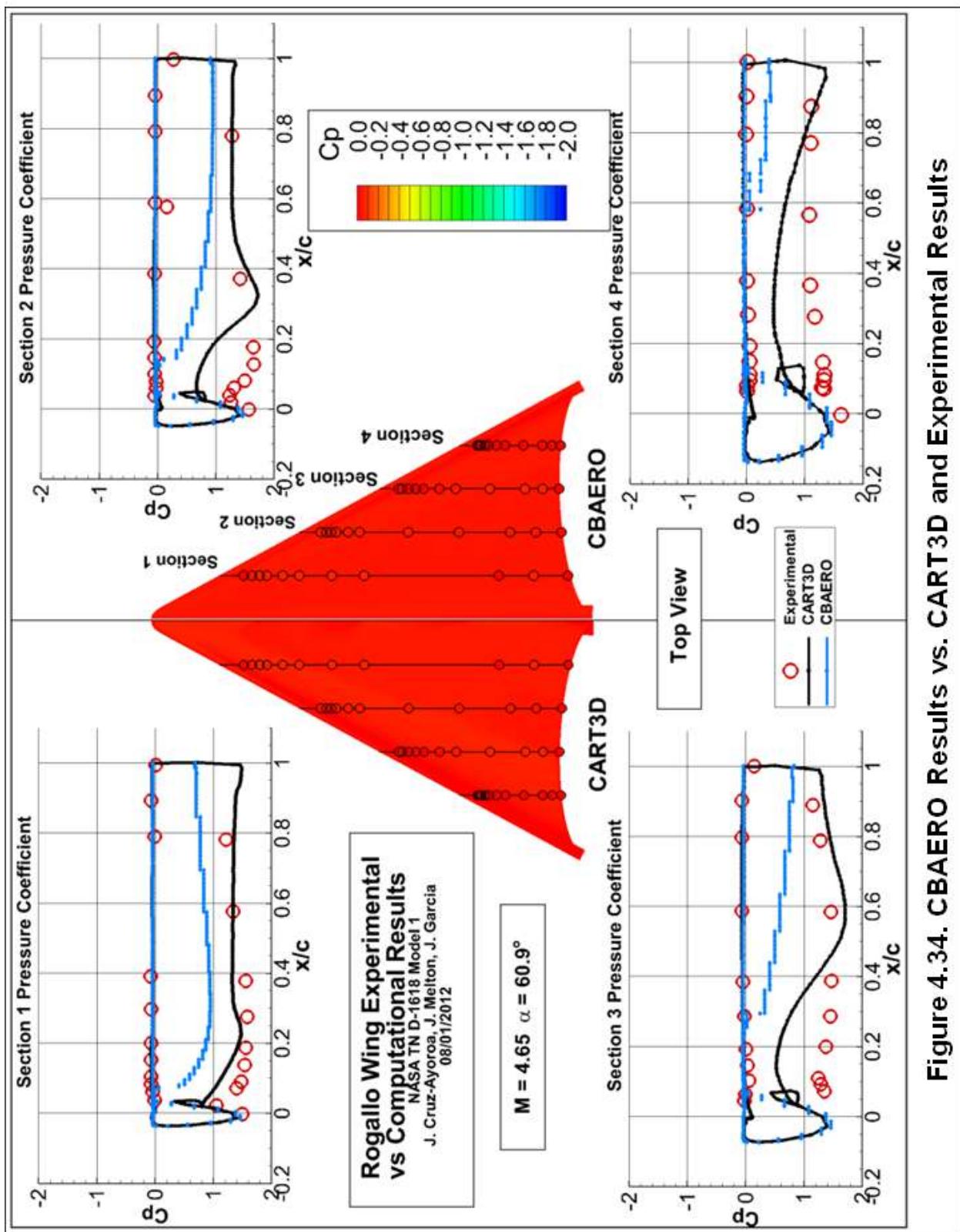
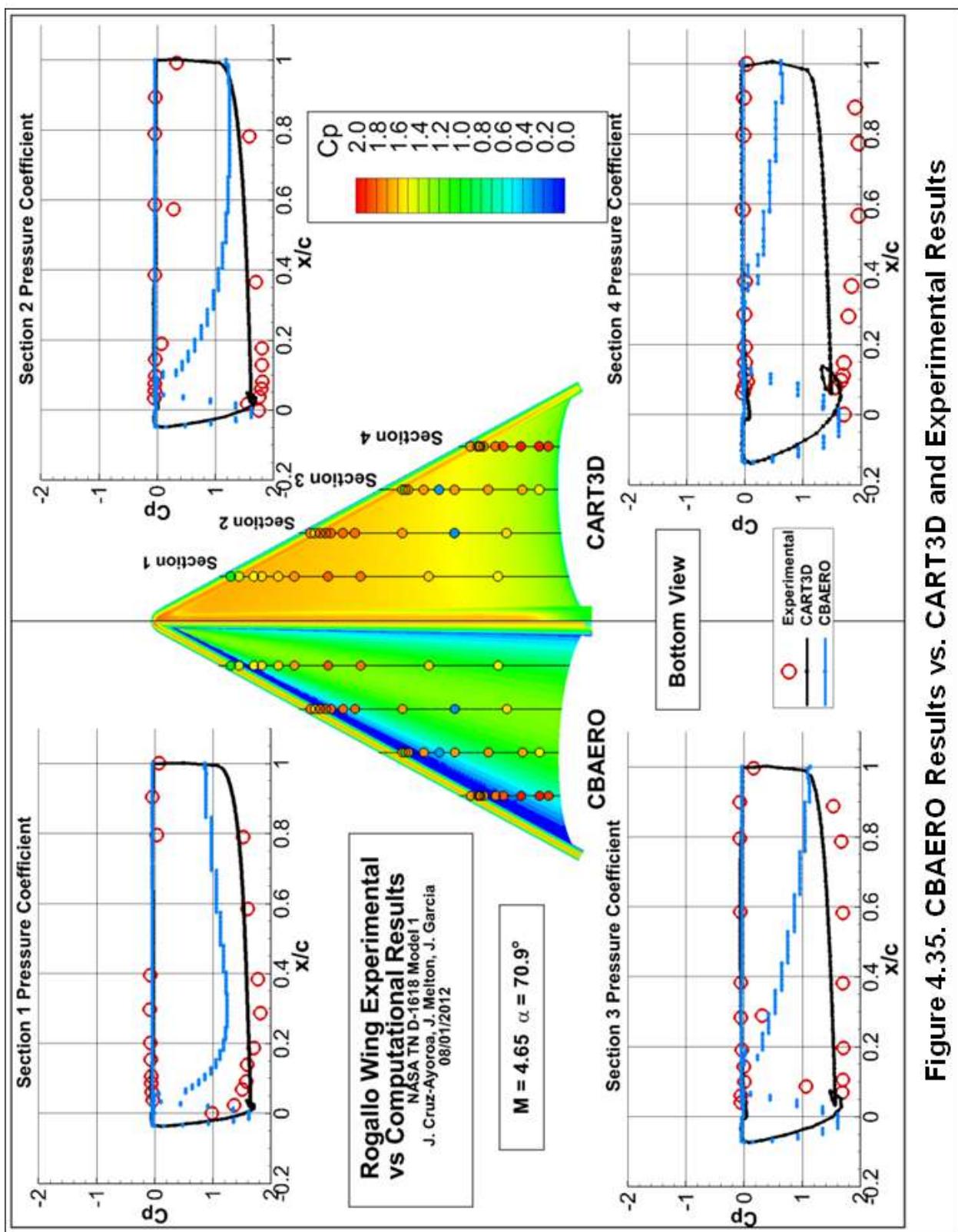
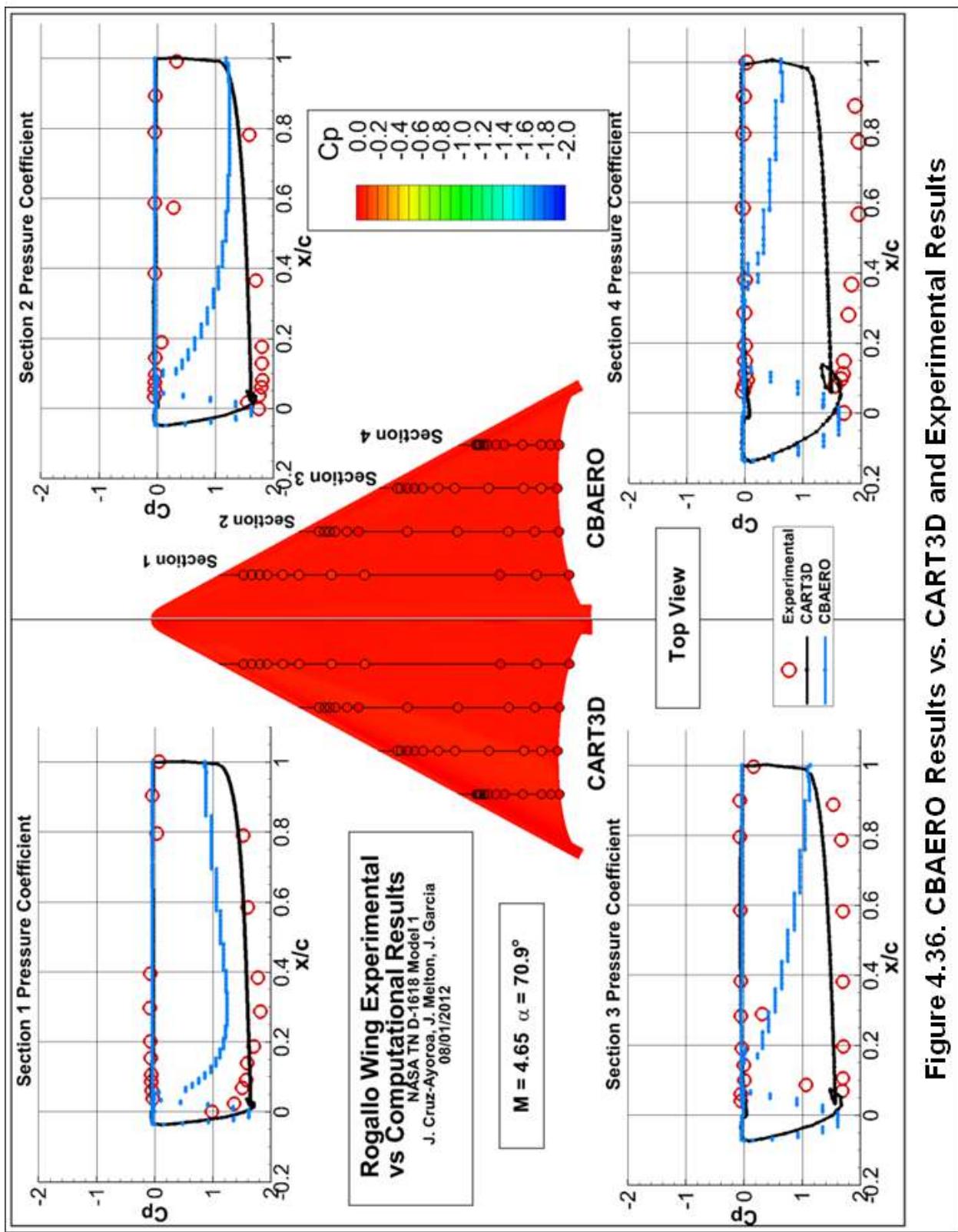


Figure 4.34. CBAERO Results vs. CART3D and Experimental Results



**Figure 4.35. CBAERO Results vs. CART3D and Experimental Results**



**Figure 4.36. CBAERO Results vs. CART3D and Experimental Results**

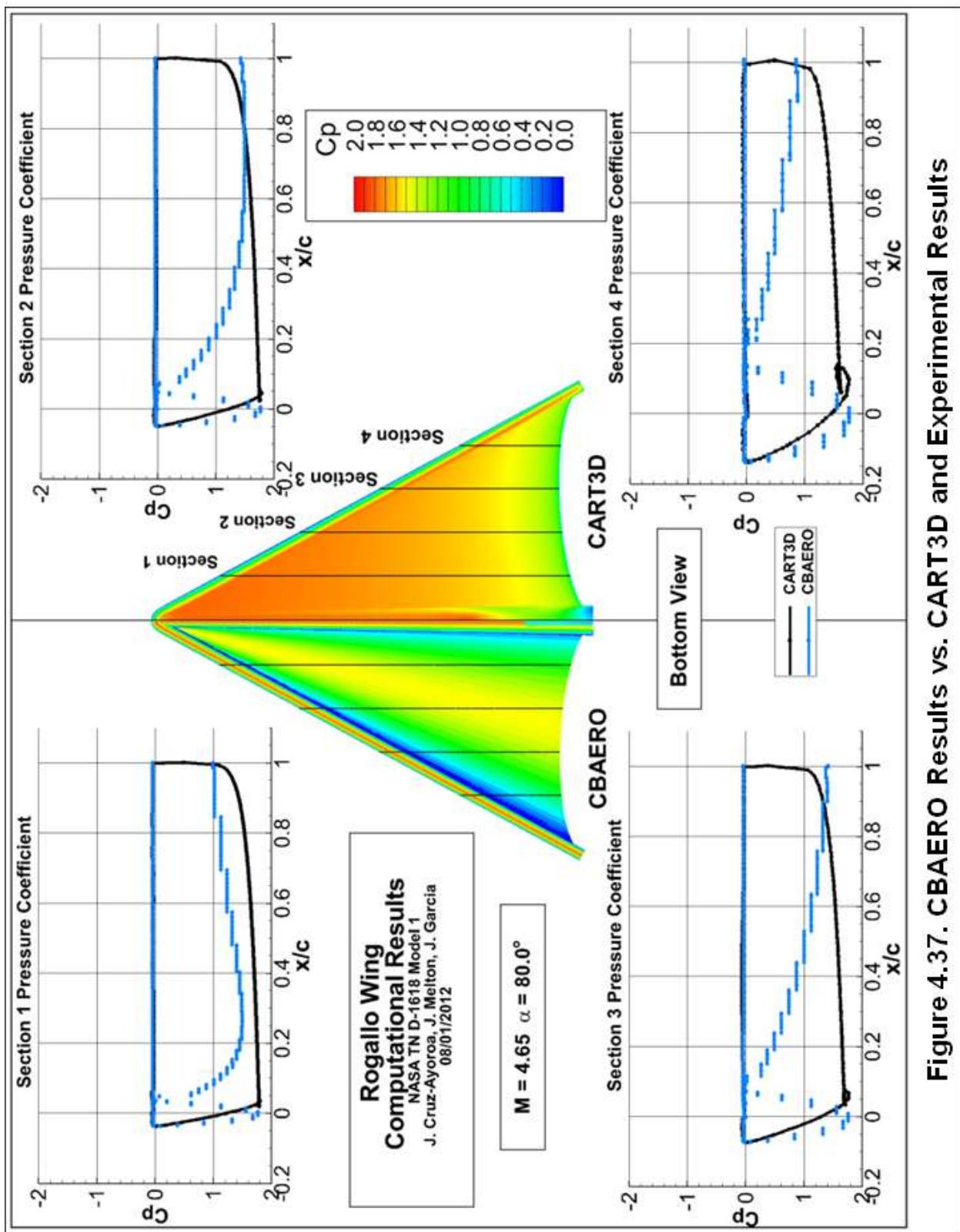
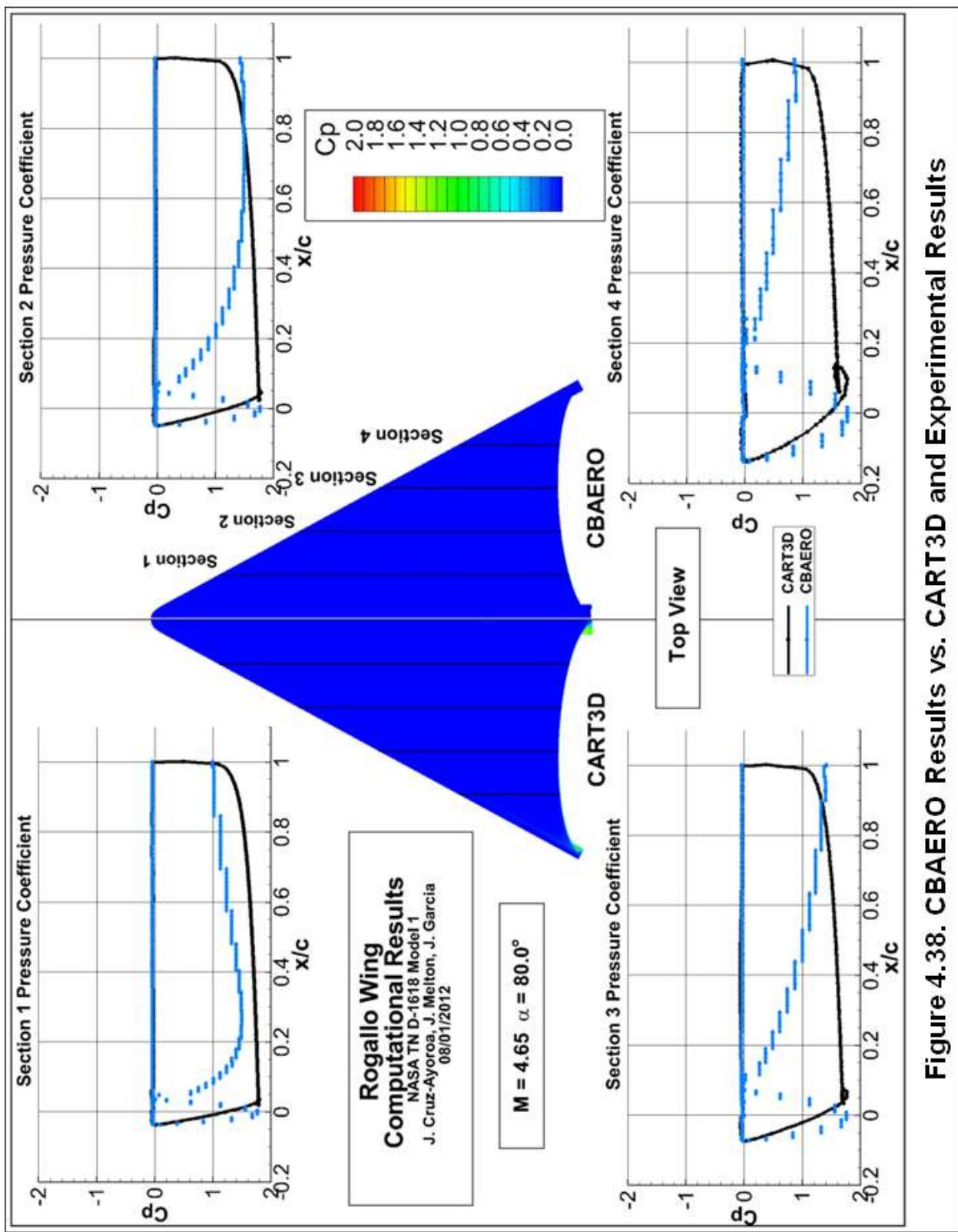


Figure 4.37. CBAERO Results vs. CART3D and Experimental Results



**Figure 4.38. CBAERO Results vs. CART3D and Experimental Results**

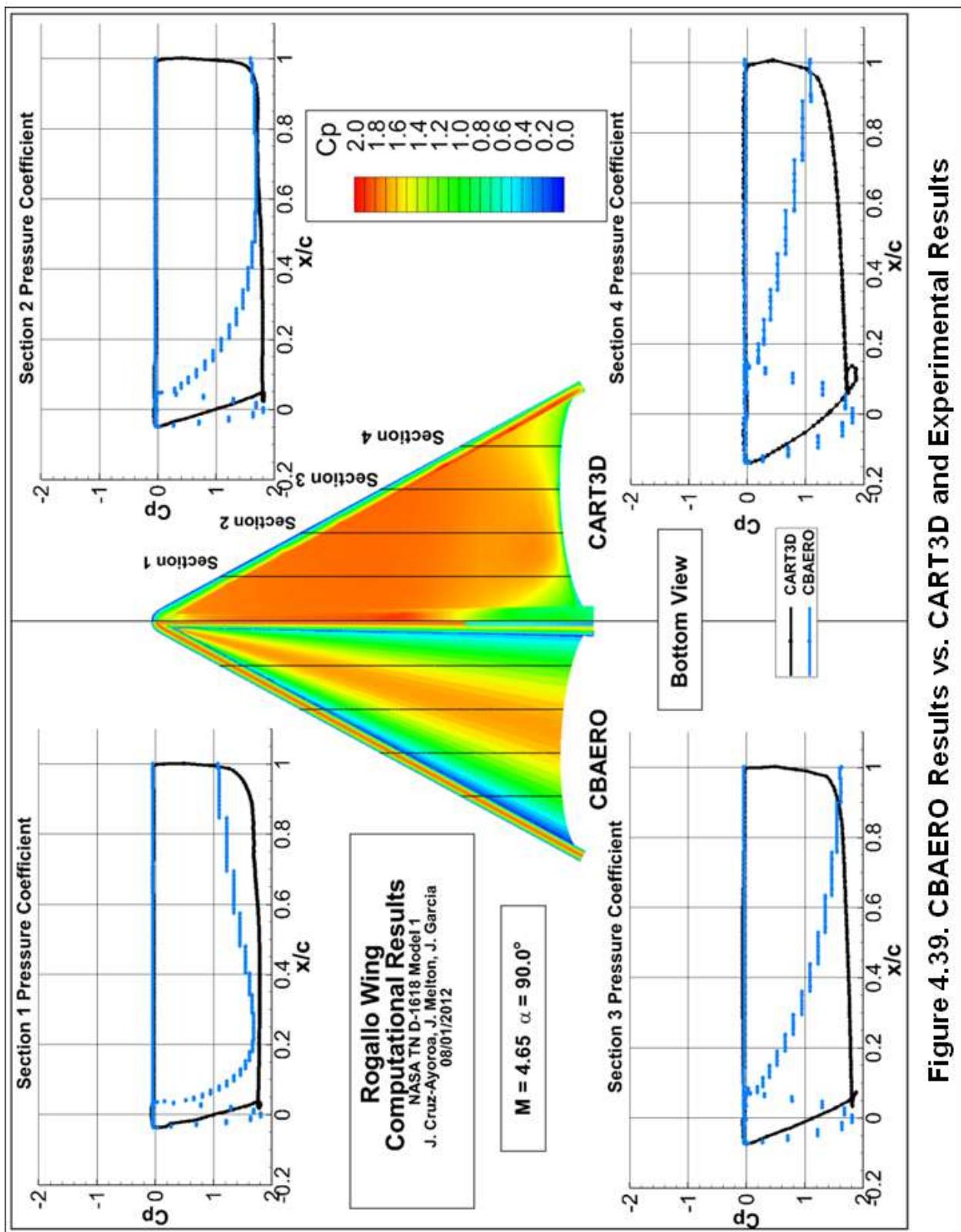
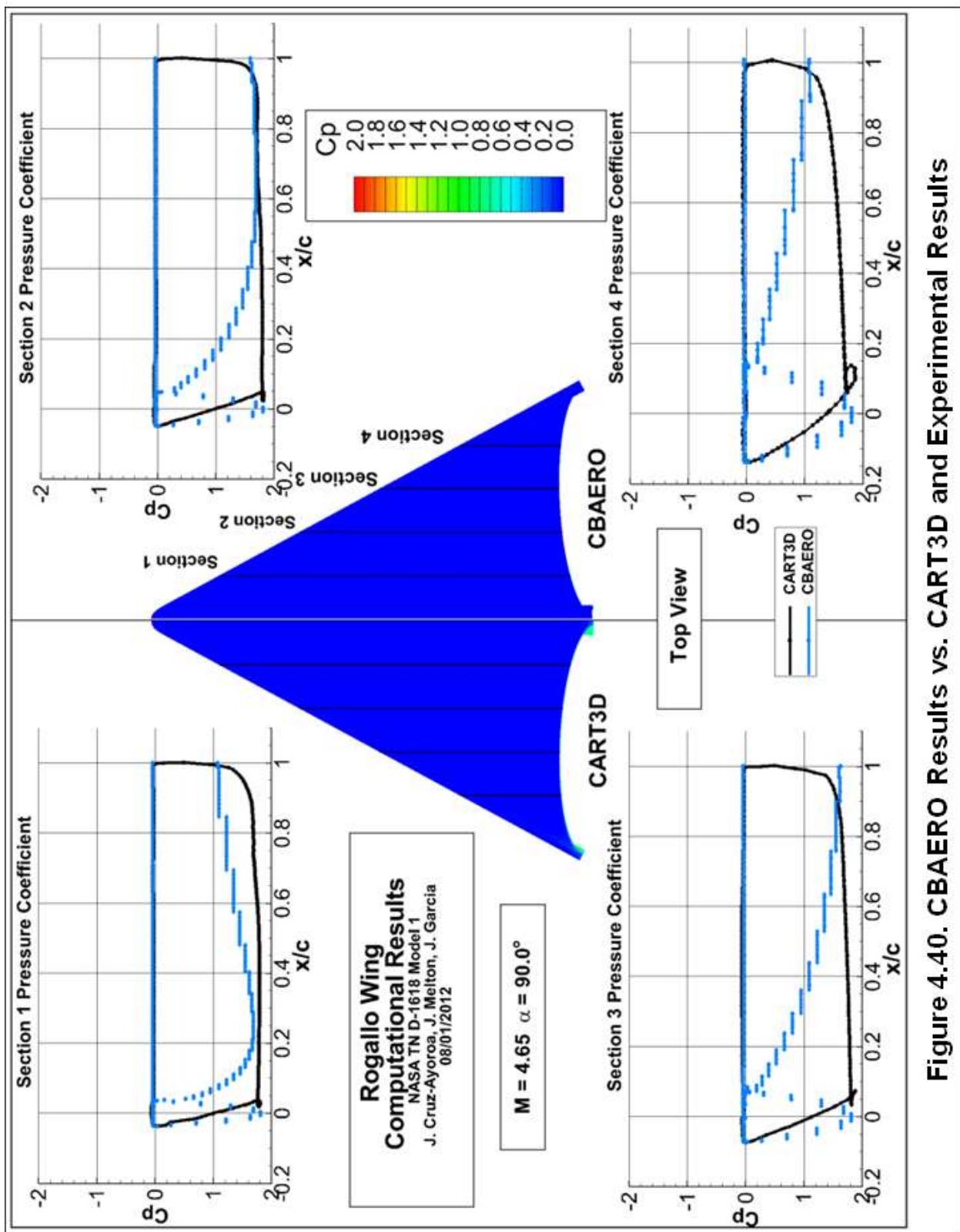
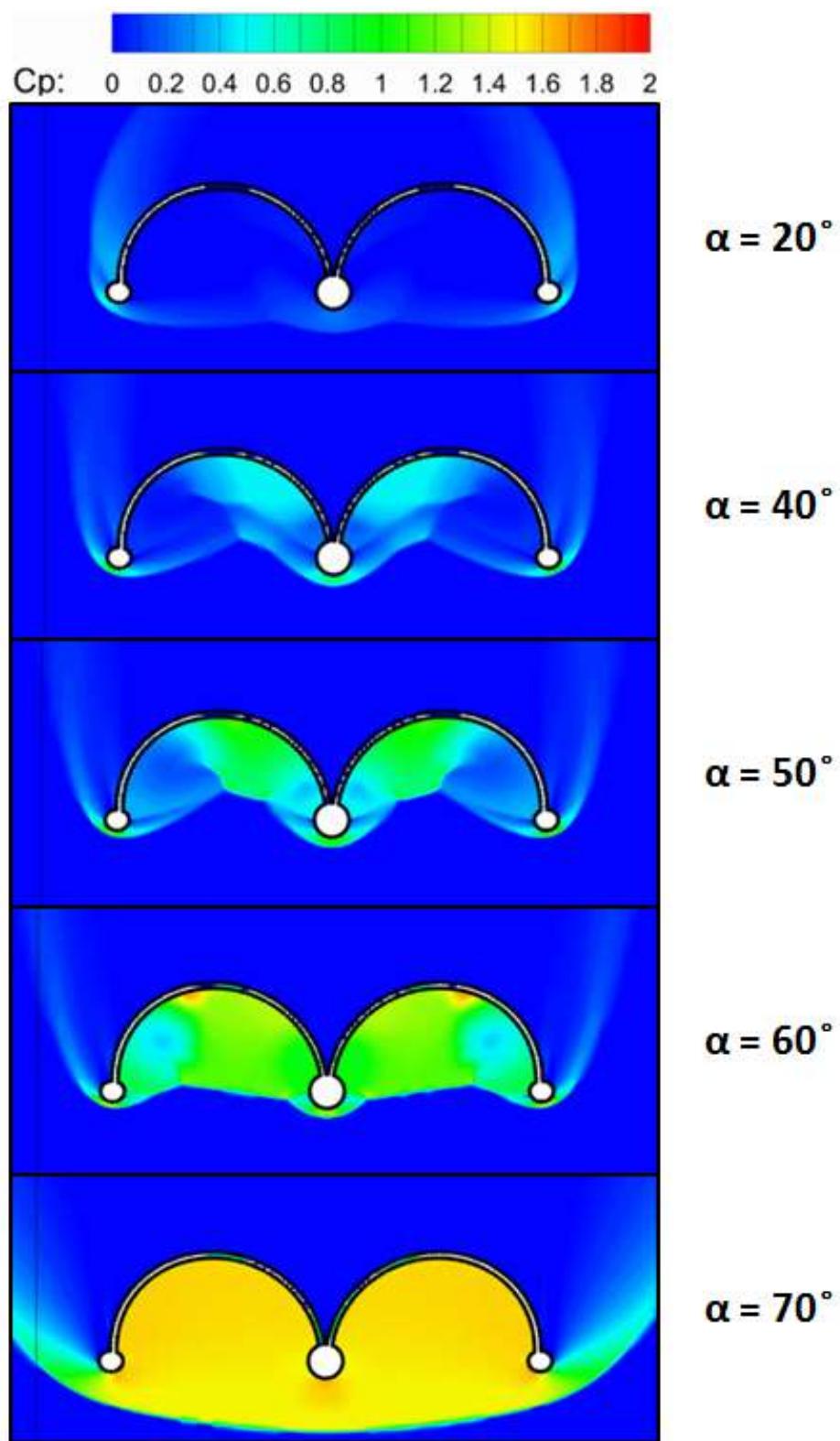


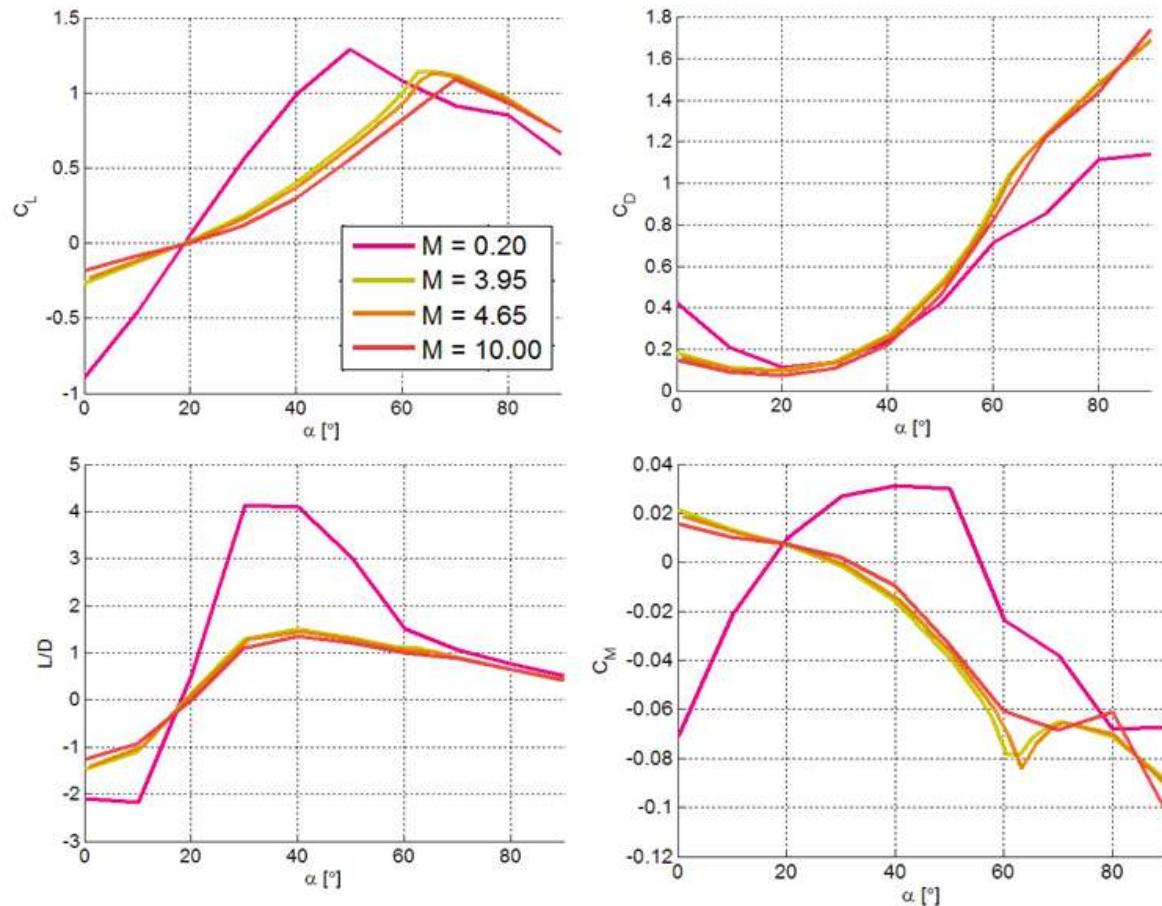
Figure 4.39. CBAERO Results vs. CART3D and Experimental Results



**Figure 4.40. CBAERO Results vs. CART3D and Experimental Results**



**Figure 5. CART3D Mid-keel Section Contour Plots of Pressure Coefficient for Parawing at Mach 4.65**



\*Reference area is projected area from top view

\*Reference length is keel length

\*Moment coefficient reference point located at 60% keel length from front to back

**Figure 6. CART3D Aerodynamic Coefficient Results for Parawing at Various Mach Numbers**